A Chemical Synthesis Paradigm for *in utero* Repair of Spina Bifida

Sarah E. S. Michel

A dissertation submitted to the University of Bristol in accordance with the requirements for award of the degree of Doctor of Philosophy in the Faculty of Science, School of Chemistry, 20th of September 2019.

Number of words: 52478

Abstract

Spina Bifida - literally meaning "*split spine*" in Latin - is the most common birth defect with 0.2 % occurrence worldwide. It is due to foetus' spine failing to close during the first month of pregnancy, resulting in the exposure of nerves to the amniotic fluid, with permanent consequences affecting both cognitive and psychometric capacities. To date no treatment exists and the damage to the nerves is irreversible. However, a possible solution could lie in the so-called "double hit hypothesis", which conjectures that covering the opening in the spinal cord either with a material non-permeable to the amniotic-fluid would protect the nerves or with a matrix for the tissue to grow on would prevent the induced life-long complications.

This project aims to design, synthesize, and characterise biocompatible hydrogels from functionalised polymers and crosslinked microgels which would adhere to the spina bifida opening to form either a tough and highly flexible protective wound dressing that seals the nerves from the amniotic fluid or provide a scaffold for cells to spread on. Hydrogels appear as a material of choice in tissue engineering because of their elasticity and tensile strength very close to human tissues. Recent research in wound healing has highlighted the potential of polysaccharides as adhesive, biocompatible materials.

To this end, chitosan was derivatised with carbic anhydride to provide a range of functionalised polymers that could be crosslinked *via* thiol-ene photoclick chemistry. The mechanical properties of the resulting hydrogels could be varied by controlled and preliminary cell studied highlighted their potential applications in tissue engineering. Alternatively, microgels could be successfully prepared by using water-in-oil nano-emulsions as templates, with gelation facilitated by *in situ* photo-initiated cross-linking. Both materials presented limited cytotoxicity and demonstrated promising initial properties for *in utero* management of Spina Bifida. In the course of this study, unexpected gelation condition of chitosan was also observed which were not precedented in literature. A new gelation mechanism was proposed which could be of interest to the scientific community.

Acknowledgments

Firstly, I would like to thank my supervisors, Wuge Briscoe and Carmen Galan, for proving me wrong with my initial thoughts about sugar chemistry and polymer physics by offering me such a fascinating and challenging project, as well as for their continuous guidance and support.

I would like to address a very special thanks to Mark Denbow who is at the very heart of this project and whose passion convinced me to join the polymer chemistry side.

I thank Kevin Booker-Milburn and the Bristol Chemical Synthesis CDT who facilitated my undertaking a PhD and provided me with the opportunity to explore and discover many research areas. I am also grateful to EPSRC for funding.

I greatly benefitted from the help and expertise of several collaborators, including Craig Butts and Paul Lawrence who did a great job improving NMR conditions of my polymers, Jean-Charles Eloi for looking at the SEM of all these boring hydrogels and Judith Mantell for the TEM. I am also very grateful Sara Rogers and Jacques Jestin for their help on the Sans2d (ISIS, UK) and PA20 (LLB, France) beamlines which contributed to some of the results present in this thesis. I also thank Luke Elliott for his help with the photochemistry and Margaret Saunders who kindly provided me with some of her precious BeWo cells.

I would like to dedicate a very special thanks to the Briscoe and the Galan group members, present and past, who have always been there to help and support me through this PhD and who made the daily life – and the conferences! – so enjoyable and unforgettable. It is a very difficult task to name people without forgetting anyone, but I would particularly like to mention Lauren Matthews for her so precious experience with neutron scattering and beam lines, Anna Slastanova who always spots the little details that make a presentation so much better, Fabien Dutertre, Victoria Levario-Diaz who got me started with cell work, and the members of the new Galan lab and office who really make the days so enjoyable – Sylvain even if he keeps breaking my Lego stable, Shyam for bearing with me whatever my mood, and Teo, always so enthusiastic.

Finally, I would like to thank my parents Regine and Alain, my sisters Audrey and Julie and my boyfriend Tristan for their invaluable support – with a special mention to Julie for her sharp eye to align every pixel of my posters and getting me started on a graphic tablet for some of the illustrations of my thesis, and whose last trip in Bristol writing up with her really made a difference.

Author’s Declaration

I declare that the work in this dissertation was carried out in accordance with the requirements of the University's Regulations and Code of Practice for Research Degree Programmes and that it has not been submitted for any other academic award. Except where indicated by specific reference in the text, the work is the candidate's own work. Work done in collaboration with, or with the assistance of, others, is indicated as such. Any views expressed in the dissertation are those of the author.

SIGNED: ..... DATE:.....

Table of contents

List of Figures

List of Tables

List of Schemes

List of Abbreviation

AB ..... *Alamar Blue*

AcOH .....*Acetic acid*

AF .....*Amniotic fluid*

ALG .....*Alginate*

ASC.....*Amniotic stem cells*

ATRP .....*Atom transfer radical polymerisation*

CA ..... *Carbic anhydride*

calcein AM..... *acetoxymethylcalcein*

CDI..... *1, 1'-carbonyldiimidazole*

ChS..... *Chondroitin sulfate*

Col.....*Collagen*

Coum..... *Coumarin*

CS..... *Chitosan*

CuAAC . *Copper(I)-catalysed azide-alkyne cycloaddition*

Cys .....*Cysteine*

D *Deuterium*

DA..... *Diels Alder*

dab.....*Debye-Buesche-Anderson*

DCC .....*Dicyclohexylcarbodiimide*

Dex.....*Dextran*

d_h *Hydrodynamic diameter*

DI ..... *Deionised*

DIC.....*1,3-Diisopropylcarbodiimide*

DLS .....*Dynamic light scattering*

DMAc .....*Dimethylacetamide*

DMEM ..*Dulbecco`s modified eagle media*

DMF .....*Dimethylformamide*

DMSO .....*Dimethylsolfoxide*

DOPA.....*Dopamine*

DOSY ..... *Diffusion ordered spectroscopy*

DS ..... *Degree of substitution*

DTNB*5,5′ -dithio-bis(2-nitrobenzoic acid (Ellman's reagent)*

DTT.....*Dithiothreitol*

DVS .....*Divinyl sulfone*

DX.....*Double-crosslinked*

ECM..... *Extracellular matrix*

EDC .....*1-Ethyl-3-(3-dimethylaminopropyl)carbodiimide*

EDTA..... *Ethylenediaminetetraacetic acid*

EthD-III..... *Ethidium Homodimer III*

FDA ..... *Food and Drug Agency*

FTIR..... *Fourier-transform infrared spectroscopy*

G *Glucuronic acid*

G' ..... *Stotage (elastic) modulus*

G'' ..... *Loss (vicous) modulus*

GAG..... *Glycosaminoglycan*

Gel.....*Gelatin*

GlcN..... *D-glucosamine*

GlcNAc .....*N-acetyl-D-glucosamine*

HA.....*Hyaluronic acid*

HDF .....*Human dermal fibroblasts*

HLB ..... *Hydrophilic-lipophilic balance*

hMSC..... *Human mesenchymal stem cells*

HOBt.....*Hydroxybenzotriazole*

HRP..... *Horse-radish peroxidase*

HS .....*Heparin sulfate*

HS-PEG$_2$-SH..... *2,2′ -(ethylenedioxy)diethanethiol*

IEDDA ..... *Inverse-electron demand Diels Alder*

IRG.....*Irgacure 2959*

kDa.....*Kilodalton*

L_c *Correlation length*

LCST. *Lower critical solution temperature*

LVER .....*Linear viscoelastic region*

M *Mannuronic acid*

MAP..... *Microporous-annealed particle*

MES ..... 2-*ethanesulfonic acid*

MR .....*Microgel-reinforced*

MWCO.....*Molecular weight cut-off*

nb..... *Norbornene*

nb-*ald* ..... *norbornene-carboxyaldehyde*

nb-COOH...*Norbornene-2-carboxylic acid*

NHS.....*N-hydroxysuccinimide*

NSC.....*Neural stem cells*

o/w.....*Oil-in-water*

pAAm.....*Poly(acrylamide)*

PBS .....*Phosphate buffer saline*

PEG.....*Poly(ethylene glycol)*

pHEMA *Poly(2-hydroxyethylmethacrylate)*

PIT.....*Phase inversion temperature*

PLA ..... *poly(lactic acid)*

PLC .....*Poly(lactide caprolactone)*

pMAA .....*Poly(methacrylic) acid*

pNIPAM.....*Poly(N-isopropylacrylamide)*

PTFE .....*poly(tetrafluoroethylene)*

PVA.....*Poly(vinyl alcohol)*

PVAc..... *Poly(vinyl acetate)*

pVCL.....*Poly(N-vinyl caprolactam)*

RAFT ...*Reversible addition-fragmentation chain transfer polymerisation*

r_c *Core radius*

R_g*Radius of gyration*

RGD.....*Arginine-glycine-aspartate*

r_h *Hydrodynamic radius*

R_s *[SH]:[nb] molar ratio*

S80 .....*Span 80*

SANS .....*Small-angle neutron scattering*

SB .....*Spina Bifida*

SEM ..... *Scanning electron microscopy*

SLD.....*Scattering length density*

SPAAC ..... *Strain-promoted azide-alkyne cycloaddition*

SR..... *Swelling ratio*

T20..... *Tween 20*

T80..... *Tween 80*

TBA ..... *Tetrabutylammonium*

TCEP..... *tris(2-carboxyethyl)phosphine hydrochloride*

TCO ..... *trans-cyclooctene*

TEM.....*Transmission electron microscopy*

Tet-Coum.....*Coumarin-functionalised tetrazine*

TNB^{2-} .....*5-thio-2-nitrobenzoic acid*

TOC ..... *Total organic content*

TPP .....*Sodium tripolyphosphate*

TRASCET..... *Trans-amniotic stem cell therapy*

w/o..... *Water-in-oil*

ξ *Mesh size*

ν *Span 80: Tween 80 weight ratio*

Associated Publications and Contributions

Chapters 3, 4, 5 and 6 share many of its methods and results with a paper of which I am the first author:

> Michel, S. E. S.; Dutertre, F.; Denbow, M. L.; Galan, M. C.; Briscoe, W. H., Facile Synthesis of Chitosan-Based Hydrogels and Microgels through Thiol–Ene Photoclick Cross-Linking. *ACS Applied Bio Materials* **2019,** *2* (8), 3257-3268

Chapter 7 shares many of its methods and results with a Master Thesis which I supervised:

> Kilner, A. (2019) 'Studying the Effect of Chirality on the Properties of Chitosan Hydrogels'

Whilst all the data presented in this thesis is my own, some of it was obtained with the assistance and advice of my collaborators, who include Dr. L. Elliott (flow photochemistry), Dr S. Rogers and Dr J. Justin (SANS acquisition), Dr. J.C. Eloi (SEM), Dr J. Mantell (TEM), Dr. F. Dutertre (nano-emulsion formulation), L. Mathews (SANS analysis), A. Kilner (preliminary studies on hydrogel synthesis) and Dr. M. Saunders who kindly provided the BeWo cells.

1 Introduction

1.1 Spina Bifida

1.1.1 Definition, causes and consequences

Spina bifida (SB), literally “split spine” in Latin, is one of the most common malformations resulting from a failure in the neural tube closure during the first weeks of pregnancy with consequences ranging from loss of skin sensation in its least severe form – SB Occulta - to paralysis and mental disorders in its most significant form – SB Myelomeningocele- depending on the location and the severity of the defect (Figure 1-1).[1, 2] While the administration of folic acids in the early prenatal period and over the first month of pregnancy has been shown to prevent up to 70 % of SB cases,[3] the origins of this condition are not yet fully understood and are known to arise from both genetic and environmental factors[1].

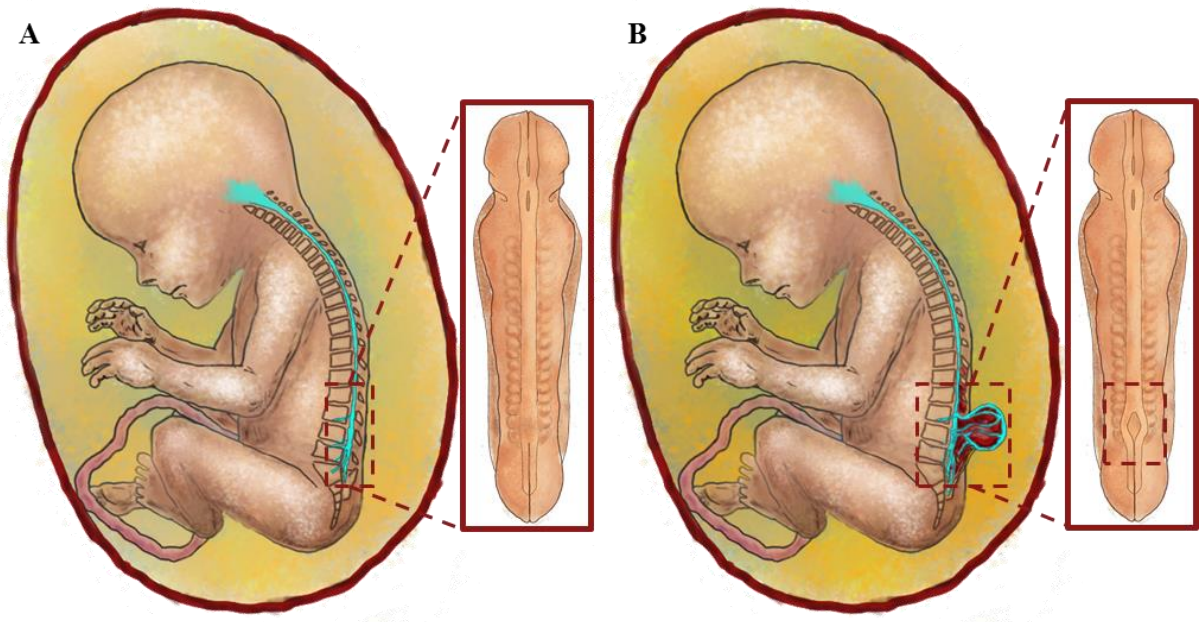

Figure 1-1. (A) Normal and (B) SB-complicated foetal development. Adapted from ref[4]

SB can be diagnosed within the first 20 weeks of gestation by ultrasound or by measuring the levels of acetylcholinesterase and α-fetoprotein in the amniotic fluid (AF).[1, 5,] Even if this diagnosis occurs fairly early on in pregnancy, no treatment is available to date. The wound is normally closed within 48 hours after birth, however this does not allow the repair of the related neurologic consequences, and individuals suffering from SB require lifelong medical assistance.[6]

1.1.2 Rationale for *in utero* therapy and preliminary results

In the 1990's, the concept of the double hit hypothesis emerged for the first time. The first hit refers to the failure of the neural tube to close, while the second one refers to the damage of the nerves occurring in the AF.[7] Much research has been conducted on sheep and mice showing that this second hit is mostly responsible for the observed life-long consequences.[8-10] In 2003 Kohl *et al.* used a poly(tetrafluoroethylene) (PTFE) patch to cover SB wounds in pregnant sheep.[11] The study showed that the patch efficiently sealed the nerves from the AF, enabling the sheep to give birth to healthy lambs in most cases. The introduction of the patch, however, required traumatic surgery to reach the foetus as well as stapling to be fixed around the wound, which can give rise to future complications.

Currently *in utero* surgeries are offered in the US and in some of Europe and have provided a significant improvement in the management of SB.[12] However, open foetal surgery remains extremely invasive and challenging owing to the small size of the defect, its difficult access and the complexity of the biological fluid around it (*i.e.* the AF). Classic surgical methods must be adapted to minimise post-traumatic surgery disorders.[13]

1.1.3 Design of an ideal material for a non-invasive treatment of Spina Bifida

More recently new biocompatible materials have been developed for surgeries, with very good sealing properties which reduce the need for stitching. While the small size of the defect makes *in utero* surgery highly challenging, it also designate the use of an injectable sealant as an incredibly simple alternative, as the defect is detectable early in pregnancy – while it is small and the damage to the nerves is still minimum - through echography and can be easily accessed with a needle.

The first improvement was the use of fetoscopy, a medical procedure involving a thin fibre optic tube, equipped with a camera, which is inserted in the uterus to allow for either foetus visualisation or to obtain amniotic samples. This technique, far less invasive than open surgery, is currently used for foetal surgeries. Common commercially available sealants, such as fibrin glue, failed to address SB requirements because of poor tissue adhesion and elasticity over time as the foetus grows.[14, 15] Over the last decade several synthetic or biopolymers have been used as sealants in SB-induced defects in sheep, with results ranging from improved epidermal ingrowth to reduced damage to the spinal cord and improved neurological functions. For example, Peiro *et al.*[16] and Fontecha *et al.*[17] used a silicone-based and a silicone/collagen-based sealant respectively, which completely covered the tissue and allowed for improved neuronal function. Fetoscopy, however, punctures the foetal membrane, possibly causing AF

leakages and complications.[18] Perrini *et al.* reported a catechol-functionalised branched poly(ethylene glycol) (PEG) polymer which successfully sealed the amniotic membrane in rabbits by mimicking the mussel catechol glue.[14, 19, 20] This very promising material is currently under investigation.

Although significantly more efficient than not covering the wound, this approach only allows to minimize further nerve damage and does not restore any lost neurological function nor repair the spinal cord and would be useless if performed too late in pregnancy.[21]

1.1.4 From a passive, protecting material to an active wound healing scaffold

Recent studies and reviews have highlighted the use of bioactive materials that favour cell regeneration and can be used as a scaffold for cells to grow and to regenerate the damaged tissue.[22-26] This strategy, called tissue engineering, takes advantage of a wide range of materials, derived from natural or synthetic polymers,[27] organic or inorganic,[28, 29] which can be formulated as hydrogels,[30] sponges, or fibres,[31] tailored to the targeted application. An increasing number of papers report the use of these systems in the management of chronic wounds,[32] severe burns[33] or neuronal defects[34, 35] with observations ranging from improved healing and wound closure to actual tissue regeneration, including neural tissues.

SB defects are excellent candidates for a tissue-engineering based approach, owing not only to the small size of the defect[13] but also to the unique *in utero* wound healing mechanisms, different from the adult, leading to more efficient and scarless wound closure.[36, 37] This is partly due to the amount of stem cells, growth factors and other key components present *in utero* involved in tissue regeneration. Therefore, designing a material able to take advantage of this environment is highly attractive.

Such bioactive coverings have been reported for the management of SB over the last decade,[12] although in relatively small number. Materials used include cellulose,[38] poly-(lactic acid) (PLA)[39] and poly(lactide caprolactone) (PLC).[40] Neural stem cells (NSC)[21, 40] have also been injected at the wound site. All these scaffolds were incorporated using surgery on mice and sheep. A better preservation of the spinal cord was systematically observed, as well as an improved closure of the defect with some neovascularisation and cell differentiation. Even if these studies constitute an important proof-of-concept for a tissue-engineering-based approach, none of them has achieved a complete coverage of the defect with a fully preserved neuronal function to date.

This last decade has also seen the emergence of stem cell-based therapies. Fauza *et al.* noticed that the use of NSC favoured spinal cord repair to born children or adults and decided

to inject NSCs to foetus bearing SB defects. The experiment, conducted on lamb models, showed significant improvements in the size reduction of the defect after as little as 14 days.[21] This pioneering work resulted in the development of trans-amniotic stem cell therapy (TRASCET) which showed very promising results on lambs,[41] dams[42] or rabbits.[43] Although promising in animals, these strategies have recently shown reduced efficiency in human clinical trials, and the incorporation of a matrix such as collagen (Col), polymer hydrogel or decellularizing tissues further supports cell growth. The incorporation of cytokines, neurotrophic factors or growth factors in these scaffold would allow preservation of the nerves, while favouring the formation of a new tissue.[44] Stem cells therapies, however, remain in their infancy and their approval by the food and drug agency (FDA) may hinder their applications.[45]

1.2 Project requirements: an injectable hydrogel for *in utero* repair of Spina Bifida

This project aims at developing an injectable scaffold that would cover the SB defect *in situ*, protect it from the AF and favour its healing. The liquid scaffold precursor would be injected using a fetoscope equipped with a sheath. The site of injection can be controlled by ultrasound, while the material should be generated *in situ* by curing at the proper wavelength, allowed by the optic tube (Figure 1-2). The generated material must then adhere strongly around the defect and protect it from the AF, while presenting lower adhesion to the foetal membrane or to other skin regions after its placement to prevent its displacement after injection. In addition, it must be non-toxic and sterilisable.

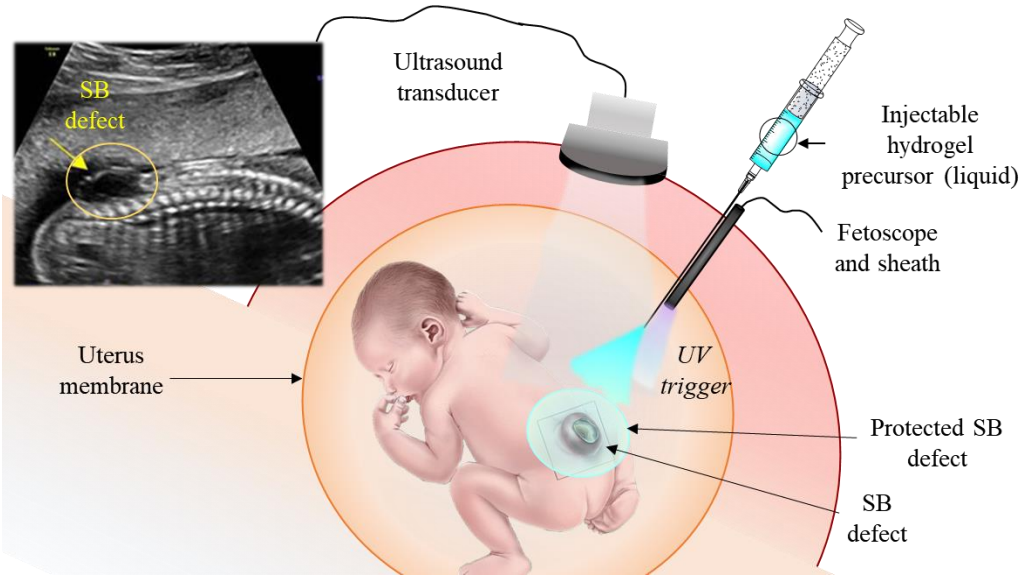

Figure 1-2. General approach to protect the SB defect in utero. Echograph photo from Foetal Treatment of New England website. The foetus illustration is taken from ref.[46]

Two main approaches can be envisaged, each with special requirements (Table 1-1): the design of a sealant which would cover the nerves over the whole duration of pregnancy, and a tissue engineering-based approach using a matrix to promote *in utero* tissue formation. In both approaches, the ability of the material to repair the neural tube will be essential; the sealants currently developed are not addressing this issue and must therefore be used early enough to limit further damage.

Table 1-1. Comparative requirements for the two approaches selected.

Property	**Selected Approach**	
	Tissue Engineering	**Sealant**
Immediate skin adhesion Low adhesion post-injection Injectability and in situ formation Sterilisation Non-toxicity Nerve repair	Required	
Defect repair	Required	Not required
Biodegradable	Required	Not required
Elasticity	Not required	Required
AF-impermeable	Not required	Required

An efficient sealant must present strong under-water adhesion, be sufficiently elastic to allow for its extension as the foetus grows, and limits AF contact with the nerves. As the material will only stimulate neural tube repair – and not the closure of the defect - it should not be biodegradable and therefore highly elastic to adapt to the growth of the foetus. If a sufficient elasticity cannot be achieved and the material is sufficiently easy to use, several injections through pregnancy can be considered.

On the other hand, the design of a matrix to promote cell growth and repair requires to be biodegradable with degradation kinetics matching the formation of the new tissues. No protection is expected to the AF and so the requirements for elasticity and strong adhesion are not as important. The incorporation of biomolecules and/or amniotic stem cells (ASC) should also be envisaged to favour adequate repair.

1.3 Hydrogels, a material of choice for tissue engineering

Ideal materials for wound dressings and tissue engineering are hydrogels as their swollen 3D structure is an excellent mimic of human tissues and provides an appropriate scaffold for cells to grow on.[30, 47, 48] Hydrogels are hydrophilic, macromolecular networks resulting from the cross-linking of water-soluble polymers swollen in water.[46] Their final properties can be adjusted according to the polymer chosen, the mode of cross-linking, as well as the synthesis conditions such as polymer concentration or degree of reticulation, allowing their design to be tailored to the need.

1.3.1 Hydrogel precursors

1.3.1.1 Biopolymers

Biopolymers are naturally occurring molecules which are divided into three classes: proteins, DNA and polysaccharides. Most are biodegradable and bioactive and are therefore highly attractive in biomedicine. Their resulting hydrogels are generally mechanically weak and often require chemical functionalisation to improve their properties.[47] They are also more heterogeneous in structure and suffer from greater batch-to-batch irregularities as they are extracted from natural sources.

The extracellular matrix (ECM) is a complex arrangement of proteoglycans and glycosaminoglycans (GAG) interacting with the membrane through intracellular protein receptors, such as β-glycans, CD44 or integrins, which promote adhesion through the well-known arginine-glycine-aspartate (RGD) peptide sequence (Figure 1-3). Hydrogels developed or functionalised with the natural substrate of these receptors favour cell adhesion and consequent growth and development. The most common materials used in tissue engineering are therefore based on proteins such as Col or fibronectin – both involved in integrin-mediated interactions – and on polysaccharides, in particular GAG such as hyaluronic acid (HA), chondroitin sulfate (ChS) or heparin sulfate (HS).[47] In particular, Col and HA are extensively used as they are the main components of ECM.[31] Col can present some immunogenicity as well as solubility issues because of its triple helix structure, and is therefore sometimes preferred in its denaturised form, gelatin (Gel), which retains several properties of Col such as the promotion of cell adhesion, proliferation and differentiation.[49] The incorporation of RGD peptides into hydrogels or synthetic precursors is a frequent technique to include biological adhesion mechanisms while limiting the incorporation of bigger proteins.[50]

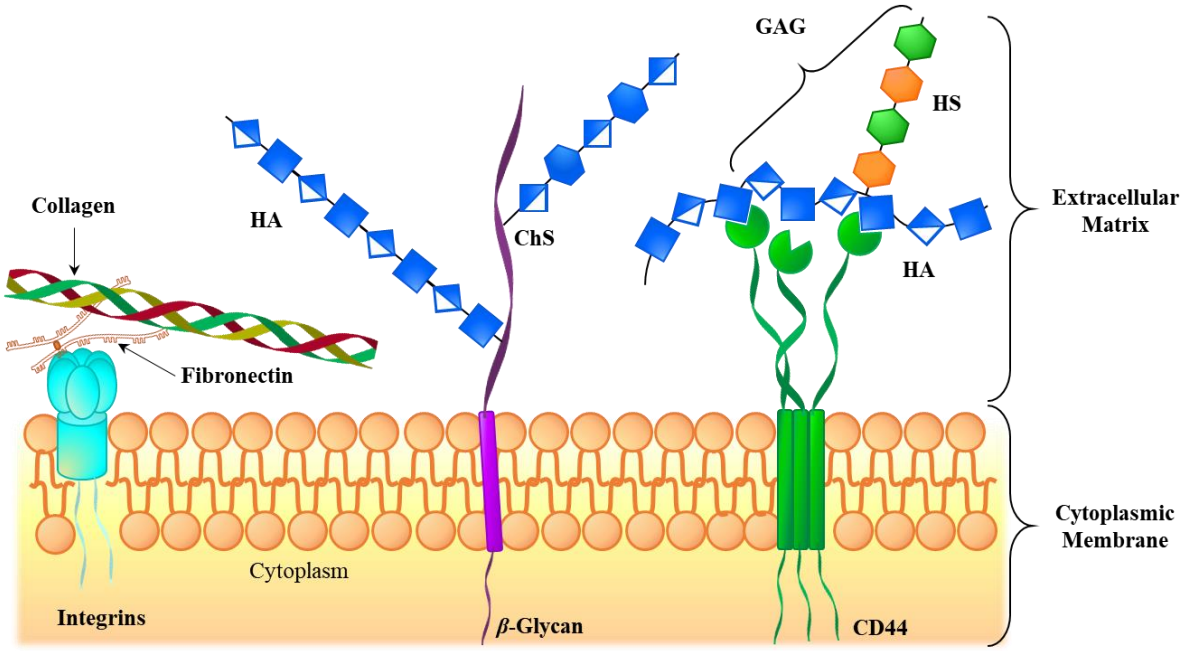

Figure 1-3. Schematic representation of the extracellular cell matrix (ECM) composition. Legend: HA: hyaluronic acid; ChS: chondroitin sulfate; HS: heparin sulfate, GAG: glycosaminoglycan.

1.3.1.2 Synthetic polymers

The first polymeric hydrogels were reported in 1960 by Wichterle *et al*. as crosslinked poly(2-hydroxyethylmethacrylate) (pHEMA) which was later used as contact lenses.[51] The field has then quickly expended to a wide range of monomers, among which PEG – a standard bioinert polymer[52] – poly(N-isopropylacrylamide) (pNIPAM) – widely used for its temperature-responsivity near body temperature[53] - and poly(urethanes) – frequently used in the fabrication of long-term implants[54] (Figure 1-4).

Synthetic polymers are highly desirable due to their reproducible properties and the close control over their structure, molecular weight and mechanical properties. However, their toxicity, their biodegradability and their ability to interact with biological environments and to stimulate wound healing should be carefully studied.[47, 55]

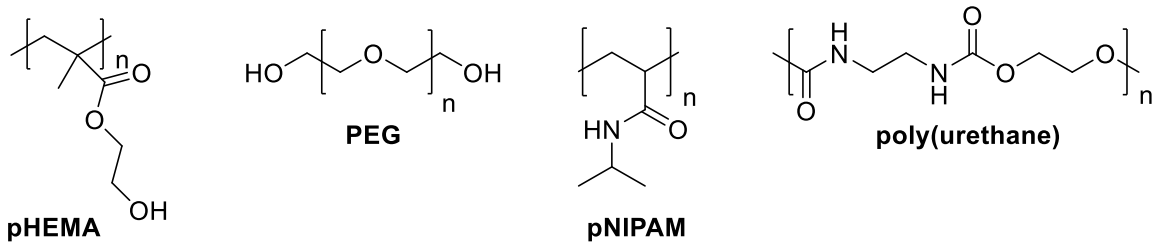

Figure 1-4. Commonly used synthetic polymers in biomedical hydrogels.

1.3.2 Hydrogel synthesis

Hydrogel formation results from the crosslinking between polymer chains through either physical interactions – such as electrostatic or hydrogen bond – or by the formation of covalent bond, also known as chemical crosslinking.

1.3.2.1 Chemical hydrogels

Chemical – or covalent – hydrogels are strong networks obtained either from the polymerisation of reactive monomers or by crosslinking pre-formed polymers. The structure of the parent polymers as well as an appropriate choice of crosslinking chemistry allows to control the final hydrogel architecture and in turn to tailor its mechanical properties to the intended application.[56] (Meth)acrylates are probably the most widely used polymer precursors due to the wide range of functional starting materials commercially or synthetically available and their efficient radical-mediated polymerisation. Although acrylate (co)polymerisation yields random networks, the development of sophisticated controlled polymerisation techniques, such as atom transfer radical polymerisation (ATRP)[57] or reversible addition-fragmentation chain transfer polymerisation (RAFT), allows fine tuning of the final polymer or hydrogel structure using macro-initiators, which has been shown to improve hydrogel degradation.[58] These polymers are synthetically more challenging to obtain and the reaction conditions, especially regarding the radical initiator toxicity, prevent their straightforward translation to hydrogel formation.

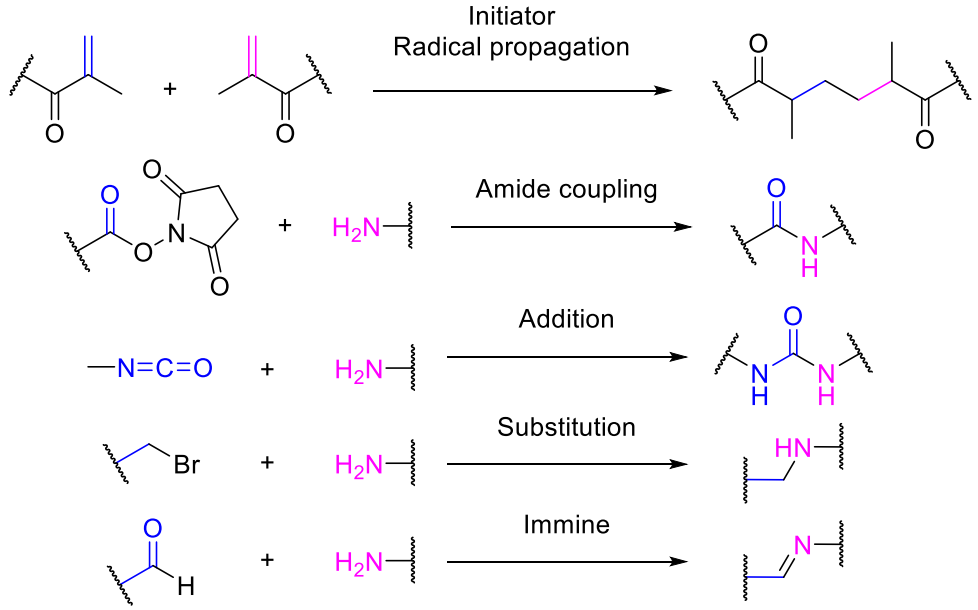

Scheme 1-1. Main reactions used for hydrogel synthesis.

A more accessible method to obtain a better control over the hydrogel network is to perform selective crosslinking through condensation reactions of complimentary functionalised polymer chains, with crosslinked tetra-arm PEGs of identical length generally considered as the gold standard for homogeneous networks.[59-61] A variety of reactions have been reported for this application, ranging from amide or ester formation – usually through N-hydroxysuccinimide (NHS)-activated chemistry[60] - to addition reactions involving haloalkanes,[62] isocyanates[63] or aldehydes.[64] These reagents, however, are extremely reactive and not compatible with physiological conditions as side reactions are extremely likely. Enzyme-mediated crosslinking can also be performed between specific amino acid residues, for example tyrosine oxidation mediated by horse-radish peroxidase (HRP); HRP however can induce immunological response *in* vivo, and the required use of H_2O_2 can lead to cell toxicity.[65]

Materials chemistry greatly benefitted from the development of click chemistry, a term defined by Sharpless in 2001 as a high yielding, biorthogonal reaction proceeding even at low concentrations of reactive groups and under physiological conditions.[66-68] The most famous click reaction is the copper(I)-catalysed azide-alkyne cycloaddition (CuAAC). To bypass copper toxicity various copper-free alternatives have been developed, such as Diels Alder (DA), inverse-electron demand Diels Alder (IEDDA), strain-promoted azide-alkyne cycloaddition (SPAAC) or photo-initiated thiol-ene. Although strain-promoted reactions are extremely attractive due to their near entire biocompatibility and extremely fast reaction kinetics, they are also synthetically challenging, with expensive starting materials, several steps and/or toxic catalysts needed, thus highly hindering their scale up and their wide application. Click chemistry also requires to pre-functionalise the polymers, which may be challenging with biopolymers.[66, 69]

In this context, the radical-mediated thiol-ene photoclick (Figure 1-5) reaction is a very attractive compromise, as it takes advantage of widely available alkenes and thiols starting materials, the latter being readily incorporated into peptides or proteins *via* cysteine (Cys) residues. In addition, the thiol-ene is photo-activated, which provides spatio-temporal control over the crosslinking process,[70] while several biocompatible, visible-light activated photoinitiators have been successfully employed, such as Eosin Y[71] or riboflavin.[72] Although technically a low-wavelength (260 nm) UV photoinitiator, Irgacure 2959 (IRG) remains the most commonly used, as it can generate enough radicals to initiate gelation when excited at 365 nm.[73] The thiol-ene is often compared to or confused with the base-catalysed nucleophilic thiol-Michael addition between thiols and activated alkenes such as (meth)acrylates or

maleimides.[74] While widely used, undesired acrylate copolymerisation[75] or disulphide bond formation – favoured under basic conditions[76] – can occur, while thiol-maleimide reaction can be reverted under acidic conditions.[77]

Table 1-2. Common click-chemistry reactions in hydrogel synthesis and their main characteristics.

Reaction	Advantages	Limitations	Ref
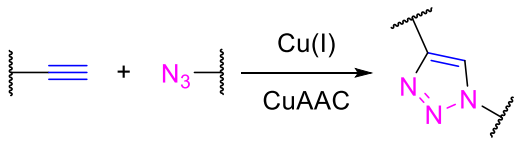	Biorthogonal Available reagents	Copper toxicity	*78-80*
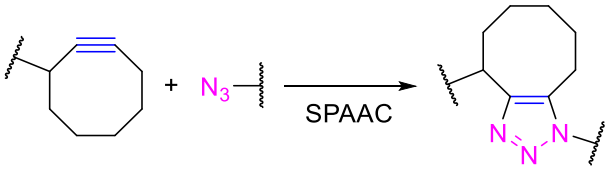	Biorthogonal Copper-free	Cyclooctyne synthetic availability	*81, 82*
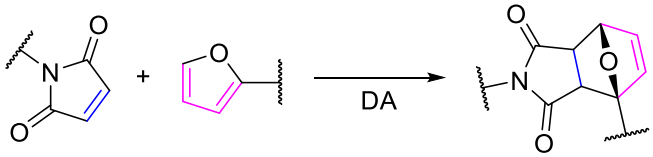	Thermoreversible Facilitated in water	Slow kinetics Competition with thiols	*83-85*
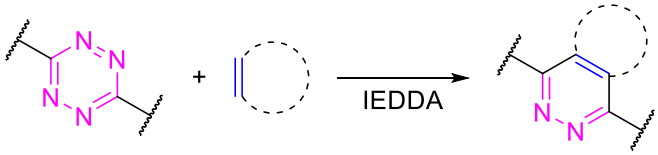	Biorthogonal Copper-free Fast kinetics	N_2 side-product Tetrazine synthesis	*86-89*
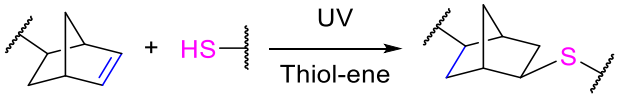	Spatiotemporal control Fast kinetics Available reagents	Possible radical toxicity Competition with thiols	*90-93*

The thiol-ene, on the other hand, can benefit from norbornene (nb), a bicyclic strained alkene highly stable under physiological conditions yet highly reactive towards radicals driven by the strain release from an sp^2 alkene to an sp^3 alkane (Figure 1-5).[94, 95] Nb-based thiol-ene are not very sensitive to oxygen, highly advantageous over other radical-mediated reactions, and the gelation kinetics can be controlled by varying the power of the excitation source and the photoinitiator concentration, while the curing time impacts on the final material

properties.[70, 75] Several examples of thiol-ene hydrogels have been reported, based on either synthetic or on biopolymers – Gel,[96] alginate (ALG),[97] HA[98] – with very fast gelation kinetics and highly attractive properties for biomedical applications such as stem cells encapsulation,[99] controlled drug release,[75] photopatterning[98] or cell culture.[72]

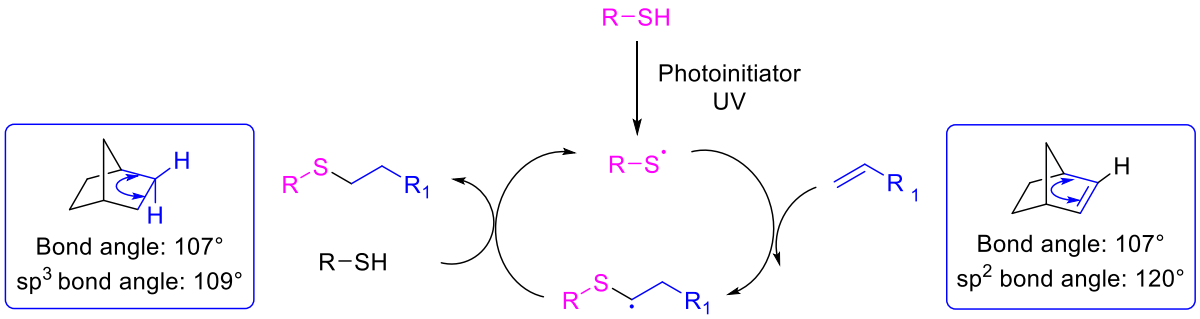

Figure 1-5. Thiol-ene mechanism and the bond angle release occurring in norbornene.

1.3.2.2 Physical hydrogels

Physical hydrogels result from non-covalent crosslinking mechanisms of the polymer chains through hydrogen bonds, ionic associations, metal coordination, hydrophobic interactions, host-guest inclusion complexes formation and chain entanglement.[56] Unlike their chemical counterparts, gelation is very quick and can be triggered through a wide variety of stimuli such as pH, temperature or ionic strength; all these mechanisms are generally reversible and can be used in self-healing strategies.[100-102] Although strong networks can be obtained, no control over the final structure is possible due to the random formation of crosslinking points.[59]

The most common example of biologically relevant physical hydrogel is probably pNIPAM, whose chain conformation in water transforms at 32°C from a solvated to a collapsed state driven by strong hydrogen bond interactions. This lower critical solution temperature (LCST), very close to body temperature, has driven a considerable interest for drug delivery applications or for *in situ* applications. A similar transition occurs for Gel, which undergoes a sol-gel transition below 25°C due to the formation of triple helixes.[103] Ionic hydrogels can be obtained from ALG in presence of several di- or trivalent ions such as Ca^{2+}, Ba^{2+} Sr^{2+} or Fe^{3+}.[104, 105] The catechol moieties or dopamine (DOPA), inspired by the mussel adhesive protein, is also widely used in the design of biomedical sealants due to its high adhesion which can be modified by varying the pH or the concentration of Fe^{3+}.[18, 106]

1.3.3 Microgels

Microgels are crosslinked polymer colloids that swell in a good solvent or when the pH approaches the pK_a of the polymer subchains if these comprise polyacids or polybases.[107] As opposed to nanoparticles they are soft, deformable and can swell or deswell in response to

external environment while retaining a 3D structure.[108] Their application in the biomedical area takes advantage of their highly swollen core which can be loaded with drugs and biological molecules to protect and slowly release them.[109] More recently, they have also been incorporated into macroscopic hydrogels to improve their properties.[110] Microgels obtained from monomers are typically obtained by precipitation polymerisation, while the use of pre-formed polymers generally relies on nano-emulsion templates.

1.3.3.1 Microgel synthesis through nano-emulsions

Nano-emulsions are kinetically stable liquid-in-liquid dispersions with droplet dimensions below 100 nm stabilised by surfactants, which lowers the surface tension at the oil/water interface.[111, 112] They are termed oil-in-water (*o/w*) – "normal" - or water-in-oil (*w/*o) – "reverse" - nano-emulsions depending on the dispersed phase and have found tremendous applications in the food industry, biomedical area, or as template to the synthesis of more complex structures. As opposed to micro-emulsions, they are not thermodynamically stable and require an energy input, typically shearing or sonication (Figure 1-6); low-energy methods also exist, like phase inversion temperature (PIT), routinely used in industry.[112] Although efficient, high-energy methods can damage fragile biomolecules, leading for example to polysaccharide depolymerisation.[113]

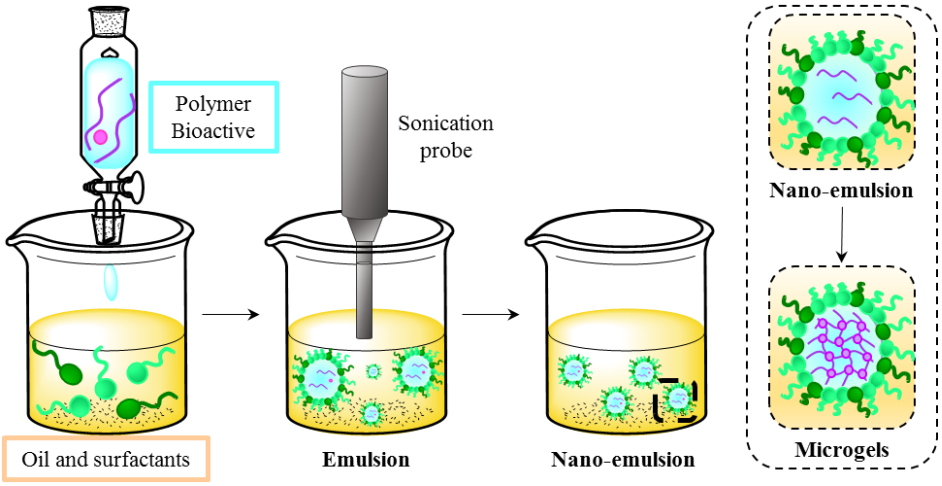

Figure 1-6. W/o nano-emulsion templated synthesis of microgels through high energy methods.

The surfactant plays a crucial role in the nano-emulsion stabilisation and must be chosen carefully. Their properties greatly depend on their structure; for example, non-ionic surfactants – like the Span and Tween family presented in Figure 1-7 - are generally preferred to stabilise charged polymers emulsions.[114] As a general guideline in the choice of an adequate surfactant system, the hydrophilic-lipophilic balance (HLB) system developed by Griffin can be used, whereby the amount of hydrophilic and hydrophobic groups present on the surfactant

is quantified and ranked between 0 (completely hydrophobic) and 20 (purely hydrophilic).[115] The more stable emulsion for a given class of surfactants will be obtained by matching the HLB value of the surfactant mixture with the one of the continuous phase. Typically *w/o* and *o/w* emulsions require HLB < 10 and HLB > 10 respectively.[116]

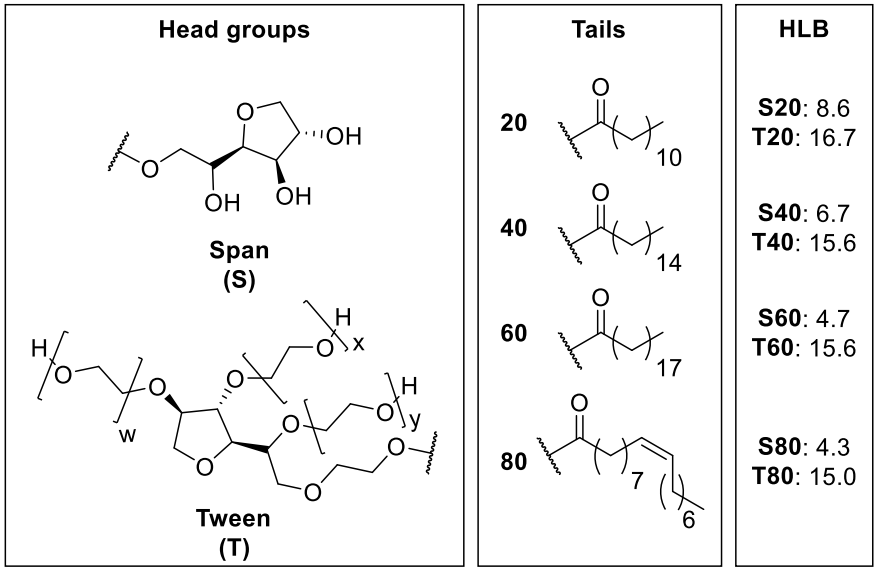

Figure 1-7. Structure and HLB values of selected surfactants of the Span and Tween family.

Nano-emulsions destabilisation mostly occurs through Ostwald ripening, whereby droplets of different sizes grow at different rate due to their different solubility in the continuous phase. Although nano-emulsions' small dimensions and fast diffusion generally prevents them from creaming, Ostwald ripening can lead to coalescence or flocculation and eventually to creaming (Figure 1-8). All these mechanisms have been widely studied and the incorporation of a third component, such as a hydrophobe trapped in the droplets[117] or a co-surfactant of different HLB, can improve the stability by modifying the droplet diffusion rate.[118] Theoretical models to predict nano-emulsion stability[119] and droplet dimensions have been reported and are summarised elsewhere.[119]

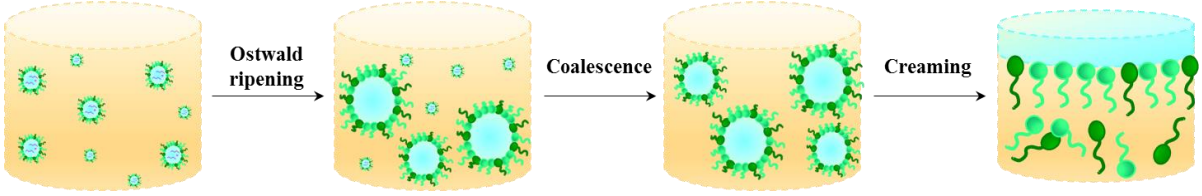

Figure 1-8. Nano-emulsion destabilisation by Ostwald ripening leading creaming.

Compared to precipitation polymerisation techniques, emulsions are general templates as they do not require special properties from the gel precursor while allowing control over the droplet size by varying the nano-emulsion composition. It has been shown that unlike micro-

emulsions, nano-emulsion droplets can be considered as nano-reactors stable over the polymerisation process, as they are not subject to a loss of thermodynamic stability as the reaction progresses.[117] It is worth noting that the crosslinking of pre-formed polymers is different from polymerisation reactions as all components should be initially present in the micro-emulsion reactor, although the excess of surfactant and empty micelles may affect their repartition.

Microgels can be obtained by *w/o* nano-emulsions, where a polymer (or hydrophilic monomer)-rich water phase is dispersed in an oil phase containing surfactants, which absorb at the droplet surface, thus improving its stability. Gelation is then triggered by the addition of the crosslinking reagent or by applying the appropriate stimulus, such as a temperature change (Figure 1-6). The microgels are finally recovered and washed from residual surfactants by centrifugation, precipitation or dialysis. Water-soluble molecules like drugs or bioactives can be encapsulated in the microgels by dissolving them with the polymer prior to gelation.[109] Nano-emulsion templates have been successfully used for the synthesis of both synthetic and biopolymer microgels like PEG,[120]ALG[121], dextran (Dex)[122] or HA.[123]

1.3.3.2 Hydrogels containing microgels

As discussed in section 1.3.1 hydrogels are generally weak materials and their inner structure – *i.e.* the nature of the crosslinks and their ability to dissipate stress - is key to their mechanical properties: in a non-homogeneous network, the stress concentrates in the weakest areas, leading to ruptures (Figure 1-9A). Although homogeneous hydrogel networks can be obtained – as illustrated in section 1.3.2.1 with tetra-arm PEGs[59] and RAFT pNIPAM hydrogels[58] for example – they require synthetic efforts to obtain very specific architectures from the monomers and are not applicable to biopolymers. Due to their softness and deformability, the use of microgels as hydrogel crosslinkers should allow for this energy dissipation, while broadening the range of hydrogel precursor available; their homogeneous distribution in the gel matrix is ensured by their solubility (Figure 1-9B).[124]

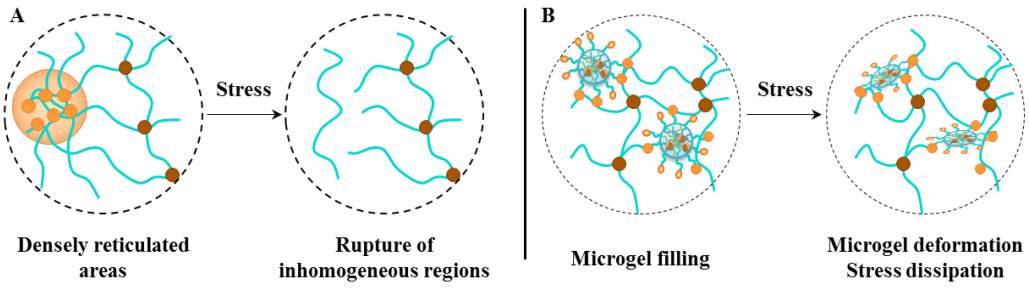

Figure 1-9. Stress dissipation in (A) a hydrogel without and (B) with microgel filling.

Hu *et al.* reported microgel-reinforced (MR) hydrogels by the incorporation of monodisperse microgels into poly(acrylamide) (pAAm) matrix. The microgels (5 μm in diameter) were synthesized from either cationic, anionic and neutral precursors and were incorporated in the synthesis process through acrylate polymerisation. The hydrogel mechanical resistance was greatly improved by the incorporation of the microgels, independently of their charge, which was attributed to the different moduli of the microgels compared to the hydrogel.[124, 125] The microgels were not covalently bonded to the network in this study.

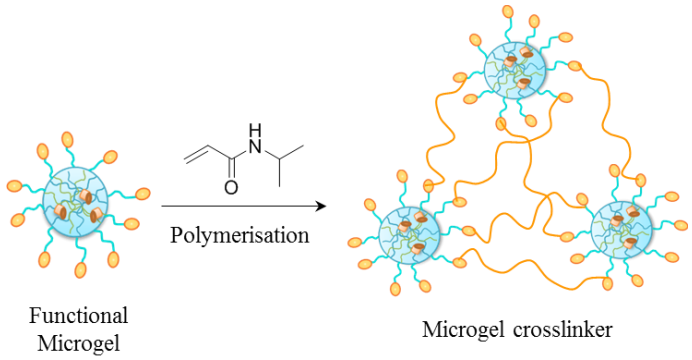

Figure 1-10. Covalent incorporation of microgel in hydrogels.

A year later, Li *et al*. reported pAAm hydrogels crosslinked with amine-functionalised pNIPAM microgels (Figure 1-10). The properties of the final material were greatly dependant on the grafting density and the amount of microgels incorporated, with higher microgel content leading to decreased swellings and improved rheological properties and stress resistance – up to 150 times. A comparison with physically entrapped pNIPAM microgels showed comparable resistance, but a leakage of the microgels occurred with time, probably due to their smaller diameters (~ 0.5 – 1.5 μm). More interestingly, pNIPAM microgels conferred thermo-responsivity to the hydrogels closed to 32°C, although the transition was not as sharp as for the pure microgels.[126] The incorporation of pNIPAM microgels into pNIPAM hydrogels also resulted in faster shrinkage and presented an improvement of the release of encapsulated Rhodamine B of 20 to 80%, attributed to the faster response of the microgels compared to the bulk macrogels (Figure 1-11).[127]

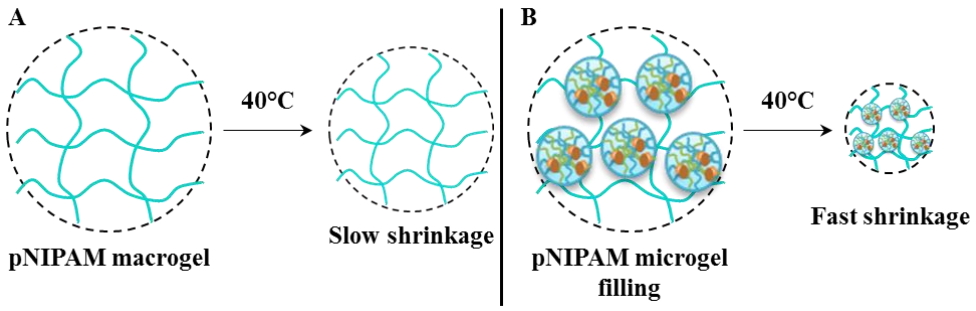

Figure 1-11. (A) Temperature response of pNIPAM macrogels and (B) with pNIPAM filling.

Microgels were also used as crosslinkers to generate hydrogels from pre-formed polymers. Sivakumaran *et al.* reported the covalent or physical incorporation of pNIPAM microgels into covalently crosslinked hydrazide-functionalised carboxymethyl cellulose/oxidised Dex hydrogels as a drug release system. Covalently incorporated microgels improved only slightly the mechanical properties but drastically decreased the initial burst effect and the overall drug release due to constriction in the microgel structure.[128] Due to their higher surface area and faster response towards physico-chemical stimuli microgels offer consequent improvement in drug delivery applications.[129]

The incorporation of microgels into hydrogels have proven highly valuable for tissue engineering as it provides fine tuning over the pore size and mechanical properties while allowing for microgel functionalisation or loading with bioactives or cells to promote cell adhesion or differentiation.[129, 130] Douglas *et al*. took advantage of the incorporation of loosely crosslinked pNIPAM microgels into fibrin hydrogels as a very simple way to introduce pores of controlled dimension in a gel network, allowing for concomitant high, clinical fibrin concentrations to be reached while maintaining mesh sizes favourable for cell infiltration (Figure 1-12).[131] As the microgel only allowed for the incorporation of a fixed mesh size, the methodology should be applicable to a wide range of chemical structures bearing possible functionalisation. HA microgels were also covalently crosslinked with HA polymers through hydrazone[132] or photochemistry,[133] improving the hydrogel enzymatic stability while retaining their non-toxicity. Finally, Rose *et al.* encapsulated superparamagnetic iron oxide nanoparticles in RGD-functionalised hexa-arm PEG microgels which were magnetically aligned and consequently congealed by embedding into a hydrogel network. The use of microgels allowed for reduced iron-induced cell toxicity while their functionalisation was required for cell adhesion; the magnetic alignment recreated anisotropic matrixes known to impact on cell guidance and ultimately wound healing. The functionalisation of the microgels as well as the

polymer chosen as hydrogel precursor shed light on cell interactions and fibrin production relevant to tissue engineering.[134]

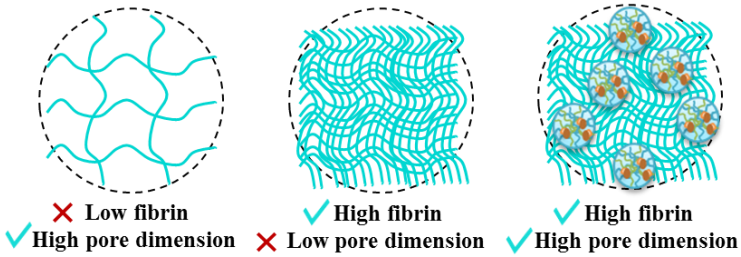

Figure 1-12. Application of microgel-filling concentrated fibrin hydrogel porous networks.

1.3.3.3 Microgels as reactive monomers

Hu *et al.* took advantage of the very fast response of microgels to external stimuli to design new hydrogel networks from the covalent binding of gel microparticles. Temperature-responsive microgels derived from divinyl sulfone (DVS)-crosslinked hydroxypropyl cellulose were successfully reacted together in the presence of DVS to yield a structured hydrogel whose temperature-induced shrinkage was twice as fast as the macro hydrogel's (Figure 1-13). The concept was extended to various other microgels such as pNIPAM or poly(vinyl alcohol) (PVA) with nm dimensions which could also be combined, suggesting the versatility of the method.[135] Similar work was performed by Cho *et al.* where amine-functionalised pNIPAM microgels were crosslinked with glutaraldehyde. The resulting hydrogels maintained their shape and presented twice as fast shrinking kinetics which were not impacted by the addition of fluorescent moieties or silica particles.[136]

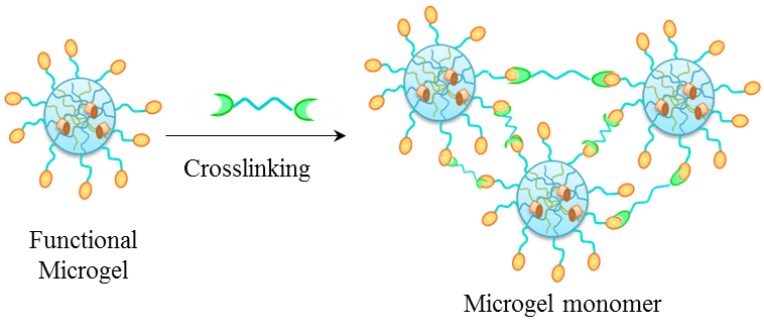

Figure 1-13. Crosslinker-mediated microgel assembly into hydrogel.

Microgels as monomers have recently proven very advantageous in tissue engineering. Pioneering work was performed by Griffin *et al.* with multi-arm PEG microgels decorated with RGD and transglutaminase peptides bearing vinyl sulfones. The PEG microgels were crosslinked by metalloprotease cleavable peptides bearing Cys residues and further crosslinked together through amide bond facilitated by the Factor XIII enzyme using the transglutaminase

peptides. The resulting hydrogel, termed microporous-annealed particle (MAP), presented homogeneous networks with pore size ranging between 10 to 35 μm from microgel building blocks of ~ 30 – 150 μm in diameter. The resulting hydrogels were injectable and modulable, supported fibroblasts and human mesenchymal stem cells (hMSC) growth and invasion, while presenting faster healing abilities and lower immune response compared to the analogue hydrogel, which was attributed to their unique connected porosity.[137] Willits *et al.* later used similar PEG microgels crosslinked in the presence of Col to design hydrogels of similar internal structure but whose stiffness could be easily tuned from 0.1 to 0.8 kPa. All substrates supported efficiently the growth of Schwann cells, whose role in neural regeneration is crucial.[138] Xin *et al.* used thiol-ene crosslinked, RGD-decorated PEG microgels to design MAP hydrogels which successfully supported hMSC encapsulation and growth with significant effect of the network mechanical properties which could be efficiently adjusted by changing the crosslinking density.[139]

All the microgel crosslinking presented above required the addition of a crosslinker. Liu *et al.* focused on the direct crosslinking of a residual functional group present on the microgel surface. Poly(methacrylic) acid (pMAA) copolymer microgels were synthesized by emulsion polymerisation and further decorated with methacrylate moieties. The resulting microgels were suspended in water and subsequently swollen under basic conditions due to the carboxylate moieties, resulting in shell inter-penetration bringing the methacrylate functions in proximity. Subsequent crosslinking was performed through radical-initiated methacrylate polymerisation (Figure 1-14).[140] This methodology was successfully applied to other weak polyacids, crosslinkable shell[141] or polybases, as demonstrated with poly(vinyl amine) microgels,[142] the only technical requirement being to perform the swelling step prior to crosslinking in an appropriate pH range. The resulting networks, termed double-crosslinked (DX) microgels, presented excellent mechanical properties and minimal swelling. Compared to the PEG crosslinked microgels presented above they possess very small porosity due to the small size of the microgel monomers (< 350 nm) and their very close proximity imposed by the absence of crosslinker. The properties of DX hydrogels could be further controlled by modifying the microgel initial structure[143] or crosslinking different microgel populations[144] while the monomer design allowed to incorporate more functionality.[145] These DX hydrogels hold promising potential as degenerated intervertebral disc replacement,[146] currently under clinical investigations[130] and have been recently used as nanoprobes for the sensing of hydrogel environmental changes.[147]

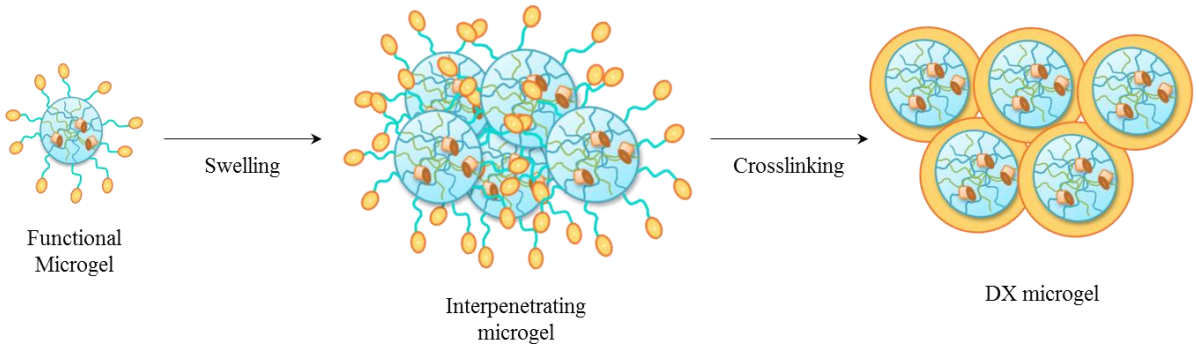

Figure 1-14. Synthesis of double crosslinked (DX) microgels.

1.4 Polysaccharide-based materials

While synthetic polymers provide flexibility over the final material properties, they often lack biological features required for essential cell interactions, as discussed in section 1.3.1.2. Among biopolymers, polysaccharides have greatly contributed to the development of tissue engineering and to the biomedical field in general as cheap and abundant yet biocompatible, biodegradable and bioactive materials owing to their similarities with the GAG and glycoproteins of the ECM. Although most of them present a high charge density often used to design physical hydrogels, they also contain numerous functional groups of different reactivities enabling their crosslinking and tailored functionalisation. The main limits of polysaccharides reside in their polydisperse structure regarding molecular weight distribution or monomer arrangement.[148-150] The polysaccharides most commonly used in wound healing or tissue engineering, summarised in Table 1-3, will be presented with their main characteristics followed by polysaccharide functionalisation strategies.

1.4.1 Polysaccharides in tissue engineering and wound healing

1.4.1.1 Alginate

ALG is an anionic linear polysaccharide extracted from several algae from the brown sea weed family[151] composed of repeating disaccharide units of β-1,4-D-mannuronic acid (M) and α-1,4-L-guluronic acid (G) residues.[148] As discussed in section 1.3.2.2 ALG G blocks interact strongly with divalent ions such as calcium or barium to generate ionic gels whose properties are therefore directly dependent on the M/G ratio.[104, 151, 152] ALG does not support cell growth and need to be preliminary functionalised either with RGD[152] peptides or by $NaIO_4$ oxidation to incorporate aldehyde moieties, resulting in both better degradation rates and improved cell adhesion through covalent bonds. Oxidised ALG, however, yields weaker gels compared to native ALG, and is generally mixed with polyamines to generate covalent hydrogels through

Schiff base crosslinking.[153] In this respect the lysine residues of Gel designate it as an attractive crosslinker as it also provides the missing cell adhesion motives of ALG.[154] Chitosan (CS) crosslinkers have also been reported for liver tissue engineering.[155]

Table 1-3. Commonly used polysaccharides in wound healing and tissue engineering.

Polysaccharide	Benefits	Limitations
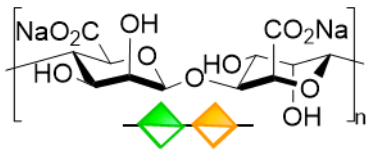 **Alginate** (ALG)	Ionic gelation No enzymatic degradation Promotes cell spheroids Poor protein binding affinity	Poor mechanical properties Cell adhesion requires functionalisation
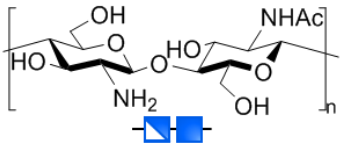 **Chitosan** (CS)	Antimicrobial Structurally similar to GAG Promotes wound healing and neural repair	Brittle Solubility issues
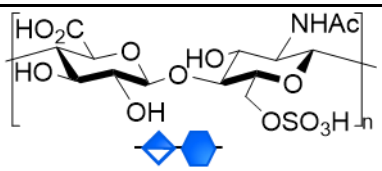 **Chondroitin sulfate** (ChS)	Chondro-protective Anti-inflammatory Cartilage component Proteoglycan structure	Highly hydrophilic Solvability
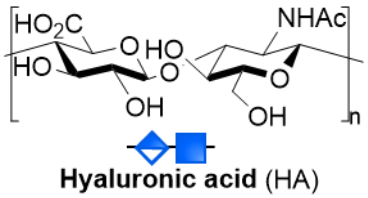 **Hyaluronic acid** (HA)	High viscoelasticity Chondro-protective ECM component Promotes cell proliferation and adhesion	Poor mechanical properties Fast enzymatic degradation

1.4.1.2 Chitosan

CS is the only cationic natural polysaccharide consisting of *β*-1,4-D-glucosamine (GlcN) and *β*-1,4-N-acetyl-D-glucosamine (GlcNAc) units. CS is generally obtained by deacetylation of at least 50 % of GlcNAc residues of chitin.[156] The presence of free amines imparts CS with mucoadhesion properties, haemostatic action and antibacterial activity, while its similarities with GAGs provide a favourable environment for cell adhesion or proliferation.[157-160] CS hydrogels can be easily obtained by simple mixing with polyanions like ALG or sodium tripolyphosphate (TPP); alternatively covalent hydrogels can be obtained by exploiting the

high nucleophilicity of its amine groups with glutaraldehyde or genipin. While both crosslinking procedures are fast, they yield heterogeneous networks and the crosslinkers are also susceptible to self-polymerise; in addition, unreacted glutaraldehyde presents significant toxicity.[159]

These inherent properties, along with CS good processability and easy functionalisation have placed it under the spotlights of not only the biomedical area, but also in wastewater treatment,[113] food packaging[161] or cosmetics.[162] CS micro- and hydrogels have shown particularly promising applications in wound healing and tissue engineering as they allow for efficient delivery of fragile bioactives such as growth factors or proteins.[150, 157, 159, 163] In addition, CS alone induces wound healing, enhances vascularisation and reduces scaring. It was also shown to support attachment and proliferation of various cell lines such as fibroblasts, nerve cells or chondrocytes.[164, 165]

1.4.1.3 Chondroitin sulfate

ChS is an anionic linear glycosaminoglycan consisting of *β*-1,4-D-glucuronic acid and *β*-1,3-N-acetyl galactosamine units bearing sulfate groups either at the 4 or at the 6 position. ChS is a key component of cartilages and presents both anti-inflammatory and chondro-protective activities, promotes proteoglycan secretion and tissue integration, and ultimately wound healing and cartilage repair. ChS sulfation profile – *i.e.* the location and the amount – triggers different cell interactions or biological pathways and achieving selective sulfation of polysaccharides is of particular interest in research.[148, 166] ChS high solubility, however, requires its incorporation in other matrixes to achieve sufficient stability and mechanical properties. ChS is frequently combined with HA and Col or Gel to recreate artificial ECM,[167] while CS/ChS scaffolds have shown promising applications in wound healing.[168, 169]

1.4.1.4 Hyaluronic acid

HA is an anionic linear glycosaminoglycan consisting of alternating *β*-1,4-glucuronic acid and *β*-1,3-N-acetylglucosamine units. As a key component of synovial fluid, cartilage and extracellular matrix, it has been widely used for biomedical applications as drug delivery vector or tissue engineering scaffold.[170, 171] Although it presents several remarkable properties, such as lubrification, shock absorption, stimulation of chondrocyte metabolism and several chondroprotective roles, it presents very poor mechanical properties and a very fast biodegradation.[148] Chemical modification, including intramolecular crosslinking[98, 172] and polymer conjugation,[170] are frequently used to overcome these limits. More recently the ability

of HA to bind to CD44 receptors has also attracted a great interest for targeted drug delivery strategies.[173, 174]

1.4.2 Polysaccharide functionalisation

Polysaccharides greatly benefit from chemical functionalisation to improve their mechanical properties either by more selective crosslinking methods or by the grafting of other polymers.

1.4.2.1 General routes for polysaccharide functionalisation: hydroxyl functions

Polysaccharides present several hydroxyl groups that can be functionalised as esters, ethers or carbamates (Scheme 1-2).[175] Although it is generally accepted that the substitution will favour the primary O6 position, mixtures of products are generally obtained, with similar reactivities of the secondary hydroxyl groups observed; the O2 position is some time preferred over the others for steric hindrance, [176] but complete control requires several protecting group modifications. [177, 178] Selective modification can be obtained with selective enzymes such as galactose-6-oxidase but with a severe limitation regarding the substrate scope. In addition, polysaccharide functionalisation is typically performed in water due to their poor solubility in organic solvent, and the competition between the nucleophilicity of the hydroxyl groups and that of water yields very poor degree of substitution (DS).[176]

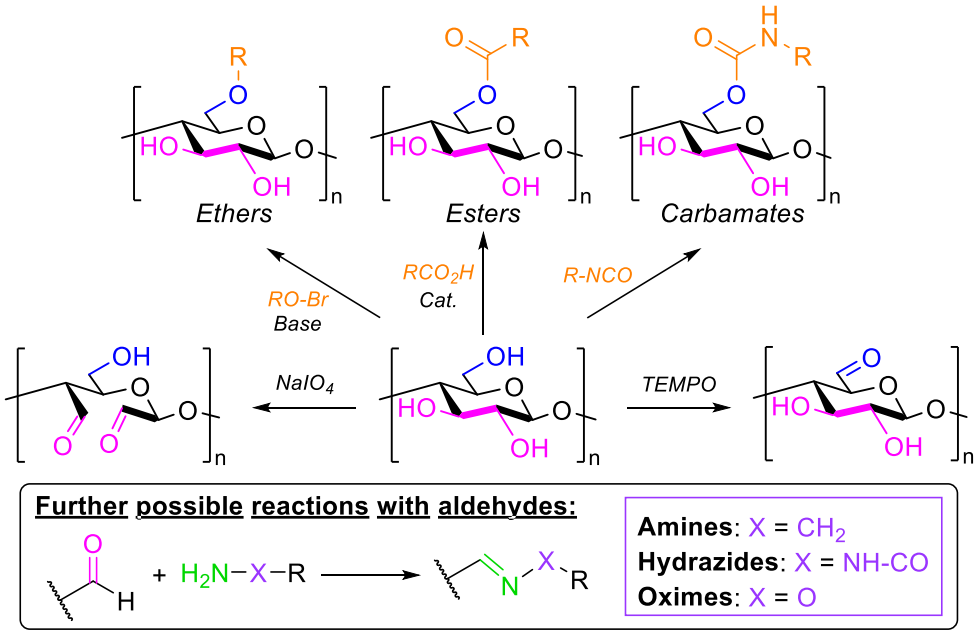

Scheme 1-2. Main reactions involving hydroxyl moieties onto polysaccharides.

Selective hydroxyl groups functionalisation exploits oxidation of primary alcohols into aldehydes using TEMPO[179, 180] or Dess Martin.[181] TEMPO oxidation is very common among polysaccharides but the pH and the amount of co-oxidising agent used – typically H_2O_2, NaOCl or enzymes - must be carefully controlled to prevent further oxidation into carboxylic acid.[179,

[182] Aldehydes can also be selectively obtained by the cleavage of *syn* diols mediated by $NaIO_4$[183] or enzymes.[184] The introduction of aldehyde groups both increases the water-solubility of polysaccharides[185] and provides a useful handle for selective functionalisation *via* reductive amination,[186] Schiff base formation,[187] hydrazide addition[188] or oxime ligation.[189] It is worth noting that CS oxidation with TEMPO leads to immediate reaction with the amine groups.[190]

1.4.2.2 Polysaccharide functionalisation through carboxylic acid functions

Carboxylic acids – either naturally present as for HA or introduced by TEMPO oxidation – can be selectively activated prior to reaction with alcohols or amines to yield esters and amides respectively (Scheme 1-3).[175] Amides are generally preferred as they are less sensible to hydrolysis; amines are also more nucleophilic than alcohols which limits side-reactions with the polysaccharide backbone. Carboxylic acid activation is traditionally performed with carbodiimide coupling agents such as DCC, DIC or the water-soluble EDC and activating agents like NHS or HOBt.[175] Amides have also been formed using CDI[191] or enzymes.[192] Typically DS of about 20 % are obtained in water as the intermediate is susceptible to hydrolysis.[193] Polysaccharide solubility in organic solvents can be improved by cation exchange with tetrabutylammonium (TBA) leading to higher DS by amide substitution.[194, 195] Huerta *et al*. showed that converting the sodium salt form of HA to the acid form was sufficient to solubilise it in DMSO, with consequent DS as high as 90% reported for amide bond formation.[193]

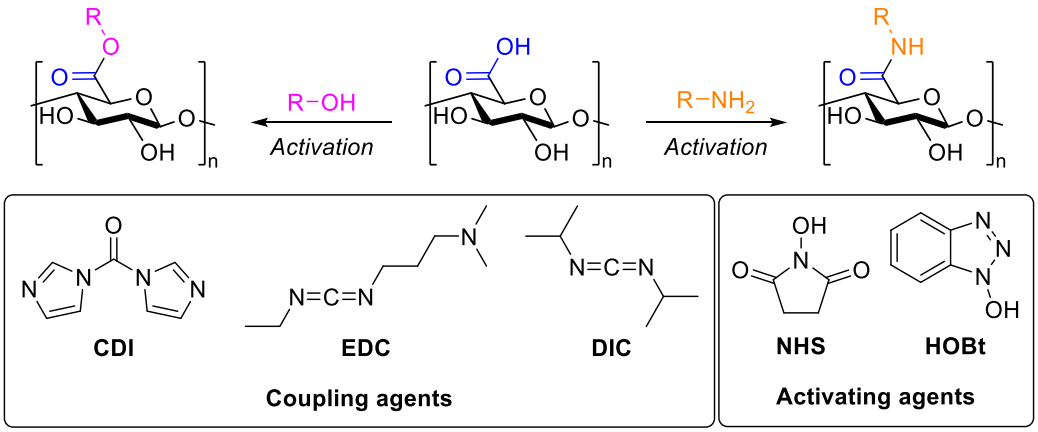

Scheme 1-3. Main reactions involving carboxylic moieties onto polysaccharides.

1.4.2.3 Polysaccharide functionalisation through amine functions

The higher nucleophilicity of CS amine groups compared to hydroxyl groups allows simultaneously for higher reaction efficiency and selectivity. CS can be reacted under mild acidic conditions with NHS-activated esters or anhydrides to obtain amides, the latter yielding

higher DS. The selective amine addition onto aldehydes through Shiff base,[196] followed or not by reductive amination[197] is an elegant method to obtain highly substituted products. Nucleophilic substitutions with haloalkanes or additions onto isocyanates are also possible but less preferred due to possible competition with the primary alcohol. Selective O6 reaction is possible following amine protection.[198] CS functionalisation also include carboxyethylation[199] and trimethylation[200] to improve water-solubility.

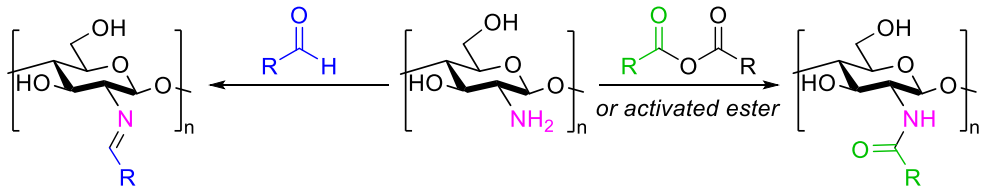

Scheme 1-4. Main reactions involving amine moieties onto polysaccharides.

1.4.3 Polysaccharide functionalised hydrogel precursors

As presented in section 1.4.1 polysaccharide materials benefit from the incorporation of polymers or bioactive moieties to improve their bioactivity and their mechanical properties. The incorporation of pNIPAM for example can provide temperature-responsivity,[149] while CS/polyurethane composites are promising candidates for implants.[201] The incorporation of Pluronics F127, a thermo-responsive copolymer, to DOPA-functionalised CS resulted in thermo-responsive sealants with potential applications in surgery.[202] Polysaccharide functionalisation also include the incorporation of bioactive moieties such as RGD peptides to favour adhesion.

As mentioned in section 1.3.2.1 chemical hydrogels result in better-defined networks and improved properties. This particularly profits polysaccharides which suffer from their polydisperse and non-regular monomer arrangement. The functionalisation of polysaccharides with (meth)acrylates is frequently used to generate hydrogels either through their direct crosslink or their polymerisation with monomers such as acrylamide (AAm) or NIPAM, which in turns confers temperature response;[203] controlled polymerisation has even been reported through the synthesis of adequate RAFT or ATRP precursors, as reviewed elsewhere.[204] CS-methacrylate, obtained from CS derivatisation with methacrylate anhydride, is a very common precursor for photo-crosslinked materials.[205] Photo-crosslinkable CS have also been obtained by functionalisation with *para*-azidobenzoic acid whose gelation occurs through light-initiated nitrene crosslinking. When conjugated to the angiopeptide QHREDGS the resulting hydrogels supported heart cells attachment and survival for up to 5 days.[206]

Click chemistry reactions have also been widely applied to polysaccharides and are part of numerous reviews on polysaccharide-based materials.[69, 175, 207, 208] A wide range of clickable groups, such as alkynes/azides,[186, 193] tetrazines/nb,[86, 209] oxanorbornadiene[210] or maleimide[211] have been developed. Thiol-ene photoclick precursors, which have the advantage to present an additional spatiotemporal control over the gelation, are typically obtained by (meth)acrylation. Nb-functionalised ALG[97] and HA[98] polysaccharides have also been reported; the first CS example was developed during this work.

1.5 Proposed approach

In light with literature, the different requirements identified in section 1.2 can be addressed using the following strategies, summarised in Table 1-4 and illustrated in Figure 1-15.

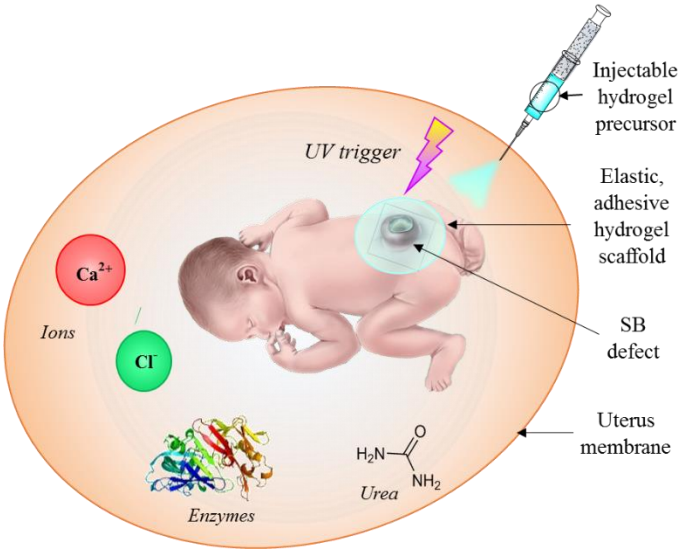

Figure 1-15. Proposed general approach for the design of an in utero treatment of SB highlighting the environment conditions to consider. The foetus illustration is taken from ref.[46]

As discussed in section 1.3 hydrogels are a material of choice for tissue engineering as they provide a swollen 3D network similar to natural tissues. Additional biological properties can be incorporated depending on the chosen hydrogel precursor, either inherently active biopolymers or functionalised synthetic polymers. For simplicity, the focus was made on polysaccharides as they are widely studied and already clinically used as hemostatic[212] or as fillers[213] for example. HA and CS are materials of choice owing to their similarity with the ECM. Both HA and HA receptors are highly present *in utero* and are thought to be involved in foetal wound healing mechanisms.[214] HA biodegradation however is expected to be fast in these conditions. CS on the other hand is not only degraded slower but also generates stronger materials and favours neural wound healing, which would be needed to repair any possible

damage caused over the first months of pregnancy; its positive charge on the other hand allows it to interact with negatively charged cells or ECM while conferring antimicrobial properties.

Table 1-4. Proposed approach to address the challenges of in utero *therapy.*

Property	**Tissue Engineering**	**Sealant**	**Solution**
Immediate skin adhesion	Required		Radical-initiated crosslinking
Low adhesion post-injection	Required		
Injectability and in situ formation	Required		
Sterilisation	Required		Polysaccharides
Non-toxicity	Required		
Nerve repair	Required		
Defect repair	Required	Not required	
Biodegradable	Required	Not required	
Elasticity	Not required	Required	Flexible crosslinks
AF-impermeable	Not required	Required	Tight mesh size
Approach	**Hydrogel**	**DX microgels**	

Adhesion and fast formation can be simultaneously addressed by using radical-initiated crosslinking as free radicals would also react with skin at the site of injection, which can be controlled by echography – an ultrasound-based medical imaging technique routinely used in foetal medicine. Among the radical-mediated crosslinking reactions introduced in section 1.3.2.2 the thiol-ene is of particular interest as it is extremely fast, with gelation below 1 min reported, while the use of nb as the alkene part allows for high selectivity and low side-toxicity as it reacts very quickly with radicals but is highly stable *in vivo*. Interestingly, while several nb-functionalised biopolymers have been reported, no example of CS existed. Side-toxicity with thiols contained in Cys residues should be avoided by the local injection where the concentration of crosslinker will be more important than those of proteins. The photoactivation allows for temporal control of the production of radicals and no undesired adhesion should occur once the light source is switched off. Medical probes are routinely used at hospital and present the ability to switch from visible to UV light *in situ* with control over the wavelength,

which can be matched to an appropriately chosen thiol-ene photoinitiator excitation wavelength. The thiol-ene also offers an elegant way to control the elasticity, mechanical strength and biodegradability of the resulting hydrogel network by modifying the crosslinking density, which could be tuned for each different SB case depending on its severity for example.

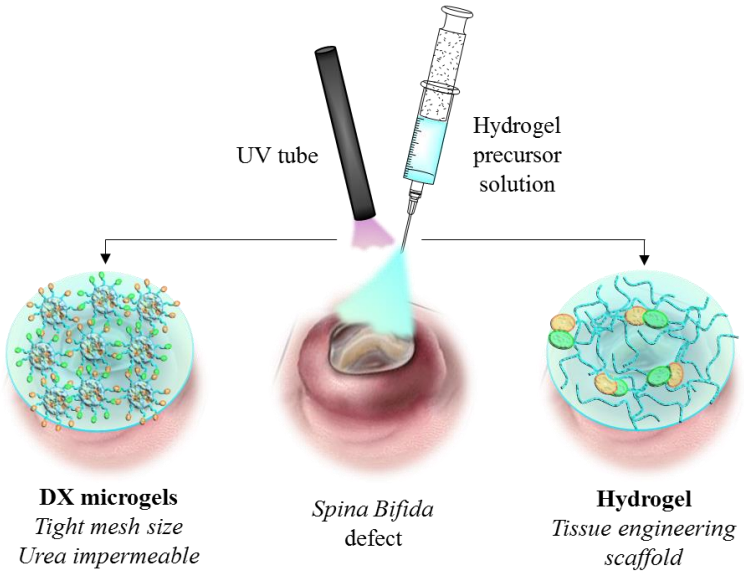

Figure 1-16. Compared approach for the development of a sealant (left), designed as a network of DX microgels, or of a tissue engineering scaffold (right), designed as a hydrogel.

While hydrogels have proven their potential in tissue engineering their use as sealants and as a protection from the AF is less trivial. The permeability can be controlled by the degree of reticulation and the mesh size of the network, where tighter mesh sizes limit swelling and reduce the water content. Strong adhesion with limited deformation is expected in this case. As the foetus will continue to grow with time, the sealant should ideally promote tissue closure and be slowly enzymatically degraded; several injections during pregnancy can also be considered as the procedure is expected to be simple and the material readily available. Such high mechanical properties can be obtained by crosslinking microgels (DX microgels) instead of polymer precursors, as presented in section 1.3.3.3 and illustrated in Figure 1-16. The dimension and the structure of the microgels will impact on the final hydrogel properties, providing an additional handle to its final properties. The degradation of DX microgels is also expected to be slower, as reported with HA.[132] Finally the microgels can be loaded with growth factors to favour healing mechanisms or cell recruitment.

1.6 Thesis outline

Chapter 2 introduces the main techniques used in this work – namely dynamic light scattering, small angle neutron scattering and rheology – focusing on the physical theory, the instrumentation as well as the data analysis in light with reported works.

Chapter 3 presents the synthesis and characterisation of the first nb-functionalised CS, named CS-nb. The synthesis of the related thiolated CS, names CS-SH, is also reported. The reactivity of CS-nb towards thiols is finally verified, as a proof-of-concept for its use as a hydrogel precursor.

Chapter 4 covers the synthesis, characterisation and preliminary cytotoxicity testing of several CS-nb hydrogels developed as potential tissue engineering scaffolds for the management of SB through a wound healing approach.

Chapter 5 presents the optimisation and characterisation of *w/o* nano-emulsion templates developed for the synthesis of CS-nb microgels, intended as building blocks for the synthesis of DX microgels to seal the SB defect *in utero*.

Chapter 6 contains the synthesis, characterisation and preliminary cytotoxicity testing of different CS-nb microgels obtained from the template presented in Chapter 5.

Chapter 7 reports the unexpected formation of non-covalent CS-nb hydrogels. A mechanism for this unprecedented gelation is proposed and the resulting materials are characterised. Although not intended for SB applications, their cytotoxicity was also investigated.

This thesis concludes in **Chapter 8** with a summary of the main findings and possible future directions.

2 Methods

This chapter introduces and describes the main techniques used to study and characterise the hydrogels and microgels synthesized: dynamic light scattering (DLS), small-angle neutron scattering (SANS), and rheology. Specific experimental protocols will be given in each subsequent chapter.

2.1 Scattering techniques: generalities

Scattering is a non-destructive technique, allowing for the study of materials in solution. In a typical scattering experiment, a monochromatic radiation of wavelength λ and intensity I_0 is directed towards a sample, which is deviated from its trajectory with an intensity depending on the scattering angle 2θ (Figure 2-1A). The scattered intensity is recorded as a function of the scattering vector $\vec{q}$ which in the case elastic scattering is defined as:

$$\left\|\vec{q}\right\| = \frac{4\pi}{\lambda} \sin\theta \qquad (2\text{-}1)$$

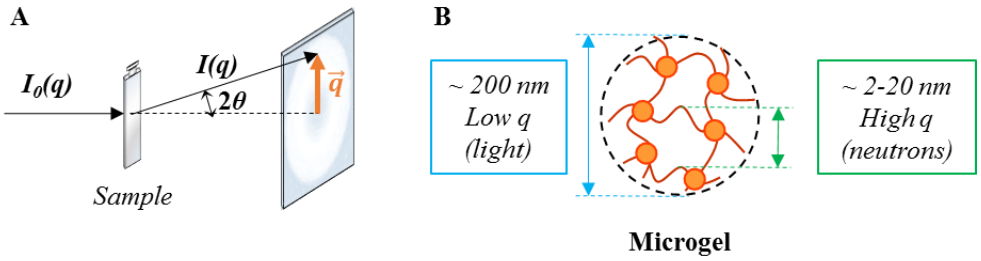

Figure 2-1. (A) Typical scattering experiment configuration, and (B) illustration of the investigation of different length scales in a single material.

The size of the detectable objects is directly related to the wavelength of the radiation (or source) used and to the scattering angle. Therefore, the use of different scattering sources allows for the investigation of different length scales. An example is given in Figure 2-1B, where a microgel hydrodynamic diameter can be obtained from dynamic light scattering measurements while the network mesh size can be obtained with neutron scattering.

Table 2-1. Scattering sources characteristics: q *range, probed length scale and contrast origin.*

Scattering source	*q* range (Å^{-1})	Size length scale (nm)	Contrast
Light	$10^{-5} < q < 5.10^{-3}$	10 - 1000	Refractive index
Neutron	$10^{-3} < q < 1$	0.1 - 100	Isotopes
X-ray	$10^{-2} < q < 10$	0.1 - 10	Electron density

2.2 Dynamic light scattering

Light scattering intensity constantly varies with time due to the movement of particles dispersed in a medium, creating local concentration gradients. Dynamic light scattering (DLS) monitors the mobility of materials in solution by measuring the intensity fluctuations with time at a given scattering angle. This is done by normalising the auto-correlation function $G_2(t)$:

$$g_2(t) = \frac{G_2(t)}{\langle I(t)\rangle^2} = \frac{\langle I(0)I(t)\rangle}{\langle I(t)\rangle^2} \qquad (2\text{-}2)$$

$g_2(t)$ is related to the electric field intensity $g_1(t)$ which depends on particles relaxation. In the assumption of Brownian motion, this leads to:

$$g_2(t) = \langle I\rangle^2 + \left[g_1(t)\right]^2 = \langle I\rangle^2 + \left[\mathrm{e}^{-\frac{t}{\tau}}\right]^2 \qquad (2\text{-}3)$$

where τ is the particle relaxation time and $\langle I\rangle^2$ is the average intensity of the fluctuations described by a Gaussian function. τ can be further related to the diffusion coefficient of the particles D by:

$$\tau = \frac{1}{D\,q^2} \qquad (2\text{-}4)$$

In particular, when $q \rightarrow 0$ the corresponding auto-diffusion coefficient of a hard sphere D_0 is directly related to the hydrodynamic radius r_h by the Stokes-Einstein equation:

$$D_0 = \frac{k_b T}{6\pi\,\eta_s\,r_h} \qquad (2\text{-}5)$$

where k_b is the Boltzmann constant, T is the temperature, and η_s is the viscosity of the solvent. Fitting $g_2(t)$ to an exponential expression according to Eq (2-3) allows to experimentally determine τ which in turns can be related to D_0 through Eq (2-5).[215]

2.3 Small angle neutron scattering

Small angle neutron scattering (SANS) experiments were performed at two different beamlines which will be briefly presented in section 2.3.1. The theory of SANS will be presented in section 2.3.2 and the data analysis in section 2.3.3.

2.3.1 Neutron scattering facilities

2.3.1.1 Sans2d beamline (STFC Rutherford Appleton Laboratory, Didcot, U.K)

Sans2d is a time-of-flight small-angle diffractometer at the ISIS Pulsed Neutron Source (STFC Rutherford Appleton Laboratory, Didcot, U.K.) where neutrons are produced by a spallation source.[216, 217] A q-range of 0.00156 – 0.49090 $Å^{-1}$ was achieved utilizing an incident

wavelength range of 1.75 – 12.75 Å and employing an instrument set up of L_1 = L_2 = 12 m, with a rear 1 m^2 detector offset vertically 75 mm and sideways 8 mm. The beam diameter was 8 mm.

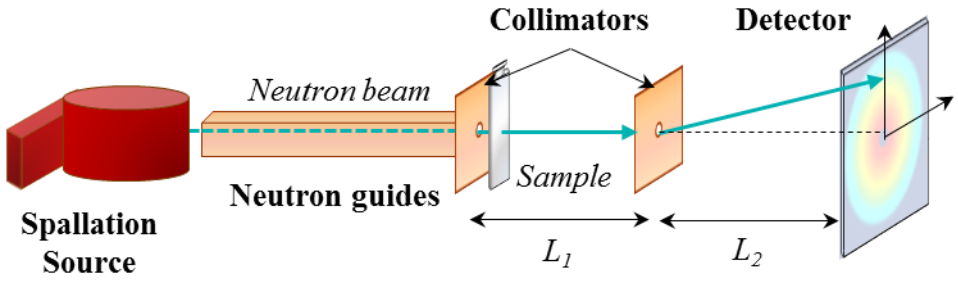

Figure 2-2. Schematic of a SANS diffractometer with a spallation source (Sans2D).

Each raw scattering data set was corrected for the detector efficiencies, sample transmission and background scattering and converted to scattering cross-section data ($\partial\Sigma/\partial\Omega$ vs. q) using the instrument-specific software Mantidplot. The data was placed on an absolute scale (cm^{-1}) using the calibration from a standard sample of known scattering length density (e.g. a solid blend of hydrogenous and perdeuterated polystyrene) in accordance with established procedures[218] Data fitting was performed with SasView 4.1.2 software.

2.3.1.2 PA20 beamline (Laboratoire Léon Brillouin, CEA Saclay, France)

PA20 is a time-of-flight small-angle diffractometer at the Laboratoire Léon Brillouin (CEA Saclay, France) where neutrons are produced by the nuclear reactor Orphée.[219] The desired neutron wavelength is selected with a monochromator and the resulting beam is directed towards the sample (Figure 2-3). The following combination of wavelengths and configurations was used to allow for an overall q range of 0.0008 – 0.3 Å^{-1}:

- Wide angles: L = 2 m; λ = 15 Å so that 0.02 < q <0.3 Å^{-1}
- Intermediate angles: L = 8 m; λ = 15 Å so that 0.004 < q <0.05 Å^{-1}
- Small angles: L = 18 m; λ = 6 Å so that 0.0008 < q <0.01 Å^{-1}

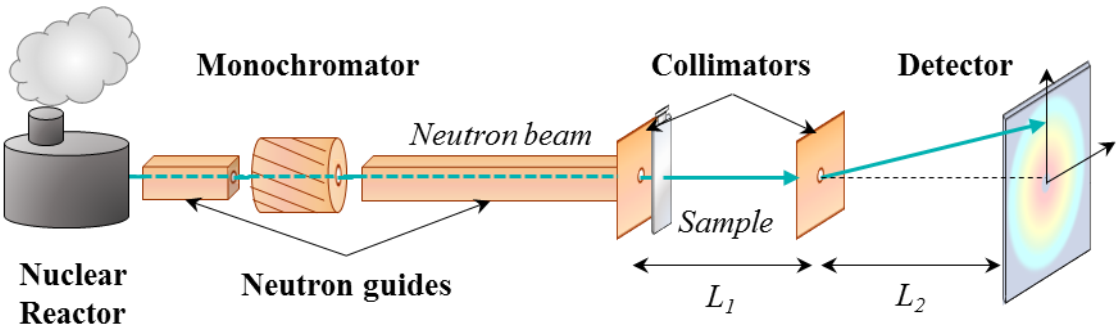

Figure 2-3. Schematic of a monochromatic diffractometer (PA20).

Each raw scattering data set was corrected for the detector efficiencies, sample transmission and background scattering, converted to scattering cross-section data and stitched together using the instrument-specific software Penguin. Data was processed with SasView 4.1.2 software.

2.3.2 Neutron scattering experiments

2.3.2.1 Typical experimental setup

In a typical SANS experiment, a sample is irradiated by a neutron beam $\vec{k_i}$ of initial magnitude $\frac{2\pi}{\lambda}$ where λ is the neutron wavelength. The intensity of the elastically scattered neutrons, described by the wave vector $\vec{k_f}$, is recorded as a function of the scattering angle 2θ where θ is typically within the range of 0.2° to 20°. The scattered intensity, measured in 2D, is finally radially integrated to obtain the 1D scattering intensity profile I as a function of the wave vector q (Figure 2-4).[220, 221]

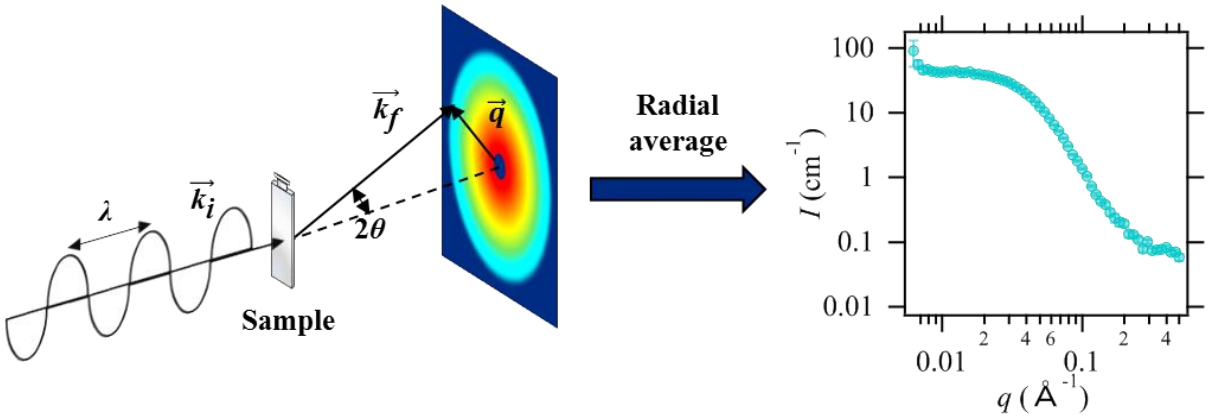

Figure 2-4. Schematics of a SANS experiment: data acquisition and processing.

2.3.2.2 Neutron contrast

The elastic scattering intensity *I(q)* is separated in two contributions:

$$I(q) = I_c(q) + I_{ic} \quad (2\text{-}6)$$

where I_c and I_{ic} are respectively the coherent and non-coherent contributions to scattering. I_c is dependant of q and contains structure-related information, while I_{ic} is constant and depends on the material composition only.

I_c and I_{ic} are highly sensitive to the nucleus composition. For instance, the incoherent contribution of hydrogen (^{1}H) is significant, while it is negligible for deuterium (D, ^{2}H) and for most common atoms (Table 2-2). As a result, deuteration considerably impacts on the scattering while minimising the effect on the overall material structure, as represented by the scattering length b_i for an atom i.

Table 2-2. Neutron scattering cross sections and scattering length of most common atoms.

	Coherent cross section (10^{-24} cm^2)	**Incoherent cross section (10^{-24} cm^2)**	**Scattering length (10^{-13} cm)**
^{1}H	1.7583	80.27	-3.739
^{2}H	5.5592	2.05	6.671
^{12}C	5.559	0	6.646
^{14}N	11.03	0.5	9.360
^{16}O	4.232	0	5.803

The scattering length density (SLD) ρ_x of a compound x is given by:

$$\rho_x = \frac{\sum_i b_i}{v} N_A \qquad (2\text{-}7)$$

where v is the molar volume of compound x and $\mathcal{N}_A$ is the Avogadro number.

The scattering length density ρ_{phase} of a phase containing multiple compounds and the contrast $\Delta\rho$ between two phases 1 and 2 can be respectively calculated as:

$$\rho_{phase} = \sum_k \phi_k \rho_k \qquad (2\text{-}8)$$

$$\Delta\rho = |\rho_1 - \rho_2| \qquad (2\text{-}9)$$

where ϕ_k is the volume fraction of components k. Adjusting the scattering length density of the solvent by playing on the H/D ratio allows to selectively contrast-match parts of a system (Figure 2-5).

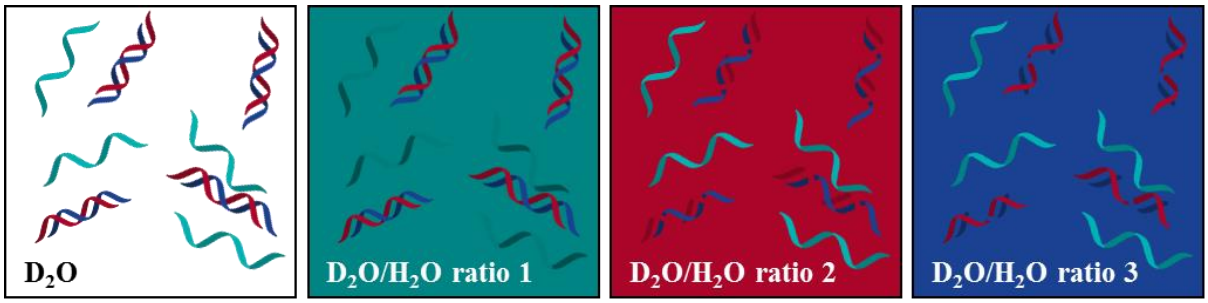

Figure 2-5. Illustration of contrast variation with different solvent scattering length densities.

2.3.3 Data processing

2.3.3.1 Scattering theory

The scattering intensity can be expressed as:

$$I(q) = n.P(q).S(q) \qquad (2\text{-}10)$$

where n is a constant related to the particle contrast and concentration, $P(q)$ is the form factor describing the scattering from individual particles and $S(q)$ is the structure factor which represents inter-particle interactions. In the case of spherical particles n can be expressed as:

$$n = \frac{N}{V} V_P^2 \Delta\rho^2 \qquad (2\text{-}11)$$

where $\frac{N}{V}$ is the number density of particles, V_P is the particle volume and $\Delta\rho$ is the contrast.

The form factor of a uniform spherical particle of radius R can be calculated as:

$$P(q) = 4\pi R^3 \frac{sin(qR) - q R cos(qR)}{(qR)^3} \qquad (2\text{-}12)$$

The simplest way to account for the radius polydispersity is to incorporate a Gaussian distribution function:

$$D(R,\langle R\rangle,s) = \frac{1}{2\pi s \langle R\rangle} e^{-\frac{(R-\langle R\rangle)^2}{2s^2\langle R\rangle^2}} \qquad (2\text{-}13)$$

where s represents the relative size polydispersity and $\langle R\rangle$ is the mean radius diameter. Polydispersity can also be expressed by the Schulz-Zimm distribution function:[222]

$$D(R) = \left[\frac{z+1}{\langle R\rangle}\right]^z \frac{R^2}{\Gamma(z+1)} e^{-(z+1)R} \qquad (2\text{-}14)$$

where $\langle R\rangle$ is the mean radius diameter, Γ is the Gamma function and z is related to the standard deviation σ by $z + 1 = 1/\sigma^2$. The form factors of cylinders, ellipsoids, core-shell structures or polymer chains in solution are also known.

The interaction of non-deformable, homogeneous hard spheres can be modelled by the following structure factor:

$$S(q) = 1+\frac{N}{V} 4\pi \int (g(r) - 1) \frac{\sin(qr)}{qr} r^2 dr \qquad (2\text{-}15)$$

where $g(r)$ is the pair correlation function which represents the average of the normalized density of atoms in a shell of thickness dr situated at the distance r from the centre of a particle. This assumes particle interactions based only on their excluded volumes and neglects any electrostatic interactions. Nevertheless, this expression is widely used as it presents an analytical solution when using the Percus-Yevick approximation, which relates mathematically the direct and indirect correlations of particles.[223] In the case of dilute solutions, the inter-particle interactions are negligible and the structure factor can be approximated as $S(q) \sim 1$.

2.3.3.2 Guinier approximation

The Guinier approximation stipulates that the form factor of any particles can be represented by a Gaussian function in the low q region regardless of their shape. For dilute solutions – where the structure factor is negligible – the scattering can therefore be approximated as:

$$I(q) \sim P(q) \sim I_0 \, e^{-\frac{R_g^2}{3} q^2} \tag{2-16}$$

where R_g is the radius of gyration and I_0 is the intensity extrapolated to $q = 0$. R_g is independent of the system intensity and of its shape in solution. The radius R of a homogeneous sphere can be obtained from R_g by the following equation:

$$R = \sqrt{\frac{3}{5}} \, R_g \tag{2-17}$$

R_g accounts for the hydration layer of a particle and is sensitive to inter-particle interactions at higher concentrations or polydispersity. R_g is typically obtained by plotting $\ln(I(q))$ as a function of q^2 – known as the Guinier plot – whose slope equals $\frac{R_g^2}{3}$. The Guinier approximation must satisfy $q.R_g < \sqrt{3}$.[220]

2.3.3.3 Porod's law

The Porod's law is performed in the high q region ($qR_g >> 1$) where the scattering intensity follows an asymptotic decay:

$$I(q) = S.q^{-D} + background \tag{2-18}$$

where S can be related to the surface area of the particles and D is the fractal dimension of the object, obtained as the slope of the $\log(I(q))$ against $\log(q)$ plot. D provides useful information on the morphology of the system, where D varies between 1 (corresponding to rigid rods) and 4 (corresponding to small particles of smooth surfaces) (Figure 2-6). Polymer solutions typically present a slope $D = 5/3$ for fully swollen coils in good solvent and $D = 2$ for polymer chains in Θ solvent,[224] while a slope between 2 and 3 is a signature of a mass fractal, defined as a structure containing branching and crosslinking points and therefore typically found in crosslinked polymer gel. A slope comprised between 3 and 4 corresponds to a surface fractal and indicates rough interfaces between particles.[220]

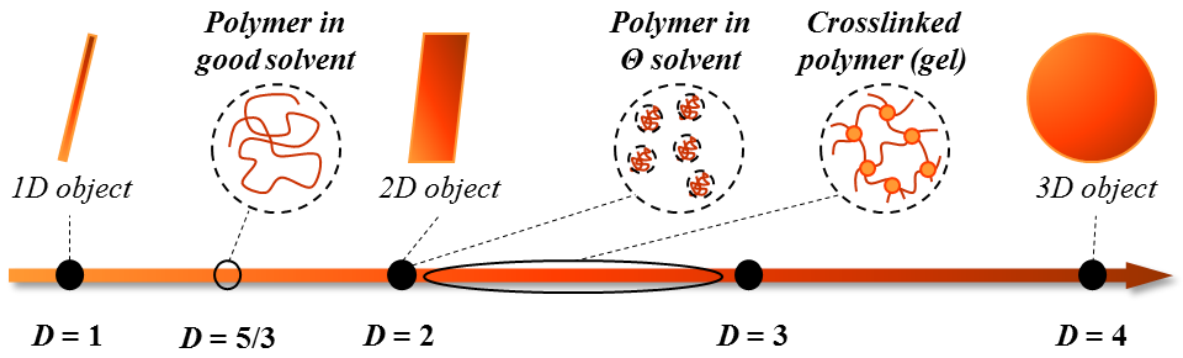

Figure 2-6. Illustration of Porod's law for various shape objects.

2.3.3.4 Guinier-Porod plot

As the Guinier and the Porod regions are valid in different regions of the spectra, Hammouda reported a procedure to calculate them simultaneously using the following equations:[225]

$$I(q) = \frac{A}{q^s} e^{-\frac{R_g 2}{3-s} q^2} \quad \text{for } q < q_1 \tag{2-19}$$

$$I(q) = \frac{B}{q^D} \quad \text{for } q > q_1 \tag{2-20}$$

where A and B are respectively the Guinier and the Porod scale factors, and s is a dimensional parameter used to describe non-spherical objects. For spherical or 3D objects $s = 0$ which leads to the classic Guinier approximation:

$$I(q) \sim P(q) \sim I_0 \, e^{-\frac{R_g^2}{3} q^2} \tag{2-21}$$

Platelets are characterised by $s = 1$ and rods by $s = 2$. A, B and q_1 and are imposed by the continuity of the function over the whole q range, so that D and R_g are independent and q_1 can be calculated as:

$$q_1 = \frac{1}{R_g} \sqrt{\frac{3D}{2}} \tag{2-22}$$

It is worth noting that q_1 does not need to be calculated in prior and that these calculations should not include the background region.

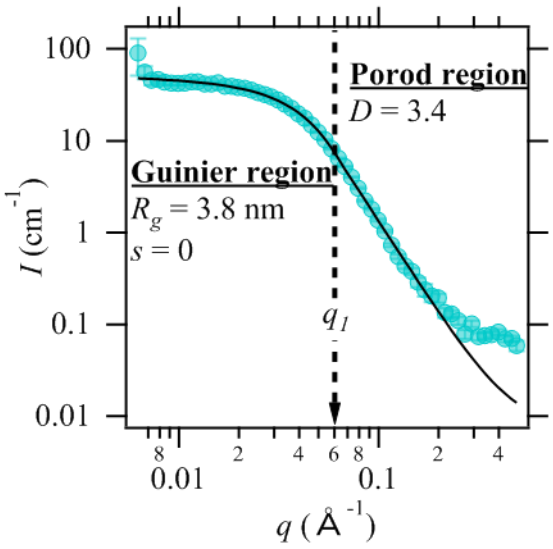

Figure 2-7. Scattering intensity of Span 80/Tween 80 micelles in d-cyclohexane (blue) and the corresponding Guinier-Porod plot (black line).

2.3.3.5 Kratky plot

Kratky plots – $q^2.I(q)$ *VS* q – are performed in the high q region. They are particularly used in the study of polymer in solution. The scattering intensity of an ideal polymer chain following Gaussian statistics follows $I \sim q^{-2}$ – as seen in 2.3.3.3 – and will therefore present a plateau on the corresponding Kratky plot. On the other hand, a crosslinked polymer network – such as a gel – presents a mass fractal so that I varies proportionally to $\sim q^{-2} – q^{-3}$, which results in the formation of a peak (Figure 2-8).[220] These plots have been used to confirm hydrogel formation.[61, 224]

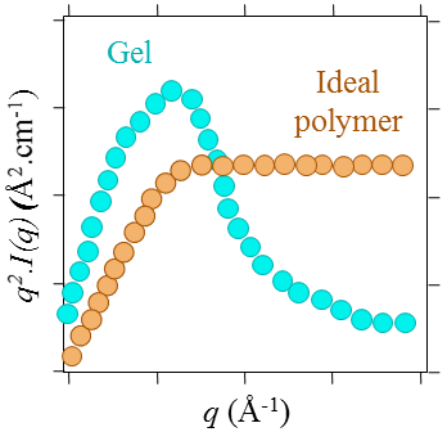

Figure 2-8. Schematic representation of a Kratky plot for ideal polymer in solution (brown) and crosslinked polymers such as gels (blue).

2.3.3.6 Nano-emulsion modelling

Reverse nano-emulsions consist of water droplets dispersed in a non-water-miscible phase - referred to as the oil phase – and stabilised by a surfactant film. The scattering of these objects is generally well represented by the sum of a polydisperse water core surrounded by a surfactant shell:

$$P(q) = C.F^2(q) + background \qquad (2\text{-}23)$$

where C is a constant accounting for the geometry and the contrast and *F(q)* is:

$$F(q) = \frac{3}{V_s}\left[V_c(\rho_c - \rho_s)\frac{sin(qr_c) - qr_c\, cos(qr_c)}{(qr_c)^3} + V_s(\rho_s - \rho_{solv})\frac{sin(qr_s) - qr_s\, cos(qr_s)}{(qr_s)^3}\right] \qquad (2\text{-}24)$$

where V_s and V_c are the volume of the whole particle and of the core respectively, r_c is the radius of the particle core and r_s the radius of the whole particle with core radius r_c and shell thickness t and ρ_c, ρ_s and ρ_{solv} are the scattering length density of respectively the core, the shell and the solvent. Nano-emulsions droplets are polydisperse, which is generally accounted for by adding a Gaussian function to the core radius r_c and to the shell thickness t.[222, 226]

Gradzielski *et al.* investigated the scattering of *o/w* micro-emulsions based on $D_2O/C_{10}D_{22}$ and $C_{10}E_4$ surfactants. In these conditions the scattering length densities of the $C_{10}D_{22}$ core ρ_c and of the D_2O solvent ρ_{solv} were almost equal, which allowed them to model the scattering as a polydisperse Gaussian shell.[227] Although discrepancies were observed in the low q region, the data fitted correctly in the low and medium q regions which allowed for the determination of r_c and to the shell thickness t. The introduction of a hard sphere structure factor did not yield satisfactory scattering, suggesting that a more complex description of the inter-particle interactions should be envisaged.

Foster *et al.* studied *w/o* micro-emulsions based on D_2O/C_6D_{12} and stabilised by $C_{12}E_6$, a non-ionic surfactant. They found that the scattering densities of the core and of the solvent were too different to allow the Gaussian shell model developed by Gradzielski *et al.* to describe the scattering, which was attributed to an impurity in the D_2O.[226] They introduced individual scattering from the core/shell and from the shell/solvent interfaces. They obtained good fits in the high and intermediate q ranges, which yielded to the values of the shell thickness and of the water core respectively. The introduction of a hard sphere structure factor yielded lower scattering intensity in the low q region, consistent with the charged nature of the emulsion droplets and their resulting repulsion. Using a structure factor of sticky hard spheres, on the other hand, allowed to effectively represent the behaviour in the low q region. Interestingly,

the values or r_c and t obtained with $S(q) = 1$ and with a sticky hard sphere structure factor were identical, suggesting that the approximation $S(q) \sim 1$, although incorrect, is enough to characterise the micro-emulsion droplets, as reported in earlier studies.[228, 229]

De Molina *et al.* studied *w/o* and *o/w/o* nano-emulsions consisting of D_2O/C_6D_{12} with Span 80 (S80) and Tween 20 (T20) non-ionic surfactants.[222] They observed various microstructures depending on the water volume fraction used, ranging from micelles to reverse vesicles, some of them with multiple encapsulated vesicles. The scattering of the water droplets was well decsribed by a polydisperse core-shell sphere accounting for both the D_2O core ρ_c and of the C_6D_{12} solvent ρ_{solv} with a hard sphere structure factor and a Schulz-Zimm function to account for the polydispersity of the water core r_c.

The use of a core-shell model requires the knowledge of the scattering length density of the shell and hence the surfactant composition at the interface. Foster *et al.* calculated the surfactant solubility in cyclohexane through the study of phase diagrams for various surfactant mass fraction γ_b.[226] The same method was used to determine the composition of shells after addition of block copolymers.[230] De Molina *et al.* used contrast-match scattering experiments to the surfactant head groups so that only the water-oil interface is visible.[222] They did not find differences in the resulting core dimension r_c while the shoulder featuring the surfactant shell was no longer visible, strongly suggesting that the solvation of the surfactant shell was not visible by SANS, and used therefore the scattering length density of the surfactant mixture for ρ_s.

2.3.3.7 Hydrogel modelling

Geissler *et al.*[224, 231, 232] first proposed a gel scattering function $I_{gel}(q)$ as a combination of a liquid-like ($I_L(q)$) and a solid-like ($I_S(q)$) scattering terms modelling the polymer chain in solution and the crosslinking points respectively:

$$I_{gel}(q) = I_L(q) + I_S(q) \tag{2-25}$$

The polymer contribution $I_L(q)$ is typically given by a Lorentzian equation:

$$I_L(q) = \frac{I_L(0)}{1+\xi^2 q^2} \tag{2-26}$$

where ξ is the correlation length, which represents the mesh size of the gel network.

For an ideal homogeneous crosslink hydrogel, the mesh size is the only characteristic length of the network internal structure, representing the distance between crosslinking points; tetra-arm PEGs[60] or click hydrogels[61] for instance are generally considered as ideal networks. In practice, inhomogeneities can arise from incomplete crosslinking or the formation of highly

reticulated regions of high scattering (Figure 2-9).[233] These inhomogeneities are typically described by one of the following functions: another Gaussian term, an exponential function or with the Debye-Buesche-Anderson (DAB) model as will be discussed below.[233, 234]

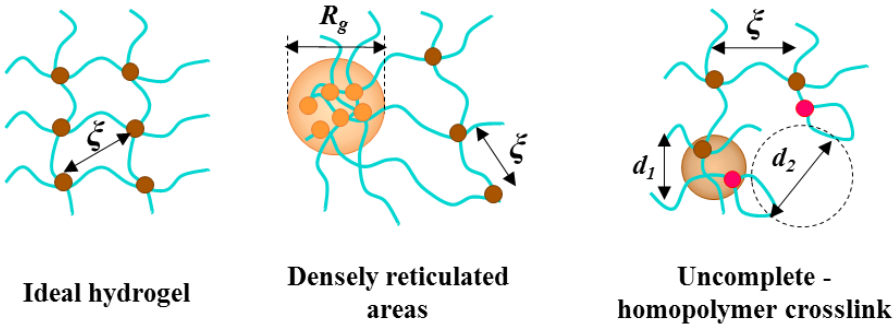

Figure 2-9. Illustration of an ideal hydrogel network and possible inhomogeneities.

These inhomogeneities - or solid-like behaviour $I_S(q)$ – were first introduced by Mallam *et al.*[232] as an exponential:

$$I_s(q) = I_s(0)\, e^{-\Xi^s q^s} \tag{2-27}$$

where Ξ is the mean size of the solid-like uniformities and s is a positive constant. In particular, if $s = 2$ – which was observed for end-crosslinked poly(dimethylsiloxane) (PDMS) gels in toluene – $I_S(q)$ follows a Gaussian distribution, which leads to the following expression for $I(q)$ by Shibayama *et al.*:[224]

$$I_{gel}(q) = \frac{I_L(0)}{1+\xi^2 q^2} + I_s(0) e^{-\frac{R_g^2 q^2}{3}} \tag{2-28}$$

where R_g is the radius of gyration of the polymer rich domain, with $R_g = \sqrt{3}\,\Xi$. Although $s = 2$ gave satisfactory fits for pNIPAM hydrogels, poly(vinyl acetate) (PVAc) gels were better fitted with $s = 0.7$, consistent with a randomly covalently crosslinked gel.[231] Finally, for hydrogen bonding-rich networks such as PVA hydrogels, $I_L(q)$ varies accordingly to the mass fractal D according to:[231]

$$I_L(q) = \frac{I_L(0)}{\left(1 + \frac{D+1}{3}\,\xi^2 q^2\right)^{D/2}} \tag{2-29}$$

It is worth noting that for a mass fractal of $D = 2$ the classic Lorentzian equation is recovered.

More recently, Hammouda *et al.* investigated poly(ethylene oxide) (PEO) clustering mechanism leading to gel formation. The system was well modelled by the addition of a Lorentzian equation describing the polymer chain scattering and a Porod scattering term representing the clusters:[235]

$$I(q) = \frac{A}{q^D} + \frac{C}{1+(q\xi)^m} + background \quad (2\text{-}30)$$

where D is the Porod exponent of the system, m is the Lorentzian exponent, ξ is the correlation length and A, C and the background are all constant. This model was also used by Saffer *et al.* in their study of photo-chemically crosslinked PEG hydrogels through thiol-ene chemistry.[61] The Lorentzian exponent is related to the polymer-solvent interactions, with $m < 2$ characteristics of efficient polymer solvation and $m > 2$ typically representative of polymer chains in a θ solvent. For $m = 2$ the classic Lorentzian component is recovered, which was shown by Mears *et al.* to model well non-interacting pNIPAM microgels with a Porod decay in q^{-4}.[236]

Hyland *et al.* used SANS to investigate the mesh size of physical polysaccharide-based hydrogels containing calcium ions[237] or peptides[238]. Following on the work of Debye-Anderson-Bueche (DAB) they calculated the mesh size of the network as:

$$I(q) = A\frac{L_c^3}{\left(1 + q^2L_c^2\right)^2} + background \quad (2\text{-}31)$$

where L_c is the correlation length of the system and A is a constant. Although this equation was initially developed to characterise the porosity of inhomogeneous solids,[239] Soni *et al.* observed a good correlation between L_c and their PDMS gels in toluene.[240] This equation is sensibly different as it does not present a term to account for the covalent crosslinking points in the low q region. It also exhibits a q^{-4} behaviour in the high q region, indicating smooth interfaces between the polymer chains and the solvent, while the Lorentzian equation classically assumes a q^{-2} behaviour. Crompton *et al.* combined this equation with a Lorentzian term to describe physical chitosan/glycerophosphate hydrogels, where the Gaussian term – coming from the DAB relation – accounted for the solid-like inhomogeneities.[241]

The formation of highly reticulated regions can create sharp binderies between the swollen polymer chains and densely, solid-like frozen crosslinks, which can result in a scattering peak described by a broad Lorentzian peak:[61, 242]

$$I(q) = \frac{\mathrm{A}}{q^n} + \frac{1}{1+\left(\left|q+q_0\right|^\xi\right)^2} + \mathrm{B} \quad (2\text{-}32)$$

where q_0 is the peak position, related to the d spacing between the frozen crosslinks:

$$q_0 = \frac{2\pi}{d_0} \quad (2\text{-}33)$$

2.3.3.8 Microgel modelling

As for hydrogels, the scattering of microgels can be expressed as the sum of the intensity from the dynamic polymer chains $I_L(q)$ and from the crosslinked particles $I_S(q)$. While the polymer chain mobility is still appropriately modelled by a Lorentzian function, different description of the solid-like component has been reported depending on the material dimensions and morphology. In addition, inter-particle interactions must be considered as it may result in an additional structure factor *S(q)*.

Mears *et al.* simply described $I_S(q)$ of non-interacting pNIPAM microgels by a Porod law in the low q region (q = 0.01 – 0.1 Å^{-1}) following a q^{-4} dependence:[236]

$$I(q) = \frac{A}{q^4} + \frac{I_L(0)}{1+(q\xi)^2} \tag{2-34}$$

where A and $I_L(0)$ are constant. The addition of sodium dodecyl sulfate (SDS), an ionic surfactant, resulted in the formation of charged aggregates which required the introduction of a structure factor *S(q)* proposed by Hayter and Penfold to account for the additional charges.

Following on this work, Saunders studied pNIPAM microgels under dilute conditions so that $S(q) \sim 1$. The microgel core was represented by a Porod form factor representing a crosslinked core of surface area S_T and a solvated shell of thickness σ so that:[243]

$$I(q) = \frac{2\pi S_T(\Delta\rho)^2}{q^4} e^{-\sigma^2 q^2} + \frac{I_L(0)}{1+(q\xi)^2} \tag{2-35}$$

where $\Delta\rho$ is the contrast. Although very simple as not accounting for the deformations of microgels, this model gave valuable insights into the internal structure of pNIPAM microgels and allowed for a linear relationship between R_g and ξ to be drawn. This study took advantage of the very monodisperse nature of pNIPAM microgels, suggesting that these results may not translate to more polydisperse systems.

To account for a more accurate structure of the microgels, Stieger *et al.* represented the solid-like scattering contribution of pNIPAM microgels as a polydisperse fuzzy sphere with a densely crosslinked core and a shell consisting of loose polymer chains, whose form factor *P(q)* was calculated as:[244]

$$P(q) = \left[3 \frac{\sin(qR) - qR\cos(qR)}{(qR)^3} e^{-\frac{\sigma^2}{2}q^2} \right]^2 \tag{2-36}$$

where σ represents the width of the smeared particle surface – that is, the standard deviation from the average height of the fuzzy interface – and R is the particle radius, which is represented by a Gaussian function to account for particle polydispersity. The scattering of concentrated microgel suspensions was satisfactorily described following the addition of a simple hard

sphere structure factor.[245] This more sophisticated model was successfully used by Aguirre *et al.* to study thermo-responsive oligo-ethylene glycol microgels.[246]

Finally, the scattering of core-shell microgels such as pNIPAM[247] or poly(N-vinyl caprolactam) (pVCL)[248] can also be expressed as a combination of one term for the crosslinked core and one final term for the shell; these models, however, require a very good understanding of the microgel structure and cannot be easily transferred to new systems.

2.4 Rheology

Rheology is the study of flow and deformation of materials under an applied force suited to soft materials, whose properties lie between those of an ideal solid and of an ideal viscous fluid.[249] The deformation of these so-called viscoelastic materials is modelled by the combination of a term describing an ideal solid whose deformation σ_s is directly proportional the applied strain γ according to Hooke's law:

$$\sigma_s = G.\gamma \qquad (2\text{-}37)$$

and the addition of a term describing an ideal viscous liquid whose deformation σ_l persists if the constraint is applied according to Newton's theory:

$$\sigma_l = \eta \frac{d\gamma}{dt} \qquad (2\text{-}38)$$

where G is the elastic modulus and η is the Newtonian viscosity.

2.4.1 Dynamic rheology: theory

In a dynamic rheology experiment, the sample is subjected to a sinusoidal deformation $\gamma(t)$:

$$\gamma(t) = \gamma_0.sin(\omega t) \qquad (2\text{-}39)$$

where γ_0 is the initial amplitude, ω is the deformation – related to the frequency $f = \frac{2\pi}{\omega}$. The resulting material deformation follows a sinusoidal law with a phase-shift δ:

$$\sigma(t) = \sigma_0 \, sin(\omega t + \delta) \qquad (2\text{-}40)$$

For a purely elastic material – *i.e.* an ideal solid – $\delta = 0$ while for a purely viscous material – *i.e.* an ideal liquid - $\delta = \frac{\pi}{2}$. $\sigma(t)$ can be further rearranged as:

$$\sigma(t) = \sigma_0 \sin(\omega t)\cos\delta + \sigma_0 \cos(\omega t)\sin\delta \qquad (2\text{-}41)$$

From this equation the storage (or elastic) modulus G' and the loss (or viscous) modulus G'' are defined by:

$$G' = \frac{\sigma_0}{\gamma_0}\cos\delta \qquad (2\text{-}42)$$

$$G'' = \frac{\sigma_0}{\gamma_0} \sin\delta \qquad (2\text{-}43)$$

$$tan\,\delta = \frac{G''}{G'} \qquad (2\text{-}44)$$

where G' and G'' quantify the energy stored and lost respectively during a strain cycle. The dominance of a solid-like behaviour results in a loss factor tan δ < 1 while a liquid-like behaviour presents tan δ > 1. A hydrogel typically presents $G' > G''$.

2.4.2 Amplitude or stress sweep measurements

In an amplitude sweep experiment, a stress of an increasing amplitude is applied to a material with a constant frequency. In these conditions, a viscoelastic material presents a constant response to an applied stress up to a certain point, knows as the yield stress γ_C where it starts to flow. The range of stress where G' and G'' are constant ($\gamma < \gamma_C$) is known as the linear viscoelastic region (LVER) (Figure 2-10). Most rheology experiments are performed within the LVER as both G' and G'' and independent of the strain, so that any observed deformation can be attributed to the frequency. Non-linear rheology can also be performed. It is worth mentioning that the LVER is directly dependant on the chosen frequency.

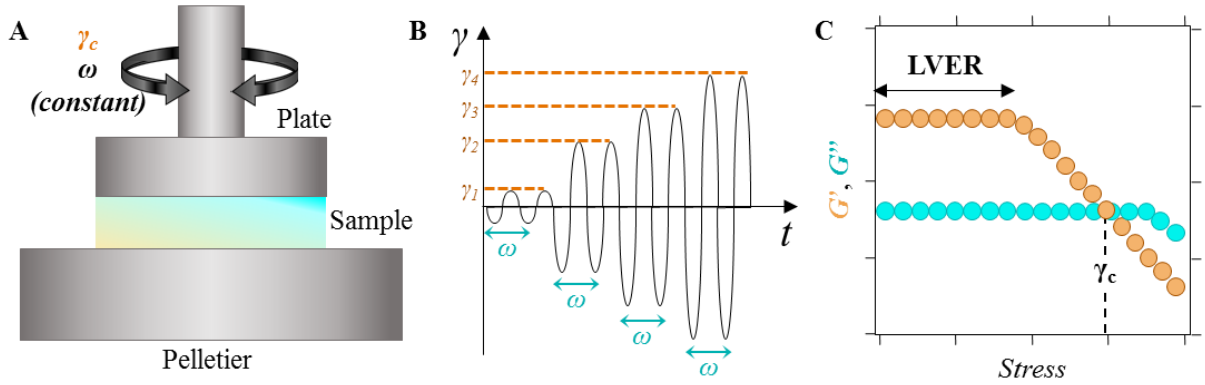

Figure 2-10. Amplitude sweep measurements: (A) experimental setup, (B) evolution of the amplitude with time for a given frequency, and (C) typical data.

2.4.3 Frequency sweep measurements

In a frequency sweep experiment a constant stress γ on the LVER is applied while the frequency is varied. For a strongly connected material such as a crosslinked hydrogel G' and G'' are independent of the frequency, while the solid-like and viscous-like behaviour of softer materials such as physical hydrogels varies with frequency. A crossover of G' and G'' may occur, with important variations by an order of magnitude typically observed (Figure 2-11).

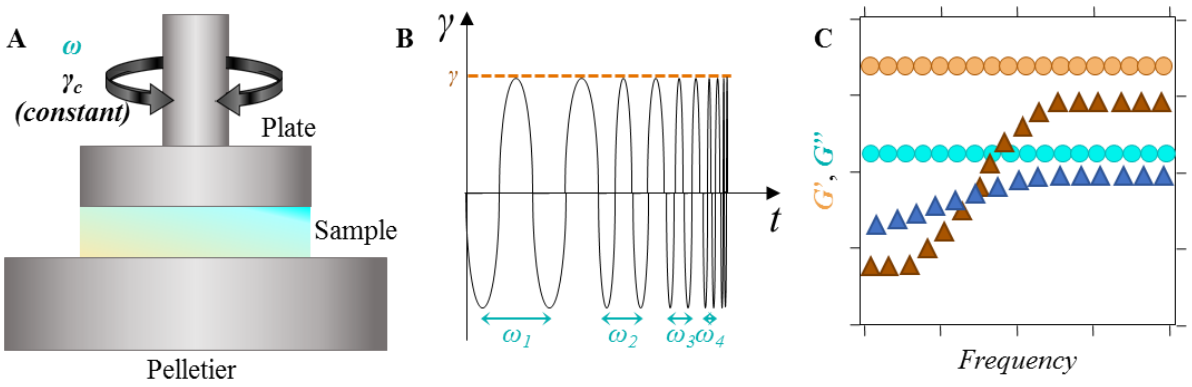

Figure 2-11. Frequency sweep measurements: (A) experimental setup, (B) evolution of the frequency with time for a given amplitude, and (C) typical data for covalently (circles) and physically (triangles) crosslinked hydrogels.

3 Polymer synthesis and characterisation

3.1 Introduction and aims

This chapter covers the synthesis and the characterisation of a novel photocrosslinkable chitosan hydrogel precursor. As discussed in the Chapter 1, chitosan (CS) is a promising material due to its biocompatibility and its bioactivity, namely its antibacterial properties and its ability to favour wound healing and tissue regeneration. Photo-crosslinkable CS hydrogel precursors are typically obtained by radical-initiated step-growth polymerisation or thiol-ene photoclick after (meth)acrylation functionalisation. To limit acrylate side reactions, a new CS derivative was designed based on norbornene (nb), a more stable derivative yet more reactive towards radicals. The synthesis and characterisation of this derivative, as well as its reactivity towards model thiols, will be discussed.

3.2 Methods

CS (low molecular weight 50-190 kDa, deacetylation degree (DD) = 76 % calculated by ^{1}H NMR – see Figure 3-1) was purchased from Sigma. Carbic anhydride (mostly endo, CA) was obtained from Acros. Imminiothiolane hydrochloride was received from Carbosynth. Other reagents were purchased from Sigma, Acros, Fluka or Lancaster and used as received. Dialysis against deionised (DI) water (MilliQ; resistivity 18.2 MΩ cm and total organic content (TOC) < 4 ppb) were performed using a SnakeSkin dialysing tubing with a molecular weight cut-off (MWCO) of 10 kDa (Thermo Scientific).

^{1}H NMR were recorded with a Varian VNMR S600 equipped with an HCN triple resonance cryogenic probe at 40 °C to sharpen the water peak and to allow for more accurate integration of the nb peaks. DOSY NMR were performed on a Varian spectrometer (500 MHz) at 25°C with a pulse length of 2 ms and a diffusion time of 500 ms. Pulse gradients were increased in 16 steps from 2% to 95% of the maximum gradient strength (53.5 G/cm) in a linear ramp. FT-IR was performed on a were recorded on the neat compounds using an ATR sampling accessory on a Perkin Elmer Spectrum One spectrometer.

3.2.1 Determination of the deacetylation degree (DD) of CS

DD was obtained by integrating the singlet at 1.92 ppm (*a*,CH_3 of GlcNAc units, blue, 3H) and the singlet at 3.04 ppm (*b*, H2 of GlcN and GlcNAc units, yellow, ^{1}H) as described by Hirai at al.[250]

$$DD = 1 - \frac{\frac{I_a}{3}}{I_b} \quad (3\text{-}1)$$

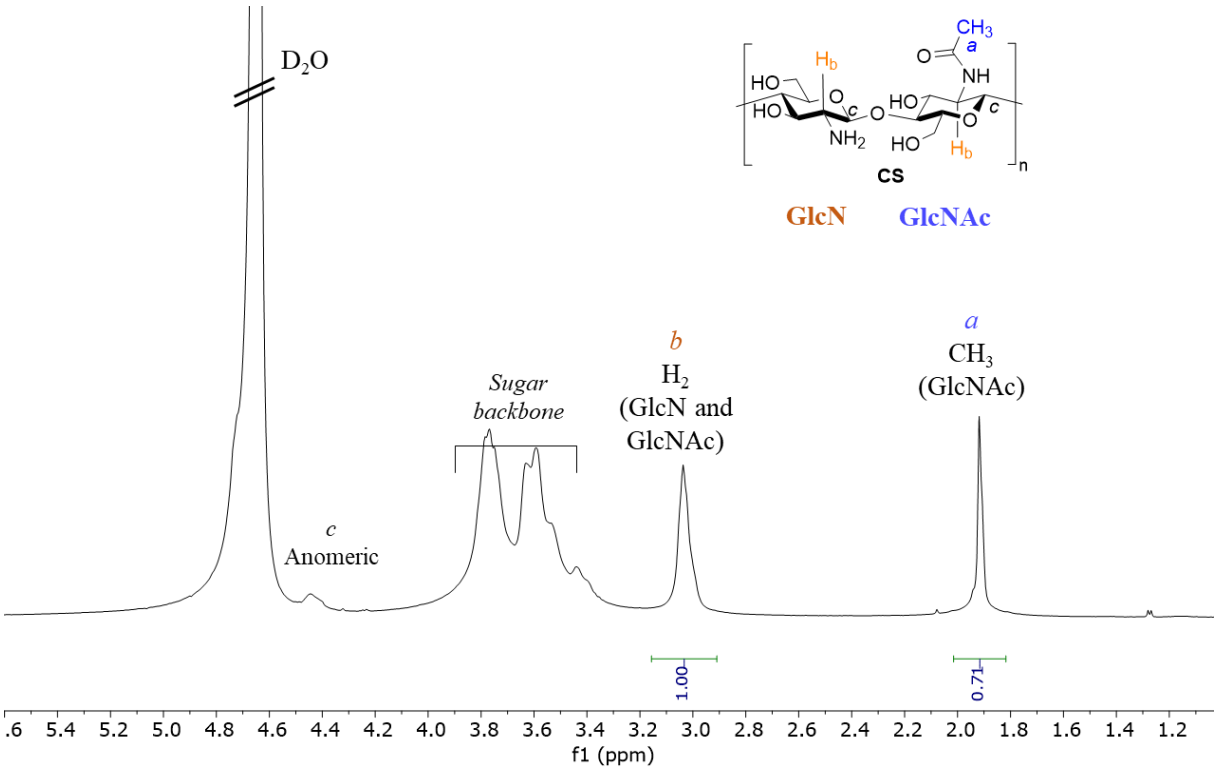

Figure 3-1. Determination of the deacetylation degree (DD) of CS by ^1H NMR.

Using Equation (3-1) with I_a = 0.71 and I_b = 1: DD = 76 %

3.2.2 Synthesis of CS-nb-*ald*

CS (1 g, 5.90 mmol of amine group) was dissolved in 100 mL of DI water by slow addition of acetic acid until pH reaches 5 then norbornene-carboxyaldehyde (nb-*ald*, 0.5, 1, 1.5, 2 or 3 eq per free amine) was added. The reaction mixture was stirred for 2.5 hrs to allow for imine formation then sodium cyanoborohydride (3 eq per imine) was added and the mixture was stirred at room temperature for another 24 hrs. The resulting polymer conjugates were dialysed against 5% NaCl for 24 hrs, DI water for 48 hrs and lyophilised. Due to the very low solubility of the products CS-nb-*ald* a presat ^{1}H NMR of the product was performed in 1% DCl/D_2O (see Figure 3-2).

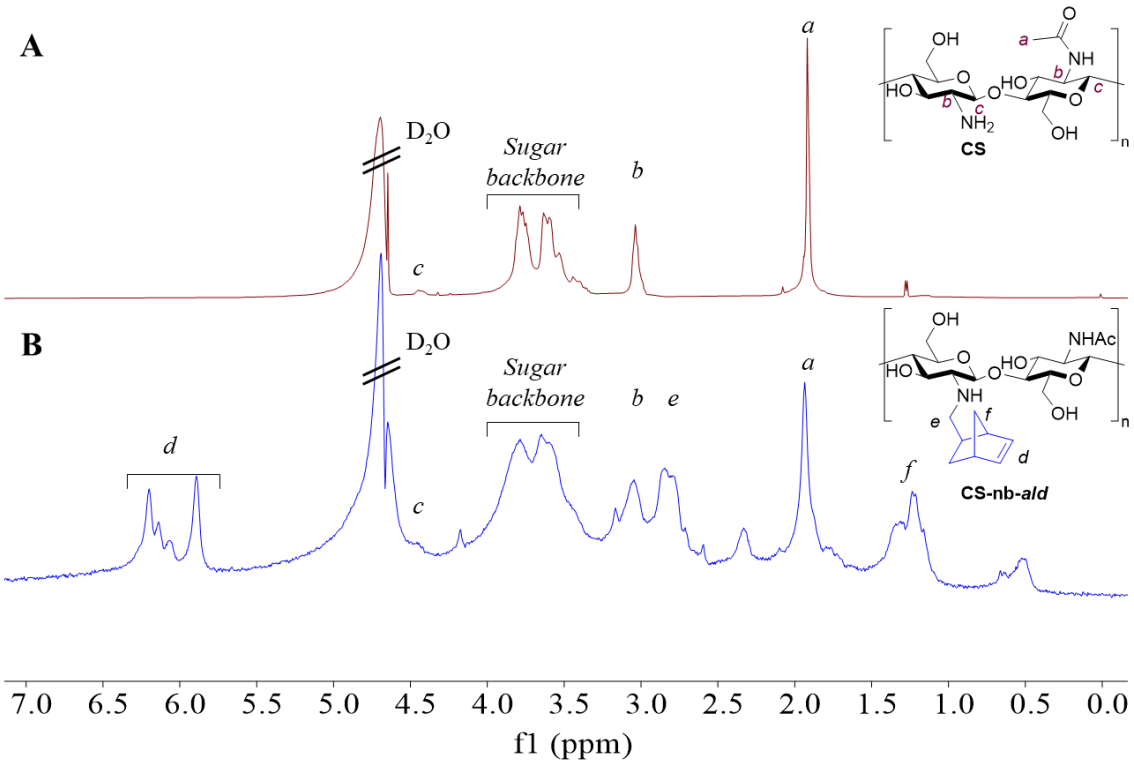

*Figure 3-2. Presat ^{1}H NMR of: A) CS and B) CS-nb-*ald *in 1% DCl/D_2O.*

3.2.3 Synthesis of CS-nb-*CDI*

CS (1g, 5.9 mmol) was dissolved in 100 mL 0.1 M 2-ethanesulfonic acid (MES) buffer adjusted to pH 5.0 by stirring at room temperature. Once solubilised, 1, 1'-carbonyldiimidazole (CDI, 2.87 g, 3 eq. per free amine) and norbornene-2-carboxylic acid (nb-COOH, 2.44 g, 3 eq. per free amine) were added, and the mixture was stirred at room temperature for 3 days. The polymer was dialysed against 5 % NaCl for 24 hrs first and then deionised (DI) water for 2 days, and then lyophilised. Due to the low solubility of the products CS-nb-*CDI* a presat ^{1}H NMR of the product was performed in 1% DCl/D_2O, which presented multiple sharp peaks attributed to remaining nb-COOH in solution (see Figure 3-3).

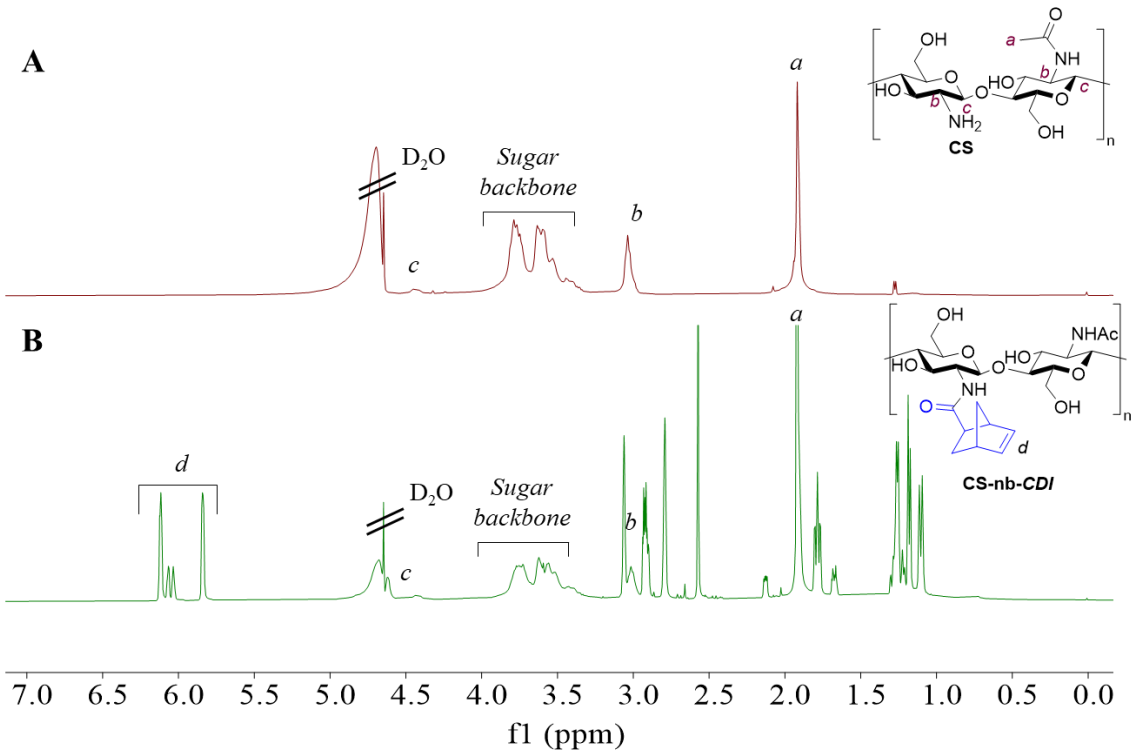

*Figure 3-3. Presat ^{1}H NMR of: A) CS and B) CS-nb-*CDI *in 1% DCl/D_2O.*

3.2.4 Purification and solubility testings of CS-nb-*ald* and CS-nb-*CDI*

Solubility was tested in aqueous solutions of dimethylsulfoxide (DMSO), dimethylacetamide (DMAc) and dimethylformamide (DMF) with and without 8% LiCl as well as in urea/LiCl/KOH mixes as previously reported.[251]

Several purification procedures were attempted: precipitation against acetone, methanol and ethanol; dialysis against DI water; dialysis against a decreasing gradient of NaCl. The efficiency of the removal of non-covalently bonded nb was measured by DOSY. Only dialysis against a decreasing gradient of NaCl successfully removed the unreacted material, which is due to the screening of charges by NaCl reducing secondary electrostatic interactions between the polymer chains and remaining small molecules.[252]

3.2.5 Synthesis of CS-nb

CS (1 g, 5.9 mmol) was dissolved in 100 mL of 2% acetic acid (AcOH). Once solubilised, carbic anhydride (CA, 972 mg, 5.9 mmol) was added, and the mixture was stirred at 50 °C for 2 days. The resulting polymer conjugates were dialysed against 5% NaCl for 24 hrs, DI water for 48 hrs, and lyophilised. Effective removal of unreacted CA was verified by DOSY NMR (Figure 3-7A).

The degree of substitution (DS) was calculated by ^{1}H NMR as detailed in Equation (3-2):

$$DD = 1 - \frac{\frac{I_d}{2}}{I_b} \quad (3\text{-}2)$$

where the signals corresponding to I_d and I_b are shown in Figure 3-4.

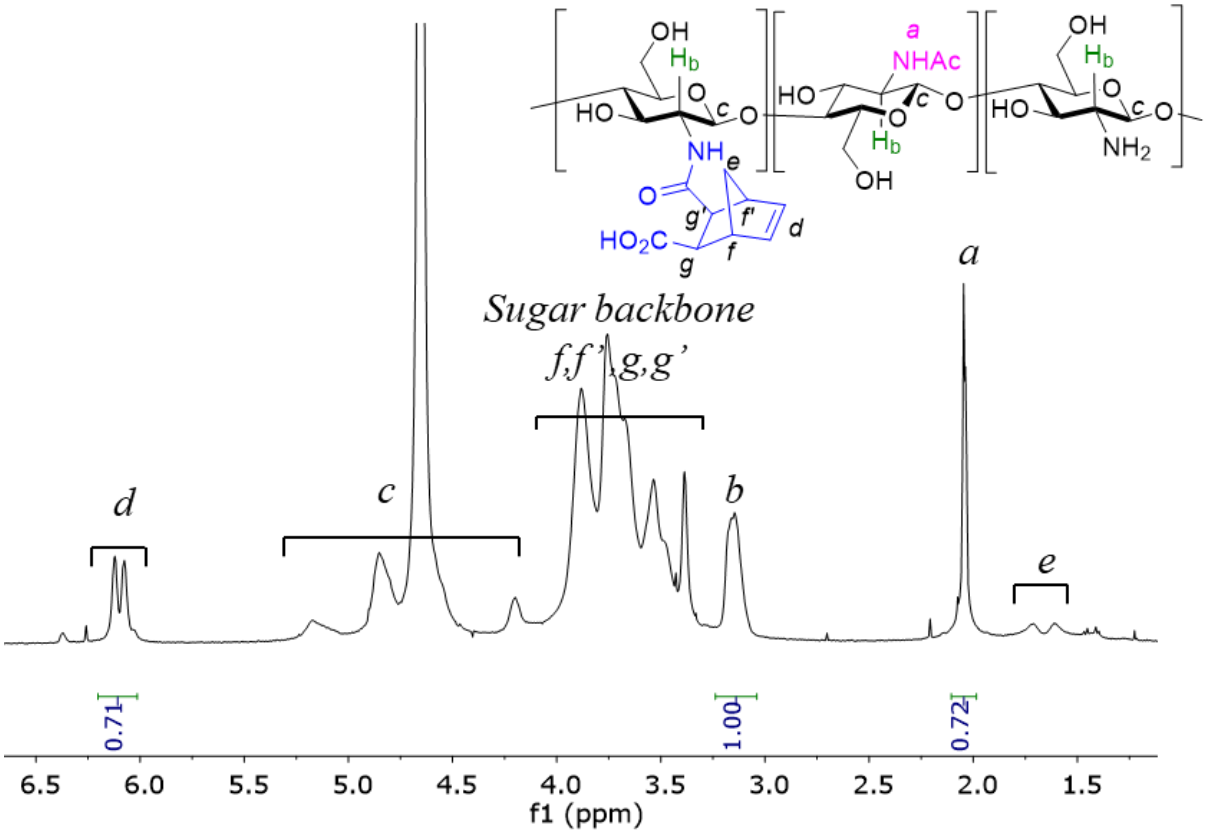

Figure 3-4. [1]H NMR of CS-nb and detailed calculation of the degree of substitution (DS).

Using Equation (3-2) in this example: $DS = \frac{\frac{0.71}{2}}{1} = 35.5\ \%$

The degree of functionalisation (DF in µmol of nb/mg of CS-nb) was calculated by ^{1}H NMR by dissolving 2-to-5 mg of CS-nb in D_2O containing 1 mM of anhydrous DMF, used as a standard as reported by Ooi *et al.*[97] as:

$$DF = I_f . C_{DMF} . V_{DMF} \frac{\frac{I_d}{2}}{m_{CS-nb}} \quad (3\text{-}3)$$

where:

I_f is the integral of the amide H of DMF (labelled *f* in Figure 3-5, 1H)

C_{DMF} is the concentration of DMF used to prepare the NMR sample (1 mM)

V_{DMF} is the volume of DMF used to prepare the NMR sample (550 µL)

I_d is the integral of the alkene peaks of norbornene (labelled *d*in Figure 3-5, 2H)

m_{CS-nb} is the mass of CD-nb dissolved to make up the NMR sample

An example of calculation is given Figure 3-5 with m_{CS-nb} = 3.10 mg, which gives:

$$\text{DF} = 1 \times 1 \times 0.550 \frac{\frac{10.61}{2}}{3.10} = 0.94 \text{ µmol nb/mg CS-nb}$$

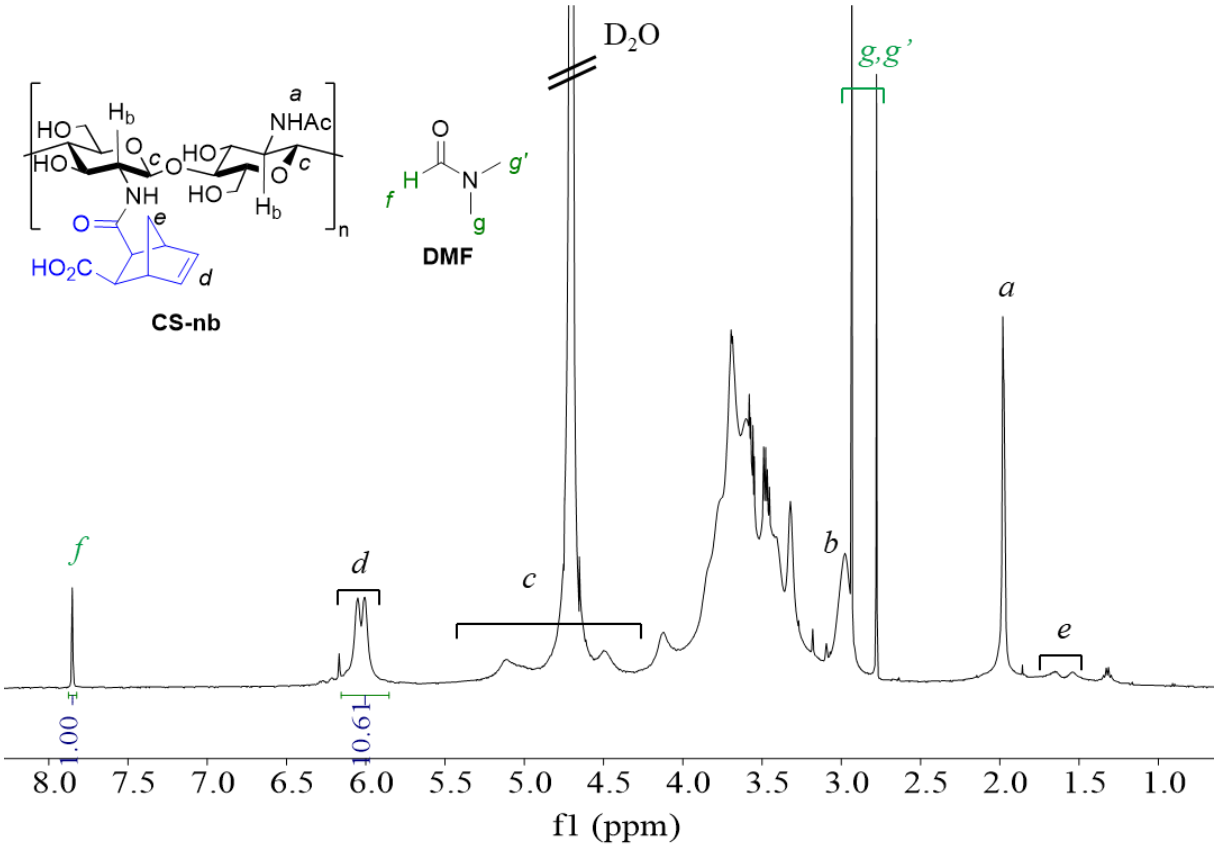

Figure 3-5. [1]H NMR of CS-nb with 1 mM DMF and detailed calculation of the degree of functionalisation (DF)

3.2.6 Optimisation of the synthesis of CS-nb by experimental design

Experimental design was performed using MODDE 9.1 software. Three parameters were studied: temperature (varied between 25 and 50 °C), reaction time (6 to 48 hrs), and equivalents of carbic anhydride (0.5 to 1.5). DS was chosen as the only variable to measure the result; the desired value was set to 50%. 11 experiments were suggested by the software (see the table in Figure 3-8), which were conducted with 50 mg of CS in 5 mL of a 2% AcOH solution. The reaction was carried out as described in Section 3.2.5 and the experimental analysis was performed with MODDE 9.1 using a standard screening design.

3.2.7 Synthesis of CS-SH

The polymer was synthesized according to a previously reported procedure.[253] Briefly, CS (500 mg, 2.96 mmol of amine group) was dissolved in 50 ml of 2% AcOH by stirring at room temperature. Once dissolved pH was adjusted to 7 by dropwise addition of NaOH 1M then imminiothiolane (81 mg, 0.592 mmol, 0.2 eq) was added. The reaction was performed at room temperature for 16 hrs and the polymer was recovered after dialysis against NaCl for 24 hrs followed by DI water for 48 hrs and freeze drying. The pH during the dialysis step was maintained to 5 to limit the formation of disulfides, which is favoured at higher pHs; a final dialysis was performed against DI water for 2 hrs to remove the excess of salts. The degree of thiolation was measured by colorimetry using Ellman's reagent according to the manufacturer protocol, using cysteine as an internal standard. The disulfides were preliminary cleaved for 2 hrs with tris(2-carboxyethyl)phosphine hydrochloride (TCEP).

3.2.8 Proof-of-concept: thiol-ene coupling

CS-nb (5 mg, 3.3 µmol nb) was dissolved in D_2O containing Irgacure 2959 (1 mg/mL, 550 µL) and combined with cysteine ([nb]:[SH] molar ratio R_s = 1:4, 1:2 and 1:1) in an NMR tube. The resulting mixture was cured with UV-B for 5 min. The reaction was studied by *in situ* ^{1}H NMR by monitoring the ratio between the alkene peak of nb and the N-acetyl group.

3.3 Results and discussion

3.3.1 Synthesis and characterisation of nb-functionalised CS polymers (CS-nb)

CS is commonly functionalised through its amine groups which higher nucleophilicity compared to hydroxyl groups allows for enhanced selectivity. Common functionalisation strategies include Schiff base reduction with aldehydes (Scheme 3-1, route *a*) and amide coupling of carboxylic acids (Scheme 3-1, route *b*). Schiff base formation represents an attractive solution due to the selectivity and the efficiency of imine formation, leading to polymers of relatively high degree of substitution (DS) compared to the amide and ester analogues.[176] Shortly after the addition of carboxyaldehyde norbornene (nb-*ald*) the polymer precipitated out of solution, even when lower concentrations of nb-*ald* where investigated, and the resulting conjugates suffered from low solubility not only in water but also in a variety of solvents known to favour CS solubility (see section 3.2.4).

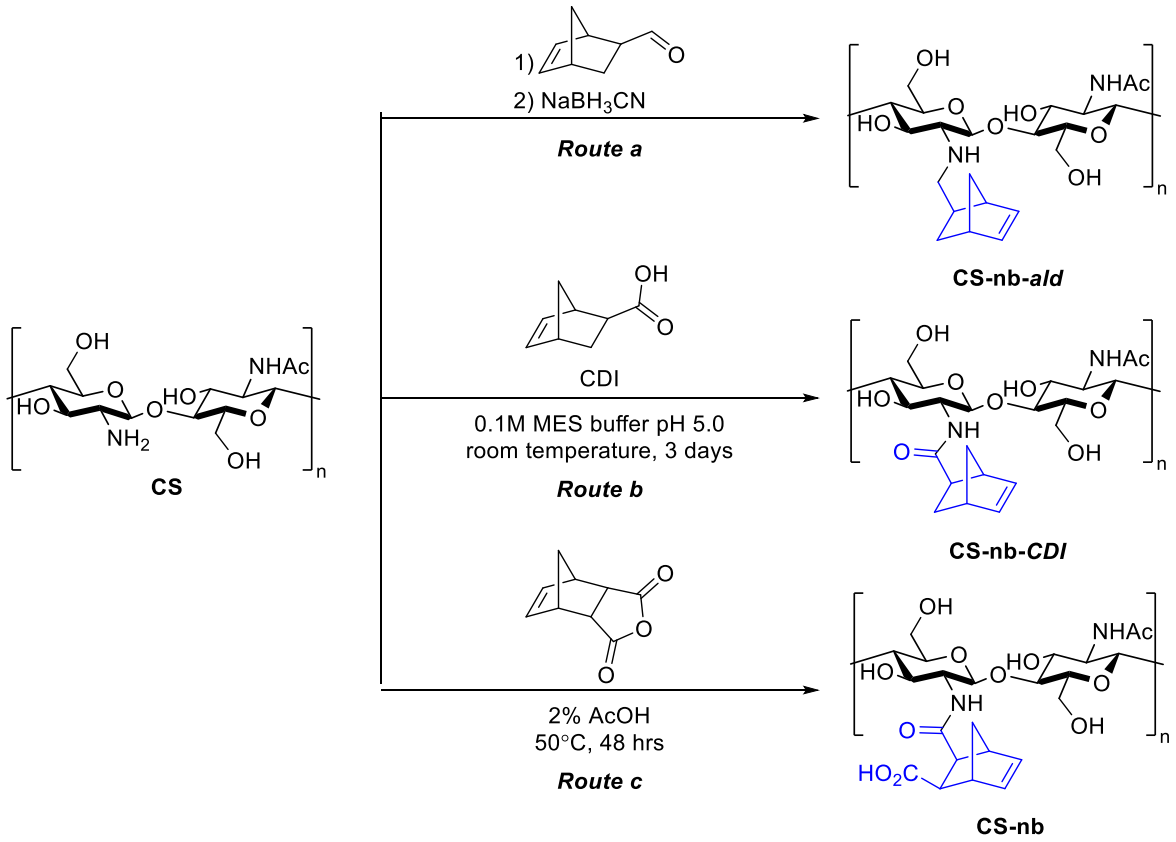

Scheme 3-1. Nb-functionalised CS polymers and their synthetic routes.

CS amidation with norbornene-carboxylic acid (nb-COOH) using CDI resulted in the successful synthesis of CS-nb-*CDI* (Scheme 3-1, route *b*) as evidenced by ^{1}H NMR (see Appendix B-B). It is noteworthy that amide coupling using EDC and NHS-activated nb-*COOH* led to mixtures of product and unreacted EDC that could not be separated by dialysis or precipitation (see section 3.2.4 for details on the purification procedures attempted). As CS-nb-*ald*, CS-nb-*CDI* suffered from low solubility, which is probably due to the reduction of the positive charge as CS amines were converted to amides, in combination to the increased overall hydrophobicity induced by the addition of nb groups.

To circunvent this, carbic anhydride (CA) was used to react with the CS amine groups, which upon ring opening resulted in the concomitant amide formation and introduction of an acid functionality on the pendant nb that led to the polymer CS-nb (Scheme 3-1, route *c*). CS-nb was not only soluble in mild acidic conditions, but also in DI water, giving solutions of final pH ~ 5 depending on the concentration of polymer used. Although the final polymer could not be directly dissolved in phosphate buffer saline (PBS) or at pH > 6 this is a massive improvement over native CS for which acidic pH or chemical modifications are required. This improved solubility likely results from both the introduction of a carboxylic acid group and by

the concomitant disruption of the hydrogen bond network as amines react, as previously reported.[254]

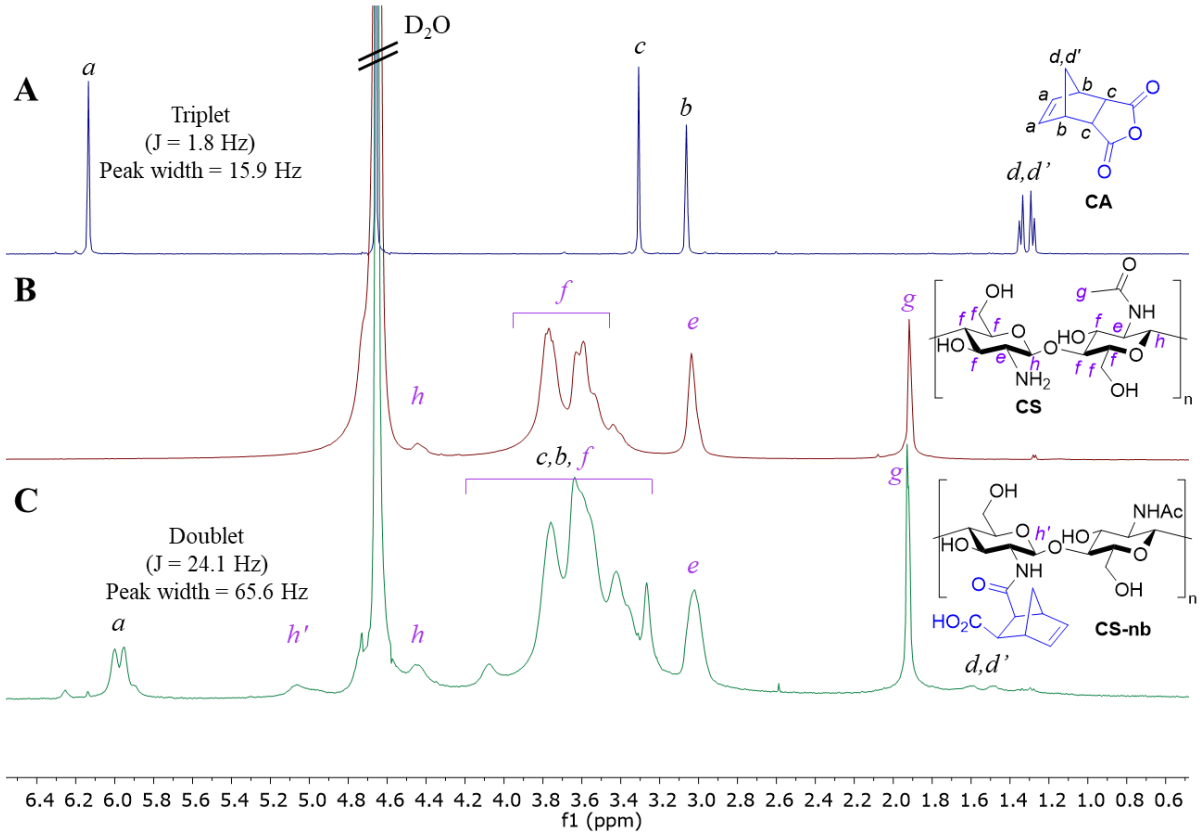

Figure 3-6. ^{1}H NMR of: CA (A), CS (B) and CS-nb (C).

The incorporation of nb into CS was confirmed by ^{1}H NMR, with the appearance of nb alkene peaks at 6.2-6.3 ppm, (Figure 3-6) and of the bridged protons at 1.7-1.9 ppm (Figure 3-6). This spectrum is consistent with previous work reported by McOscar *et al.* for carboxymethylcellulose functionalised with CA.[91] The broadening of the alkene signal from 15.9 Hz in CA to 65.6 Hz in CS-nb indicated a slower tumbling leading to faster relaxation, consistent with the covalent binding of CA to CS. In addition, the bridged protons shifted from ~ 1.6 to ~ 1.8 ppm, consistent with previous reports.[91] In addition, DOSY NMR confirmed the formation of a single species in solution, with a diffusion coefficient consistent with values expected for a polymer in solution (~ 7.10^{-8} $cm^2.s^{-1}$, compared to ~ 6.10^{-6} $cm^2.s^{-1}$ for CA, Figure 3-7A). Finally, FT-IR presented new bands at 1695 and 1570 cm^{-1} corresponding respectively to carboxylic acid C=O and to cyclic alkenes C=C stretching (Figure 3-7B).

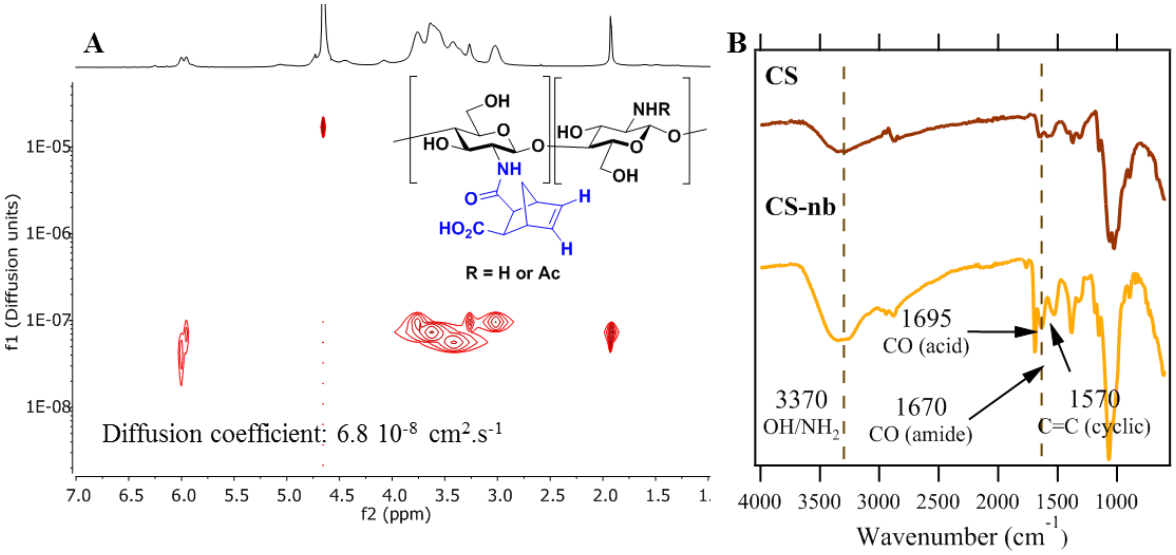

Figure 3-7. DOSY NMR (A) and FT-IR (B) of CS-nb.

3.3.2 Optimisation by experimental design

Control over the degree of substitution (DS) and the amount of crosslinking point is an important parameter for the final properties of hydrogels, with higher DS leading to stronger materials and a minimum DS needed to achieve gelation.[255] As summarised in the table in Figure 3-8, an increase in the DS of the amines by nb from 24 to 43 % was observed as the reaction time, the temperature, or the equivalent of CA increased. Figure 3-8 shows that the reaction time and the amount of CA significantly contributed to the DS (A), whilst the temperature and the reaction time in conjunction had less impact on the final DS, as suggested by the dominant green colour (B). Hence, the most efficient way to increase the DS is to increase the amount of CA and/or to increase the reaction time, rather than varying the temperature. This short screening showed that the reaction was reproducible and allowed for the generation of a reliable model (q^2 = 0.365, r^2 = 0.924). This DS is consistent with values reported for gelatin functionalisation with CA under similar conditions, where pH and nb steric hindrance were identified as the main limitations.[92, 96] As initial CS solubility required mild acidic conditions, pH could not be used as a variable in this study, and the synthesis of CS-nb was further conducted for 48 hrs with 1 equivalent of CA at 50 ºC to improve its solubility, which yielded a DS of 38%.

T (°C)	Time (hrs)	Eq. CA	Experimental DS[1] (%)	Predicted DS (%)
20	6	0.5	26.5	24.88
50	6	0.5	19.5	20.25
20	36	0.5	24.5	25.25
50	36	0.5	40	38.38
20	6	1.5	28	28.75
50	6	1.5	29.5	27.88
20	36	1.5	28.5	26.88
50	36	1.5	43	43.75
35	21	1	29.5	29.50
35	21	1	30.5	29.50
35	21	1	25	29.50

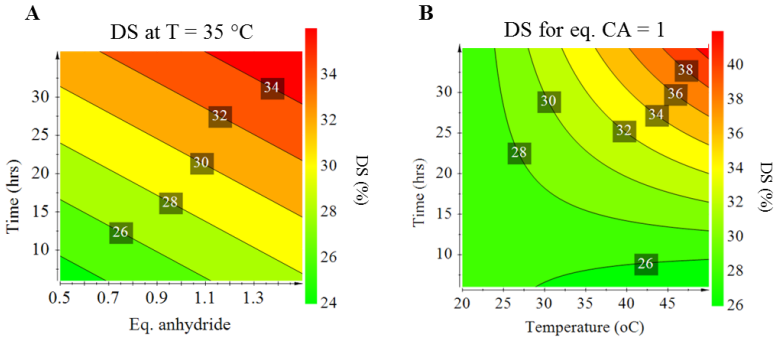

*Figure 3-8. Contour plots showing the effect of the reaction time and the equivalents of CA **2** at 35 °C (**A**) and of the temperature and reaction time for 1 eq. of CA used (**B**) on the DS of CS-nb. Degree of substitution (DS shown in mol%) obtained for a matching set of conditions, where the impact of a set of parameters on the final DS is shown by a change from green (low) to red (high).*

3.3.3 Proof-of-concept: Reactivity of CS-nb with a model thiol

Functional reactive groups added to macromolecules might not be sterically accessible for functionalisation due to solvation or chain conformation effects.[256] To assess the feasibility of the thiol-ene, CS-nb was coupled to a model thiol, cysteine (Cys, Figure 3-9A), where the thiol-ene was monitored by ^{1}H NMR by comparing the ratio between the alkene and the acetyl amine signals. As the amount of incorporated thiol increased the signal of nb decreased steadily, with a total disappearance after 5 min of irradiation for R_s = 1.9:1, confirming the accessibility of the thiol-ene reaction (Figure 3-9B-E).

The thiol-ene click reaction – such as any click reaction – is known for its high efficiency even at low concentration[66, 94] and observing only half of the nb peaks disappearing for R_s = 1:1 may appear very low. The short reaction time as well as the very low concentration of both thiols and nb imposed by NMR experiment to reduce polymer viscosity should be kept in mind. Huerta-Angeles *et al.* quantified clickable hyaluronic acid functionalisation after enzymatic reduction which allowed for NMR of non-viscous solutions. Enzymatic cleavage of CS can be performed by lysozyme[257] but requires a pH range not compatible with CS-nb solubility. Cysteine is also a hindered thiol bearing charged groups which may reduce the thiol-ene efficiency.

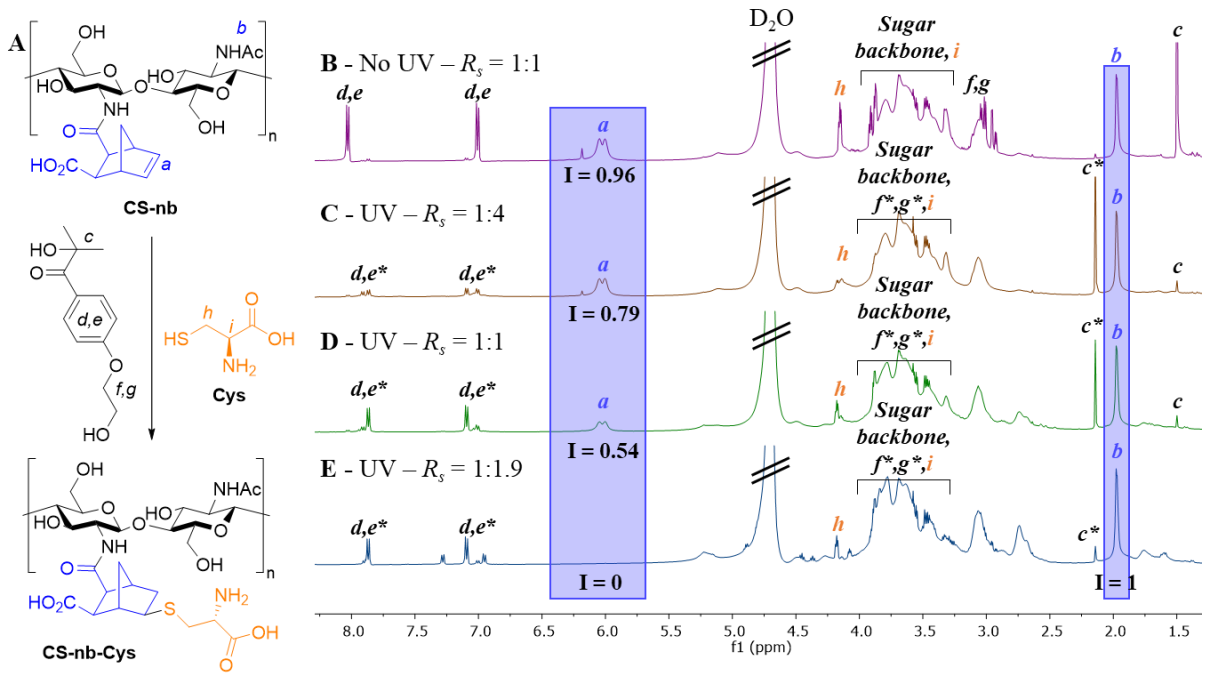

Figure 3-9. Thiol-ene coupling of Cys with CS-nb scheme (A) and the resulting ^{1}H NMR studies when R_s *is varied between 1:4 and 1:1.9 (B-E). IRG peaks after UV degradation are labelled with *.*

3.3.4 Synthesis and characterisation of thiolated CS (CS-SH)

The feasibility of the thiol-ene established, a thiolated CS (CS-SH) was synthesized to be used as a crosslinker for hydrogel synthesis to obtain purely polysaccharide-based materials. The synthesis of thiolated CS has been extensively reported in literature and optimum conditions have already been developed. Undesired *in situ* disulphide bond formation between polymer chain can be limited by acidic conditions.[252] Thiolation strategies rely on amide coupling with a thiolated carboxylic acid ; to limit polymer crosslinking, thiols can also be protected through symmetric disuldife bond formation and deprotected by mild reductions (Scheme 3-2 route *a*); amide bonds can also be obtained by amine-mediated ring opening of *γ*-thiobutyrolactone.[90] Alternatively, amine-containing biomolecules can ring-open Traut's reagent, imminothiolane, leading to concomitant thiolation and formation of a positively charged amidine, hence improving CS solubility[253] (Scheme 3-2, route *b*).

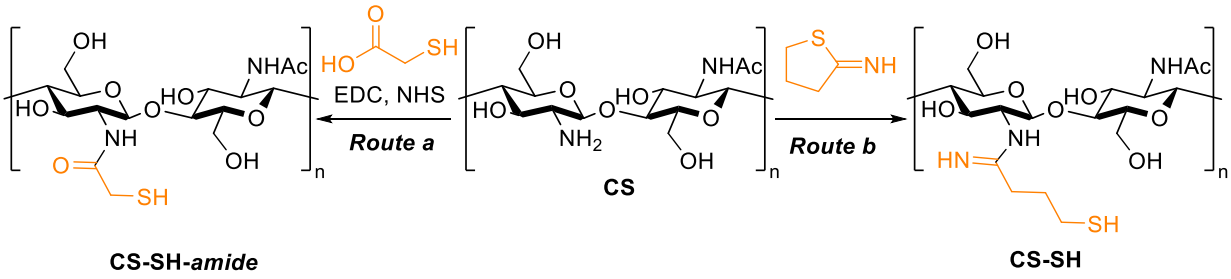

Scheme 3-2. Reaction routes to synthesize thiolated CS. Reaction conditions: a) *thiolated carboxylic acid, EDC/NHS OR disulphide dicarboxylic acid followed by TCEP reduction.* b) *imminothiolane.*

The reaction of CS with mercaptoacetic acid resulted in low-substituted, poorly soluble derivatives. Thiols, like amines, are very nucleophilic and are therefore susceptible to undergo competitive addition with activated carboxylic acids in place of amines, leading to thioesters. Although thioesters are classic intermediates for amide bond formation through native ligation,[258] they are also prone to hydrolysis (Scheme 3-3), which may explain the low DS observed. To improve solubility thiolation was performed with Traut's reagent, as it has been reported to improve CS solubility through the formation of amidine.[253] Kast *et al.* showed that this reaction is highly sensitive to pH, where neutral or basic pH promotes the nucleophilicity of the amines, while favouring competitive disulphide bond formation. They reported that optimum CS functionalisation was observed at pH = 5 which was therefore chosen for the reaction.[253] The pH was maintained slightly acidic during the dialysis to limit the formation of disulphide bridges.

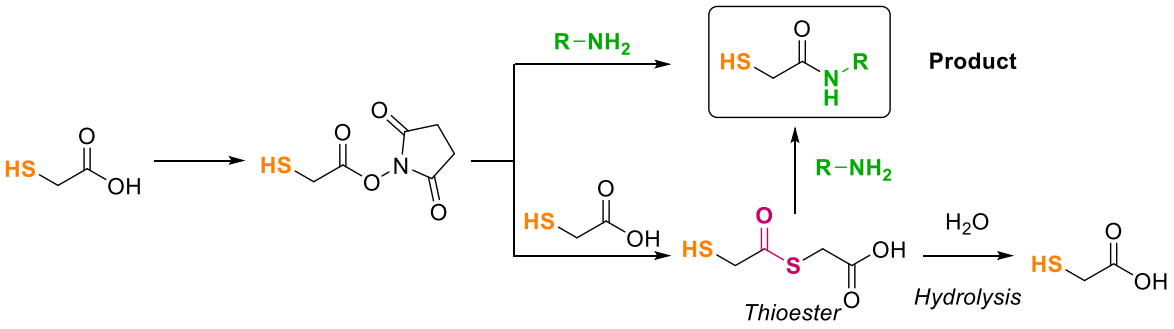

Scheme 3-3. Competitive carbonyl addition reactions between thiols and amines and the resulting side-products.

Several methods have been developed to quantify thiolation of biomolecules, ranging from chromatography to electrophoresis. UV-visible spectroscopy-based detections remain very attractive owing to their simplicity and their rapidity although they are also less sensitive. Colorimetry thiol quantification procedures typically involve the reaction of thiols leading to a

coloured compound either by covalent bond formation or by redox reaction with iodine, as developed by Bravo-Osuna *et al.*[259] The most common method remains the use of Ellman's reagent 5,5′-dithio-bis(2-nitrobenzoic acid) (DTNB) which relies on nucleophilic substitution of thiolate ions onto DTNB resulting in the formation of a yellow 5-thio-2-nitrobenzoic acid (TNB^{2-}) with strong absorbance at 410-420 nm (Scheme 3-4).[260] The reaction must be performed at basic pH to enhance thiol nucleophilicity and TNB^{2-} absorbance which can lead to solubility problems.[261] CS-nb was first dissolved in DI water and then diluted in PBS buffered to pH = 8. Thiolation contents of 0.49 µmol of thiol/mg of CS were measured using this method, consistent with the value of 0.33 µmol of thiol/mg of CS reported by Kast *et al.*[253]

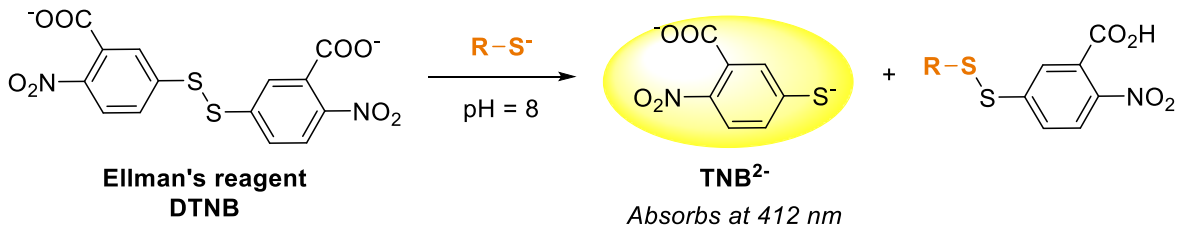

Scheme 3-4. Ellman's reaction for the quantification of thiols.

3.4 Conclusion

New photo-reactive, water-soluble CS derivatives functionalised with norbornene (CS-nb) were successfully synthesized and characterised. The degree of functionalisation could be easily tuned by adjusting mostly the reaction time and on the equivalent of CA added, with a minor effect played by the temperature. Finally, the reactivity of these nb pendant groups was proved by conjugating a model thiolated molecule, cysteine. This photocrosslinkable precursor would allow for efficient generation *in situ* generation of hydrogel scaffolds made of either macro-hydrogels or of DX microgels. The synthesis of characterisation of CS-nb hydrogels and microgels will be further discussed in chapters 4 and 6 respectively.

4 Thiol-ene click hydrogels: Synthesis, characterisation and applications

4.1 Introduction and aims

This chapter describes the synthesis and characterisation of hydrogels derived from the new photo-crosslinkable norbornene-functionalised chitosans CS-nb precursor described in Chapter 3. Gelation conditions were investigated, and the resulting hydrogels were characterised by rheology, swelling ratio measurements, and SANS. The toxicity of CS-nb and collagen loaded hydrogels towards Spina Bifida-relevant cell lines was tested, as well as its injectability and skin adhesion.

4.2 Methods

Collagen (Col) from calf skin (type 1) was purchased from Sigma. All cell culture media and reagents were purchased from Invitrogen, Life Technologies (Thermo-Fisher), except for DMEM F-12 Ham (Sigma) and EthD-III stain (Biotium). All other reagents were purchased from Sigma or as detailed in section 3.3 in Chapter 3.

4.2.1 CS-nb hydrogel synthesis

CS-nb was dissolved in 2% AcOH or DI water at the desired concentration (0.5, 1, 2 or 4 w:v%) with the photoinitiator Irgacure 2959 (IRG, 0.1 w;v%) then the chosen crosslinker (HS-PEG_2-SH, HS-PEG_{40}-SH or CS-SH, see Figure 4-1 for chemical structures) was added to the desired [SH]:[nb] molar ratio R_s (varied between 1:4 and 1:1). CS-SH was dissolved separately at the same concentration as CS-nb with 0.1 w:v% IRG and 0.02 M TCEP to cleave any disulphide bonds. The mixtures were vortexed for 30 sec and exposed to UV-A (320-400 nm, 36 W PL-L, approximative length 30 cm, Philips) or UV-B (280-320 nm, PL-L 36W/10 2G11, Philips) for the desired period of time, typically varied between 10 sec and 1 hr. Gelation was assessed by the inverted vial method.

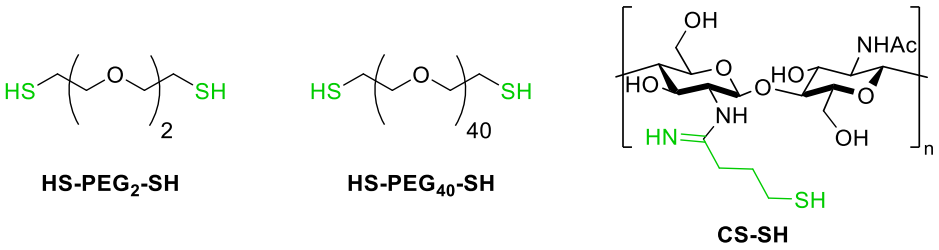

Figure 4-1. Chemical structures and abbreviations of the crosslinkers used in this work.

4.2.2 Collagen/CS-nb (Col/CS) hybrid hydrogel synthesis

Col was loaded into CS hydrogels as described in Section 4.2.1 with slight modifications. Briefly, CS-nb (4 w:v% in 0.1 w:v% IRG – 2% AcOH) and Col (1 w:v% in 2% AcOH) were combined with the desired crosslinker and diluted with 0.1 % IRG in 2% AcOH to a final composition of 2 w:v% CS-nb and 0.25 w:v% Col. The mixture was homogenised and cured with UV-A or UV-B for the desired period of time, typically varied between 10 sec and 15 min.

4.2.3 Swelling ratio

Hydrogel samples were realised by curing 200 µL of the precursor solution in a centrifuge plastic tube (2 mL) with UV B for 10 min. The resulting hydrogels were lyophilised and the dried mass, w_d, was recorded. Freeze-dried samples were immersed in the desired solution (DI water, PBS, or DI water with pH adjusted to 3 or 11 with 0.1 M HCl or NaOH). The samples were swelled for 7 days, after which the excess of liquid was wiped with filter paper and the mass of the swollen hydrogel, w_s, was recorded. The swelling ratio *SR* was calculated as: [262, 263]

$$Swelling\ ratio:\ SR = \frac{w_s}{w_d} \tag{4-1}$$

The water content W_c can also be calculated as shown in equation (4-2):

$$Water\ content:\ W_c = \frac{w_s - w_d}{w_d} \tag{4-2}$$

4.2.4 SEM images

200 µL of hydrogel was lyophilised and sectioned through the whole sample before mounting to an aluminium stub and coated with silver. Images were recorded on a Jeol IT300 SEM under high vacuum at 15.0 kV. Pore size measurements were performed with ImageJ on an average of 5 to 10 pores randomly taken from 4 images.

4.2.5 Rheology

Rheological measurements on the obtained hydrogels were performed with a Kinexus rheometer using a parallel plate geometry P20 (d = 20 mm) and a Peltier system for temperature control. The gel samples were synthesized in a 3D-printed PLA mould (diameter 21.5 mm, height 5.9 mm) from 800 µL of a pre-mixed solution of CS-nb (1, 2 or 4 w:v%), IRG (0.1 w:v%) and the chosen crosslinkers ([SH]:[nb] molar ratio R_s = 1:4, 1:2, 1:1.3 or 1:1) in 2% AcOH. Curing was performed with a UV-B lamp for 15 min on the Peltier plate. The PLA mould was carefully removed, and the hydrogel sample was loaded at a normal force of 0.1 N

(typical gap: 1.7 – 2 mm). Dynamic strain sweeps were performed at 1 Hz by varying the strain γ from 0.1 to 100 % at 25°C. Frequency sweep measurements were performed at a shear strain of 1 % by varying the frequency from 10 to 0.1 Hz. All measurements were performed in triplicates. The crosslinking density ρ_s and the mesh size ξ_a were respectively calculated as: [262]

$$\rho_s = \frac{G'}{RT} \tag{4-3}$$

$$\xi_a = \sqrt{\frac{6}{\pi \rho_s N_A}} \tag{4-4}$$

4.2.6 Small angle neutron scattering (SANS)

SANS was carried out on the Sans2d small-angle diffractometer at the ISIS Pulsed Neutron Source as described in section 2.3.1.1 in Chapter 2. Hydrogels were prepared in water tight sample cell with its design based on the sample cells available on the D22 beamline at the ILL facility (Grenoble) by curing a solution of CS-nb (2 or 4 w:v%) with the chosen crosslinker dissolved in 0.1 % IRG/1% AcOD-d_4 in D_2O. Samples were measured at 25°C. Data were background corrected with the scattering of an empty cell. The processing is discussed in Section 4.3.2.4.

4.2.7 *In situ* gelation and pork skin adhesion

CS-nb precursor solution (2 w:v%, IRG 0.1 w:v%, CS-SH, R_s = 1:1, stained with rhodamine for visualisation) was loaded in a 1 mL plastic syringe and injected through a needle (21 g, 0.8 × 40 mm) in a glass vial containing PBS with the UV-B light switched on or off.

Pork skin adhesion was assessed with a similar procedure. Briefly, a piece of pork skin (obtained from a local butcher) was placed in a crystallizer and immersed in PBS. The CS-nb precursor solution was loaded in a 1 mL plastic syringe and injected on the pork skin under UV-B. Adhesion was tested immediately after curing and after 3 days of immersion in PBS.

4.2.8 Cell culture

Human dermal fibroblasts (HDF) were cultured in Dulbecco's Minimal Essential Medium (DMEM) with 1g glucose/L and BeWo cell line (placenta cells) were cultured in DMEM media supplemented with F-12 Ham nutrient mixture. All media were supplemented with GlutaMAX™, 10% foetal bovine serum (FBS), and antibiotic-antimycotic (AntiAnti). Confluent cultures were detached from the surface using trypsin (Tryp LE Express) before experiments.

4.2.9 Cell toxicity: hydrogel synthesis and metabolic activity assays

50 µL of hydrogel was realised in a 96-well plate and sterilised with UV-B by curing for 5 min. The gels were subsequently washed with DMEM media until no colour change of the phenol red indicator was observed (2-to-7 washes depending on the hydrogel samples). The gels were equilibrated overnight and seeded with $7.5x10^3$ cells per well.

Cytotoxicity assays were performed with Alamar Blue reagent (AB, metabolic activity measurement). Briefly, at the desired timing (1, 3 or 7 days), gels were rinsed twice with PBS and the medium was replaced by FBS-free medium containing 5 % AB for 3 hrs. Supernatants were transferred in another 96-well plate and cytotoxicity was measured by recording the fluorescence of AB with a CLARIOSTAR microplate reader at room temperature (emission 545 nm, excitation 600 nm). Readings were background-corrected with non-seeded wells and gels, and data was presented compared to control, unexposed cultures, on the same plate.

4.2.10 Cell staining and imaging

Hydrogels were synthesized and seeded in a 96-well plate as described in section 4.2.9. At the desired timing (1, 3 or 7 days) gels were rinsed twice with PBS and the medium was replaced by FBS-free media containing 3 µM of calcein AM (live cells stain) and 4 µM ethidium homodimer III (EthD-III, dead cells stain) for 1 hr. Gels were subsequently rinsed twice with PBS and fixed with 4% paraformaldehyde in PBS (100 µL) for 15 min. The wells were rinsed twice, and nuclei were stained with 300 nM (0.1 µg/mL) DAPI in PBS. Plates were stored in live cell imaging solution at 4°C and imaged at 37°C by widefield microscopy using a Leica LASX live cell imaging workstation equipped with a Leica DFC365FX monochrome CCD camera (1392x1040 6.45µm pixels, 8 or 12-bit, 21 fps full frame). Excitation filters were chosen as 350/50, 480/40 and 560/40 respectively to visualise DAPI, calcein AM or EthD-III stains. Data were collected with Leica LAS-X acquisition software.

4.3 Results and discussion

4.3.1 Hydrogel synthesis conditions

The gelation conditions of CS-nb were investigated in terms of polymer concentration, curing time and crosslinker concentration. Initial screenings were performed with 2,2′-(ethylenedioxy)diethanethiol (HS-PEG_2-SH,) which is water-soluble and more flexible than frequently used dithiothreitol (DTT)[96, 264] as well as cheaper and more accessible than the longer thiolated PEGs. IRG was chosen as photoinitiator due to its water-solubility and non-toxicity;[265] although IRG maximum absorbance is at 260 nm, it is frequently used with cells

with UV-A irradiations or blue LEDs (365 nm) as its decomposition is sufficient to initiate gelation.[73] Different polymer and crosslinker concentrations were tested and gelation was assessed by the inverted vial method. At 0.5 w:v% polymer concentration, the viscosity of the dispersion increased progressively as the [SH]:[nb] molar ratio, R_s, increased from 1:4 to 1:1. However, no gelation occurred even when the UV exposure time was prolonged to 1 hr. For polymer concentrations of 1 and 2 w:v%, gels were formed instantly upon UV exposure even for R_s = 1:4 (Figure 4-2A). The completion of the reaction was confirmed by *in situ* ^{1}H NMR, evident from the disappearance of the nb peaks at 6.2 ppm (Figure 4-2CD).

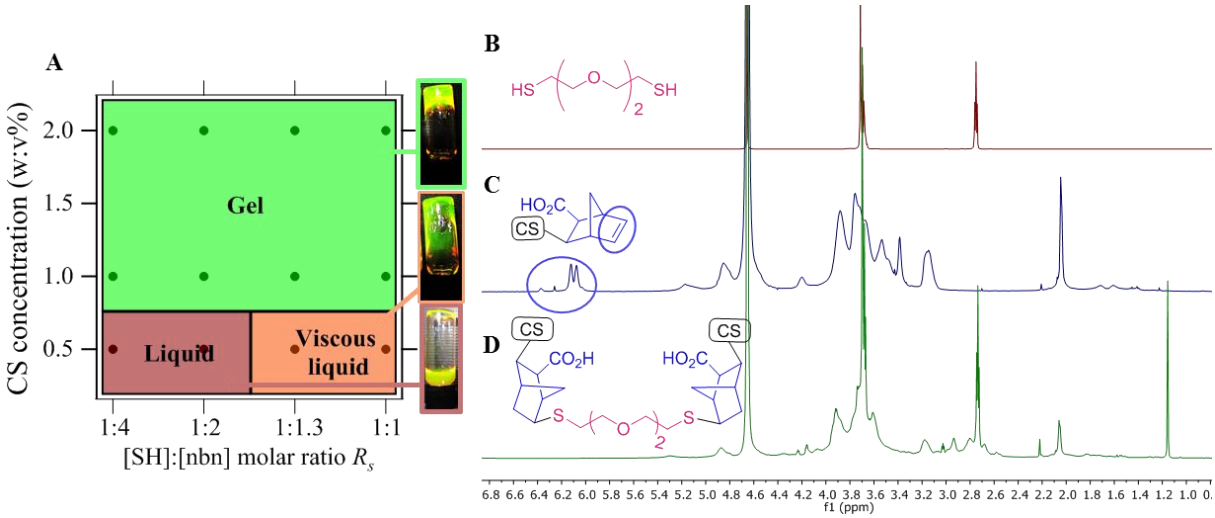

Figure 4-2. Formation of CS-nb hydrogels: hydrogel phase diagram (A) and ^{1}H NMR of HS-PEG$_2$-SH (B), CS-nb (C) and the resulting product (D).

Such fast gelation kinetics has been previously reported when nb was used as the alkene component in the thiol-ene click reaction. For instance, Lee *et al*. measured the gelation kinetics of a tetra-arm, nb-functionalised PEG with thiolated carboxymethylcellulose by photorheology. They found that gelation occurred within 5 sec, independently of the thiol content.[266] McOscar *et al.* reported a gelation time of around 30 sec for a nb-functionalised carboxymethylcellulose polymer crosslinked with HS-PEG$_2$-SH.[91] In comparison, Hachet *et al.* have previously reported dextran-[267] and HA-based hydrogels and nanogels resulting from the thiol-ene reaction between the pentenoic side chains of the polysaccharide and a thiolated PEG crosslinker.[255] Gelation occurred in 2.5 min for the fastest systems, and up to 20 min for the slowest. As their polysaccharide system and DS compare well with CS-nb, this difference in the reaction kinetics most likely arises from their terminal alkene choice, which is less reactive than nb. Overall, our results compare well with literature.

4.3.2 Hydrogel properties and characterisation

4.3.2.1 Swelling ratio

These new hydrogels were first characterised regarding their swelling ratio (SR), internal structure and rheological behaviour. It was anticipated that both lower CS-nb concentrations and crosslinking densities would result in less densely crosslinked network which in turn should result in greater SR. The effect of the crosslinker, however, was less obvious. Measurements were therefore performed for a fixed composition of 2 w:v% CS-nb and R_s = 1:1. All hydrogel materials could uptake up to 60 times their own mass of water, depending of the crosslinker used (Table 4-1). The higher SR were obtained when hydrogels were crosslinked with HS-PEG$_{40}$-SH (SR ~ 65), which is the longest and more flexible crosslinker, thus allowing for greater mobility between polymer chains and hence higher water uptake. In comparison, the swelling was smaller for both the short HS-PEG$_2$-SH (SR ~ 54) and for the multi-arm CS-SH (SR ~ 46) crosslinkers, which hold the polymer more tightly together leading to reduced swelling.

Table 4-1. Swelling ratios of 2% CS-nb hydrogels depending on the crosslinker.

	DI water	**pH = 3**	**pH = 11**	**PBS**
HS-PEG$_2$-SH	54.3 ± 5.4	64.4 ± 11	15.3 ± 5.7	12.9 ± 0.43
HS-PEG$_{40}$-SH	64.5 ± 4.4	54.5 ± 4.8	16.4 ± 1.4	19.3 ± 0.79
CS-SH	45.9 ± 16.3	54.9 ± 17	11.0 ± 2.4	9.0 ± 0.77

All hydrogels presented a pH-sensitive swelling behaviour, with SR ~ 55-65 at pH = 3 and SR ~ 10-15 at pH = 11, with a similar shrinkage observed in PBS (SR ~ 10-20). Under acidic conditions, amines get protonated leading to polymer chain repulsion and hence improved swelling, while their deprotonation under basic conditions allows for chain collapse and thus reduced swelling. Polyelectrolyte shrinkage generally occurs in the presence of salts due to ionic screening of the electrostatic interactions between polymer chains. [268] The water content (W_c) was very similar to the SR as all hydrogels were mostly constituted of water (Table 4-2).

Table 4-2. Water content of 2% CS-nb hydrogels depending on the crosslinker.

	DI water	**pH = 3**	**pH = 11**	**PBS**
HS-PEG_2-SH	53.3 ± 5.4	63.4 ± 11	14.3 ± 5.7	11.9 ± 0.43
HS-PEG_{40}-SH	63.5 ± 4.4	53.5 ± 4.8	15.4 ± 1.4	18.3 ± 0.79
CS-SH	44.9 ± 16.3	53.9 ± 17	10.0 ± 2.4	8.0 ± 0.77

4.3.2.2 Microstructure: SEM

The internal structure of the hydrogel was studied by SEM. All hydrogels presented very similar honeycomb-like structures with highly polydisperse pores of dimensions varying between ~ 20 and up to ~ 120 µm (Figure 4-3), compatible with cell seeding and infiltration. As SEM requires preliminary drying of the samples this may affect the actual structure of the hydrogels.

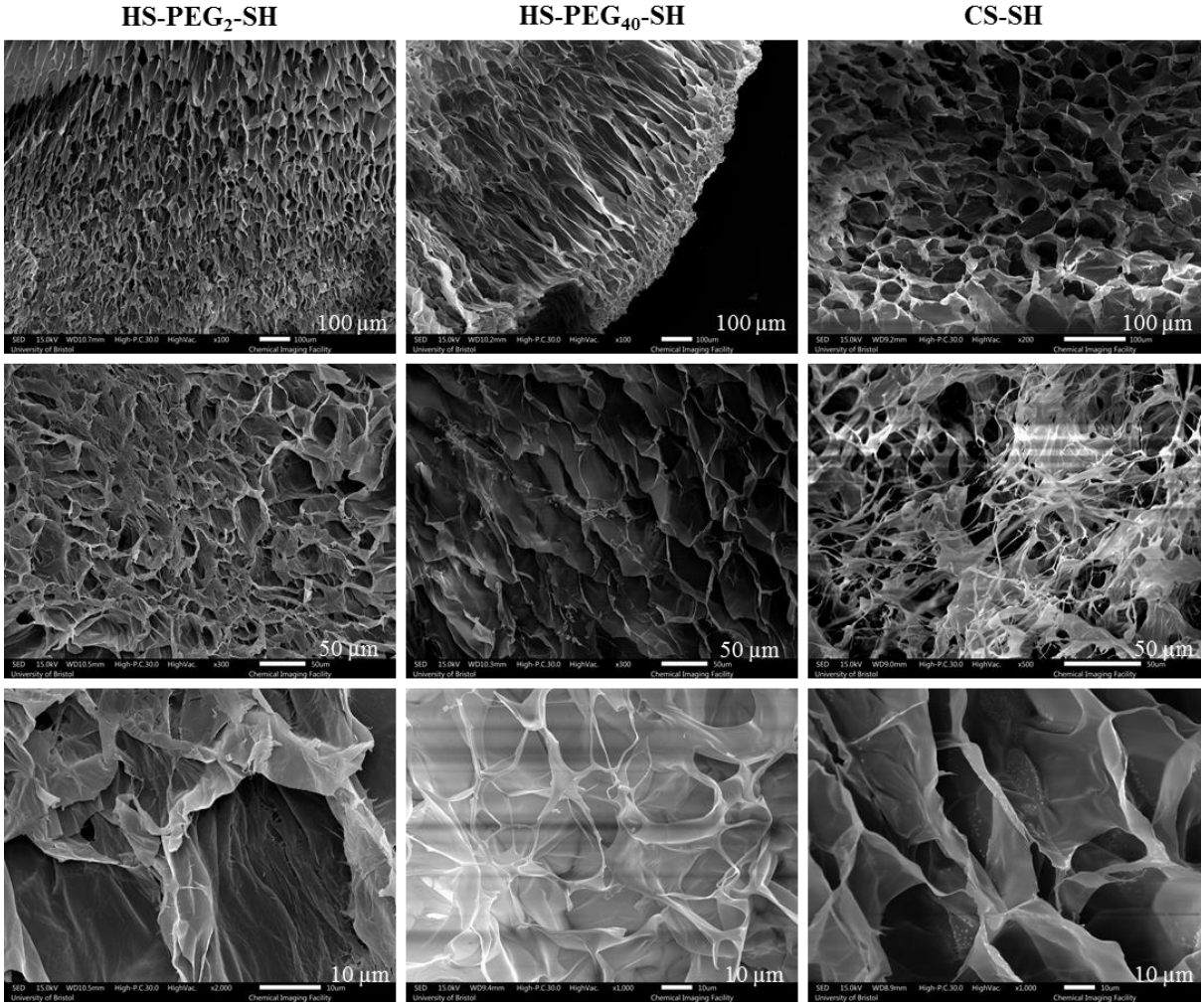

Figure 4-3. SEM images of CS-nb hydrogels crosslinked with: HS-PEG_2-SH, HS-PEG_{40}-SH and CS-SH.

The smaller pores were observed for HS-PEG$_2$-SH (d ~ 33 ± 10 µm) while HS-PEG$_{40}$-SH-crosslinked materials had bigger pores (d ~ 45 ± 15 µm). CS-SH-crosslinked samples were more polydisperse in pore dimensions, with both small pores of d ~ 30 µm but also more open geometries of dimensions ~ 60-90 µm. These observations are consistent with the differences in the SR measured, as the swelling is directly related to the ability of a material to uptake water and therefore to its mesh size.

4.3.2.3 Rheology

The rheological properties of CS-nb hydrogels were studied for different crosslinkers, R_s and CS concentrations through both amplitude and frequency sweep measurements. For all samples, the storage modulus *G'* was at least 10 times higher than the loss modulus *G''*, which is characteristic of an elastic, gel-like material. Both *G'* and *G''* were constant up to a critical strain γ_c varying between ~ 10 and ~ 60 % depending on the sample, while *G'* did not present significant frequency-dependency (Figure 4-4 to Figure 4-7).

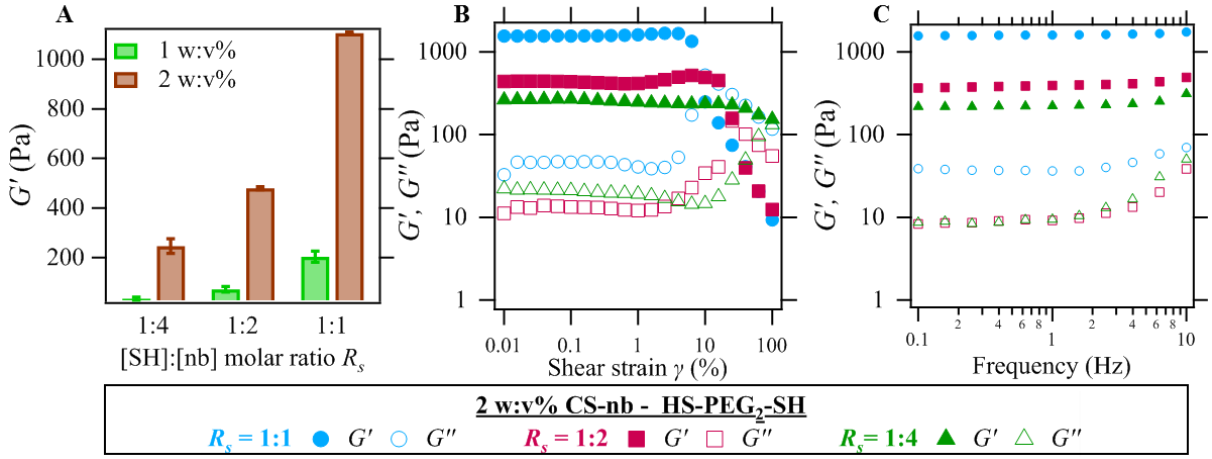

Figure 4-4. Rheology measurements of CS-nb hydrogels crosslinked with HS-PEG$_2$-SH. (A) averaged G' and G'' on the linear viscoelastic region determined by amplitude sweep measurements for various CS-nb concentrations and R$_s$. *(B) amplitude sweep and (C) frequency sweep measurements of 2% w:v CS-nb hydrogels crosslinked for various* R$_s$.

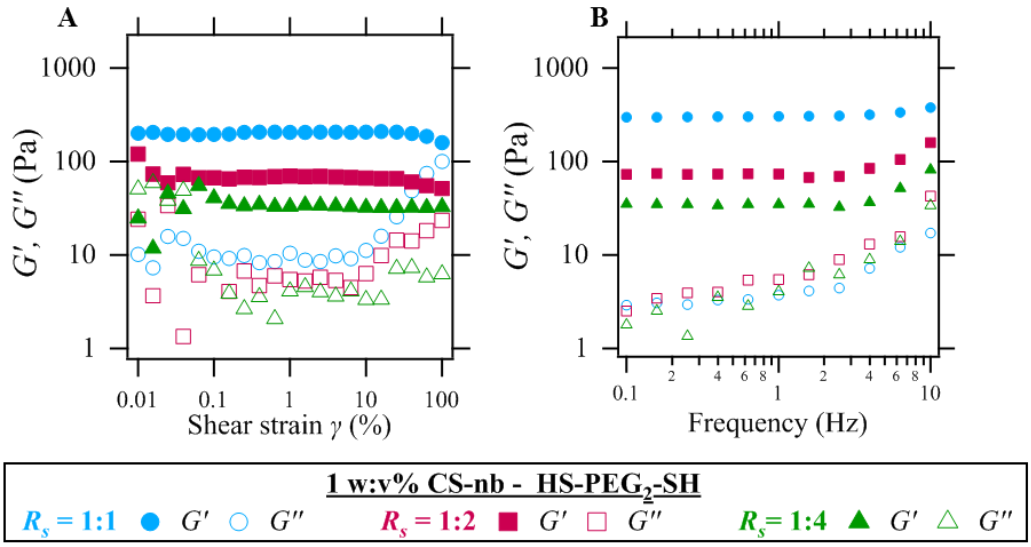

Figure 4-5. Rheology measurements of 1 w:v% CS-nb hydrogels crosslinked with HS-PEG$_2$-SH: A) amplitude sweep and B) frequency sweep measurements for various R_s.

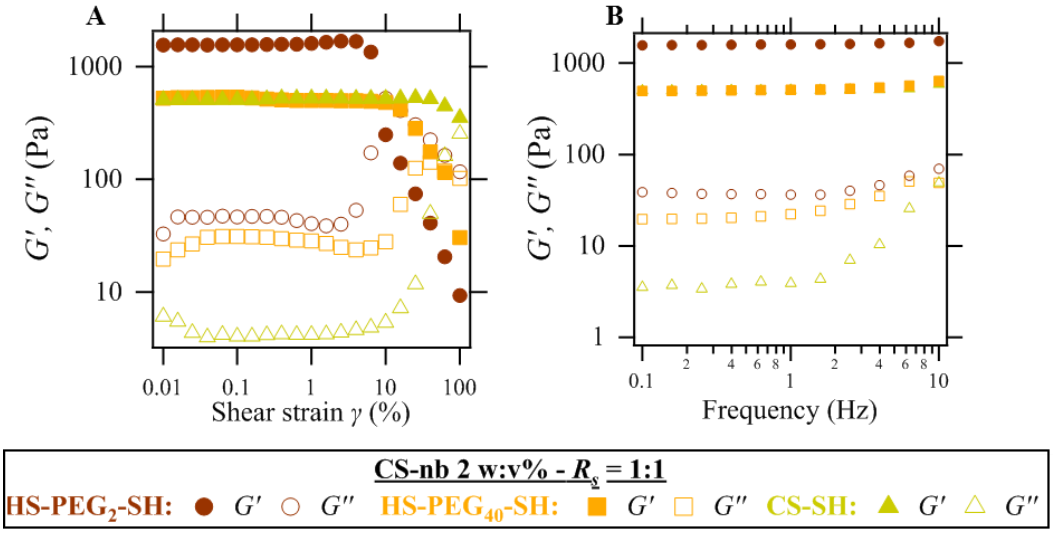

Figure 4-6. Rheology measurements of 2 w:v% CS-nb hydrogels for different crosslinkers for R_s *= 1:1. A) amplitude sweep and B) frequency sweep measurements.*

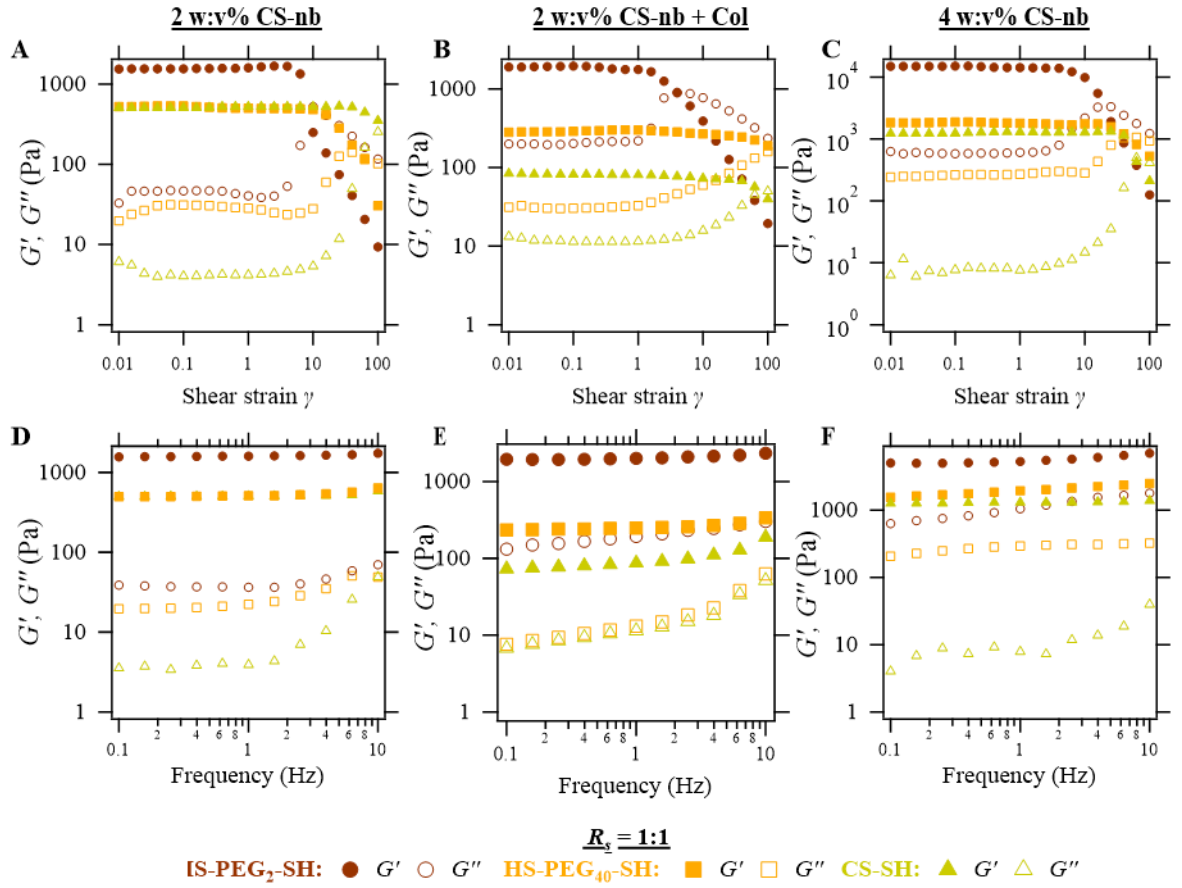

Figure 4-7. Amplitude sweep measurements of hydrogels made from: 2 w:v% CS-nb (A), collagen hybrid (B) or 4 w:v% CS-nb (C) and frequency sweep of the same hydrogels (D-F) with different crosslinkers for R_s *= 1:1.*

When HS-PEG$_2$-SH was used as crosslinker, *G'* increased both with the polymer concentration and with R_s, as a result of the formation of more crosslinking points between polymer chains. *G'* could be tuned between ~20 and ~12.5 kPa by simply varying these two parameters (see Figure 4-14A and Appendix H for the data concerning the 4% hydrogels). Similar control was achieved by Gramlich *et al.* who crosslinked hyaluronic acid with DTT, with *G'* varying between ~ 0.2 and up to ~ 100 kPa.[98] McOscar *et al.* crosslinked nb-functionalised carboxymethyl cellulose with HS-PEG$_2$-SH and observed very similar mechanical properties for R_s = 1:2 and 1:1, which they attributed to competitive chain entrapment reducing the available nb crosslinking points.[91] Their higher polymer concentration (4%) may explain why this was not observed in our experiments. The effect of R_s at 4 w:v% CS was not investigated in our study.

The rheological properties could be further adjusted by changing the crosslinker (Figure 4-8). Replacing HS-PEG$_2$-SH by the longer HS-PEG$_{40}$-SH resulted in lower *G'*, especially for high R_s (respectively *G'* ~ 1400 Pa and *G'* ~ 450 Pa for R_s = 1:1, Figure 4-8A). A shorter

crosslinker would bring polymer chains closer together after crosslinking, resulting in more compact networks and hence higher elastic modulus G'. The difference was especially pronounced for R_s = 1:1, suggesting that the shorter crosslinker leads to more efficient bridging of the polymer chains. The greater flexibility of HS-PEG$_{40}$-SH may favour intra-molecular nb crosslinking, thus reducing the efficiency of the hydrogel network formation. PEG mobility may also favour disulphide formation, thus reducing the number of thiols available for the thiol-ene crosslinking. Similarly, little differences were observed when the multi-functional crosslinker CS-SH was used, possibly due to steric hindrance as the thiol functionalities were very closed to the polymer chains. A multi-functional, less bulky crosslinker, such as a tetra-arm thiolated PEG, would be expected to result in a stiffer network, as exemplified by Mũnoz *et al.* with nb-functionalised gelatin crosslinked either with DTT or with a tetra-arm PEG.[96]

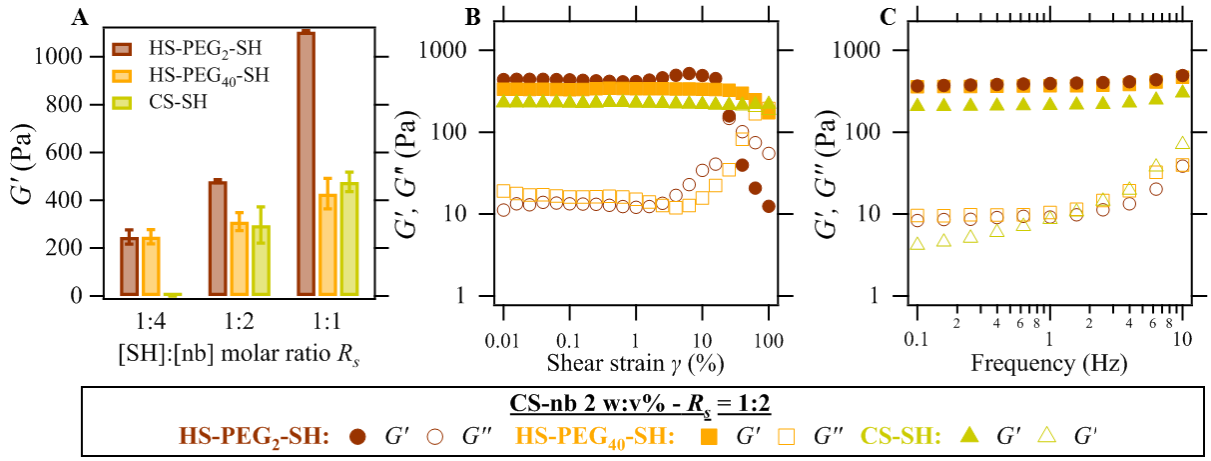

Figure 4-8. Rheology measurements of 2 w:v% CS-nb hydrogels for different crosslinkers. (A) averaged G' and G'' on the linear viscoelastic region determined by amplitude sweep measurements for various crosslinkers and R_s. *(B) amplitude sweep and (C) frequency sweep measurements of 2% w:v CS-nb hydrogels crosslinked for* R_s *= 1:2.*

Ye *et al.* studied a series of cellulose hydrogels crosslinked with divalent short epoxide crosslinkers, followed or not by a second functionalisation with PEG-terminated epoxides (M_n = 500 g/mol). The resulting double-crosslinked hydrogels were mechanically stronger than their single crosslinked analogues and could effectively dissipate strength due to the more flexible nature of the long crosslinker.[269] This could be a very simple and elegant way to improve hydrogel mechanical properties.

Overall, hydrogels of a wide range of mechanical properties (0.020-20 kPa) could be obtained by varying the polymer concentration, the ratio of crosslinked nb and the crosslinker nature, which allows for the generation of materials with mechanical properties relevant to a

wide area of biomedical applications, ranging from neural tissue engineering (~ 100 Pa) to muscle or skin cell culture (~ 10 kPa).[270]

4.3.2.4 SANS

SANS was used to study hydrogel nanostructure and to relate it to its bulk mechanical properties. The effect of CS concentration, R_s and of the crosslinker were studied. The formation of crosslinking points was evidenced by the linear increase in scattering intensity I as q decreased, related to the formation of large structures (Figure 4-9). This increase was characterized by a mass fractal of ~ 2.4 – 2.6 (Table 4-3).

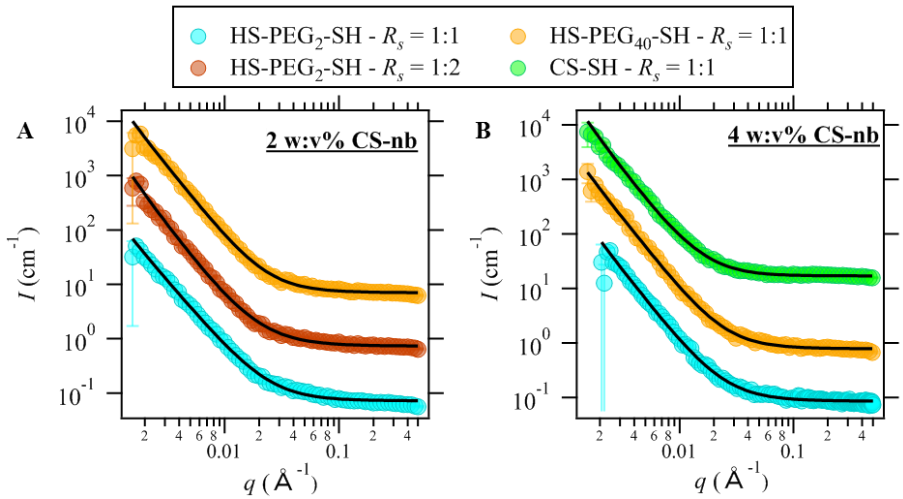

Figure 4-9. SANS data of CS-nb hydrogels. Fitted data are shown as a black line. Data have been offset (10x) on the y-axis for clarity.

As discussed in section 2.3.3.6 in Chapter 2. the modelling of the scattering of hydrogels is typically described by the sum of a scattering contribution from the polymer chains $I_L(q)$, which is characterized by the correlation length or the mesh size of the gel network ξ, and of a contribution from the scattering of clusters of greater dimensions $I_S(q)$, where the aggregate dimension can be obtained by a Guinier-like term (Eq. 2-26) or expressed as a Porod law. The mesh size is classically expressed as a Lorentzian term (Eq. 2-25) which is the predominant term in the intermediate/high q region; for hydrogen-bond rich hydrogels such as PVAc this term can be modified with the mass fractal D as reported by Geissler *et al.*[231] (Eq. 2-28):

$$I_L(q) = \frac{I_L(0)}{\left(1 + \frac{D+1}{3}\,\xi^2 q^2\right)^{D/2}} \qquad (2\text{-}28)$$

As polysaccharides are prone to hydrogen-bonding a modified expression of $I_L(q)$ was preferred. A characteristic aggregate dimension can also be calculated through the DAB model (Eq. 2-30) for two-phase structures with sharp boundaries[233, 240, 242] as performed by Ryu *et al.* for covalently crosslinked hyaluronic acid hydrogels.[242] The scattering profile of CS-nb increases according to a power law, suggesting that a single dimension, the mesh size ξ, was detected, which matches the pore dimensions measured by SEM (> 200 nm). The scattering was modelled using Eq. 2-29:[61, 235]

$$I(q) = \frac{A}{q^D} + \frac{C}{1+(q\xi)^m} + background \quad (2\text{-}29)$$

where D is the mass fractal exponent. The Lorentzian exponent m allows for diversions from the classic $m = 2$ as expected for hydrogen bond-rich networks.

Fitted data is shown in Table 4-3 and Table 4-4 for 2 and 4 w:v% hydrogels respectively. As the baseline was not flat the background scattering value B was fixed by fitting the high/intermediate q region to a power law as described by Saffer *et al.*:[61]

$$I(q) = \frac{A}{q^D} + B \quad (4\text{-}5)$$

The mesh size obtained with Eq. 2-29 for 2 w:v% hydrogels compares very well with those obtained by rheology, calculated with Eq. 4-4. As the degree of crosslinking increases from R_s = 1:2 to 1:1 the mesh size ξ decreases from ~ 29 to ~ 20 nm, consistent with more crosslinking points bringing the polymer chains in closer proximity. The use of a longer crosslinker allows for bigger ξ (19 to 27 nm) as expected. The Porod exponent, comprised between 2 and 3, is consistent with hydrogel formation, while the Lorentzian exponent is lower than 2, indicating that the polymer chains are behaving as in a good solvent.[61]

The values of the mesh size obtained from SANS fitting for the 4 w:v% hydrogels differ from those obtained by rheology, especially for HS-PEG$_2$-SH and CS-SH hydrogels (Table 4-4). The general trend of ξ increases from HS-PEG$_2$-SH to HS-PEG$_{40}$-SH is still verified. The smallest mesh size was measured for CS-SH hydrogels with SANS (11 nm) while its mechanical properties suggest a much bigger value (17 nm). Hyland *et al*. observed very different evolutions of rheological properties and ξ obtained by neutrons, and suggested that the material mechanical properties was not only a result of the network density – measured as the correlation length L_c using DAB model – but also of the fiber thickness and its packing.[238] Rheology also investigates macroscopic properties, while SANS probes the polymer chain length scale; due to the high thiolation of CS-SH and its proximity to the polymer backbone, it is likely that these hydrogels were very heterogeneous, with highly reticulated area where the

thiols could be accessed and others poorly crosslinked due to steric hindrance. The access to a smaller *q* range would provide more information on the dimension of the resulting aggregates.

Table 4-3. Summary of rheology and SANS characterisations of 2w:v% CS-nb hydrogels. Rheology: ρ_s: crosslinking density, ξ: mesh size, calculated from Eq. 4-3 and 4-4 respectively. SANS: D: fractal dimension, m: Lorentzian exponent in Eq. 2-29.

Hydrogel		**Rheology**			**SANS**			
R_s	**Crosslinker**	G' (Pa)	ρ_s (mol/m^3)	ξ_a (nm)	ξ (nm)	D	m	χ^2
1:1	HS-PEG$_2$-SH	1107	1.17	19.2	18.4 ± 3.5	2.43	1.43	3.65
1:2	HS-PEG$_2$-SH	479	0.19	25.5	29.3 ± 2.3	2.79	1.58	3.98
1:1	HS-PEG$_{40}$-SH	435	0.18	26.2	27.9 ± 4.9	2.60	1.37	3.59
1:1	CS-SH	477	0.19	25.5	-	-	-	-

Table 4-4. Summary of rheology and SANS characterisations of 4w:v% CS-nb hydrogels. Rheology: ρ_s: crosslinking density, ξ: mesh size, calculated from Eq. 4-3 and 4-4 respectively. SANS: D: fractal dimension, m: Lorentzian exponent in Eq. 2-29.

Hydrogel		**Rheology**			**SANS**			
R_s	**Crosslinker**	G' (Pa)	ρ_s (mol/m^3)	ξ_a (nm)	ξ (nm)	D	m	χ^2
1:1	HS-PEG$_2$-SH	11560	4.67	8.79	15.2 ± 0.3	2.61	1.43	1.49
1:1	HS-PEG$_{40}$-SH	1695	0.67	16.8	20.0 ± 4.7	2.60	1.42	1.83
1:1	CS-SH	1535	0.67	17.2	11.3 ± 0.7	2.73	1.95	4.37

The fractal dimension *D* is also relevant to biological studies, as shown by Hung *et al.* on agarose physical hydrogels. They synthesized a variety of hydrogels of matching rheological properties but different mass fractal, which they measured both by rheology and with SAXS. While the impact of rheology on cell culture is well-known, they were the first to observe that hydrogel fractal dimension also had a significant impact on stem cell differentiation.[271] CS-nb hydrogels studied with SANS presented very similar mass fractals $D \sim 2.6$ suggesting that cell toxicity assays may be directly correlated to the hydrogel rheological properties.

In summary, covalently crosslinked hydrogels of various mechanical properties were synthesized and characterized in terms of their swelling ratios, mechanical properties, micro- and nano-structure. Possible applications of these materials were further investigated.

4.3.3 Proof-of-concept: towards biological applications

Hydrogels of tailored shapes could be obtained using moulds. Owing to the very fast gelation kinetics, fluorescent dyes could be encapsulated without damaging their chemical structure. As an example, rhodamine B was entrapped during the gelation process. After one week of immersion in water, the gel had swollen and had lost most of its colour, confirming its release (Figure 4-10A). Although the release was not quantified, this highlights the possible application of these hydrogels for drug delivery, especially due to their improved swelling under acidic conditions, which is a common feature of tumours and infected organs.

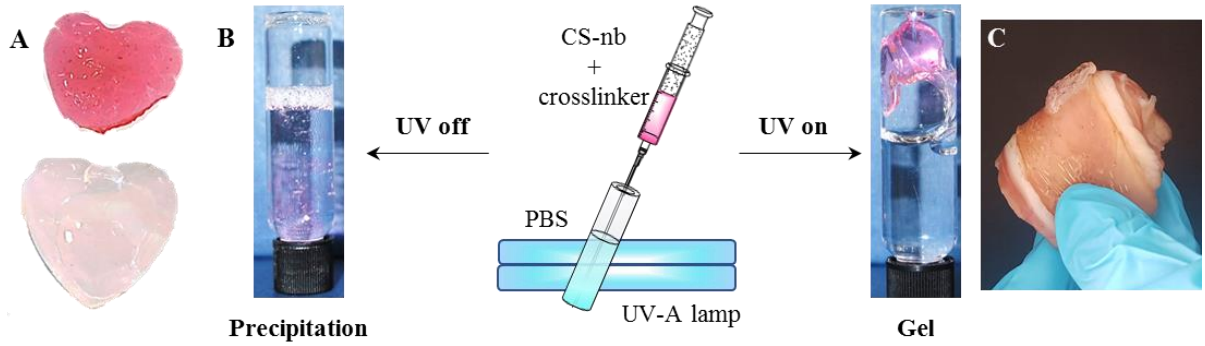

Figure 4-10. Possible applications of the hydrogels. (A) Shape-retaining heart with encapsulated rhodamine as generated (top) and after one week of storage in water (bottom). (B) In-situ *generated hydrogels in PBS. (C) Hydrogel adhesion on pork skin (*in situ *synthesised).*

In the case of Spina Bifida-related applications, *in-situ* gelation under biological conditions must be verified. Due to the low solubility of CS-nb at physiological pH, the polymer precipitated immediately when injected in a vial filled with PBS. If the injection, however, was performed while irradiating the vial with UV, a gel was formed instead (Figure 4-10B). The result was successfully reproduced when PBS was replaced with the simulated amniotic fluid.

It is important that the scaffold, once generated, adheres strongly to the foetus' skin around the defect. On the other hand, the material once generated should hold in place and present limited adhesion towards the foetal membrane. The thiol-ene being a radical-initiated reaction, it was anticipated that free radicals could also react with skin to generate adhesives. Removing the UV light, on the other hand, would stop the radical propagation and therefore

passivate the hydrogel surface, which should inhibit further adhesion. This hypothesis was assessed by introducing pork skin in PBS media and by directing the needle on the skin. The generated material adhered to the skin for up to 4 days when stored in PBS without sticking to the plastic container (Figure 4-10C). Although adhesion was not properly quantified, this highlights the potential use of these materials for bandages. Another

Finally, materials intended for biomedical applications – and especially keeping the intended application in mind – must be administered sterile. CS-nb precursor solutions containing IRG and a crosslinker were autoclaved for sterilisation. The resulting solution presented identical ^{1}H NMR to unsterilized mix and could still generate hydrogel in the presence of UV light. These preliminary results make CS-nb a promising polymer for *in utero* applications whose toxicity will be investigated next.

4.3.4 Cell toxicity assays

Hydrogels have been widely studied for cell culture as they provide a 3D structure for cells to grow and develop which is highly similar to human tissues.[272] The hydrogels developed presented a range of tuneable stiffness, which is an important parameter to allow for cell growth. Substrates favouring skin wound healing and fibroblast growth frequently present G' ~ 0.5 – 10 kPa,[211, 273, 274] which designated the selection of 6 hydrogels for initial toxicity testing (Figure 4-7). A good hydrogel candidate for a tissue engineering approach must allow cells to adhere, infiltrate and spread in the scaffold; failing to these will lead to cell toxicity, which can be assessed by metabolic activity measurements or fluorescent staining. CS-nb hydrogels were used as scaffolds to culture two different cell lines, human skin fibroblasts (HDF), a standard model for wound healing and tissue engineering applications, and placenta cells (BeWo), relevant in the context of SB. If there are several reports of HDF cells cultured in hydrogels, the literature on BeWo is reduced. Wong *et al.* grew BeWo cells on ECM mimics – Matrigel and collagen I – and found that the gel stiffness greatly impacted the cell morphology, where thick substrates triggered the formation of aggregates, while thinner ones allowed for efficient cell spreading.[275] This work, however, did not mention any physical characterisation of the materials used.

Cell viability on hydrogels of medically-relevant stiffness (0.5 – 10 kPa, Figure 4-7) was assessed by metabolic activity measurements 24 hrs after cell seeding onto the gel scaffold. All hydrogels allowed for limited cell spreading compared to the control cells seeded on a plate. Both cell lines responded very differently to the gel stiffness. The viability of BeWo cells after 24 hrs was between 60 and 80 % of the corresponding control for most gel compositions, with

comparable cell morphologies (Figure 4-11A-D). On the other hand, HDF viability was highly dependent on the substrate stiffness, with the formation of cell spherical aggregates of low viability (~ 20 – 35 %) for the softest gels, while stiffer matrixes allowed for more efficient cell spreading, comparable to that of control cells cultured in a plate and with viability up to 80 % (Figure 4-11E-H). These observations match previous work performed with fibroblasts – human or murine - on non-biofunctionalised acrylate hydrogels – *i.e.* without the introduction of peptides or sugars to impact on adhesion.[50, 276]

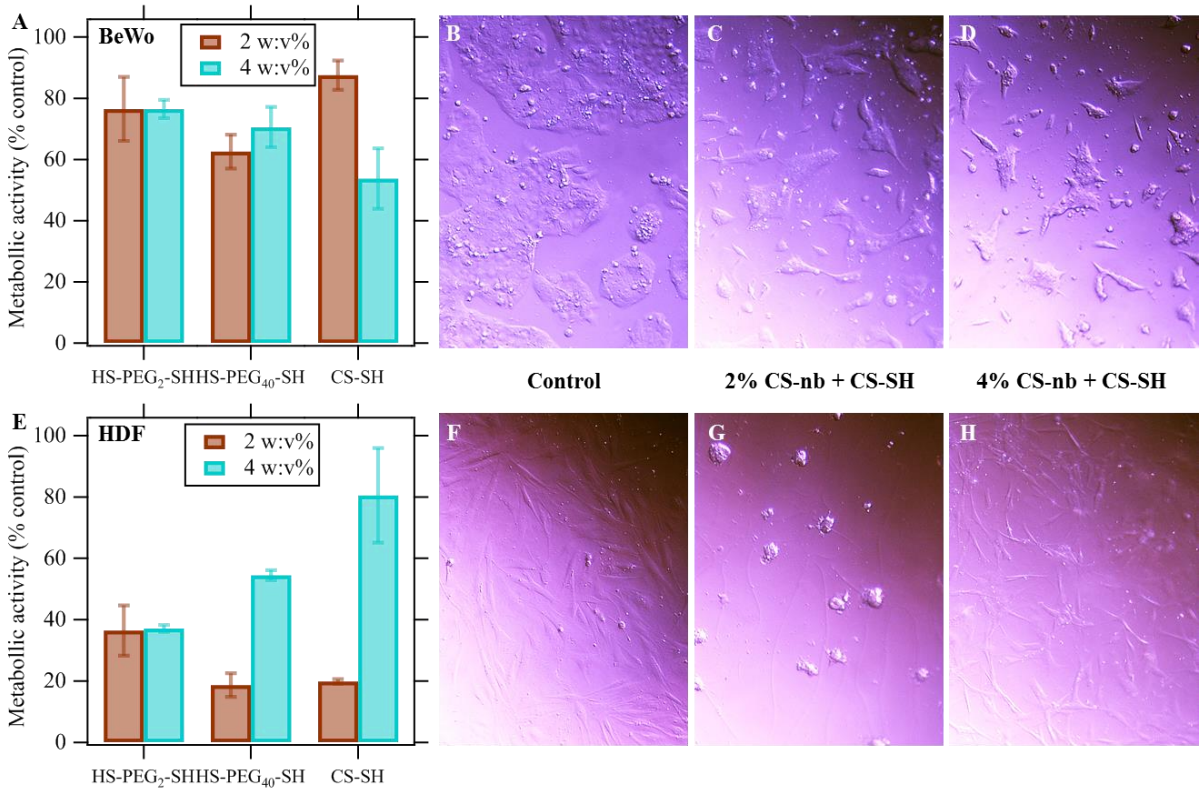

Figure 4-11. Cell viability (A, E) and imaging of BeWo (B-D) and HDF (F-H) cells 24 hrs after seeding.

HDF presented poor adhesion on the gel matrix, particularly observed during the staining procedures where numerous washes were required, and it resulted in a drastic drop in cell viability after 24 hrs as cells could not proliferate. Although CS presents similarities with GAG in the ECM, its structure often fails to promote cell adhesion[277] and functionalisation with adhesion peptides – such as RGD[278] - or proteins – like HA,[279] Col[280] or gelatin[281] – is common. It is worth mentioning that all these hybrids benefitted from the incorporation of CS to reduce their biodegradation kinetics and to improve their mechanical properties. For simplicity, Col was simply entrapped in the gel network during the gelation step, so that the final CS and Col concentrations were 2 w:v% and 0.25 w:v% respectively. The resulting hybrid

was seeded with either BeWo or HDF cells. After 3 days, BeWo cells showed very similar cell spreading, growth and morphology compared to pure CS hydrogels. HDF, however, showed a drastic improvement in their spreading, with morphologies and viabilities comparable to control cells (Figure 4-12 and Figure 4-14). This suggests that BeWo and HDF cells have very different adhesion mechanisms, which could be a way to obtain hydrogel selective skin adhesion for SB implications.

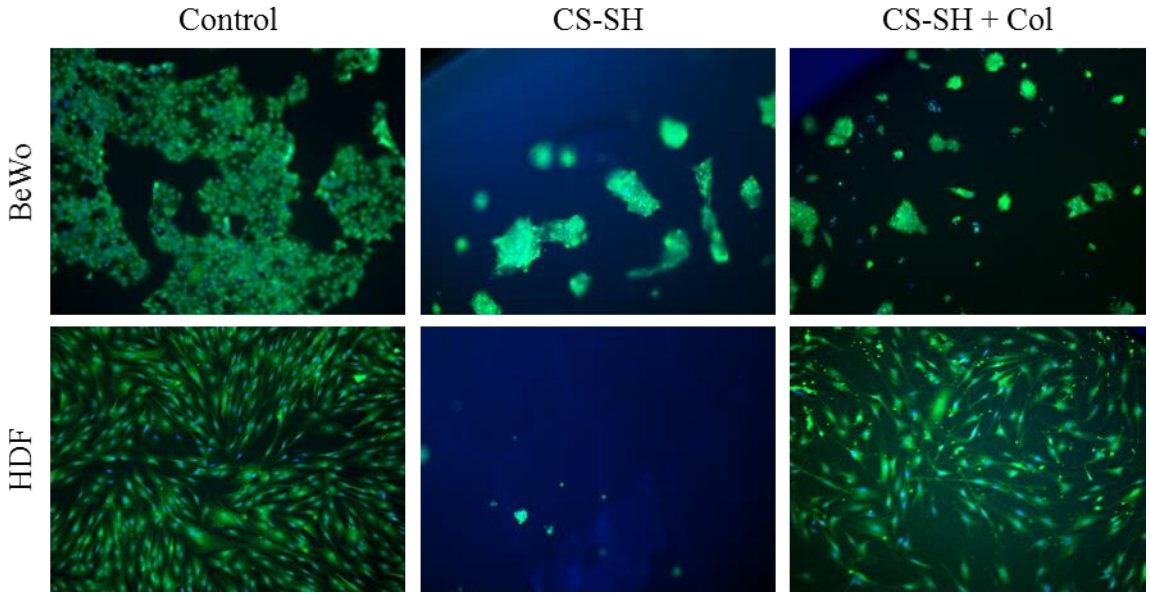

Figure 4-12. Fluorescent images of BeWo (top) and HDF (bottom) cells after 3 days of incubation on Col-loaded hydrogels compared to control cells and pure CS hydrogels.

The CS/Col hybrid hydrogels were further characterised regarding their rheological properties, toxicity and imaging. The incorporation of Col resulted in stiffer hydrogels when crosslinked with HS-PEG_2-SH, which had little impact on HS-PEG_{40}-SH crosslinked and drastically decreased the mechanical properties of CS-SH hydrogels (Figure 4-14A). The interaction between Col and CS may prevent the formation of some crosslinks, especially with CS-SH where the thiol groups are very closed to the polymer backbone. In addition, interactions between charged groups of both polymers will occur, which may reduce the crosslinking efficiency by hindering the nb moieties or increase network inhomogeneity. SEM revealed the presence of large, elongated and regularly spaced pores for HS-PEG_2-SH hydrogels, while HS-PEG_{40}-SH pores were more spherical. For both materials these structures were comparable to their analogues without Col. CS-SH hydrogels, however, presented a much more polydisperse structure, with the presence of numerous pores of smaller dimensions and random directions, as well as fibre-like regions, suggesting poor mixing between CS and Col

(Figure 4-13). These structural observations agree broadly with the rheology results, with a loss in structural organisation related to poorer mechanical properties.

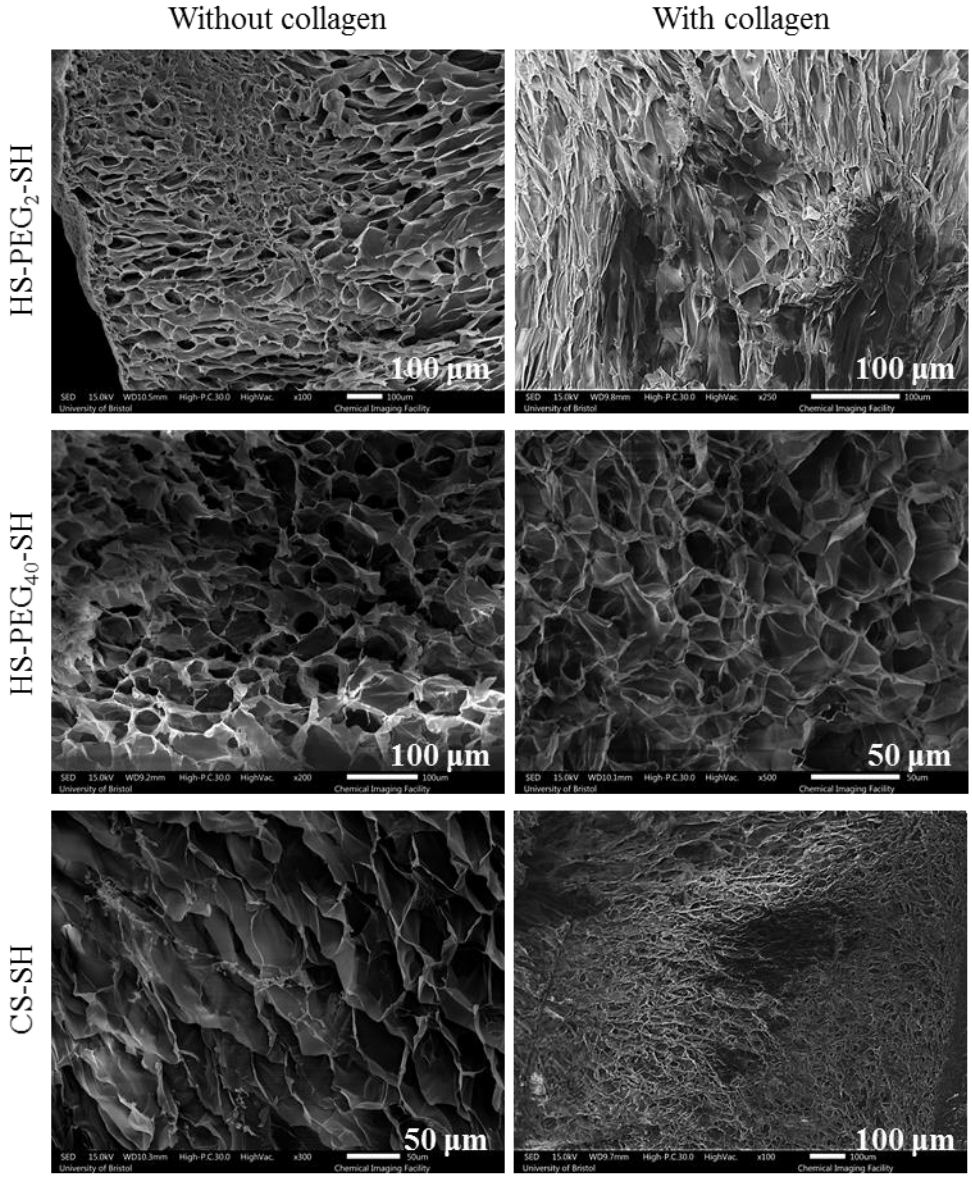

Figure 4-13. SEM images of CS-nb hydrogels without (left) and with (right) the incorporation of collagen.

Cell metabolic activity was drastically improved by the addition of as little as 0.25 w:v% of Col, with viability increasing from ~ 20 up to ~ 90 % for HS-PEG_2-SH materials after 24 hrs. Both PEG crosslinked hydrogels almost recovered 100 % of the metabolic activity of control cells cultures on a plate after 3 to 6 days, while CS-SH crosslinked materials only presented ~ 50 % of viability (Figure 4-14B-C). The improved cell adhesion is most likely due to a synergy between Col-mediated adhesion and the material mechanical properties: CS-SH/Col hybrids are much weaker (G' ~ 80 Pa) while HS-PEG_2-SH present suitable stiffness

for cell growth (G' ~ 2000 Pa). It is worth noting that only a small amount of Col was needed to significantly enhanced cell adhesion, while Col hydrogels typically require concentrations higher than 5 mg/mL to achieve good viability.[282]

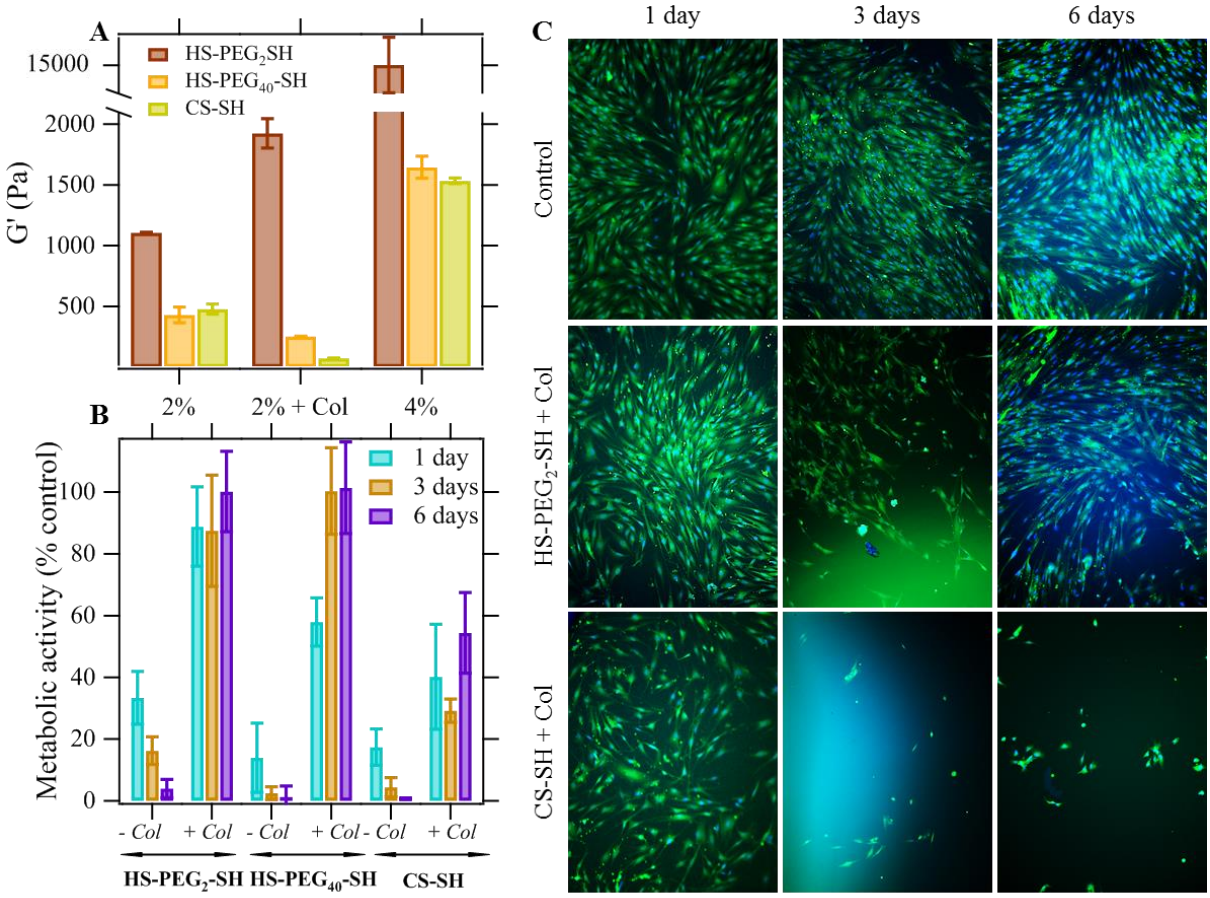

Figure 4-14. Characterisation of hydrogels investigated for cell studies. Rheological properties of all hydrogels cultured with HDF (A), metabolic activity (B) and fluorescent imaging (C) of cells after 1 to 6 days of culture on CS/Col gels.

4.4 Conclusion

Hydrogels were successfully synthesized from the new CS-nb precursor under UV exposure. The material properties could be readily tuned at the macro- and microscale by changing the crosslinking density, the nature of the crosslinker or the polymer concentration. The pore size dimensions, ranging between 20 – 100 µm and the rheological properties tuneable around 0.5 – 20 kPa are compatible with cells growth. Due to the fast gelation kinetics, hydrogels could be successfully generated under simulated amniotic fluid conditions and adhered to pork skin, while their doping with small amount of Col significantly reduced their cytotoxicity by improving cell adhesion. All these conditions make CS-nb a potential candidate for an *in utero*

repair of SB. In addition, the introduction of Col supported the growth of HDF cells, while having little effect on placenta cells, suggesting a simple way to direct selective adhesion for *in situ in utero* applications in the context of SB. In addition, the knowledge gained from hydrogel synthesis conditions will allow for the design of CS-nb microgels, as will be seen in Chapters 5 and 6.

5 Nano-emulsion Templates

5.1 Aims

This chapter describes the development of reverse nano-emulsion (*o/w*) templates to support CS-nb microgel synthesis. The focus was made on concentrated systems requiring low-energy input. Systematic investigation of the oil type, surfactant composition and water phase composition resulted in stable nano-emulsions of controlled size which were robust to the introduction of polyelectrolytes and to UV, as shown by a combination of DLS and SANS measurements.

5.2 Methods

5.2.1 Nano-emulsion template

The nano-emulsions were prepared according to the procedure described by Gupta *et al*.[121] They were composed of 80 wt% of oil, 10 wt% of surfactants (Span® 80 (S80) and Tween® 80 (T80) in weight ratios varying between 20 and 100% of S80) and 10 wt% of water phase. Three oils were screened: decane which allowed a comparison with published results,[121] cyclohexane which had a similar viscosity to decane but a lower boiling point thus making its removal easier, and mineral oil which is biocompatible and FDA-approved. The water phase consisted of either DI water or 1 w:v% of cationic (chitosan, CS) or anionic (alginate, ALG) polysaccharide in different solvent, as detailed in Table 5-1. For solubility reasons CS was dissolved in 1% AcOH. S80 and T80 were chosen as they are widely used in biomedical applications; they are also neutral, which was expected to minimise electrostatic interactions with the charged polysaccharides.

Table 5-1. Water phase composition investigated.

Polymer	Solvent	Parameter studied
-	DI water	Control nano-emulsion
CS	1% AcOH	Positive charge (polycation)
CS-nb	1% AcOH	Hydrophobic segments
ALG	DI water	Negative charge (polyanion)
ALG	PBS	Ionic strength

The water phase was added dropwise to a mixed solution of surfactants in the desired oil phase at 700 rpm. The nano-emulsion was stirred for at least 10 min. DLS measurements were performed using a Malvern Nano Zetasizer zs with a 633 nm laser in a glass cuvette, immediately after dilution of 100 µL of the nano-emulsion into 900 µL of oil to avoid multiple scattering from concentrated and turbid nano-emulsions. Nano-emulsion dilution in pure solvent increases the risk of coalescence or Ostwald ripening and may lead to bigger measured diameters. As the measurements were performed immediately after dilution these effects were considered negligible. Autocorrelation functions were measured at a scattering angle of 173° at 25 °C and processed using the Malvern software package.

5.2.2 Nano-emulsion crosslinking

Nano-emulsions were synthesized as described above, with a water phase consisting in 1% w:v CS-nb solution in 0.1 % w:v IRG in 1 % AcOH to which was added the crosslinker HS-PEG_2-SH to give R_s varying between 25 and 100 %. The nano-emulsion was crosslinked either in batch by exposing the stirred nano-emulsion to UV-B for 30 min or in flow using the device developed by Booker-Milburn *et al.*[283] and described in Figure 5-1.

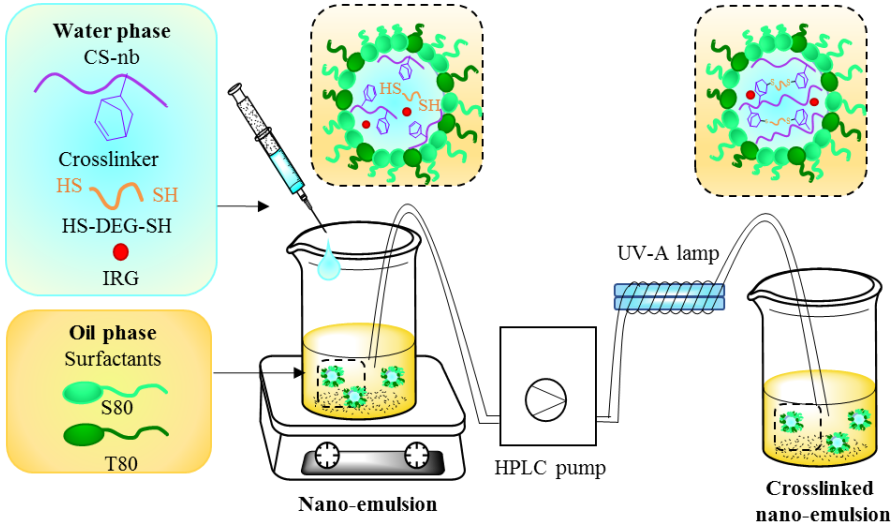

Figure 5-1. Synthesis of crosslinked microgels in flow using UV light in a flow reactor.

Briefly, the nano-emulsion was pumped through a UV-permeable tubing wrapped around a domestic UV-A lamp. The flow rate *r* could be tuned to vary the crosslinking time between 4 and 15 min. The crosslinked microgels were collected at the end of the device (Figure 5-1) and their hydrodynamic diameter d_h were measured by DLS after dilution in the appropriate solvent (cyclohexane or decane) as described in section 5.2.1.

5.2.3 SANS studies

SANS was carried out on the Sans2d diffractometer at the ISIS Pulsed Neutron Source as described in section 2.3.1.1 in Chapter 2. Nano-emulsions were prepared as described in section 5.2.1 from hydrogenated or deuterated cyclohexane or water to provide different contrasts corresponding to the shell (A), the whole droplet (B) or the core (C ; Figure 5-2). The surfactant weight ratio between S80 and T80 was ν = 4:6. All samples were loaded in a 1 mm quartz cuvette.

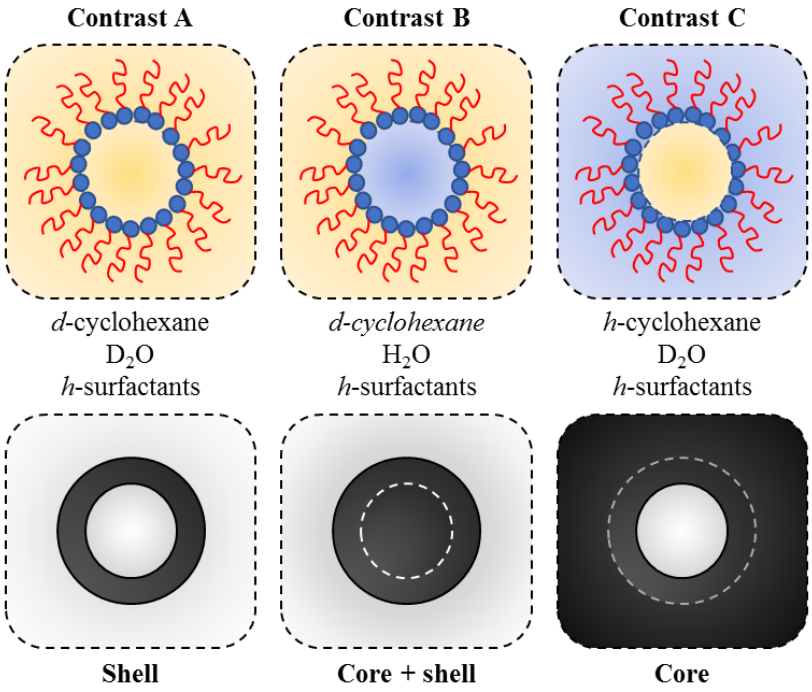

Figure 5-2. Contrasts investigated for the SANS studies of the nano-emulsion template.

Multiple scattering occurred for all samples (Figure 5-3), which was corrected by performing the data analysis with the shortest incident wavelengths (1.75-2.75 nm).

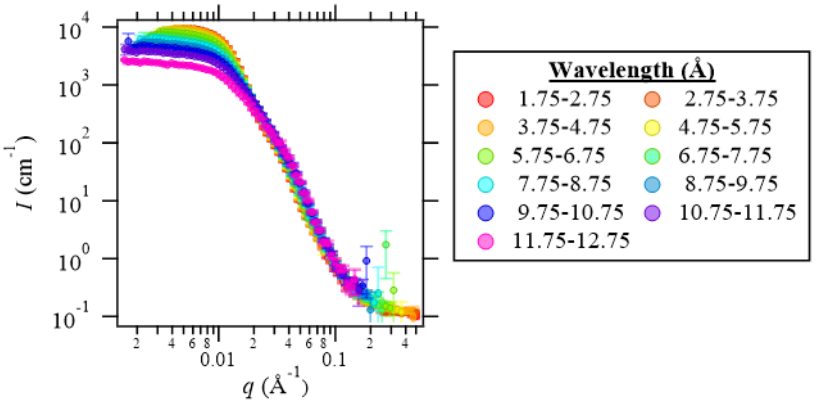

Figure 5-3. Verification of multiple scattering on nano-emulsion samples, evident from the wavelength-dependent scattering intensity I(q).

The data analysis will be discussed in section 5.3.5. Briefly, the size of the nano-emulsion droplets was first evaluated using the Guinier approximation in the low *q* region (0.008-0.025 $Å^{-1}$). The scattering of the shell (contrast A) was fitted to a core-shell model with a hard sphere structure factor and with a Schulz-Zimm polydispersity distribution. The nano-emulsion droplet (contrast B) and the core (contrast C) were fitted to a polydisperse sphere. The SLDs used for fitting are given in Table 5-2; the SLD of the surfactant shell was fixed as 0.96 – which is the surfactant mixture SLD - as de Molina *et al.* showed that the solvation was negligeable.[222] The stability of the nano-emulsions over the measurement period was confirmed by re-scanning nano-emulsions obtained from contrast C after 18 hrs and showed identical scattering profiles (data not shown).

Table 5-2. Calculated scattering length density (SLD). Surfactant SLDs were calculated from ref [222].

Component		Formula	Mass density (g/mL)	SLD ρ (10^{10} cm^{-1})	SLD ρ of mixtures (10^{10} cm^{-1})
h-water		H_2O	0.997	-0.559	-0.544
h-acetic acid		$C_2H_4O_2$	1.05	1.047	(1% AcOH)
d-water		D_2O	1.106	6.367	6.330
d-acetic acid		$C_2D_4O_2$	1.119	5.428	(1% d-AcOD)
CS		$(C_6H_{11}O_4N)_{710}$	1.1	1.32	5.921 (1% d-AcOD) -0.389 (1% AcOH)
h-cyclohexane		C_6H_{12}	0.778	-0.278	
d-cyclohexane		C_6D_{12}	0.893	6.705	
Span 80	Head	$C_7H_{11}O_6$	1.10	1.394	For S80:T80 ν = 4:6: 1.172 (head groups) -0.212 (tails) 0.960 (total)
	Tail	$C_{17}H_{33}$	0.800	-0.212	
Tween 80	Head	$C_{47}H_{91}O_{26}$	1.12	0.774	
	Tail	$C_{17}H_{33}$	0.800	-0.212	

5.3 Results and discussion

5.3.1 Optimisation of the nano-emulsion template

Nano-emulsions are kinetically stable liquid-in-liquid dispersions with droplet dimensions below 100 nm stabilised by surfactants. We focused on a low energy methodology developed

by Gupta *et al.*[121] to generate concentrated nano-emulsions, using a system made of 80 wt% of oil, 10 wt% of surfactants (S80 and T80) and 10 wt% of water. The impact of the oil type and the surfactant composition on the nano-emulsion stability was first investigated with surfactant compositions varying between ν = 1:0 to 3:7 weight ratios of S80/T80 (Figure 5-4). As T80 was added to the cyclohexane or decane nano-emulsions, the turbidity decreased, transforming from white cloudy suspensions (ν = 1:0 to 6:4 for cyclohexane, Figure 5-4A, and 1:0 to 7:3 for decane, Figure 5-4B, respectively) progressively to pale blue (ν = 1:1 and 6:4, respectively for cyclohexane and decane), and to a transparent suspension (ν = 4:6 and 1:1, respectively for cyclohexane and decane, indicated by white rectangles on Figure 5-4), after which a pale blue colour was obtained. For S80:T80 ratio higher than ν = 3:7, phase separation occurred as soon as the stirring was stopped. These visual observations correlated with the hydrodynamic radius d_h measured by DLS (Figure 5-4D), which decreased from d_h ~ 150-200 nm down to d_h ~ 40 nm when the nano-emulsion was optically transparent, and then increased slightly as the turbidity increased again.

These observations agreed with previous work by Robin *et al.* performed in cyclohexane, where aggregates of ~150-200 nm were observed when only S80 was used, while the nano-emulsion turbidity decreased with the addition of T80; in addition, d_h decreased from ~100 to ~40 nm. No stable nano-emulsion could be generated when only T80 was used.[284] Our results do not show a clear trend between the nano-emulsion droplet size and the surfactant composition. Davies *et al.* also reported that S80/T80 mixtures in cyclohexane could lead to both spherical and sheet-like morphologies depending on the concentration range, which may account for these discrepancies.[284]

While both cyclohexane and decane allowed for the formation of translucent nano-emulsions at low S80 weight ratio which remained stable over 2 months, emulsions formulated in mineral oils showed a different behaviour. No optically clear emulsion could be obtained, and phase-separation occurred between several min and up to 5 hrs as the stirring was stopped. While milky emulsions were observed for ν = 1:0 to 9:1, further increasing T80 decreased the nano-emulsion turbidity from white to pale blue up to ν = 4:6, after which the turbidity increased again. At ν > 2:8, no stable emulsions could be generated (Figure 5-4C). This was accompanied by d_h decreasing from ~ 150 to ~ 100 nm and increasing to ~ 300 nm for ν > 6:4 (Figure 5-4D).

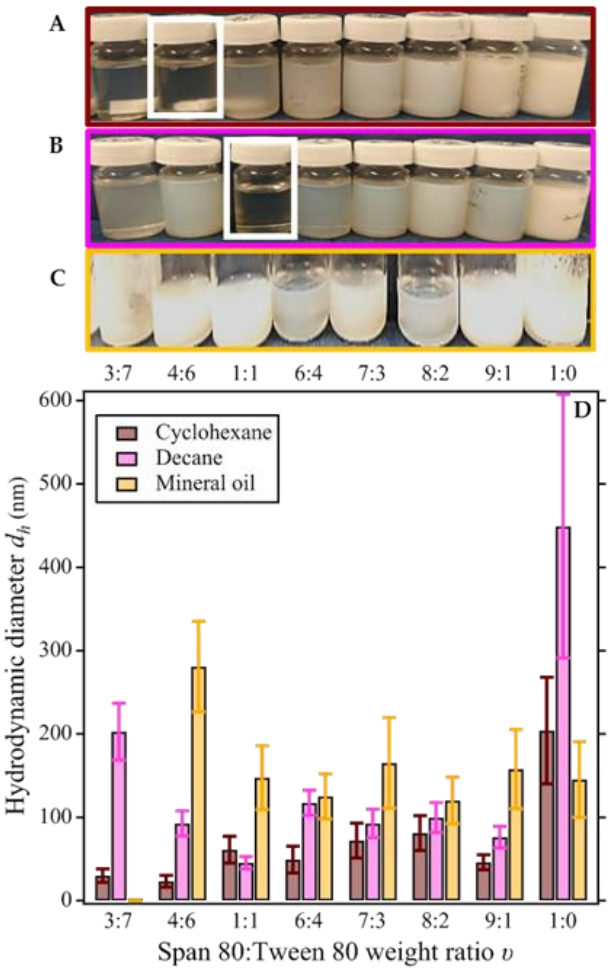

Figure 5-4. Visual observations of control nano-emulsions generated with: A) cyclohexane (brown), B) decane (pink), C) mineral oil (orange) for different surfactants ratios ν, and D) the corresponding hydrodynamic diameter d_h measured by DLS. Optimum nano-emulsion formulation was obtained for cyclohexane and decane consisted respectively of ν = 4:6 and ν = 1:1 (white rectangles in A and B).

The diameter of nano-emulsion droplets has been shown to be highly dependent on the viscosity of both the continuous and the dispersed phases as well as the homogenisation procedure. For instance, Grupta *et al.* developed a scaling parameter $We_{crit,\ d}$ to predict the nano-emulsion droplet size based on these three parameters and successfully applied it to several oil-in-water nano-emulsions. They found that nano-emulsion droplet diameter decreased with an increase in the continuous phase viscosity μ_c according to $d_h \sim \mu_c^{-5/12}$ – and therefore smaller droplets would be expected with mineral oil.[119] It is worth noting that the model was valid in a viscous turbulent regime, which also typically required high-energy homogenisation such as high pressure homogenisation or ultrasonication.[119] Our work,

however, used a low-energy mixing procedure, which may not sufficiently disperse the water droplets in the continuous phase, leading to phase-separation as observed.

All these elements, *i.e.* turbidity, low-stability, and d_h > 100 nm, strongly indicate that the mineral oil led to the formation of emulsions while cyclohexane and decane both gave stable nano-emulsions. We thus did not further pursue using mineral oil.

5.3.2 Nano-emulsion robustness: water phase composition

To investigate the feasibility of using these nano-emulsions as templates for microgel synthesis, the water phase composition was varied to include weak polyelectrolytes of different charges (CS, polycationic and ALG, polyanionic), hydrophobicity (CS-nb, bearing hydrophobic nb groups) and salts (PBS). When a solution of 1 w:v% CS or CS-nb in 1% AcOH was used as the water phase, the diameter of the resulting nano-emulsion droplets was largely the same, with a minimum diameter observed for the same optimal surfactant composition in both decane (ν = 1:1 (Figure 5-5 A-D) and cyclohexane (ν = 4:6), confirming the feasibility of using these nano-emulsions as template to generate microgels.

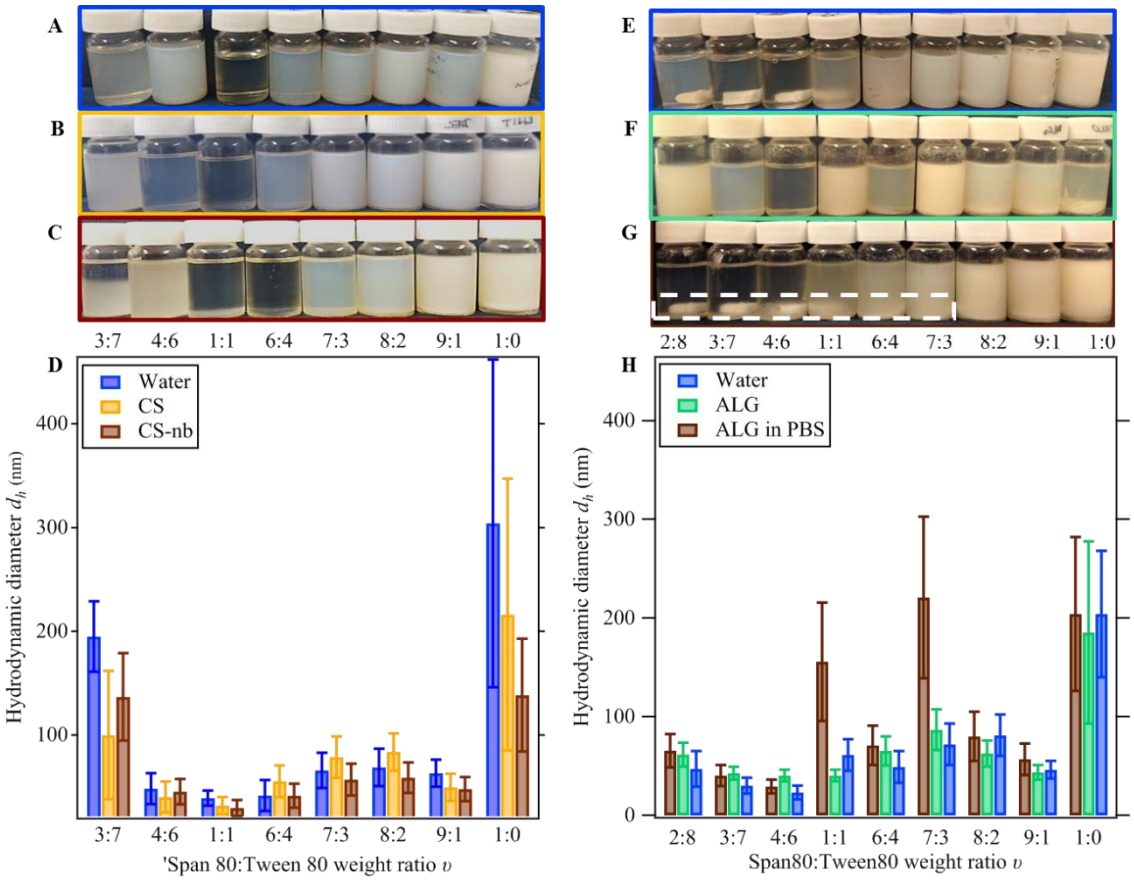

Figure 5-5. Nano-emulsion stability studied by DLS when varying the water phase from water (A) to CS (B) and CS-nb (C) in decane (D) and in from water (E) to ALG (F) with PBS (G) in cyclohexane (H). The dashed rectangle highlights the formation of precipitate.

Similarly, the nano-emulsions were not impacted by the addition of ALG in the water phase, a weak polyanionic polymer, while the addition of salt resulted in immediate polymer precipitation (Figure 5-5 E-H for the cyclohexane results). Overall, these results confirmed the possible application of these nano-emulsion templates to the synthesis of polyelectrolyte microgels.

5.3.3 Optimisation of the conditions for the crosslinking of microgels in flow

To ensure efficient and complete photo-crosslinking, adequate UV illumination is usually facilitated either by long exposure time or expensive, high power light source. Here a simple flow chemistry reactor made of FEP tubing wrapped around a domestic UV-A lamp was used.[283] This method allowed for an optimal and homogeneous exposure of the nano-emulsion to the UV light, as it was pumped through the tubing. In addition, the crosslinking time could be tuned between 1 and 30 min by varying the flow rate. Using the optimised nano-emulsion conditions in this set-up, we investigated the feasibility of microgel crosslinking in flow by gauging the nano-emulsion stability with DLS after pumping and UV exposure at different pump rates *r* (Table 5-3), using 1 w:v% CS in 1% AcOH as the water phase.

Table 5-3. Optimisation of the crosslinking conditions in flow.

Pump rate *p* (rpm)	**Flow rate *r* (mL/min)**	**Exposure time t_e (min)**	**Nano-emulsion appearance after UV exposure**	**Microgel diameter after UV exposure d_h (nm)**
0	0	0	Pale blue dispersion	33.3 ± 6
50	3.86	12.9	Cloudy; phase separated; precipitates obtained	-
100	7.47	11.3	Slightly cloudy; single phase	73.9 ± 50
150	11.1	7.57	Same as the initial nano-emulsion (pale blue dispersion)	38.5 ± 8
200	14.7	5.37		31.5 ± 6
250	18.2	4.22		33.3 ± 6

A minimum of *r* = 150 rpm was required to maintain nano-emulsion stability during pumping and UV exposure, as demonstrated by DLS measurements of the nano-emulsion at the entrance and at the exit of the flow reactor (Table 5-3). Slower reactions (*r* = 100 rpm) resulted in droplet coalescence, as shown by both an increase in the nano-emulsion turbidity and by an increase in the hydrodynamic diameter d_h from ~ 30 nm to ~ 70 nm. At *r* = 50 rpm CS was visibly expelled from the water phase and recovered as a solid. We suggest that this

loss of stability is related to the forces applied to the nano-emulsion during pumping, which are different from mechanical stirring. Based on these results, it was decided to proceed to crosslinking at a flow rate of 200 rpm as it allowed for a quick crosslinking without affecting the nano-emulsion stability. This methodology was further used to crosslink up to 50 g of nano-emulsion in less than 5 min.

5.3.4 Synthesis of the microgels

Using the optimised flow-UV curing condition, CS microgels were obtained using the afore-described nano-emulsion templating method with a water phase consisting of 1 w:v% of CS-nb in 1% AcOH, 0.1% of IRG, and a designated amount of HS-PEG$_2$-SH crosslinker. The impact of three different surfactant compositions, corresponding to the optimised formulations, and four different crosslinker concentrations (calculated to vary the theoretical R_s from 1:4 to 1:1), were studied when the nano-emulsions were generated in both cyclohexane (Figure 5-6) and decane,[285] comparing the diameter of the crosslinked microgels (brown) to the control uncrosslinked nano-emulsions. For a given surfactant composition, the size of the microgel diameter did not vary significantly after crosslinking and was not affected by the [SH]:[nb] molar ratio R_s, thus demonstrating the robustness of the nano-emulsions and supporting its use for future microgel synthesis, as will be described in Chapter 6.

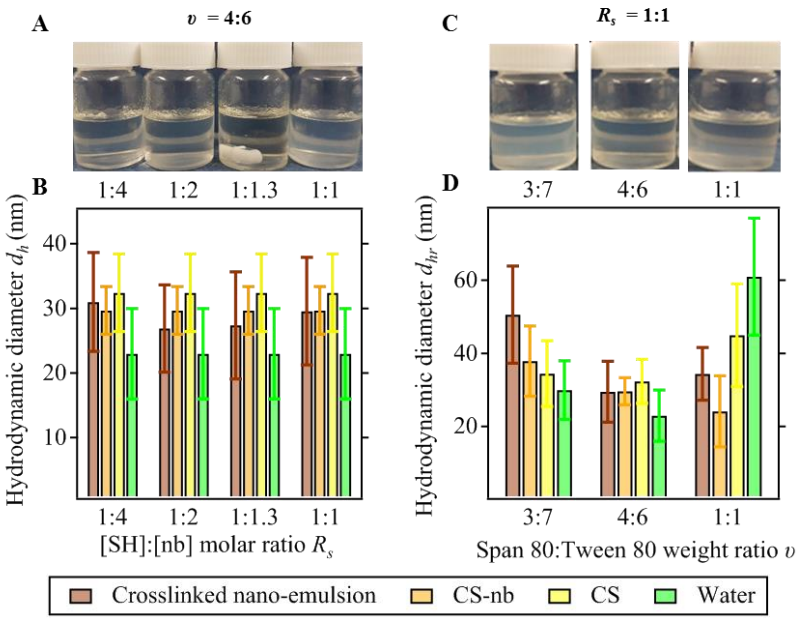

Figure 5-6. CS microgels made from the nano-emulsion templating method using cyclohexane as the oil phase. Photos of CS nano-emulsions generated from: (A) a surfactant ratio S80:T80 υ = 4:6 when varying the [SH]:[nb] molar ratio R_s, from 1:1 to 1:4 ; (C) different ratios υ of S80:T80 varying between 3:7 and 1:1 for R_s = 1:1. The corresponding hydrodynamic diameters d_h, measured by DLS, are shown respectively in (B) and (D).

5.3.5 SANS studies of the nano-emulsions

The nano-emulsions were further studied using SANS. The formation of S80/T80 micelles in *d*-cyclohexane was confirmed by their scattering profile showing a typical q^{-4} decay in the high q region, characteristic of small objects, which could be described as a polydisperse spherical object (Figure 5-7A) of dimensions comparable with other work.[222, 286] Upon addition of D_2O the scattering profile changes drastically, with a sharp increase in the scattered intensity proportionally to q^{-2} in the high q region, followed by a shoulder and an increased intensity proportional to q^{-4} in the low q region (Figure 5-7B). These features are typical of the formation of core-shell objects.[222, 226] As described in section 2.3.3.5 in Chapter 2, nano-emulsions can be typically represented from the scattering contribution of the aqueous core, the surfactant shell and the solvent, all of which can be enhanced by varying the contrast between these three components (Figure 5-2 and Figure 5-7B). As opposed to the surfactant shell, the scattering of the aqueous core and of the whole droplet (core + shell) present a distinctive q^{-4} decay in the low q region and can both be modelled as a polydisperse sphere.[286]

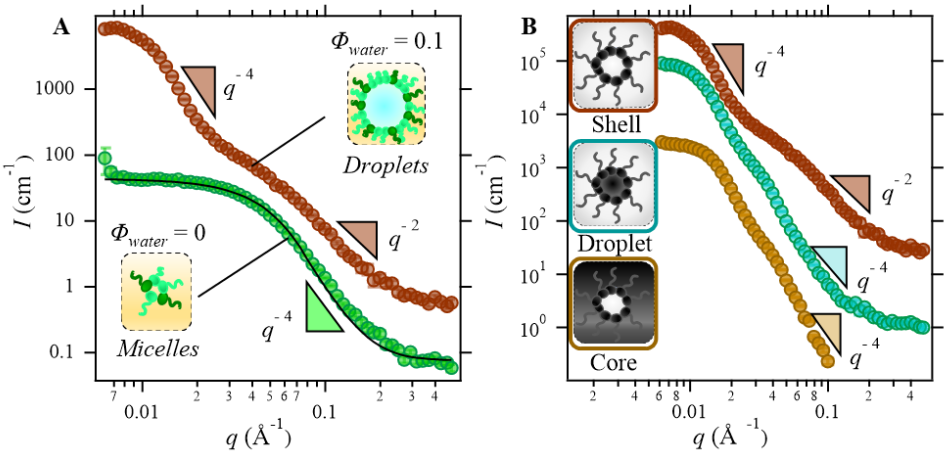

Figure 5-7. Typical SANS profile. (A) S80/T80 micelles in C_6D_{12} before (green) and after (brown) the addition of D_2O and the key features of the resulting scattering profile. (B) Scattering of the different nano-emulsion constituents. The scattering curves have been offset (10x) on the y-axis for clarity.

As a first approximation, the radius of gyration R_g of the nano-emulsion droplet and of the surfactant layer were obtained from the Guinier approximation in the low q region (Table 5-4). All contrasts showed R_g was only slightly affected by the addition of CS and CS-nb (R_g ~ 17 nm) while an increase to R_g ~ 24 nm was observed after UV crosslinking. Comparing the radius of gyration of the nano-emulsion droplet with those of the core suggested t_{shell} ~ 1.5 nm which almost doubled after UV curing. These very basic first estimates are in good agreement

with the values reported by Malo de Molina *et al.* who studied S80/T20 nano-emulsions in cyclohexane.[222] For all the contrasts, R_g was smaller than R_h which should not be observed as R_h accounts for the hydration layer. Due to the high concentration of these nano-emulsions, samples had to be diluted 10 times before DLS measurements to reduce multiple scattering. It was assumed that proceeding to dilution immediately before measurement would not affect the measured diameter. As SANS measurement timescale does not allow for immediate measurement after dilution, all data were recorded from the concentrated nano-emulsions which did show multiple-scattering, as mentioned in section 5.2.3.

Table 5-4. Hydrodynamic radius (R_h) and radius of gyration (R_g) obtained by DLS and SANS respectively for the investigated nano-emulsions.

Water phase composition	**DLS**	**SANS**		
		Contrast A	**Contrast B**	**Contrast C**
	R_h **(nm)**	***R_g droplet* (nm)**	***R_g droplet* (nm)**	***R_g core* (nm)**
Water	11.5 ± 3.5	15.1 ± 0.5	17.9 ± 0.2	14.0 ± 0.2
CS	16.2 ± 3.0	18.8 ± 0.6	17.3 ± 0.2	17.1 ± 1.1
CS-nb	14.8 ± 1.9	19.0 ± 0.6	17.7 ± 0.2	17.7 ± 0.4
Crosslinked	14.8 ± 3.8	24.6 ± 0.3	24.1 ± 0.3	20.7 ± 0.6

The scattering of the shell is represented by contrast A (Figure 5-8A). In the high q region, the scattering intensity of the shell increases proportionally to q^{-2} which yields information of the shell thickness t_{shell}. A local maximum followed by a local minimum occur next, whose distance is related to the droplet polydispersity. The intensity finally increases proportionally to q^{-4} which corresponds to the scattering of the inner core before reaching a plateau.[226, 230] The position of these local minima and maxima remains similar when CS or CS-nb are added to the nano-emulsions, with smoother transition between these extremes, suggesting an increase in the polydispersity. After UV exposure, the position of both the minima and the maxima were shifted to higher q values, indicating a thinning of the shell or a change in the core/shell contrast due to the crosslinking of the polymer chains. The scattering was modelled as a core-shell structure in a restricted q range covering only the q^{-2} and the q^{-4} increase as they have been shown to be enough to obtain the core radius and the shell thickness.[226] A hard sphere structure factor was added as performed in previous work.[222, 226, 286] The scattering data were successfully fitted in the high-medium q region, whereas the fit

quality deteriorated in the low q region, with fitted intensities lower than the measured ones. These observations match well with the work of Foster *et al.* who showed that fitting in the low q region required to introduce a sticky hard sphere form factor, which is more complex and computationally demanding. They showed that the values of the shell thickness and of the core radius were identical for both structure factors[226] As the resulting fitting parameters were not affected, we kept a simple hard sphere description. The nano-emulsion droplets presented a core radius r_c of ~ 10 nm and a surfactant film thickness t_s of ~ 2 nm not affected by the addition of CS or CS-nb (Table 5-5). This film thickness is consistent with values reported by De Molina *et al.* in their study on S80/T20 surfactants in *d*-cyclohexane while their core radius was around twice as big, consistent with the lower surfactant concentration they used.[222] After UV crosslinking, however, the fit quality degraded, possibly related to a change in the crosslinking density impacting on the SLDs or on the core form factor. Data analysis suggested that t_s remained unchanged while r_c decreased to ~ 7 nm. Although uncertainties on these last values are considerable, this further confirms the efficiency of the crosslinking process.

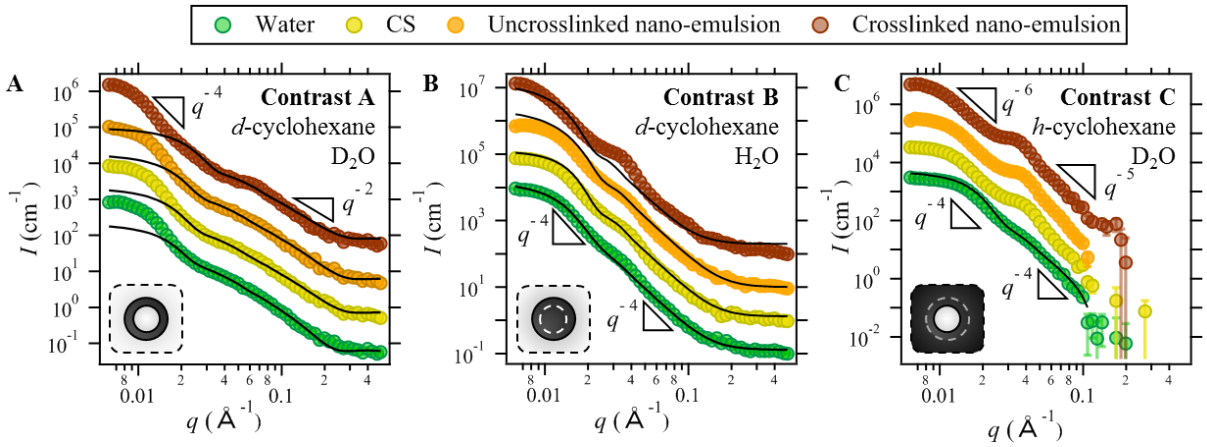

Figure 5-8. Scattering profile for the investigated contrasts and water phase composition. The scattering curves have been offset (10x) on the y-axis for clarity.

The scattering of the whole droplet is shown by contrast B (Figure 5-8B). As observed in contrast A, no difference in the scattering profile can be seen when CS and CS-nb were added to the water phase. After crosslinking, however, the position of the shoulder is shifted towards the low q region, indicating the formation of bigger objects. Due to the low contrast between the hydrogenated water core and the hydrogenated surfactants, the scattering can be modelled as those of a polydisperse sphere.[286] The fit quality was considerably worse than for the core-shell fit, even when restricting to a lower q range and when considering different structure factors. Attempts were made using a core-shell model, although the contrast between the core and the shell is low ($\Delta\rho$ = 1.5). The overall fit was not improved, and the overall

dimension of the core + shell obtained this way matched well the estimated radius of the water droplet obtained from a polydisperse sphere model. The determination of the exact shape of nano-emulsions generally requires serial dilution measurements,[287] which was not performed in our study. Remaining micelles may contribute to the overall scattering, especially as the surfactant concentration is important (~135 mM). Foster *et al.* added a scattering contribution coming from cylindrical micelles.[230] The addition of a contribution from the ellipsoidal micelles (shown in Figure 5-7A) did not improve the overall fit.

*Table 5-5. Fitting parameters obtained from all contrasts for different nano-emulsion compositions using a core-shell (contrast A) or a polydisperse sphere (contrasts B and C) description. *: no relevant fitting parameters was obtained.*

Water phase composition	**Contrast A**		**Contrast B**	**Contrast C**
	r_c **(nm)**	t_s **(nm)**	$r_{droplet}$ **(nm)**	r_c **(nm)**
Water	10.5 ± 0.2	2.22 ± 0.08	17.5 ± 0.02	14.5 ± 0.02
CS	9.91 ± 0.1	1.80 ± 0.08	18.0 ± 0.02	*
CS-nb	9.39 ± 0.1	1.78 ± 0.09	16.7 ± 0.14	*
Crosslinked	7.27 ± 0.2	1.71 ± 0.16	22.4 ± 0.02	*

Similar observations were made for the scattering of the core, represented by contrast C (Figure 5-8C). The addition of CS or CS-nb into the nano-emulsion had a greater impact on the scattering intensity, as shown by the formation of a sharper peak at $q \sim 0.04$ Å^{-1}. This change was even more pronounced after UV crosslinking, with an increase in intensity and a shift to lower q values representative of bigger objects of different SLD. The final q^{-4} region was less modified after UV, suggesting that the shell was mostly affected by the crosslinking procedure. The use of *h*-cyclohexane should not allow for the visualisation of interfering free micelles in solution, but the use of hydrogenated solvent resulted in significant incoherent scattering and reduced the data quality in the high q region. Data were analysed as polydisperse spheres in a restricted q range (0.01-0.09) to limit both multiple scattering (low q) and incoherent scattering (high q). As in contrast B, the fit quality was rather poor, especially after the addition of polymer in the water phase, even when accounting for a surfactant shell surrounding the droplet. In particular, an increase in the scattering slope from q^{-4} to q^{-5} after the addition of CS and q^{-6} after UV curing were observed, which are not compatible with a sphere model. Nevertheless, the similarities observed after the addition of CS or CS-nb support the robustness

of the nano-emulsion templates for microgel synthesis, while the shift in the shoulder peak position and intensity after UV curing indicates the efficiency of the crosslinking.

5.4 Conclusions

Stable, concentrated nano-emulsion templates were successfully obtained from FDA-approved surfactants and low-energy methods. The impact of different oils on nano-emulsion droplet size and stability was investigated. Optimised nano-emulsion formulations were found based on cyclohexane, whose low boiling point makes its removal easy, and whose robustness towards various water phase composition and crosslinking conditions was confirmed by DLS and SANS. The synthesis of microgels based on these templates will be described in Chapter 6.

6 Microgels

6.1 Aims

This chapter describes the characterisation and potential applications of CS-nb microgels obtained from the nano-emulsion templating method described in Chapter 5. The materials were characterised by DLS, ζ potential, TEM and SANS, which provided information at different length scales on the impact of both synthesis and environmental parameters on their properties. The microgels were successfully functionalised using tetrazine ligation and presented non-significant toxicity against HDF cells, designing them as attractive targets for functionalised scaffolds in the biomedical area.

6.2 Methods

6.2.1 Microgel synthesis

The microgels were obtained using the nano-emulsion template described in Chapter 5. Unless specified otherwise, the template consisted of 80 wt% cyclohexane, 4 wt% S80, 6 wt% T80 and 10 wt% of water phase (1 w:v% CS-nb in 1% AcOH, 0.1 % IRG and the desired crosslinker). The crosslinking was performed either in batch or in flow.

Several purification procedures where attempted, including microgel precipitation (in ethanol, methanol or acetone) and dialysis. Precipitation gave insoluble aggregates which could not be resuspended in water. Dialysis gave soluble products, but a significant amount of surfactant was still present, as verified by ^{1}H NMR. Freeze dried microgels did not resuspend homogeneously, presumably due to microgel entanglement happening in the drying process.

Optimum conditions were found by centrifugal dialysis followed by vacuum oven concentration, which allowed for solubility at high concentration (> 20 mg/mL). The optimal microgel purification procedure was as follows. First, microgels were separated by centrifugation (1 hr 4000 rpm) from the suspension. The pellet formed was transferred into a Vivaspin® 20 concentration centrifugation tube (10 kDa cut-off) and washed with EtOH/H_2O (with 1% AcOH) mixtures (3:1, 1:1 and 1:3 ratio successively, 1 hr 4000 rpm each) and then with 1% AcOH in H_2O (3x, 1 hr 4000 rpm). The microgel suspension was transferred in a glass vial and concentrated in a vacuum oven (40°C). The microgel concentration was determined by freeze drying a 50 µL aliquot. Microgel diameters and ζ potentials were measured with a Malvern Nano Zetasizer zs as described in section 4.3.1 in Chapter 5 with a

microgel concentration of 0.75 mg/mL and solvent parameters adapted to the background electrolyte.

6.2.2 TEM

The samples were prepared by negative stain using uranyl acetate (3 %) on glow discharged grids. 5µL of microgel suspensions (0.5-1 mg/mL) was incubated on the grid for 1 min and the excess was wicked away; the procedure was then repeated with 5 µL of stain. The samples were observed in a Tecnai 12 BioTwin TEM at 120 kV with images captured using an FEI Eagle 4k × 4k camera.

6.2.3 SANS studies

As samples could not be freeze-dried, the synthesis was performed as described in section 6.2.1 by replacing H_2O/AcOH by D_2O/AcOD-d_4 in the crosslinking and in the washing steps. All samples were prepared at 15 mg/mL in the final solvent (1% AcOD-d_4/D_2O with or without NaCl, $CaCl_2$, urea-d_4 (*d*-urea); deuterated PBS (*d*-PBS) or D_2O with pH adjusted with DCl or NaOD) and measured in 2 mm-thick quartz cuvettes.

The effect of the nano-emulsion composition on the microgel structure was studied on the Sans2D diffractometer (ISIS, Didcott) and the impact of environmental conditions (salts, urea, pH) was recorded on the PA20 diffractometer (LLB, Saclay). Samples from different synthesis batches were used, which were combined prior to solvent evaporation and resuspension in the appropriate solvent to reduce batch-to-batch variability, although this was anticipated to lead to increase polydispersity. The SANS beamlines were described in section 2.3.1 in Chapter 2. A background correction was performed from a cuvette containing D_2O for the pH-dependency series, 1% AcOD-d_4/D_2O with the presence of *d*-urea or *d*-PBS if needed. The absence of multiple scattering was verified at ISIS. (Figure 6-1). The data processing is discussed in section 6.3.1.

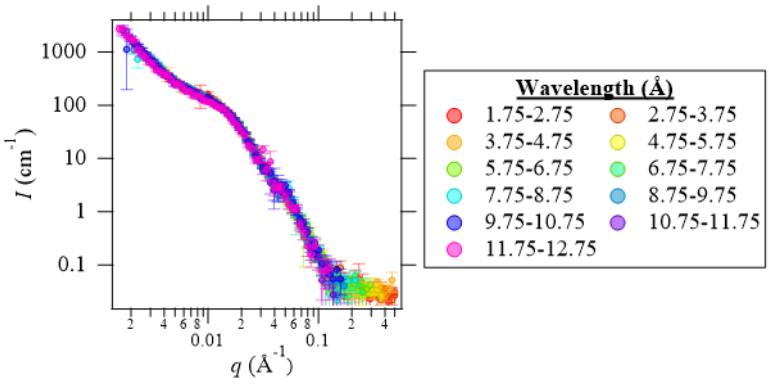

Figure 6-1. Verification of absence of multiple scattering on microgel samples, evident from the wavelength-independent scattering intensity I(q).

6.2.4 Synthesis of Tet-Coum for microgel functionalisation

Tet-Coum was synthesized as reported by Devaraj *et al.*[288] following the reaction scheme shown in Scheme 6-1.

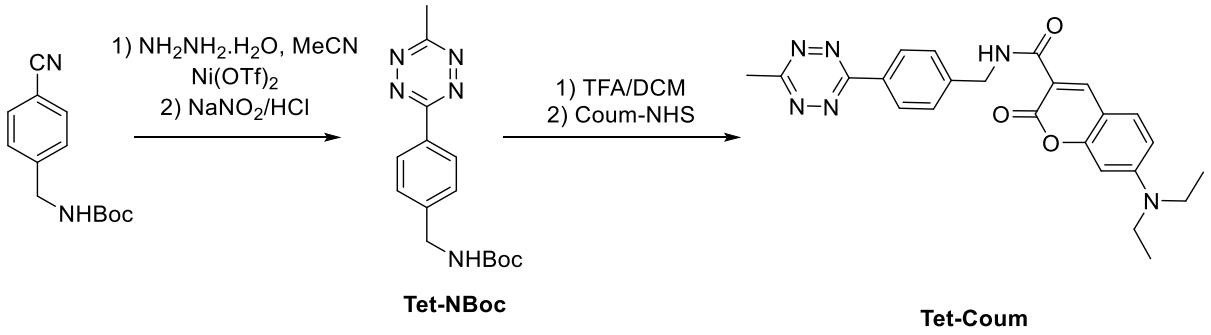

Scheme 6-1. Synthetic route to Tet-Coum.

6.2.4.1 Synthesis of Tet-NHBoc

Tet-NHBoc was synthesized according to previously reported procedures.[289] Briefly, tert-Butyl N-[4-(cyanophenyl)methyl]carbamate (232 mg, 1 mmol) was combined with acetonitrile (525 µL, 10 mmol), $Ni(OTf)_2$ and hydrazine monohydrate (2.4 mL, 50 mmol) in a sealed tube. The tube was heated to 65°C for 36 hrs, after which the mixture had turned dark purple. $NaNO_2$ (1.4 g, 20 mmol) was dissolved in 5 mL DI H_2O and added to the mixture, followed by dropwise additions of 2M HCl until pH reached 3 and gas formation stopped. The resulting pink solution was extracted with ethyl acetate (5x), and the combined organic layers were washed with brine, dried over $MgSO_4$, filtered and concentrated under vacuum to afford a pink solid which was purified by column chromatography (hexane:ethyl acetate 4:1) to afford the desired compound as a pink solid (67 mg, 22.5 %). ^{1}H NMR (400 MHz, $CDCl_3$ – see Figure 6-2 for the peak attribution) δ 8.54 (d, J = 8.2 Hz, 2H, *b*), 7.49 (d, J = 8.1 Hz, 2H, *c*), 5.00 (bs, 1H, *e*), 4.43 (d, J = 5.7 Hz, 2H, *d*), 3.09 (s, 3H, *a*), 1.47 (s, 9H, *f*). ^{13}C NMR (101 MHz, $CDCl_3$ - see Figure 6-3 for the peak attribution) δ 167.35 (*b*), 164.06 (*c*), 156.07 (*i*), 144.10 (*g*), 130.94 (*d*), 128.34 (*e* or *f*), 128.19 (*e* or *f*), 79.98 (*j*), 44.53 (*h*), 28.54 (*k*), 21.29 (*a*). m/z (ES+): expected 246.0991 ([M-Boc]+), found 246.10.

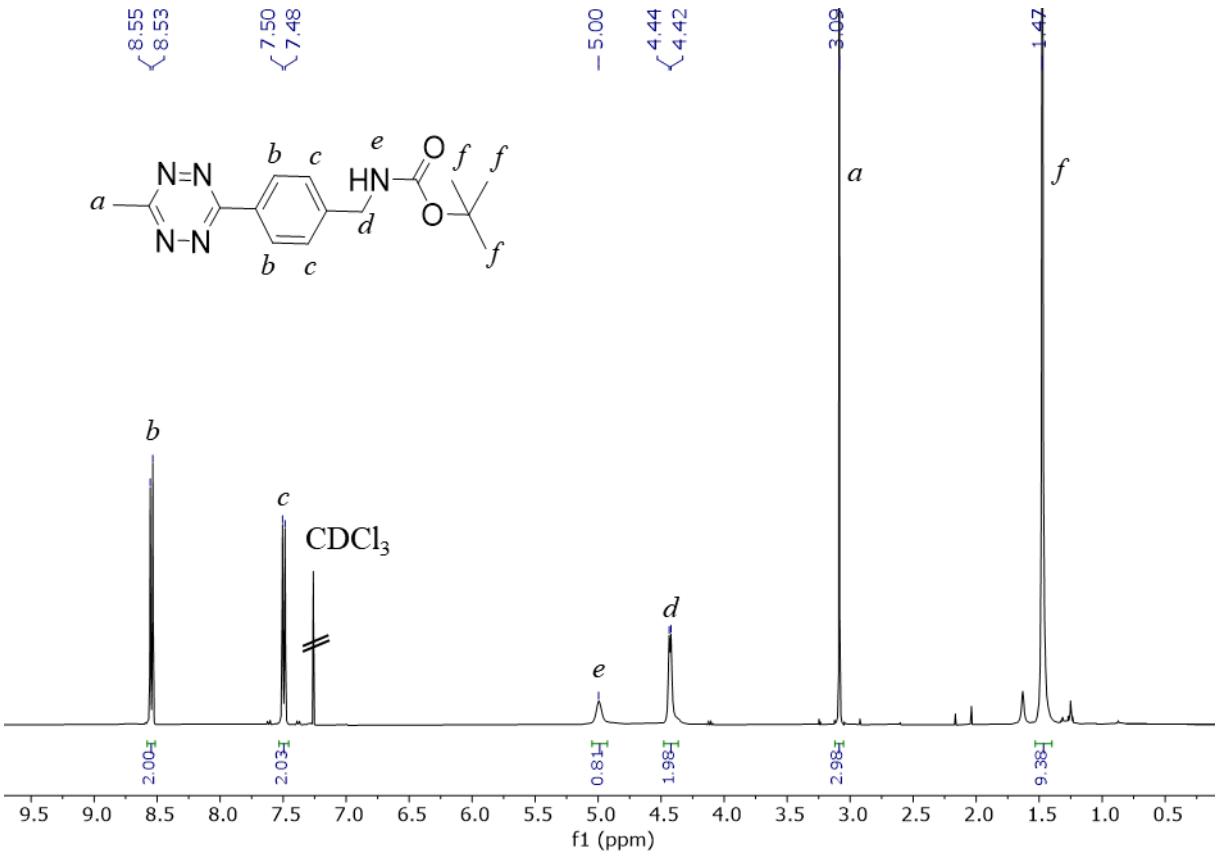

Figure 6-2. [1]H NMR of Tet-NHBoc and its peak attribution.

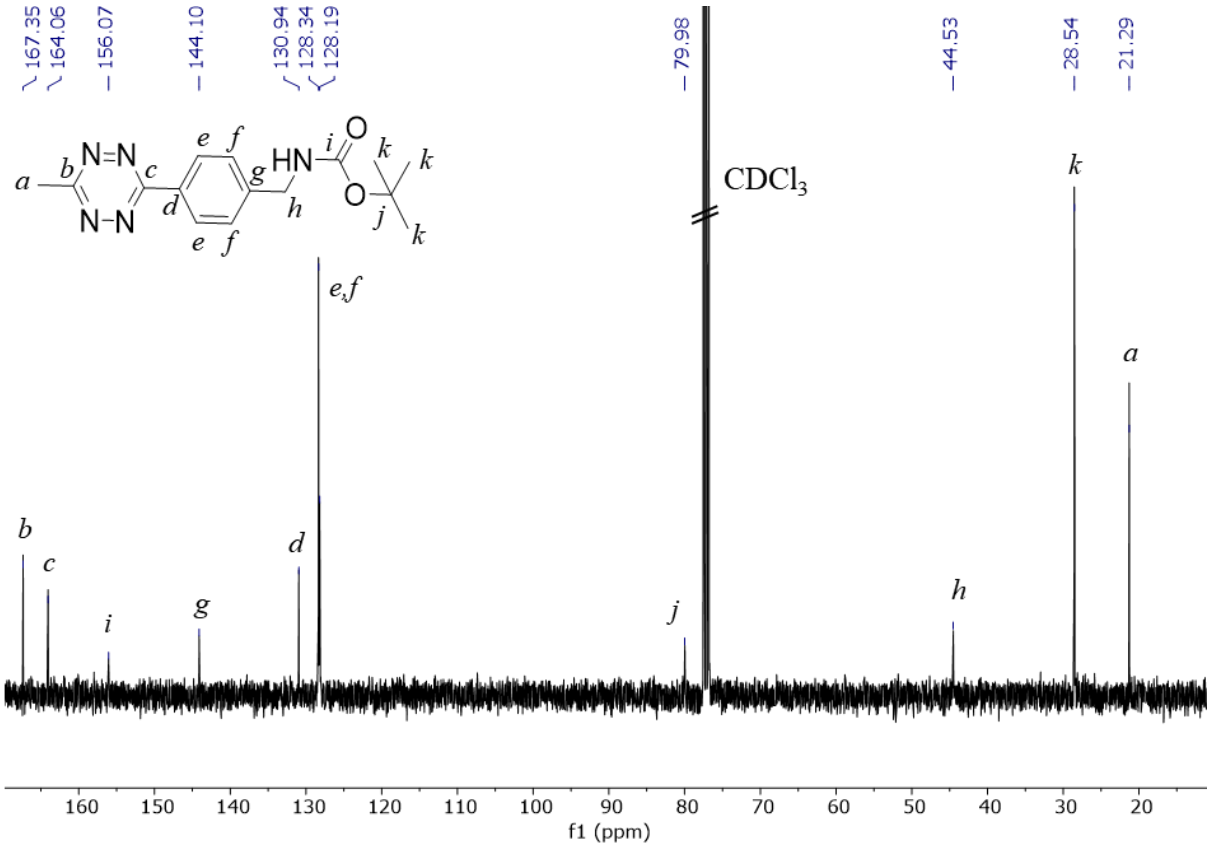

Figure 6-3. [13]C NMR of Tet-NHBoc and its peak attribution.

6.2.4.2 Synthesis of Tet-Coum

Tet-NHBoc (13 mg, 45 µmol) was first deprotected by stirring in TFA/DCM (1:1, 1 mL) for 1.5 hrs. The deprotection was monitored by TLC. Solvent was removed under vacuum and the resulting pink solid was dissolved in DCM (1 mL). Triethylamine (100 µL, 360 µmol) was added followed by NHS-activated coumarin (Coum-NHS, 20 mg, 45 µmol). The reaction mixture was stirred in the dark at room temperature for 2 hrs and the product was purified by flash chromatography (1:1 hexane-ethyl acetate) and isolated as an orange-red solid (7 mg, 35%) The compound composition was assessed by HPLC and presented both characteristic absorption bands at 420 and 515 nm of coumarin and tetrazines respectively. ^{1}H NMR (400 MHz, $CDCl_3$) δ 9.31 (bs, 1H), 8.74 (d, J = 14.8 Hz, 1H), 8.60 – 8.53 (J = 8.1 Hz, 1H), 7.60 (dd, J = 17.8, 8.1 Hz, 2H), 7.45 (dt, J = 8.6, 3.6 Hz, 2H), 6.66 (dd, J = 9.0, 1.8 Hz, 1H), 6.51 (s, 1H), 4.76 (d, J = 5.9 Hz, 1H), 4.69 (d, J = 6.0 Hz, 1H), 3.46 (q, J = 7.0 Hz, 4H), 3.09 (s, 3H), 1.23-1.28 (m, includes t, J = 9.0 Hz).

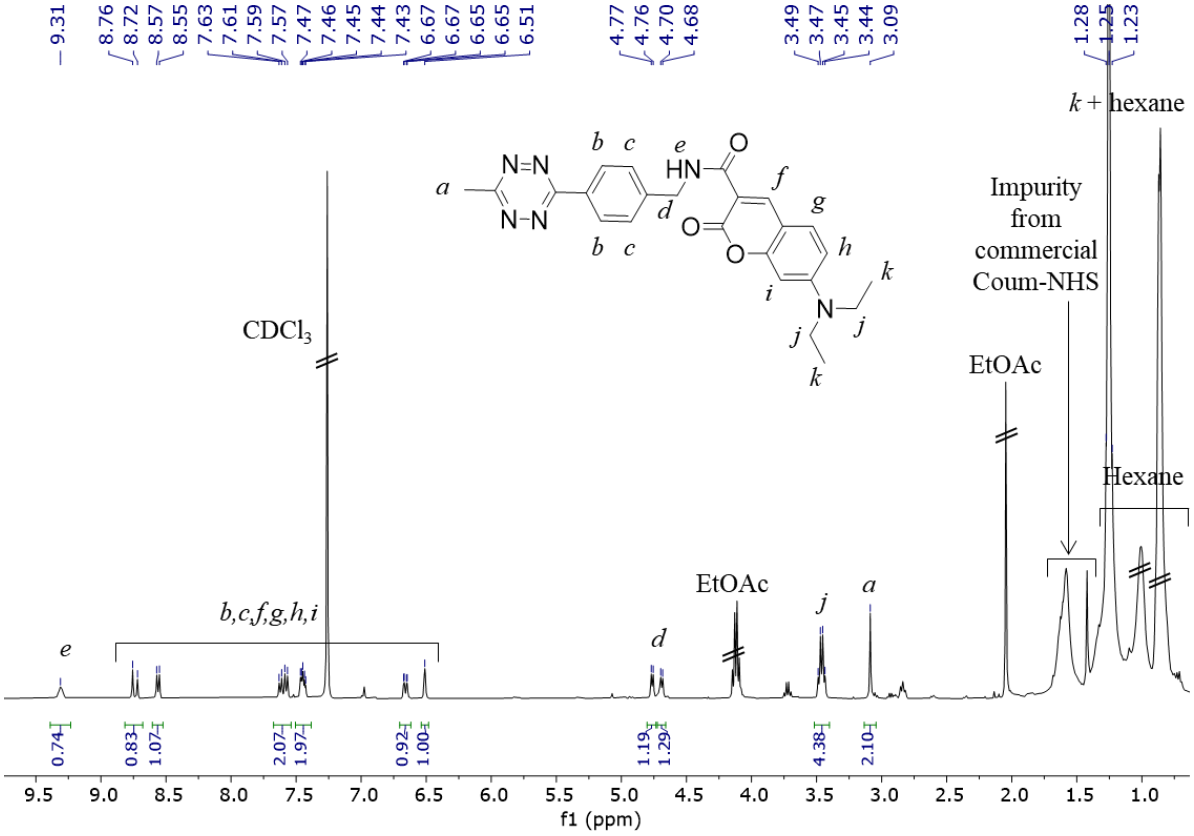

Figure 6-4. ^{1}H NMR of Tet-Coum and its peak attribution.

6.2.5 Fluorescence-monitoring of microgel functionalisation

The microgels (HS-PEG_2-SH, R_s = 1:2) were resuspended in DI water at a final concentration of 0.5 mg/mL in a quartz cuvette (1 cm pathlength) to which Tet-Coum was added to a final concentration of 1 µM. The ratio between unreacted nb and Tet-Coum was 1:1, assuming 100%

yield for the thiol-ene crosslinking in the microgel synthesis step. The reaction was monitored by fluorescence spectroscopy using a Perkin-Elmer LS45 fluorimeter with an excitation at 420 nm. The emission spectra were recorded in the wavelength range of 460 - 600 nm.

6.2.6 Microgel toxicity

HDF cells were cultured as described in section 4.3.9 in Chapter 4 and plated at 5×10^3 cells/well in 96-well plates. The cells were incubated 24 hrs before plating with microgels (HS-PEG_2-SH, R_s = 1:1) at concentrations varied between 1000 and 2 µg/mL (4 replicates per condition, i.e. toxicant concentration and time point, all performed in triplicates) for 1, 2 or 5 days. At the required incubation time, the media was removed, and wells were rinsed twice with PBS. Metabolic activity and cell viability were measured respectively with AB and calcein tests as described previously. All results were background-corrected with a solution of media containing the two dyes and expressed as a percentage of control consisting of cells not exposed to microgels.

6.3 Results and discussion

6.3.1 Microgel synthesis

The impact of the nano-emulsion composition – both the oil phase (surfactant composition, oil type) and the water phase (CS concentration, crosslinker type and concentration) – as well as the environment – pH, ionic strength, urea - on the final microgel structure was systematically assessed by a combination of scattering techniques (DLS and SANS).

6.3.1.1 Impact of the nano-emulsion composition

The effect of the nano-emulsion composition was investigated on HS-PEG_2-SH crosslinked microgels. Once washed and resuspended in water, the microgels showed a significant swelling, with nano-emulsion crosslinked water droplets of d_h ~ 30 to 60 nm - depending on the oil type and on the surfactant ratio v – compared to microgels of d_h ~ 100 to 400 nm as measured by DLS (Figure 6-5). This swelling is a classic behaviour of microgels in a good solvent and consistent with the behaviour of the corresponding hydrogels. Microgel aggregation may also contribute to the increased measured diameters.

The surfactant composition had a drastic impact on the size of the swollen microgel. When cyclohexane was used as the oil phase, 3-fold (v = 1:1) to 8-fold (v = 3:7) swelling was observed. The swelling, on the other hand, was more homogeneous for decane-based nano-emulsions (between 1.6- and 5-fold). Unexpectedly, the diameter of the final microgel was not directly related to the crosslinked nano-emulsion diameter, whose composition was based on

an optimised surfactant composition. This could suggest some confinement of the accessible nb moieties depending on the water droplet diameter, preventing the crosslinker from accessing the reactive moieties, thus leading to incomplete crosslinking – and hence affecting the swelling differently.

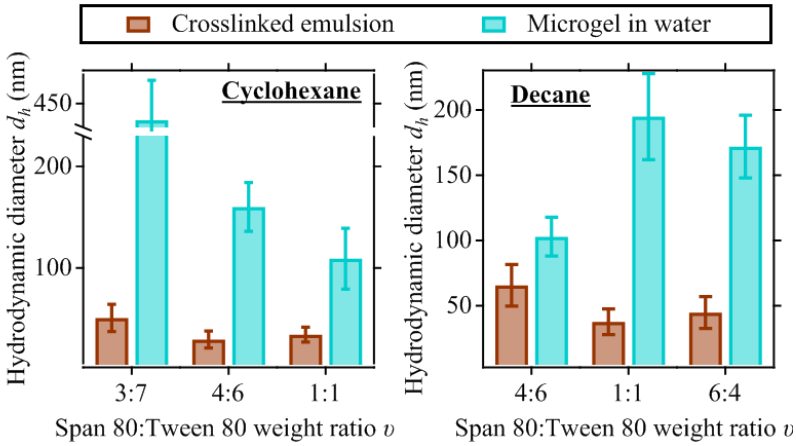

Figure 6-5. Impact of the nano-emulsion formulation on HS-PEG$_2$-SH crosslinked CS microgels hydrodynamic diameter measured by DLS.

6.3.1.2 Impact of the crosslinking density

The microgel diameter could be further controlled by choosing the [SH]:[nb] molar ratio R_s. As R_s decreased from 1:1 to 1:2 the hydrodynamic diameter of the swollen microgel d_h increased from ~ 200 to ~ 160 nm when cyclohexane was used as the oil phase and from ~ 195 to ~ 230 nm with decane-based nano-emulsions (Figure 6-6AB). As for hydrogels, the higher the degree of reticulation, the tighter the packing of the polymer chains, which in turns limits the water uptake, reducing the swelling. However, when R_s was further decreased to 1:4 d_h decreased to ~ 140-150 nm for both nano-emulsion formulation. This could either suggest the formation of smaller objects, or of a change in the microgel geometry, which would affect the DLS measurements. The microgel geometry was further assessed by TEM, and confirmed that while spherical objects where obtained for R_s = 1:1 and 1:2 a lower [SH]:[nb] ratio resulted in the formation of poorly defined objects of variable geometry (Figure 6-7). These very loosely crosslinked materials result in either highly swollen, poorly defined objects, or in non-reacted polymer chains. Based on this evidence, a minimum [SH]:[nb] ratio of R_s = 1:2 was required for the formation of well-defined microgels.

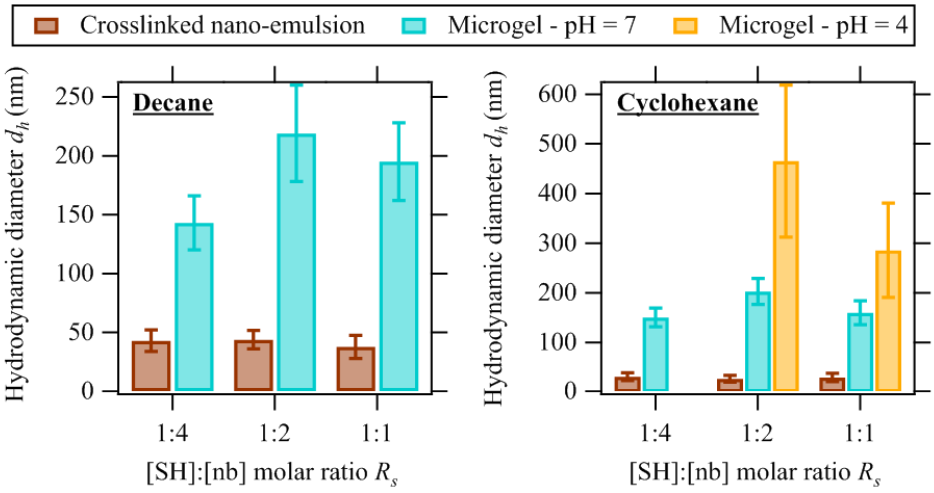

Figure 6-6. Impact of the degree of crosslinking on HS-PEG$_2$-SH crosslinked CS microgels hydrodynamic diameter formulated from (A) decane and (B) cyclohexane, measured by DLS.

As pH decreased from neutral (pH ~ 7) to acidic (pH ~ 4) d_h doubled, due to the protonation of the amines leading to an increased repulsion between the polymer chains as detailed in section 4.4.2.1 in Chapter 4 (Figure 6-6AB), which is further supported by an increase in the zeta potential from $\zeta \sim +12$ mV at neutral pH to $\zeta \sim +40$ mV at mild acidic pH. CS microgels and nanoparticles often present $\zeta \sim +50$ mV; [290] the slightly lower values measured are consistent with the introduction of carboxylate groups on the nb moieties, as well as with the presence of T80 surfactant on the surface of the microgel by ^{1}H NMR (Figure 6-7) This pH-responsivity could be beneficial for drug delivery in the case of cancer or bacterial infections, where the intracellular pH is acidic.[291]

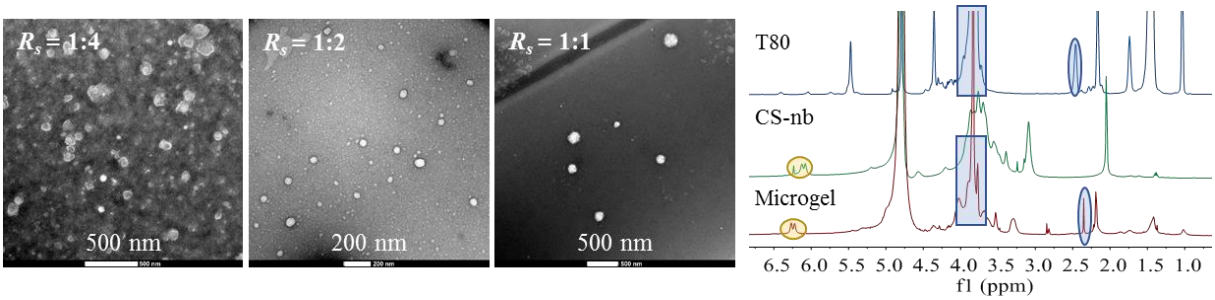

Figure 6-7. Microgel characterisations: TEM of HS-PEG$_2$-SH crosslinked CS microgels with R_s varied between 1:4 and 1:1 and ^{1}H NMR of the corresponding microgels (R_s = 1:2) compared to CS-nb and the surfactant T80.

6.3.1.3 SANS analysis

The microgel swelling was further related to the internal nanostructure and its mesh size using SANS measurements. A typical scattering profile is shown in

Figure 6-8A and presents the following features: the scattering intensity increases in the high q region proportionally to q^{-4}, consistent with small and swollen objects in solution. A first, low intensity shoulder appears at q ~ 0.06 Å^{-1} followed by a sharper one at q ~ 0.01 Å^{-1}, suggesting two characteristic length scales in the network: the mesh size ξ and an aggregate dimension resulting from highly crosslinked regions in the microgel network (see Figure 2-9) which has been associated with network inhomogeneity in hydrogels.[61] Compared to pNIPAM microgels, both shoulders are very broad and no oscillations are observed,[243] suggesting polydispersity. The intensity continues to increase in the low q region proportionally to q^{-2}. The investigated q range was ~ 0.002-0.5 Å^{-1} corresponding to a length scale of ~ 1.5 – 300 nm, which is lower than the hydrodynamic diameter of the swollen microgels under acidic conditions (Figure 6-6B), consistent with the absence of a plateau in the low q region. In addition, previous studies on microgels performed at similar concentrations report the presence of a structure factor resulting from microgel interactions.[244, 246] Although samples were not optically transparent, no multiple scattering occurred. The formation of a crosslinked network can be further verified by a Kratky plot with the appearance of a peak in the low q region, typical signature of highly scattering, frozen crosslinks, when solvated polymers present a linear increase (Figure 6-8B).[61]

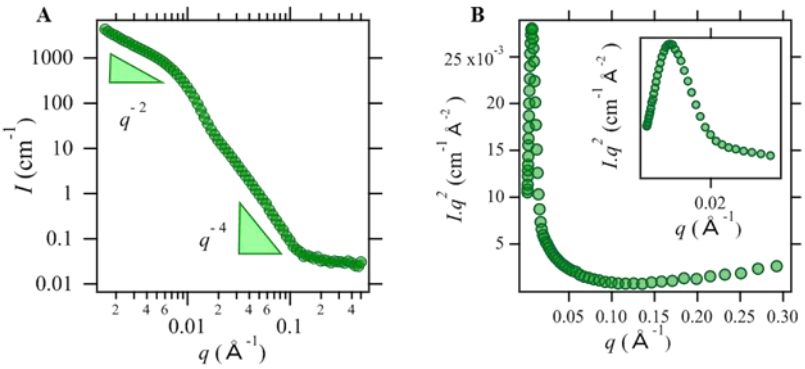

Figure 6-8. (A) Typical scattering profile of HS-PEG$_2$-SH crosslinked CS microgels and (B) the corresponding Kratky plot. The increase in the high q *region is due to incoherent scattering.*

As discussed in section 2.3.3.7 in Chapter 2 the modelling of the scattering of microgels is described as the sum of the contribution of the polymer chains – typically a Lorentzian function - and of the crosslinked units, which can take the form of a Porod exponent, another Lorentzian term or a Guinier-like equation.[233] For monodisperse microgels of well-known structure, this second term can be refined as the scattering of a core-shell[243, 248] or of a fuzzy sphere.[246] CS-nb microgels, however, are expected to present a polydisperse structure due to the random functionalisation of CS and the non-controlled grafting. In addition, a structure

factor may need to be added to describe the low-q region.[130] The scattering of the microgels was therefore modelled by empirical formulae, with restriction in the low q region due to inter-particle interactions (0.002 – 0.5 Å^{-1}).

As an initial approach, the aggregates were modelled by a Porod decay as performed with CS-nb hydrogels in Chapter 4:

$$I(q) = \frac{A}{q^D} + \frac{C}{1+(q\xi)^m} + background \quad (2\text{-}29)$$

where ξ corresponds to the microgel mesh size, the Lorentzian exponent m indicates the polymer chains solvation or collapse, and the Porod exponent D describes the aggregates, resulting from crosslinking inhomogeneities. The dimension of these highly reticulated points can be further estimated by adding an exponential decay as:[224, 231]

$$I(q) = \frac{I_L(0)}{\left(1 + \frac{D+1}{3}\xi^2 q^2\right)^{D/2}} + I_s(0)e^{-\frac{R_g^2 q^2}{3}} + background \quad (6\text{-}1)$$

These equations were preferred as they allow for variations on the Lorentzian exponent (m in Eq. 2-29 or D in Eq. 6-1) which can be affected by hydrogen bonding,[9] very strong in polysaccharides. When constricting m – or D - to 2 to recover the classic Lorentzian equation, no meaningful results could be obtained, even on a restricted q range. Similarly, better fits were obtained in the high q region when using the Debye-Anderson-Brumberger (DAB) equation, which presents a q^{-4} dependency of L_c – analogue to ξ:

$$I(q) = A\frac{L_c^3}{\left(1 + q^2 L_c^2\right)^2} + background \quad (2\text{-}30)$$

Table 6-1. Comparative fitted data of CS-nb microgels crosslinked with HS-PEG$_2$-SH.

R_s	DAB fit		Porod-like aggregates				*Guinier-like aggregates*			
	ξ (nm)	χ^2	ξ (nm)	n	m	χ^2	ξ (nm)	D	R_g (nm)	χ^2
1:2	5.7 ± 0.04	6.60	2.4 ± 0.04	3.8	4.1	8.18	4.7 ± 0.12	3.9	22.0 ± 0.44	4.72
1:1	6.4 ± 0.05	7.61	4.0 ± 0.06	4.0	3.6	14.8	6.4 ± 0.17	3.7	26.3 ± 0.11	4.24

Mesh sizes obtained from Eq.2-29, 6-1 or 2-30 are shown in Table 6-1 and the corresponding fitted data are presented in Figure 6-9. The fitting was performed in the high-medium q region as this is where mesh size information will be found; in addition, the low q region is likely impacted by a structure factor. Depending on the chosen equation, the mesh sizes varied between ~ 2 and up to ~ 6 nm, all larger than the fully elongated crosslinker length

(1.14 nm). Largest mesh sizes were obtained from the DAB model, which is sometimes used to describe hydrogel aggregates, while both other equations were consistent with a Porod exponent of ~ 3.7, reflecting rough inhomogeneities, likely due to the formation of hydrophobic nb crosslinks. The Guinier-like term in Eq. 6-1 estimated aggregate dimensions of R_g ~ 20-25 nm. As anticipated, both R_g and ξ increased as the amount of crosslinker increased from R_s = 1:2 to 1:1.

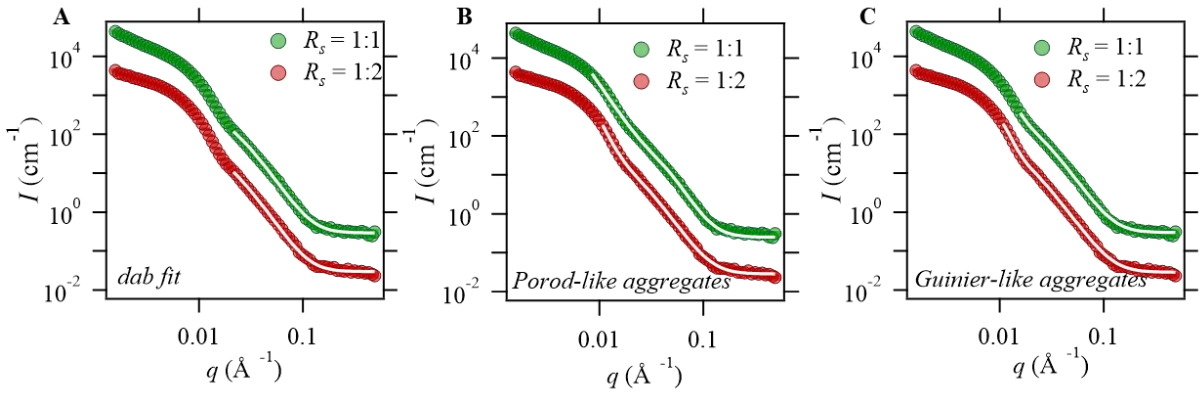

Figure 6-9.SANS data of HS-PEG$_2$-SH. The fitted data are shown as a white line for the different fits: (A) DAB, (B) Porod-like aggregates, (C) Guinier-like aggregates. Data have been offset (10x) on the y-axis for clarity.

The Lorentzian exponent (*m* in Eq. 2-29 or *D* in Eq. 6-1) of 4, on the other hand, is somewhat unexpected. This exponent is related to the excluded volume parameter υ in Flory theory.[235] Swollen polymer chain in a good solvent typically present $1/2 < \upsilon < 3/5$ with $\upsilon = 2$ corresponding to a theta solvent where both polymer-solvent and polymer-polymer interactions are equal. $1/3 < \upsilon < 1/2$ on the other hand suggests self-attracting polymer chains with poor polymer/solvent interactions. It has been shown that *m* can slightly differ from 2 for polymer gels, as accommodated in Eq. 2-29 in Eq. 6-1; however, no value greater than 3 have been reported, even for hydrogen-bond rich networks, where intra-molecular polymer chain interactions are consequent.[231] An exponent $\upsilon = ¼$ can be found in Flory theory as a description of ideal randomly branched polymers,[292] which is consistent with the nature of CS-nb - a polydisperse polymer of various chain length, randomly functionalised with nb branches, themselves randomly crosslinked with thiols. It is also found in the description of more complex crosslinked structures such as tree melts or weakly swollen randomly branched polymers where chains motion does not obey Gaussian statistics.[292]

Many reports of SANS studies of hydrogels or microgels take advantage of near-ideal structures coming from well-defined crosslinkers of known functionality and length, such as

tetra-arm PEGs[60, 61] or very well-defined microgels.[130, 243, 248] Due to the intrinsic polymer heterogeneity it seems reasonable that polymer chains do not follow Gaussian movements as ideal linear polymers do. Adapting Flory theory of branched polymer melts – supposedly a better description than dilute, non-interacting trees as gelation requires chain entanglement and overlap – the system dimension d can be calculated as:

$$d = \frac{1}{v} = 4 \qquad (6\text{-}2)$$

and the upper critical dimension d_c for which volume interactions are negligible is $d_c = 4$.[292] As $d \leq d_c$ excluded volume interactions must be considered, consistent with the formation of crosslinking points in the microgel network and the resulting formation of non-accessible regions to solvent, which may be related to the shoulder observed on the scattering profile.

The mesh size obtained from the microgels are very different from those of the hydrogels calculated both by SANS and by rheology. The crosslinking concentration investigated for hydrogels (2 and 4 w:v%) were higher than those used with microgels (1 w:v%), and the hydrogels were not in their swollen state. The mesh size of the corresponding 1 w:v% hydrogels can be estimated as ~ 30 - 40 nm by rheology, which is comparable to the aggregate dimension R_g. Rheology studies the macroscopic properties of materials and is greatly affected by network inhomogeneity. The differences between the micro- and macrogels may also result from different polymer confinement in the crosslinking step in the bulk phase and in the water droplet.

6.3.1.4 Impact of the crosslinker

The structure of the microgels can also be tuned by varying the composition of the water phase, mainly the nature of the crosslinker as well as the polymer concentration. The crosslinkers presented in Chapter 4 (HS-PEG$_2$-SH, HS-PEG$_{40}$-SH and CS-SH) were combined in the water phase to achieve different R_s and the resulting materials were studied in their fully swollen state i.e. under acidic conditions. As observed previously, lowering the thiol content resulted in more loosely crosslinked networks with greater swelling, as shown by DLS with their increasing hydrodynamic diameters (Figure 6-10A). The properties of the bulk hydrogels were dependent on the crosslinker chosen, with greater swelling observed for the longer crosslinker HS-PEG$_{40}$-SH (see section 4.4.2.1 in Chapter 4); the swelling of the microgels, however, was not significantly affected by the crosslinker used, with similar diameters obtained for all materials (d_h ~ 420 nm for R_s = 1:2 and d_h ~ 230 nm for R_s = 1:1, Figure 6-10A).

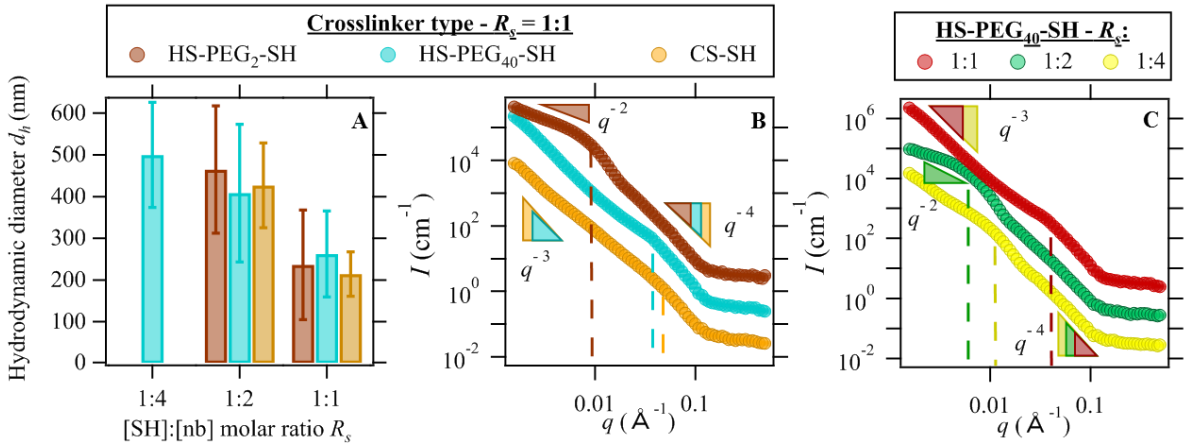

Figure 6-10. Impact of the crosslinker on CS-nb microgels studied by: (A) DLS and (B, C) SANS. The scattering curves have been offset (10x) on the y-axis for clarity.

The mesh size and the aggregate dimensions were further estimated using SANS. As for the HS-PEG$_2$-SH crosslinked microgels, the scattering initially increased proportionally with q^{-4} in the high q region until a shoulder is reached, after which the scattering evolves with a q^{-2} or a q^{-3} power law depending on the crosslinker used without reaching a maximum (Figure 6-10B and C). The second intense shoulder in the low q region was only observed with HS-PEG$_2$-SH or HS-PEG$_{40}$-SH when R_s = 1:2 or 1:4, suggesting the presence of aggregates does not occur for the more reticulated system (R_s = 1:1), which may be due to a more homogeneous network. The fit quality was greatly dependent on the presence of this second shoulder, which was best accounted for with the presence of a Guinier-like term, whereas the scattering of the microgels presenting a single shoulder was better described with a Porod exponent (Figure 6-11 and Figure 6-12; the fitting parameters are given in Table 6-2 and Table 6-3).

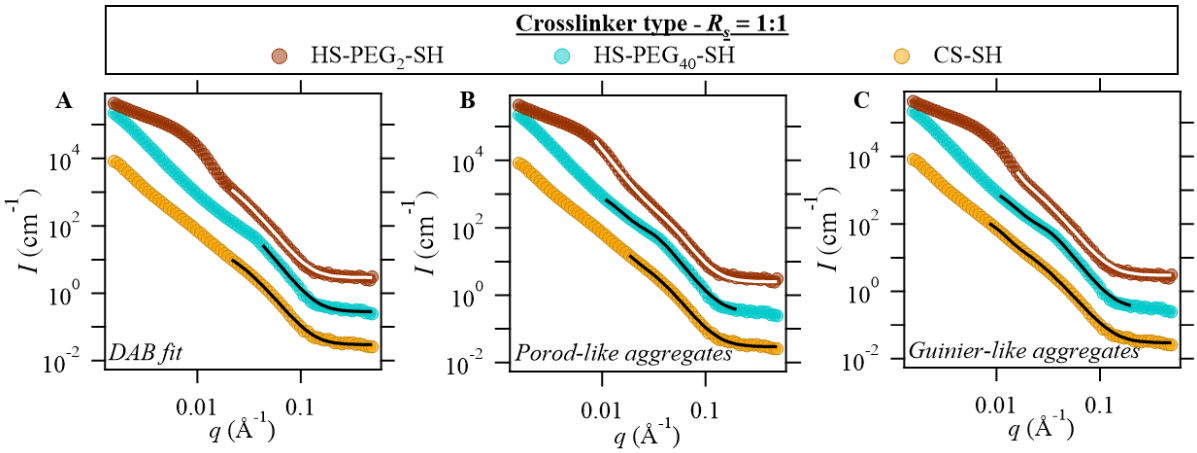

Figure 6-11. SANS data of microgels (R_s = 1:1) fitted with: (A) DAB, (B) Porod-like aggregates, (C) Guinier-like aggregates. Data have been offset (10x) on the y-axis for clarity.

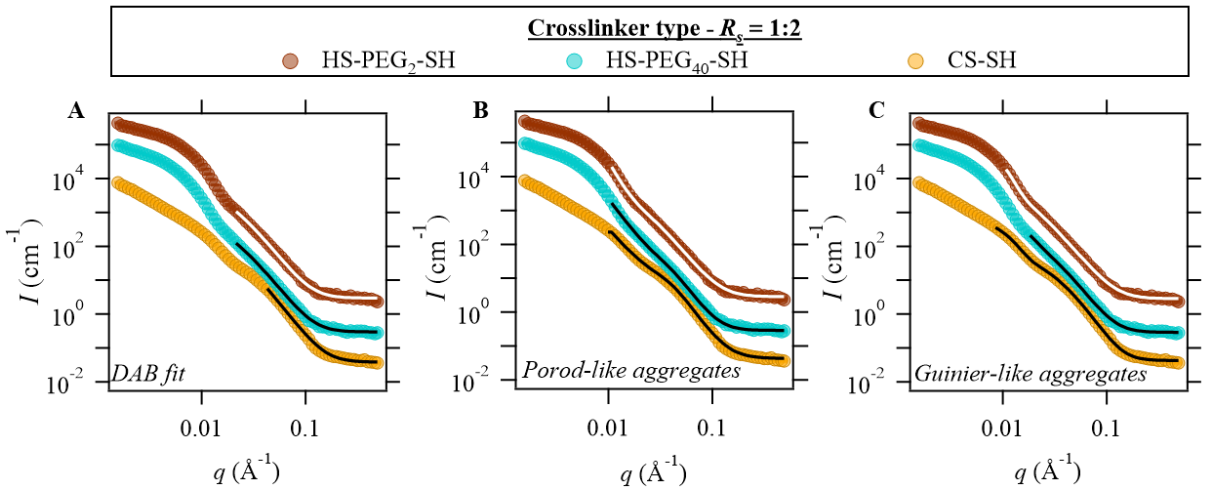

Figure 6-12. SANS data of microgels (R_S *= 1:2) fitted with: (A) DAB, (B) Porod-like aggregates, (C) Guinier-like aggregates. Data have been offset (10x) on the y-axis for clarity.*

Table 6-2. Comparative fitted data obtained for HS-PEG$_{40}$-SH microgels.

R_s	DAB fit		Porod-like aggregates				*Guinier-like aggregates*			
	ξ (nm)	χ^2	ξ (nm)	n	m	χ^2	ξ (nm)	D	R_g (nm)	χ^2
1:4	5.8 ± 0.05	5.33	2.3 ± 0.04	4.0	4.6	33.1	4.1 ± 0.12	4.0	20.7 ± 0.06	9.51
1:2	6.2 ± 0.06	5.74	2.9 ± 0.03	4.0	4.1	61.2	3.5 ± 0.18	4.2	15.3 ± 0.35	1.46
1:1	6.1 ± 0.22	6.57	2.9 ± 0.03	4.0	3.6	81.8	2.3 ± 0.04	4.0	19.4 ± 0.12	13.4

Table 6-3. Comparative fitted data obtained for CS- SH microgels.

R_s	DAB fit		Porod-like aggregates				*Guinier-like aggregates*			
	ξ (nm)	χ^2	ξ (nm)	n	m	χ^2	ξ (nm)	D	R_g (nm)	χ^2
1:2	4.5 ± 0.02	12.2	3.0 ± 0.21	3.5	4.0	23.7	4.5 ± 0.08	3.7	23.9 ± 0.16	9.61
1:1	7.2 ± 0.23	5.34	2.5 ± 0.03	3.4	4.9	3.78	2.3 ± 0.02	3.8	20.3 ± 0.04	10.2

Neither the mesh size nor the aggregate dimensions of HS-PEG$_{40}$-SH crosslinked microgels was drastically different from their HS-PEG$_2$-SH analogues, despite the different crosslinker length (Table 6-2). In addition, the higher hydrophilicity of HS-PEG$_{40}$-SH resulting from the amount of ethylene oxide units reduces the hydrophobicity of the crosslink points, probably contributing to the reduction of the scattering of the aggregates. Finally, thiols can also react together to generate disulphides, thus reducing the amount of free thiols available for the thiol-ene reaction; increasing the [SH]:[nb] ratio while using a flexible and hydrophilic

crosslinker may make this side-reaction more likely. The amount of unreacted thiols post crosslinking could in theory be determined using Ellman's test as described in Chapter 3; however, thiol accessibility decreases after crosslinking, thus reducing the reactivity of DTNB. As the reaction was performed under acidic conditions disulphide bridges formation should be prevented, although side reactions cannot be entirely discarded. Residual surfactant T80 was also detected by ^{1}H NMR post-synthesis which may interfere in the scattering data; it is unclear whether T80 is present as micelles in solution or it is interacting with CS-nb microgels.

On the other hand, CS-SH is a highly functionalised, reticulated polymer, with little flexibility. The crosslinking is therefore expected to be less efficient and to result in dispersed, densely reticulated areas. A single, low-intensity shoulder was observed for R_S = 1:1 while two very closed ones were seen for R_S = 1:2, suggesting an aggregate dimension closed to the mesh size, consistent with the high functionalisation and low flexibility of CS-SH. The Porod exponent was lower than for the difunctional crosslinkers, suggesting a less swollen and open architecture.

6.3.1.5 Impact of CS-nb concentration

As discussed in Chapter 4 CS-nb hydrogel mechanical properties, such as swelling or rheology, are dependent on CS concentration during crosslinking, as this affects chain mobility. The impact of CS-nb concentration during the crosslinking process on the final microgel structure was studied on HS-PEG$_{40}$-SH materials. Increasing CS concentration is anticipated to lead to higher crosslinking densities as more crosslinking points are available, which should result in smaller objects of better-defined internal structure.

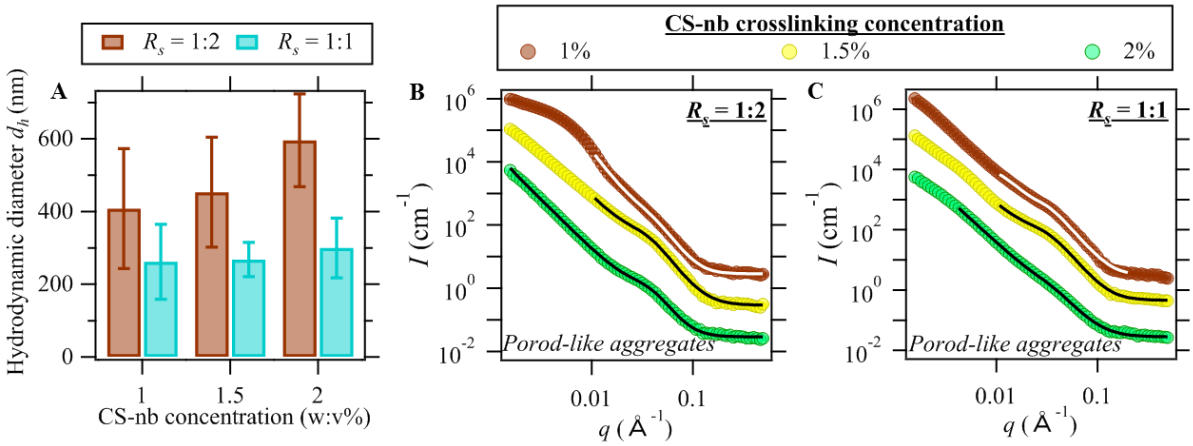

Figure 6-13. Impact of CS-nb concentration in the crosslinking process measured by (A) DLS and (B, C) SANS. Fitted data are shown as a plain line; data have been offset (10x) on the y-axis for clarity.

DLS measurements of the resulting microgels showed that CS-nb concentration did not impact on the final dimension of the microgel for R_s = 1:1 (d_h ~ 220 nm) and slightly increased from d_h ~ 400 nm at 1-1.5 w:v% to d_h ~ 600 nm at 2 w:v% for R_s = 1:2 (Figure 6-13A). This unexpected result suggests incomplete crosslinking, which may result from reduced chain mobility with increased entanglement preventing access from the thiolated crosslinker. SANS data revealed a decrease in the intensity of the first peak, shifted to the high q region, with a flattening of the scattering intensity, which increases linearly in the low q region following $q^{-2.5}$ - q^{-3} (Figure 6-13BC). This suggests the formation of more homogeneous networks with increasing polymer concentration. The slight shift of the first shoulder to higher q with increasing CS concentration confirms a decrease in ξ or in the aggregate dimension R_g as expected. Best fits were obtained from a Porod description of the aggregates which yielded ξ ~ 2.8 nm; when an exponential term was added the aggregate dimension was estimated as R_g ~ 20 nm. No correlation between ξ nor R_g could be drawn possibly due to network heterogeneity (Table 6-4 and Table 6-5).

Table 6-4. Comparative fitted data obtained from different CS-nb concentration at R_s = 1:1.

CS-nb	DAB fit		Porod-like aggregates				*Guinier-like aggregates*			
(w:v%)	ξ (nm)	χ^2	ξ (nm)	*n*	*m*	χ^2	ξ (nm)	*D*	R_g (nm)	χ^2
1	6.1 ± 0.2	6.57	2.9 ± 0.03	4.0	3.6	81.8	2.3 ± 0.04	4.0	19.4 ± 0.12	13.4
1.5	5.9 ± 0.2	4.58	3.1 ± 0.03	3.1	4	4.57	2.3 ± 0.03	4	23.6 ± 0.13	9.01
2	4.5 ± 0.04	4.08	2.8 ± 0.07	3.0	4	4.08	5.6 ± 0.22	3.4	23.8 ± 0.41	2.38

Table 6-5. Comparative fitted data obtained from different CS-nb concentration at R_s = 1:2.

CS-nb	DAB fit		Porod-like aggregates				*Guinier-like aggregates*			
(w:v%)	ξ (nm)	χ^2	ξ (nm)	*n*	*m*	χ^2	ξ (nm)	*D*	R_g (nm)	χ^2
1	6.2 ± 0.06	5.74	2.9 ± 0.03	4.0	4	61.2	3.5 ± 0.18	4	15.3 ± 0.35	1.46
1.5	7.2 ± 0.04	4.78	2.7 ± 0.03	3.1	4	8.18	2.2 ± 0.03	4	20.7 ± 0.09	11.4
2	3.7 ± 0.03	3.53	2.6 ± 0.03	3.1	4	5.20	7.4 ± 0.22	3.5	11.6 ± 0.10	2.61

6.3.2 Biologically relevant environmental conditions

The behaviour of CS polyelectrolyte microgels under physiological conditions are expected to be significantly different due to the presence of salts. *In utero* environment is also urea-rich, with possible hydrogen bond interactions with polysaccharides. Temperature, on the other hand, was not anticipated to have a drastic effect on the microgel structure, as CS is not thermo-

responsive; indeed, SANS measurements performed both at 25°C and at 37°C showed no significant differences, with slight variations present for the longest PEG crosslinkers probably due to PEG thermo-responsivity; (Figure 6-14) longer thiolated PEGs crosslinker would likely have a more pronounced effect.

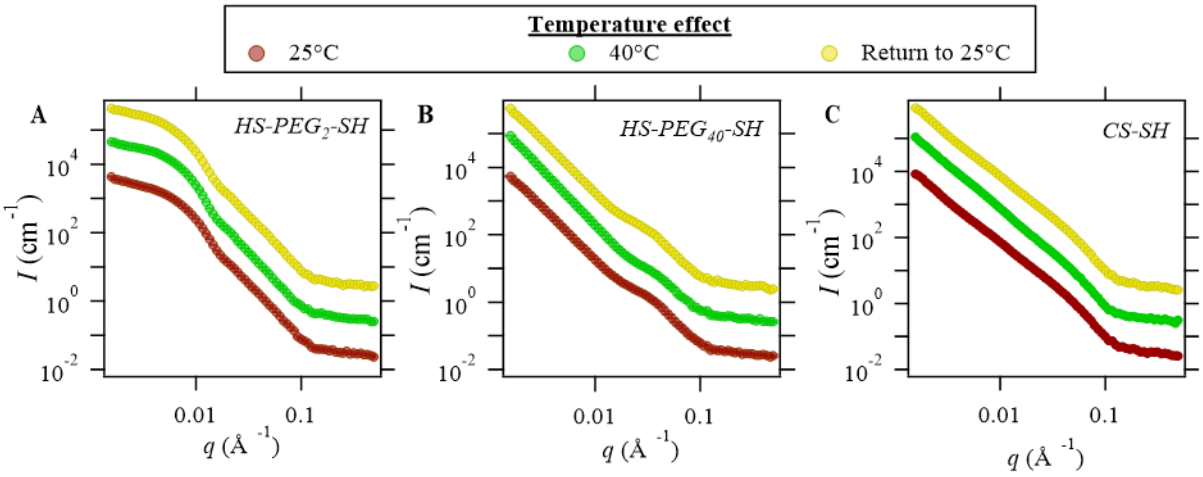

Figure 6-14. Impact of temperature on CS-nb microgels Data have been offset (10x) t on the y-axis for clarity.

The impact of the environment was studied by a combination of DLS to access the final dimension of the microgels and SANS to get details of their internal structure for two different crosslinkers (HS-PEG$_2$-SH and HS-PEG$_{40}$-SH) and a single [SH]:[nb] molar ratio (R_s = 1:1). To prevent batch-to-batch discrepancies, several microgel batches were combined and finally resuspend in the desired environmental conditions. Although this was expected to increase the overall polydispersity, this solution was preferred to ensure any measured values would be the sole result of environmental conditions. In addition, the polymer used for this new series of experiments presented a lower degree of functionalisation (DF ~ 0.65 µmol nb/mg CS *versus* ~ 1.0 µmol nb/mg CS previously). This lower DF resulted in the formation of fewer crosslinking points and thus bigger d_h were measured by DLS (Figure 6-15A). Similarly, SANS profiles for both materials were very different from those described in section 6.3.1.3, with a single, intense shoulder present for both microgels at q ~ 0.02 Å^{-1} followed by an increase in the scattered intensity following q^{-2} and a final slight upturn at q ~ 0.001 Å^{-1} (Figure 6-15B). The sample polydispersity may lead to the broadening of these signals related to the formation of internal aggregates of slightly different dimensions. The behaviour in the low q region is consistent with the formation of larger structures as measured by DLS.

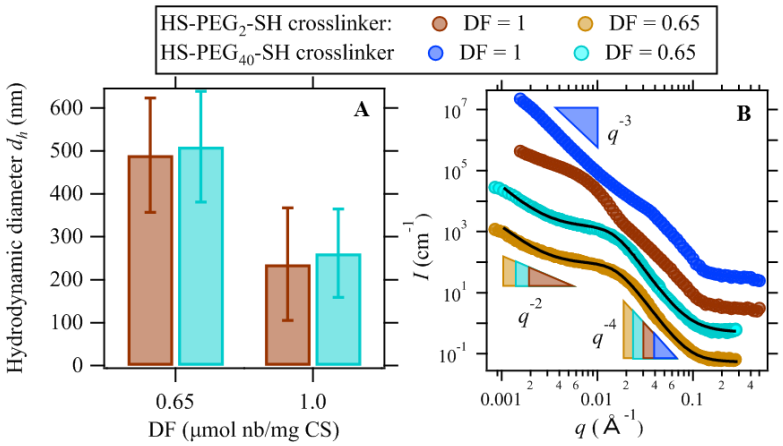

Figure 6-15. (A) DLS and (B) SANS measurements of CS-nb microgels for different DF. Fitted data are shown as a plain line; data have been offset (10x) on the y-axis for clarity.

All scattering curves presented a Lorentzian exponent $m = 4$ but a Porod exponent $n \sim 2.5$, closer to previously reported values and suggesting polymer chains in a bad solvent, probably resulting from the formation of heterogeneous crosslinks. The mesh sizes calculated from the three models presented in section 6.3.1.3 were of around 6.1 – 7.7 nm for HS-PEG$_2$-SH and 6.7 – 9.3 nm for HS-PEG$_{40}$-SH depending on the model used (Table 6-6 and Appendix M), which is larger than those obtained from the more functionalised polymer, as anticipated. The dimensions of R_g and ξ were similar, likely resulting from sample polydispersity.

6.3.2.1 Addition of salt

Due to the weak polycationic nature of CS the addition of salt and pH changes are expected to impact on the microgel swelling, as was observed for the corresponding macrogels (section 4.4.2.1 in Chapter 4). The impact of biologically relevant ions, NaCl and $CaCl_2$ – highly present *in utero* in SB pregnancies – was studied. DLS confirmed a shrinkage of the microgels, with diameters decreasing from ~ 450 nm to ~ 200 nm (Figure 6-16A and Figure 6-17A), attributed to a screening of the electrostatic interactions in the polymer chains resulting from the positively charged amines, as discussed in Chapter 4. The quality of the DLS results was affected by the introduction of ions, which may indicate aggregation.

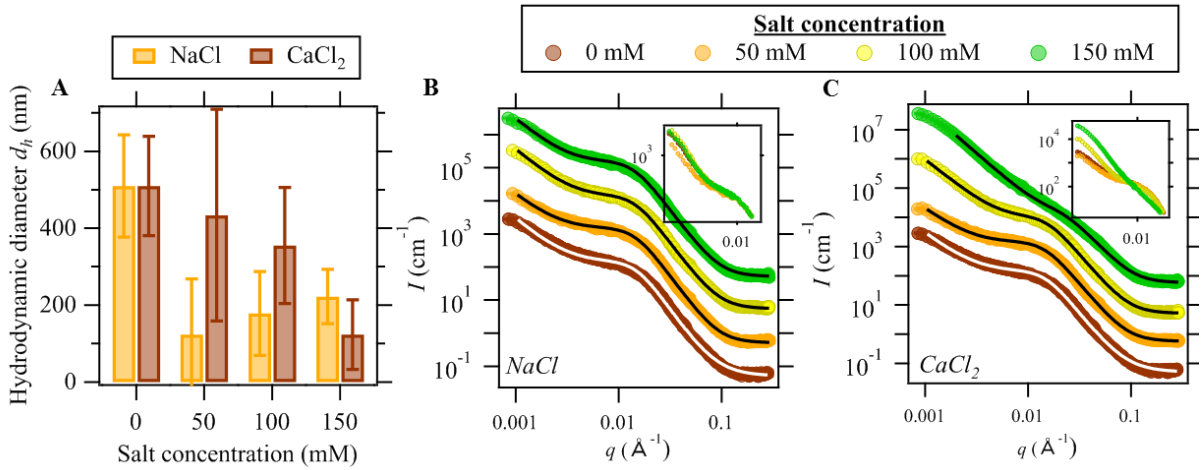

Figure 6-16. Impact of salts on HS-PEG$_{40}$-SH microgels measured by (A) DLS and (B, C) SANS. Data fitted to the Porod-like aggregates are shown as a plain line; data have been offset (10x) t on the y-axis for clarity. The insert represents an overlap of the low q *region.*

SANS measurements showed very little variations in the scattering profile, with differences only observed in the low *q* regions corresponding to bigger aggregates. The formation of smaller objects should allow for the visualisation of a plateau in the scattered intensity and a shift of the shoulder to the high *q* region; however, no changes were observed for HS-PEG$_2$-SH microgels, which contradicts DLS measurements (Figure 6-17). The polydispersity of the samples can justify the identical profile in the high *q* regions, where variations of the mesh size should be very subtle; however, the low *q* region should present different characteristics due to shrinkage.

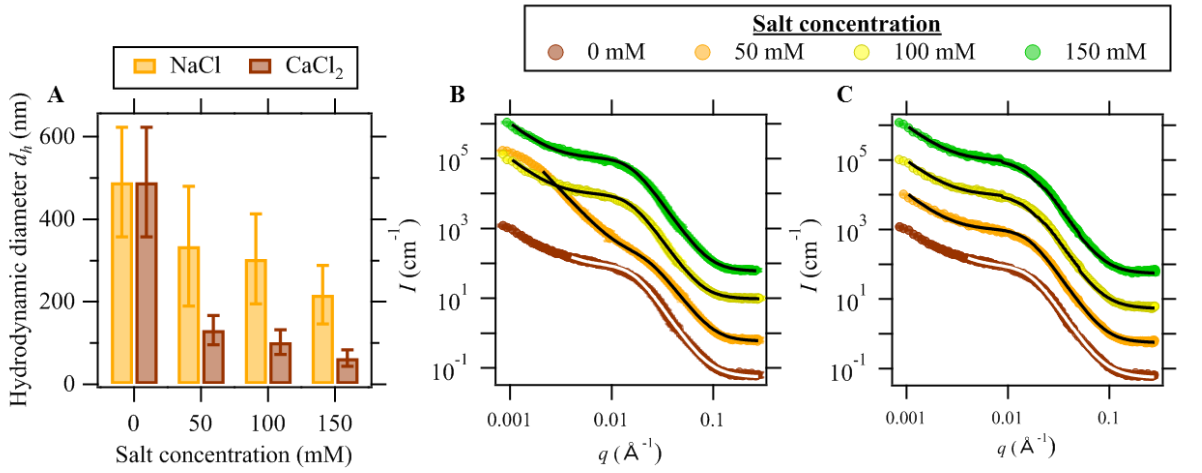

Figure 6-17. Impact of salts on HS-PEG$_2$-SH microgels measured by (A) DLS and (B, C) SANS. Data fitted to the Porod-like aggregates are shown as a plain line; data have been offset (10x) on the y-axis for clarity.

HS-PEG$_{40}$-SH crosslinked microgels were not significantly affected by the addition of NaCl with only slight variations observed in the low q region. The addition of $CaCl_2$ on the other hand resulted in a shift in the shoulder from $q \sim 0.015$ Å^{-1} to $q \sim 0.04$ Å^{-1} – consistent with a shrinkage at the mesh size length scale - and a reduction in its intensity, followed with a linear increase in the scattering intensity from q^{-2} to q^{-3} (Figure 6-16BC). This final increase, in disagreement with the sizes observed by DLS, suggest inter-particle interactions and the formation of greater assemblies through electrostatic interactions which was not observed by DLS due to the lower concentrations used (0.75 mg/mL compared to 15 mg/mL for SANS). The drastic change observed from $CaCl_2$ to NaCl may result from either the higher ionic strength investigated (twice as big compared to NaCl) or to ionic interactions between the carboxylate moieties of CS-nb - resulting from the ring-opening of CA - and divalent calcium ions. The range of concentration studied was chosen as physiologically relevant.

Table 6-6. Comparative fitted data obtained from HS-PEG$_{40}$-SH microgels for different NaCl concentrations.

[NaCl]	DAB fit		Porod-like aggregates				*Guinier-like aggregates*			
(mM)	ξ (nm)	χ^2	ξ (nm)	n	m	χ^2	ξ (nm)	D	R_g (nm)	χ^2
0	9.3 ± 1.5	0.65	6.7 ± 0.04	2.4	4.5	3.30	7.7 ± 1.9	3.6	10.0 ± 0.08	1.95
50	8.7 ± 0.9	1.10	6.9 ± 0.04	2.4	4.3	2.06	8.5 ± 0.2	4.2	25.4 ± 0.3	2.34
100	6.9 ± 0.4	0.67	6.9 ± 0.04	2.6	4.3	1.93	5.9 ± 0.2	3.9	11.2 ± 0.1	1.40
150	8.0 ± 0.7	0.57	7.1 ± 0.05	2.5	4.3	1.78	8.9 ± 0.2	4.1	25.9 ± 0.3	1.66

Table 6-7. Comparative fitted data obtained from HS-PEG$_{40}$-SH microgels for different $CaCl_2$ concentrations.

[$CaCl_2$]	DAB fit		Porod-like aggregates				*Guinier-like aggregates*			
(mM)	ξ (nm)	χ^2	ξ (nm)	n	m	χ^2	ξ (nm)	D	R_g (nm)	χ^2
0	9.3 ± 1.5	0.65	6.7 ± 0.04	2.4	4.5	3.30	7.7 ± 1.9	3.6	10.0 ± 0.08	1.95
50	8.1 ± 0.8	0.55	6.8 ± 0.03	2.5	4.3	1.62	8.1 ± 0.2	4.1	25.6 ± 0.3	1.95
100	8.6 ± 0.9	0.60	6.4 ± 0.05	2.8	4.3	1.68	9.1 ± 0.2	4.1	24.2 ± 0.3	1.37
150	7.1 ± 0.5	1.02	4.4 ± 0.08	3.0	3.9	2.93	6.1 ± 0.1	3.7	47.6 ± 0.4	4.08

The mesh size and the dimensions of the crosslinked regions obtained by fitting are given in Table 6-6 and Table 6-7. All fits presented very similar mesh sizes, Porod and Lorentzian exponents suggesting a similar internal structure at the investigated concentrations. The main differences were obtained on the aggregates dimension R_g which increased with increasing salt concentration, showing the bigger densely reticulated areas in the microgel matrix due to local collapse. As anticipated, the more drastic change was observed with the highest $CaCl_2$ concentrations, with a noticeable decrease in the mesh size and an increase in the mass fractal.

6.3.2.2 pH variations

CS being a well-known weak cationic polymer the pH-responsivity of the corresponding microgels was investigated. As seen in section 6.3.1.2 acidic conditions increased the swelling of the microgels due to the protonation of the remaining amines, also evidenced by the increase of the microgel ζ-potential from ~ + 10 to ~ + 50 mV. Little variations occurred as pH increased from 3 to 5; however, for a pH range varying between 5 and 7 the viscosity of the microgel suspension drastically increased, with a further increase in pH leading to phase separation and/or precipitation. This pH value is consistent with reported pK_a values for CS amines varying between 6 and 6.5,[293, 294] which impact on CS solubility. The SANS profile of this transition phase of increased viscosity ($5 < pH < 7$) was recorded for both microgels and presented significant differences, with an initial increase for higher q values followed by a plateau on the 0.01 – 0.1 $Å^{-1}$ q range and a final increase in the scattering intensity following q^{-2} in the low q region (Figure 6-18). The mesh size could not be estimated from the DAB model for these profiles. Both the Porod and the Guinier description of the aggregates indicated a significant shrinkage of the microgels from ξ ~ 7 nm down to ~ 1 nm and R_g ~ 10 - 20 nm down to ~ 5 nm. No measurements could be made for higher pHs due to microgel precipitation.

Interestingly, precipitation was not observed if microgels were mixed in PBS, even if $pH > pK_a$; the high salt concentration is likely contributing to the microgel stabilisation through electrostatic interactions. While HS-PEG_{40}-SH microgels presented a very similar scattering profile to microgels swollen under acidic conditions, HS-PEG_2-SH microgels were more aggregated, with ξ ~ 7 nm and R_g ~ 50 nm (Table 6-8 and Table 6-9). Studying the effect of pH in the presence of a background electrolyte concentration would be an interesting complementary experiment.

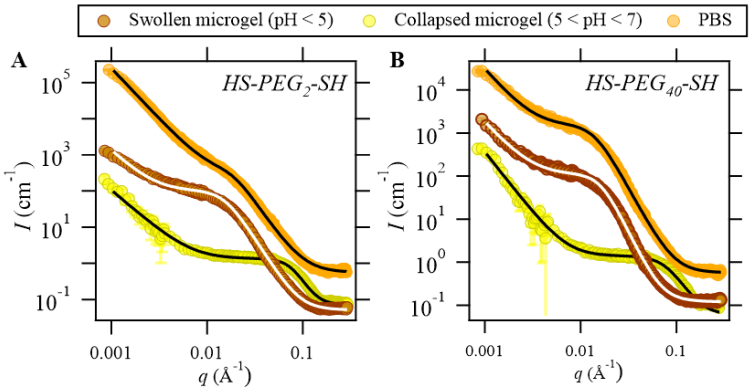

Figure 6-18. Impact of pH on (A) HS-PEG$_2$-SH and (B) HS-PEG$_{40}$-SH microgels. Data fitted to the Porod-like aggregates are shown as a plain line; PBS data have been offset (10x) on the y-axis for clarity.

Table 6-8. Comparative fitted data obtained from HS-PEG$_2$-SH microgels at different pHs.

pH	DAB fit		Porod-like aggregates				*Guinier-like aggregates*			
	ξ (nm)	χ^2	ξ (nm)	n	m	χ^2	ξ (nm)	D	R_g (nm)	χ^2
4	7.7 ± 0.9	0.46	6.1 ± 0.05	2.4	4.4	1.09	6.4 ± 0.2	3.6	9.6 ± 0.10	1.12
7	-	-	1.3 ± 0.01	2.3	4	1.59	1.8 ± 0.02	4	5.5 ± 0.02	6.48
PBS	6.2 ± 0.4	1.10	5.3 ± 0.08	2.8	4.0	3.91	5.8 ± 0.09	4.0	52.8 ± 0.8	0.86

Table 6-9. Comparative fitted data obtained from HS-PEG$_{40}$-SH microgels at different pHs.

pH	DAB fit		Porod-like aggregates				*Guinier-like aggregates*			
	ξ (nm)	χ^2	ξ (nm)	n	m	χ^2	ξ (nm)	D	R_g (nm)	χ^2
4	9.3 ± 1.5	0.65	6.7 ± 0.04	2.4	4.5	3.30	7.7 ± 1.9	3.6	10.0 ± 0.08	1.95
7	-	-	1.4 ± 0.01	2.8	4.1	1.09	2.2 ± 0.01	2.2	2.2 ± 0.01	1.04
PBS	7.7 ± 0.8	0.48	7.1 ± 0.06	2.6	4.2	1.54	8.4 ± 0.21	4.1	24.4 ± 0.35	1.24

6.3.2.3 Addition of urea

Hydrogen bonding is an important characteristic of polysaccharides, imparting for instance for their solubility. The use of hydrogen bonding disturbing agents such as urea has been shown to lead to spatial re-organisation of the polymer chains, strategy already used to dissolve poorly soluble polymers such as chitosan[251, 295] or to generate hydrogels.[296] *In utero* environment is urea-rich and may therefore impact on CS microgel properties, especially at high concentration.

The quality of DLS data deteriorated with the addition of urea, with an increase in the polydispersity. SANS measurements on the other hand presented no differences in the high q region and only showed very slight variations in the low q region, leading to similar fitted

values of ξ and R_g (Figure 6-19). A lower q region may provide more information regarding inter-particle arrangement.

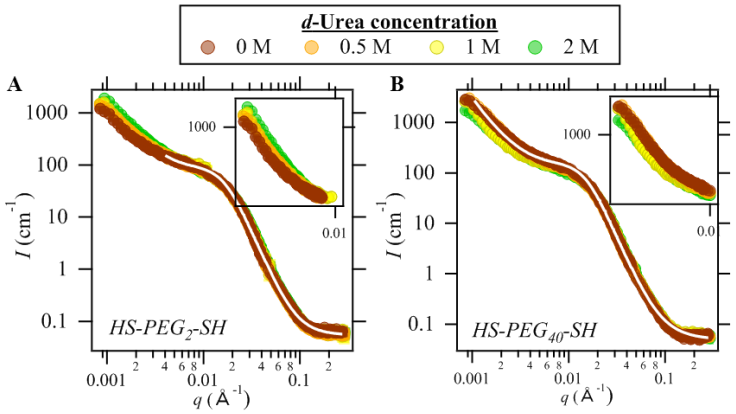

Figure 6-19. Impact of urea on the SANS profile of microgels.

6.3.3 Microgel functionalisation

TEM images (Figure 6-7) suggested that R_s = 1:2 was sufficient to provide spherical microgels, while ^{1}H NMR confirmed the presence of non-reacted nb groups (Figure 6-6E). Furthermore, the relative sharpness of these alkene peaks compared to the crosslinked CS core strongly suggests that these moieties were located on the microgel surface and could therefore be accessed in a post-microgel synthesis step to design tailored, functionalised materials. Nb can react with thiols, but also with tetrazines through inverse electron demand Diels-Alder (IEDDA). This one-step reaction is among the fastest biorthogonal click chemistry reaction and does not require the presence of radicals. The synthesis of tetrazines requires toxic and explosive reagents which limits their scale-up; however, this reaction is highly valuable when small amounts are required due to its high specificity and efficiency – which is the case of nanomaterial functionalisation.[297]

Tetrazines typically weakly absorb at 515 nm, making it difficult to use absorbance to monitor the reaction efficiency. To circumvent this, several groups have developed self-quenching tetrazines, whose fluorescence is recovered after tetrazine ligation.[298] Devaraj *et al.* in particular reported a series of FRET self-quenching probes easily derived from an amine-functionalised tetrazine with commercially available NHS-activated esters of common fluorescent labelling agents such as BODIPY, Oregon Green or Coumarin. Upon reaction with a strained alkene (*trans*-cyclooctene, TCO), the fluorescence was turned on by a factor of 3 (Coumarin) to 20 (BODIPY) after reaction of the tetrazine motif.[288] To confirm the reactivity of CS-nb microgels, coumarin-functionalised tetrazine (Tet-Coum, Figure 6-20 and Scheme 6-1) was synthesized. Within 2 min of incubation with the microgels a 2-fold increase in

fluorescence was observed, which evolved and plateaued to almost 3-fold after 10 min of reaction time, consistent with the values reported by Devaraj *et al*. for a very similar probe to Tet-Coum. This result supports the feasibility of the synthesis of more complex microgels, with decorations that could include cell targeting moieties but also more expensive antibodies or proteins, thanks to the reliability of the tetrazine ligation.

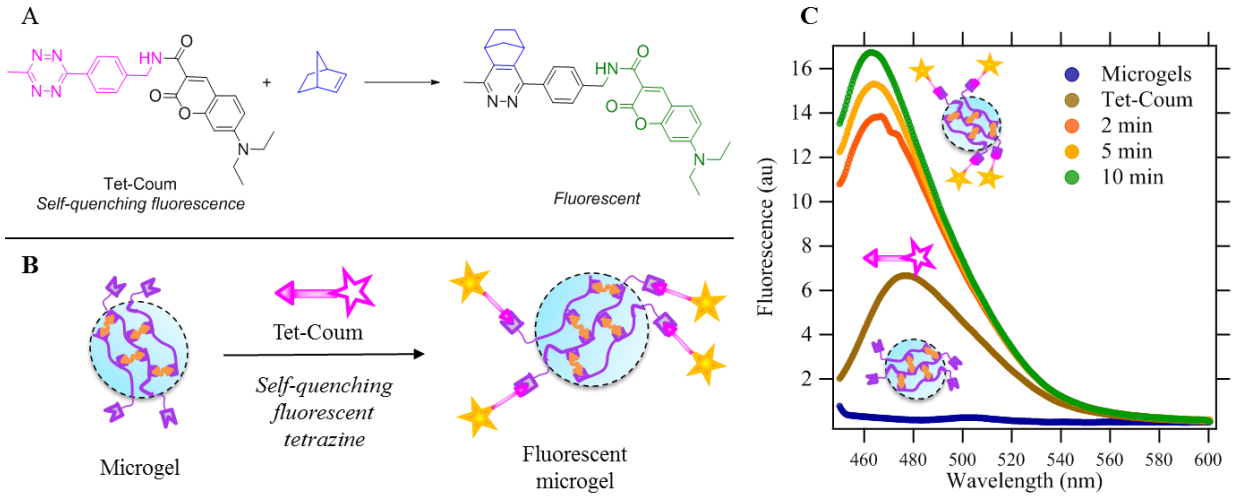

Figure 6-20. Functionalisation of microgels using tetrazine ligation. A) tetrazine ligation of Tet-Coum leading to a fluorescent molecule. B) Fluorescent-microgel synthesis using Tet-Coum. C) Fluorescence spectra of the microgels and Tet-Coum at different reaction time.

6.3.4 Microgel cytotoxicity

The toxicity of the microgels was assessed against HDF cell lines exposed to concentrations varied between 1000 and 2 µg/mL for 1, 2 or 5 days using both Alamar Blue (AB) and Calcein AM to measure cell metabolic activity and cell viability respectively. Metabolic activity was unaffected after up to 2 days, with between 90 and 100 % of activity expressed depending of the microgel concentration. After 5 days this drops to ~ 80 % for the higher microgel concentration (1 and 0.5 mg/mL) while remaining comparable to the control for the lower concentrations (Figure 6-21A). Similarly, cell viability was constant over 5 days, with lower viability observed at 1 mg/mL of microgel (~85 %) while viabilities higher than 90 % were observed otherwise (Figure 6-21B). These preliminary results demonstrate the nontoxicity credentials of the microgels for their potential use in the biomedical area.

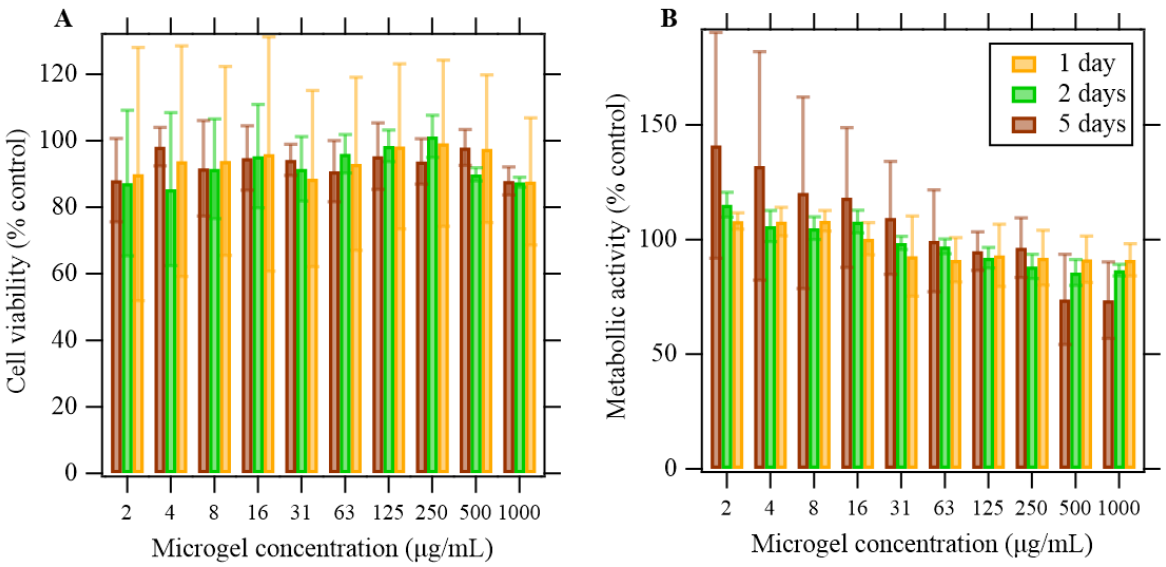

Figure 6-21. Toxicity data against HDF cell lines: metabolic activity (A) and cell viability (B). Results are expressed as a percentage normalised with respect to the control (untreated cells).

6.4 Conclusions

Microgels of tailored size and degree of crosslinking were successfully synthesized using an optimised low-energy, nano-emulsion-templated method. Tuning of the nano-emulsion composition (surfactant, oil) and of the synthesis parameters (crosslinker, crosslinking density) allowed for the obtention of microgels of various sizes, whose swelling was very sensitive to pH. Furthermore, pendant nb groups could be accessed for late-stage functionalisation through tetrazine ligation, as demonstrated by the grafting of a self-quenching fluorescent tetrazine probe, Tet-Coum. This result suggests the feasibility to use CS-nb microgels as crosslinkers or monomers in the design of more complex hydrogels which should present more homogeneous structures and improved mechanical properties. Finally, the described microgels presented non-significant toxicity against HDF cell lines and are therefore promising candidates as functional templates for biomedical applications. Although not tested as hydrogel precursors, these initial properties – *ie* modulable dimensions, reactive shell and non-toxicity – designate these microgels as potential candidates in the design of SB sealants.

7 Non-covalent hydrogels

7.1 Introduction and aims

This chapter discusses the synthesis and characterisation of unexpected non-covalent hydrogels obtained from CS-nb without the addition of a thiolated crosslinker which has not been reported before. Originally, two stereoisomers of CS-nb derived from either *endo* or *exo* carbic anhydride were synthesized to investigate the impact of the chirality of CS-nb crosslinking points – *i.e.* the nb side chains - on the hydrogel mechanical properties.[299] Surprisingly, hydrogels were obtained from both materials without the need for a crosslinker. Gelation proceeded with very fast kinetics under mild acidic conditions in the presence of IRG as photoinitiator. A gelation mechanism was proposed based on ^{1}H NMR evidences and the resulting materials were characterised and compared to the covalent hydrogels. This study highlighted the key role of the carbic anhydride stereochemistry (*endo* or *exo*) on the final hydrogel properties which were drastically different from the covalent system, designing CS-nb as a versatile precursor for hydrogels with tailored applications.

7.2 Methods

7.2.1 Materials and methods

5-norbornene-*endo*-2,3-dicarboxylic anhydride (CA-*endo*) and 5-norbornene-*exo*-2,3-dicarboxylic anhydride (CA-*exo*) were purchased from Sigma-Aldrich. (3aR,4S,7R,7aS)-hexahydro-4,7-methanoisobenzofuran-1,3-dione (nb-*h*, which corresponds to the hydrogenated form of nb-*endo*) was purchased from Fluorochem. All reagents were used as received. Other reagents were obtained as detailed in section 3.3 in Chapter 3 and in section 4.3 in Chapter 4.

7.2.2 Synthesis of chitosan-functionalised norbornene (CS-nb, CS-nb-endo, CS-nb-exo and CS-nb-*h*)

All derivatives were synthesized as described in section 3.2.5 in Chapter 3 by replacing CA with either CA-*endo*, CA-*exo* or CA-*h*. DS was calculated by ^{1}H NMR with a DMF standard as detailed in section 3.3.4 in Chapter 3.

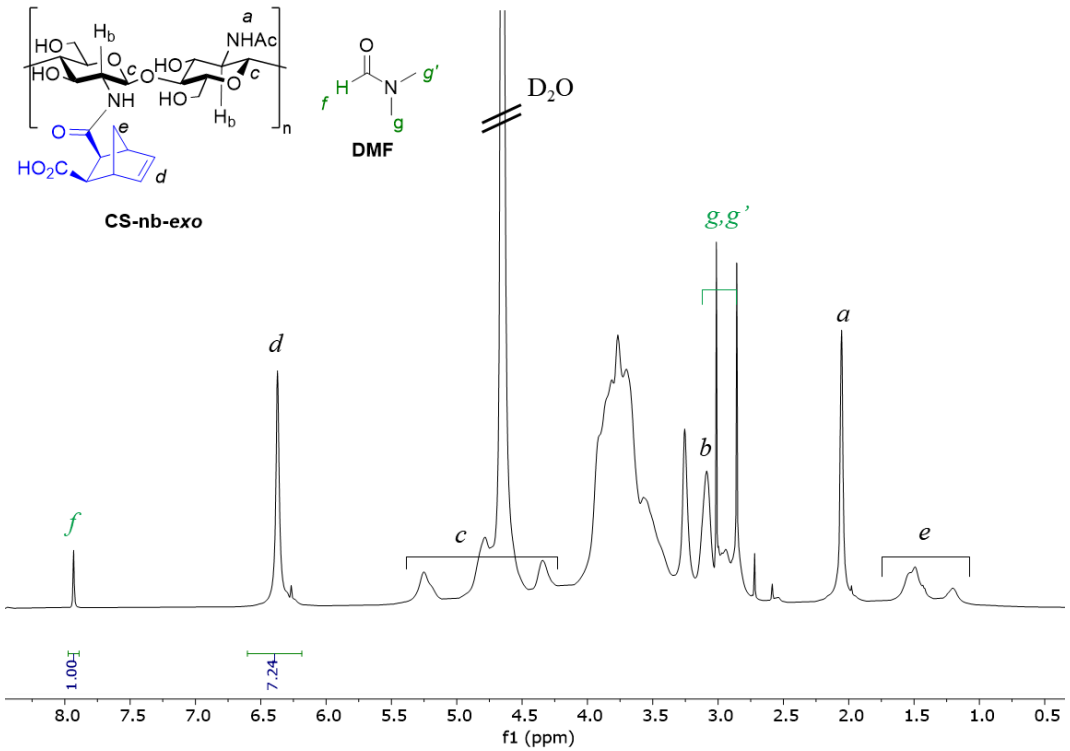

Figure 7-1. ^{1}H NMR of CS-nb-exo with 1 mM DMF. The degree of functionalisation (DF) was calculated using the integrals corresponding to the protons d and f using Equation (3-4).

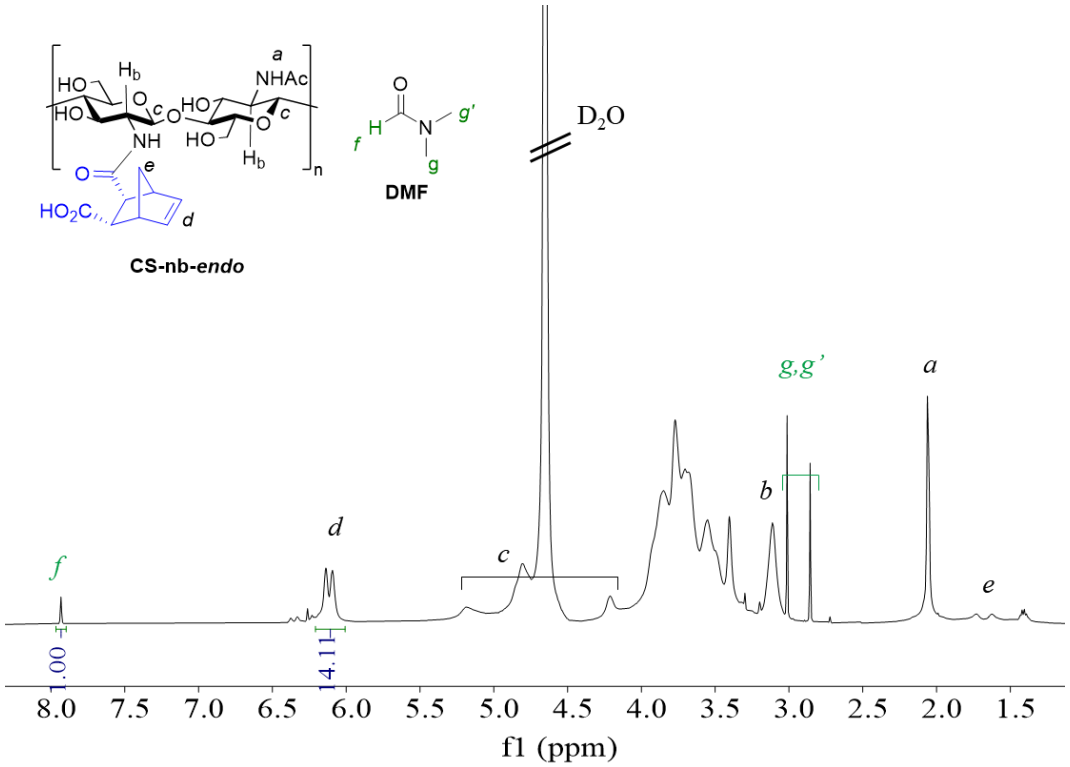

Figure 7-2. ^{1}H NMR of CS-nb-endo with 1 mM DMF. The degree of functionalisation (DF) was calculated using the integrals corresponding to the protons d and f using Equation (3-4).

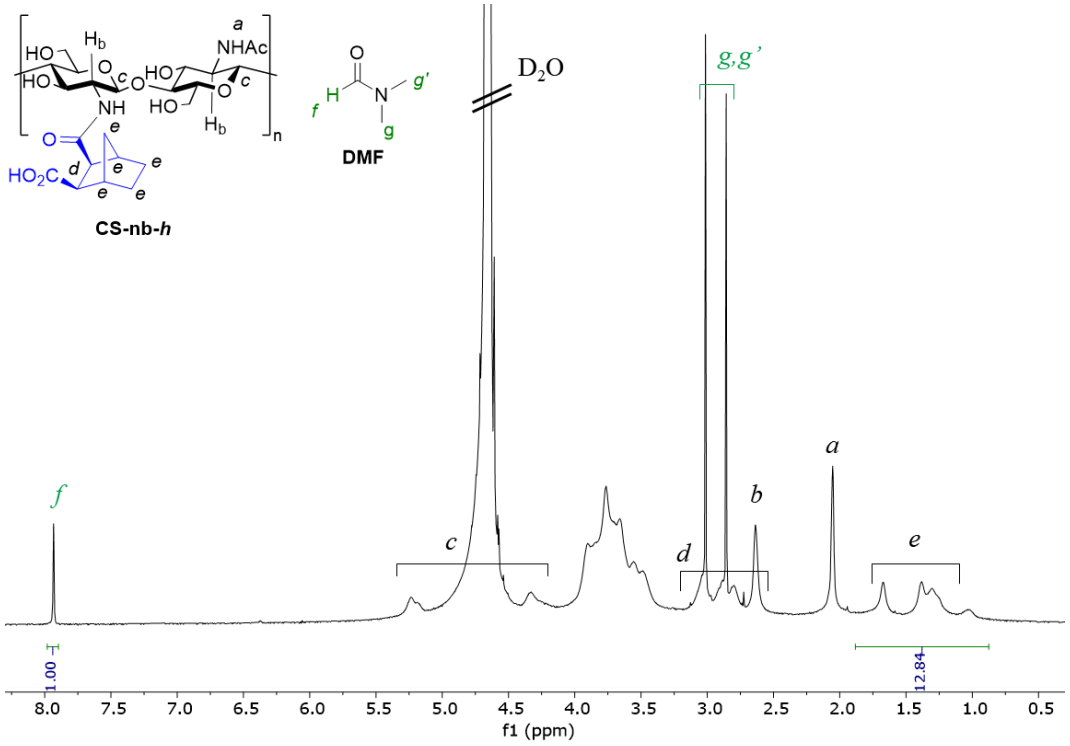

Figure 7-3. [1]H NMR of CS-nb-h with 1 mM DMF. The degree of functionalisation (DF) was calculated using the integrals corresponding to the protons d and f using Equation (7-1).

The degree of functionalisation (DF in µmol of nb/mg of CS-nb) was calculated by ^{1}H NMR by dissolving 2-to-5 mg of CS-nb in D_2O containing 1 mM of anhydrous DMF as:

$$DF = I_f . C_{DMF} . V_{DMF} \frac{\frac{I_e}{6}}{m_{CS-nb}} \quad (7\text{-}1)$$

where:

I_f is the integral of the amide H of DMF (labelled *f* in Figure 3-5, 1H)

C_{DMF} is the concentration of DMF used to prepare the NMR sample (1 mM)

V_{DMF} is the volume of DMF used to prepare the NMR sample (550 µL)

I_e is the integral of the alkane peaks of norbornene ring, excluding those part of the succinic ring (labelled *e* in Figure 3-5, 6H)

m_{CS-nb} is the mass of CD-nb dissolved to make up the NMR sample

An example of calculation is given Figure 3-5 with m_{CS-nb} = 2.10 mg, which gives:

$$DF = 1 \times 1 \times 0.550 \frac{\frac{12.84}{6}}{2.10} = 0.56 \text{ µmol nb/mg CS-nb}$$

7.2.3 Hydrogel synthesis

CS-nb -*endo* and -*exo* was dissolved in 0.1 % IRG in DI water or in 2 % AcOH to a final concentration of 0.5, 1, 2 or 4 w:v% and cured with UV-A or B for a desired period of time, varied between 5 sec and 1 hr. *Endo*- and *exo*- CS hybrid hydrogels were obtained by the same method mixing CS-nb-*endo* and -*exo* by varying the volume fraction of CS-nb-*endo* ϕ_{endo}. Gelation was assessed by the inverted vial method.

7.2.4 Mechanistic studies – polymer scale

Mechanistic investigations were performed with CS-nb-*exo* as the alkene peaks of nb appeared as a singlet. CS-nb-*exo* (75 mg, 37.5 µmol nb) was dissolved in 2 % AcOH (2 mL) with IRG (7.5 mg, 33 µmol) and the resulting mixture was cured with UV-B for 3.5 hrs. At this concentration no hydrogel was formed, and the reaction mixture gradually turned from a transparent solution to a light-yellow solution, confirming the cleavage of IRG. The resulting solution was dialysed in 5% NaCl for 1.5 days and DI water for 3 days to remove unconjugated IRG and lyophilized. The polymer structure was studied by ^{1}H NMR.

To assess the role of AcOH, the kinetics of degradation of IRG (4 mg, 18 µmol) under UV was monitored by ^{1}H NMR in D_2O or 2% AcOD-d_4 (550 µL) by exposing the NMR tube to UV for 1, 2 or 10 min.

7.2.5 Mechanistic studies – model system

In situ ^{1}H NMR was used to study the impact of pH and the reactivity of nb-*endo*/*exo*. Briefly, nb-*endo* or -*exo* (5.2 mg, 31.8 µmol) was combined with IRG (10.7 mg, 48 µmol) in DMSO-d_6 (550 µL). To study the impact of pH, AcOD-d_4 (11 µL, final concentration 2%) was added to some solutions as a control. The resulting mixtures were transferred in an NMR tube and exposed to UV-B. At defined time points (0, 1 and 2 hrs) the curing was stopped and ^{1}H NMR of the mixture was performed. The reaction was monitored by comparing the integration of the alkene peaks with the singlet of IRG at 1.38 ppm which shifts to 2.08 ppm upon irradiation. The total integration of these two singlets was maintained to 6 for quantification.

7.2.6 Swelling ratio

Hydrogel samples were prepared as described in Chapter 4 (section 4.3.4) and the swelling ratio *SR* and the water content W_c were given in Equation (4-1) and (4-2) respectively.

7.2.7 SEM images

Hydrogel samples were prepared and analysed as described in Chapter 4 (section 4.3.6).

7.2.8 Small angle neutron scattering (SANS)

SANS was carried out on the Sans2d small-angle diffractometer at the ISIS Pulsed Neutron Source (STFC Rutherford Appleton Laboratory, Didcot, U.K.) and analysed with SasView as described in Chapter 4 (section 4.3.9).

7.2.9 Rheology

Rheological measurements on the obtained hydrogels were performed as described in Chapter 4 (section 4.3.7), where low-viscosity samples were measured using a conical plate CP4/40.

7.2.10 Cell culture and toxicity assays

Human dermal fibroblasts (HDF) were cultured as described in Chapter 4 (section 4.3.11). Metabolic activity was measured as detailed in Chapter 4 (section 4.3.12).

7.3 Results and discussion

7.3.1 Synthesis of CS-nb derivatives

CS-nb derivatives were readily obtained by ring-opening CA of the desired stereochemistry with CS amine groups as described in section 3.4.1. The functionalisation was proved by ^{1}H NMR with the incorporation of alkene protons at 6.5 ppm, while the covalent interaction was confirmed by DOSY. The degree of functionalisation, assessed using DMF as an internal standard, was of 0.68, 0.59, 0.55 and 0.53 μmol nb/mg CS for CS-nb, CS-nb-*endo* CS-nb-*exo* and CS-nb-*h*, respectively.

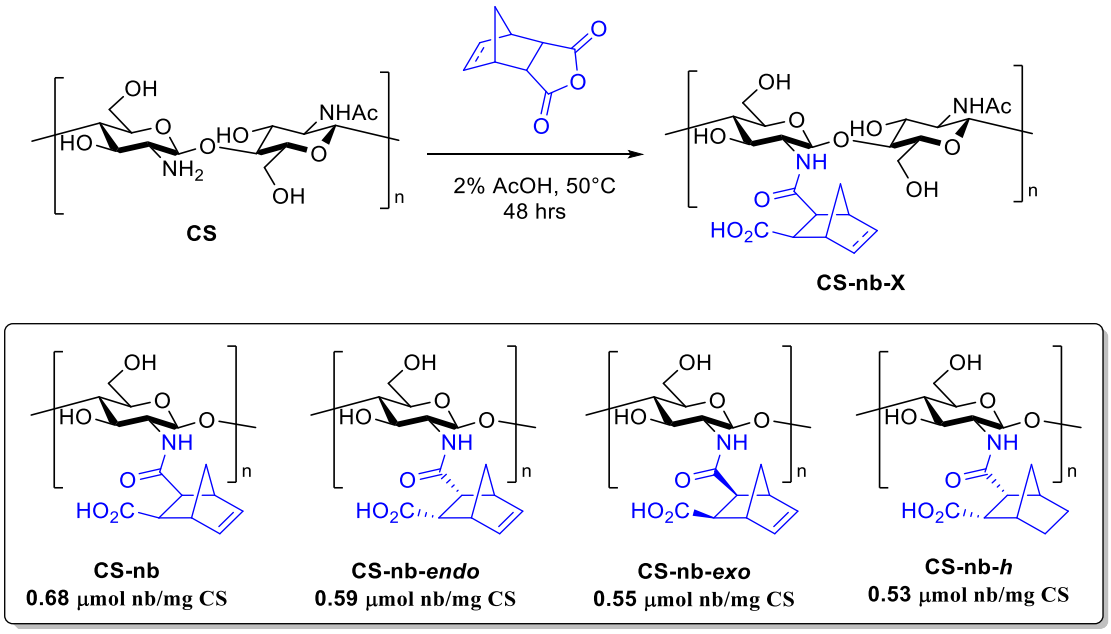

Scheme 7-1: Synthetic route to CS-nb derivatives and corresponding chemical structure of CS-nb, CS-nb-endo, *CS-nb*-exo *and CS-nb*-h.

7.3.2 Hydrogel synthesis

As shown previously, CS-nb readily generated hydrogels upon reaction with various thiolated crosslinkers in the presence of Irgacure 2959 (IRG) as a photoinitiator under both acidic and neutral conditions, which was also observed for CS-nb-*endo* and -*exo*. Surprisingly, when a premixed solution of either CS-nb-*endo* or -*exo* (2 w:v%) was exposed to UV without crosslinker, a transparent hydrogel was formed within seconds, as determined by the inverted vial method. Further gelation control experiments were conducted (Table 7-1 entries a-f) which showed that acidic conditions, UV light and IRG were all required for hydrogel formation. Interestingly, when CS-nb from a non-purified form of *endo* or *exo* CA (as the one used in Chapter 3) was used, no hydrogel was formed. ^{1}H NMR of the reagents did not show obvious differences between CA and CA-*endo*, and dialysis of CS-nb against EDTA to remove possible interfering metal traces did not lead to hydrogel formation neither. To the best of our knowledge, this is the first report of a hydrogel formed from a nb-functionalised polymer in the absence of any thiols or ruthenium catalysts.

Table 7-1: Summary of reaction conditions needed for hydrogel formation.

Entry	Reaction conditions				CS derivative (2 w:v%)				
	Crosslinker	UV	IRG	2% AcOH	-	**nb**	**nb-endo**	**nb-exo**	**nb-h**
(a)	✓	✓	✓	✓	Liq.	Gel	Gel	Gel	Liq.
(b)	✓	✓	-	✓	Liq.	Liq.	Liq.	Liq.	Liq.
(c)	-	✓	✓	✓	Liq.	Liq.	Gel	Gel	Liq.
(d)	-	-	✓	✓	Liq.	Liq.	Liq.	Liq.	Liq.
(e)	-	✓	-	✓	Liq.	Liq.	Liq.	Liq.	Liq.
(f)	-	✓	✓	-	Liq.	Liq.	Liq.	Liq.	Liq.

Hydrogel formation was further studied regarding CS and IRG concentrations (Figure 7-4) under acidic conditions. A minimum concentration of 2 w:v% for both CS-nb-*endo* and -*exo* was required, while CS-nb hydrogels were never observed even at higher polymer concentrations. IRG concentration was also critical for CS-nb-*endo* hydrogel formation, with hydrogels obtained for IRG > 1 mg/mL (Figure 7-4A). On the other hand, CS-nb-*exo* showed a very minor dependence on IRG concentrations, with even very low concentrations (0.1 mg/mL) being enough to generate soft self-standing hydrogels (Figure 7-4B). In addition,

mixtures of CS-nb-*endo* and -*exo* also resulted in hydrogel formation when IRG concentration was maintained to 1 mg/mL.

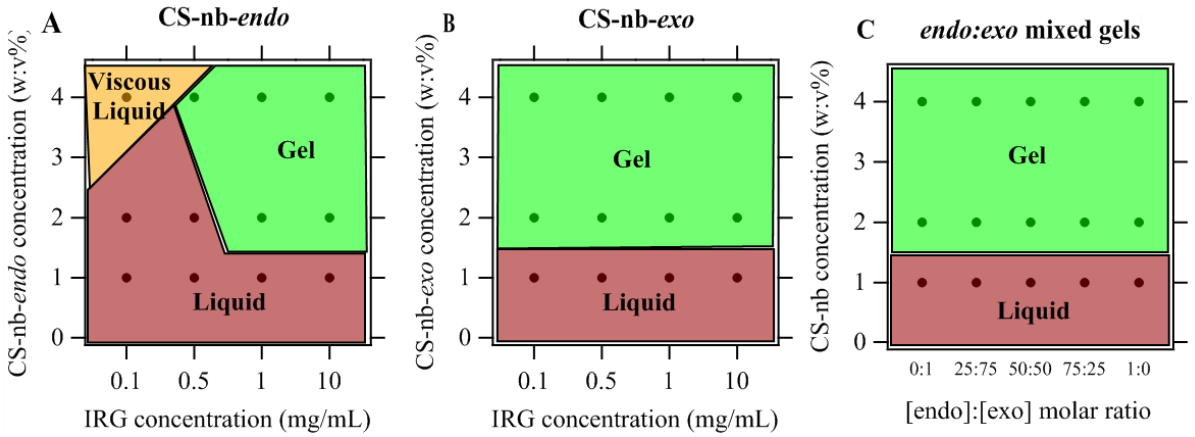

*Figure 7-4: Gel phase diagram of CS-nb-*endo ***(A)***, -exo ***(B)*** *and of mixtures* ***(C)****.*

7.3.3 Mechanism of hydrogel formation

Based on the observations summarised in Table 7-1, the following gelation mechanism was proposed (Scheme 7-2). The exposure of IRG to UV results in the formation of two radicals, which in a classical thiol-ene photoclick reaction would normally generate thiol radicals which then combines with nb moieties (Scheme 7-2A). In the absence of thiols, however, the IRG radicals have no choice but reacting directly with nb, resulting in the formation of local hydrophobic grafts on CS backbone, which self-assemble to minimise their interaction with water, resulting in hydrogel formation (Scheme 7-2B). Nb reactive radical formation is known to occur either at the alkene bond or at the bridged position.[300] To assess the reactivity centre, a hydrogenated form of CS-nb, CS-nb-*h* (Scheme 7-1) was synthesized; as no hydrogel was formed under the curing conditions (Table 7-1), the reactivity was attributed to the alkene functionality. AcOH was hypothesized to act as a catalyst either in IRG dissociation or in the radical combination step.

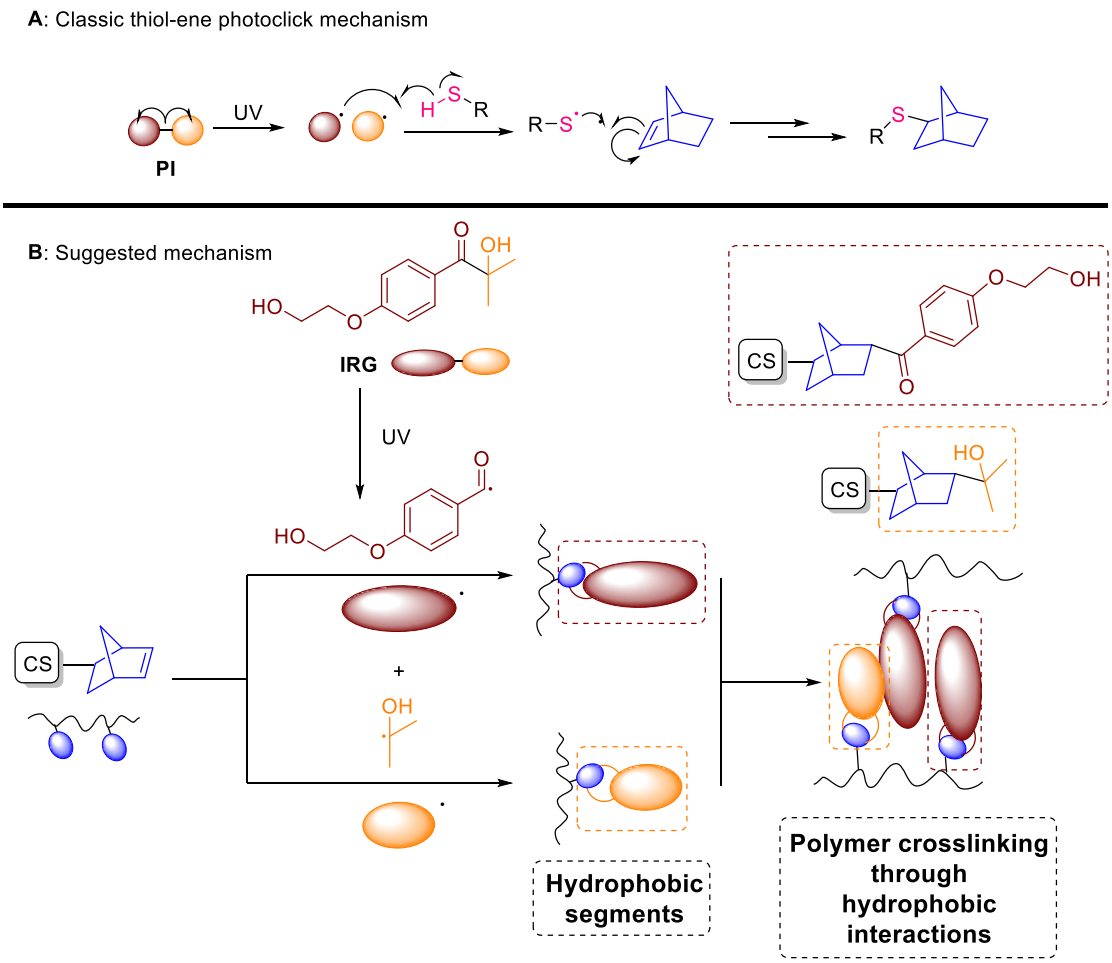

Scheme 7-2. Proposed reaction mechanism for hydrogel formation. The photoinitiator IRG is cleaved under UV exposure to give two radicals which react with the nb side-chains of CS, resulting in the incorporation of hydrophobic fragments leading polymer self-assembly driven by hydrophobic interactions and to hydrogel formation.

To confirm the covalent binding of IRG, CS-nb-*exo* was reacted with IRG *in situ* below its critical gelation concentration. The integration of the alkene peak and of the singlet of IRG were compared, and a decrease in the alkene intensity was observed after 2 hrs, when IRG was totally dissociated (Figure 7-5). The incorporation of IRG aromatic signals were further proved after extensive dialysis of the polymer, while DOSY NMR supports the presence of a single molecule in solution (Figure 7-6).

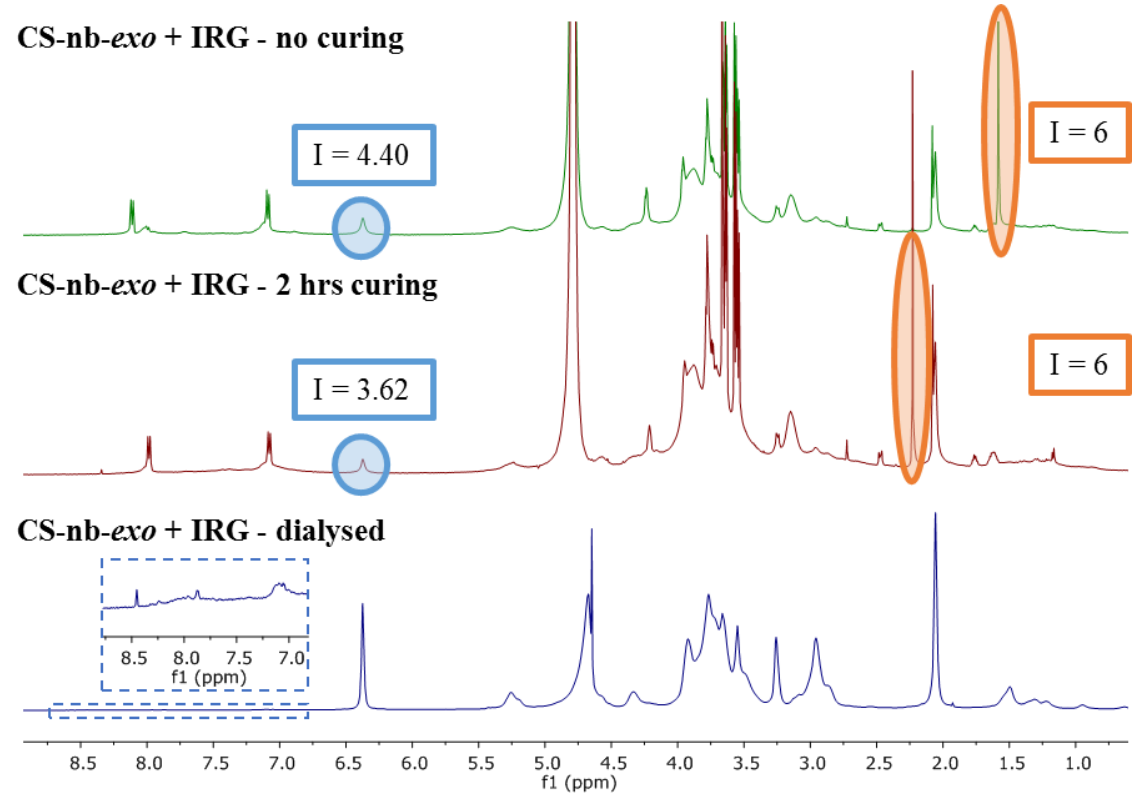

Figure 7-5: In situ *^{1}H NMR studies of CS-nb-*exo *coupling with IRG before (top, green) and after (middle, red)UV exposure, and presat of the purified resulting polymer (bottom, blue).*

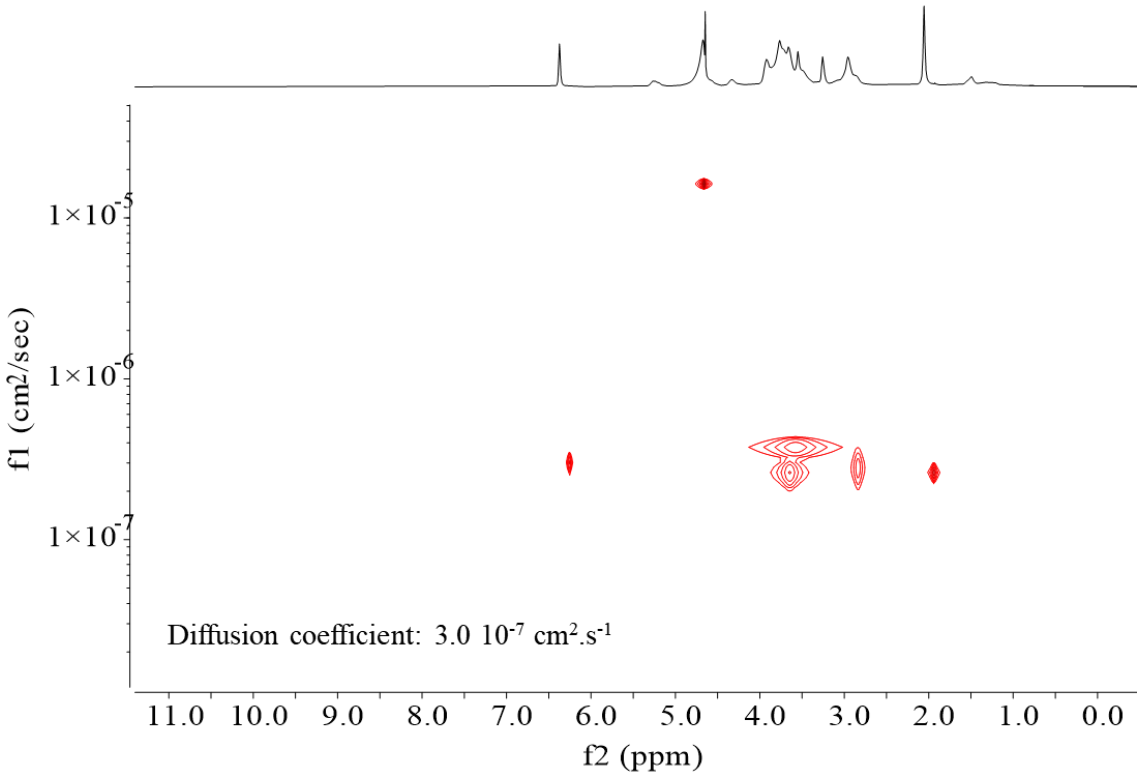

Figure 7-6. DOSY NMR of CS-nb-exo reacted with IRG under UV-B for 2 hrs after dialysis.

Mechanistic studies were further performed with CA-*endo* and -*exo* using *in situ* ^{1}H NMR by monitoring the degradation of IRG, resulting from a shift of the singlet from 1.38 to 2.08 ppm (Figure 7-7). After 1 hr, almost all IRG had reacted with CA-*exo*, which is consistent with a reduction in the intensity of the alkene peaks from 1.18 to 0.24. In the same period of time, the alkene signal of CA-*endo* was only slightly reduced (from 1.09 to 0.78). Increasing the curing time to 2 hrs had almost no impact on CA-*exo*, while it allowed for a significant improvement of the conversion of CA-*endo*. This matches well the better gelation properties of CS-nb-*exo* compared to the -*endo* which could be attributed to a more efficient crosslinking of the nb moieties.

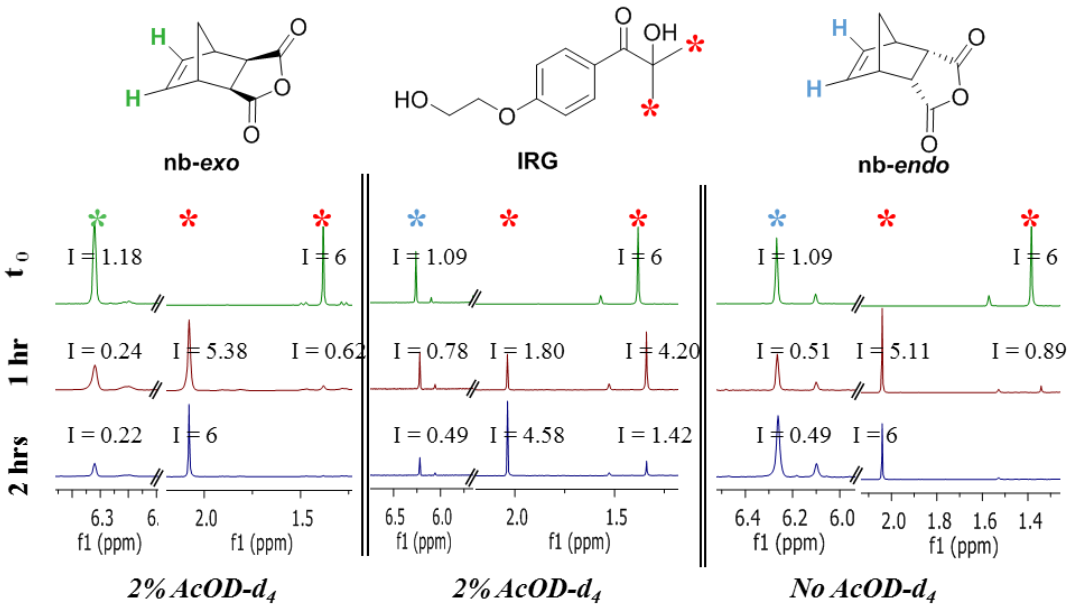

Figure 7-7. ^{1}H NMR kinetics studies of the reactivity of exo- *(left) and* endo-*nb with* (middle) or without (right) *AcOD-d4.*

To investigate the role of AcOH in hydrogel formation, IRG degradation was studied by ^{1}H NMR with and without addition of AcOD-*d4* but did not show any difference in the reaction kinetics (data not shown). On the other hand, the curing of CA-*endo* after 1 hr was slower in the presence of AcOD-*d4*, while the reactivity of the alkene was not modified. We suggest that AcOH allows for the protonation of CS-nb carboxylic acid group, leading to a more hydrophobic network and thus favouring hydrogel formation, which is not allowed by carboxylate ions present in water.

7.3.4 Hydrogel characterisation

The physico-chemical properties of these new hydrogels were measured and systematically compared to the covalent hydrogels described in Chapter 4.

7.3.4.1 Swelling ratios

The swelling ratio (SR) of CS-nb-*endo* and -*exo* hydrogels were studied for different pH and ionic strength. Both non-covalent hydrogels presented greater SR in water than the covalent networks (respectively 4 times and twice as much, Table 7-2). The use of a crosslinker covalently reticulating polymer chains reduces chain mobility, thus leading to reduced swellings. All gels presented a pH-dependent swelling, with SR ~ 100-200 at pH = 3, and a drastic 2-to-4-fold shrinkage under basic conditions or in the presence of salts. As discussed in section 4.4.2.1 in Chapter 4 the pH-responsivity is directly related to the amine protonation while the collapse results from screening of the polyelectrolyte electrostatic repulsions. [268]

Table 7-2. Swelling ratio of 2% CS-nb non-covalent or covalent (crosslinked with HS-PEG$_2$-SH) hydrogels.

	DI water	**pH = 3**	**pH = 11**	**PBS**
CS-nb-*endo*	205 ± 20	193 ± 10	11.3 ± 1.8	17.1 ± 1
CS-nb-*exo*	94.5 ± 43	113 ± 1.8	20.6 ± 1	12.6 ± 1
Covalent	54.3 ± 5	64.4 ± 11	15.3 ± 5.7	12.9 ± 0.4

7.3.4.2 Rheology

Rheology measurements confirmed the formation of elastic hydrogels ($G'>G''$) on the whole range of strain γ investigated and showed frequency-dependency, with the -*exo* hydrogel being stronger than the -*endo* materials (G' ~ 65 and 40 Pa respectively, Figure 7-8, to be compared to G' ~ 500 - 1500 Pa for the covalent hydrogels obtained at the same polymer concentration). The rheological properties of the hydrogels could be tuned from G' ~ 6 to G' ~ 800 Pa by changing CS or IRG concentration, in addition to CS-nb chirality. All -*endo* materials were weaker than the -*exo* derivatives of matching compositions. As the reactivity of CA-*exo* towards IRG is greater than CA-*endo* more efficient crosslinks should be formed, explaining the improved mechanical properties of CS-nb-*exo* hydrogels. An increase in IRG concentration improved the hydrogel mechanical properties up to an optimum concentration where it decreased again, possibly due to competitive IRG radical degradation or recombination leading to side products, thus reducing the effective formation of crosslink points. Mixing both -*endo* and -*exo* CS resulted in hybrid hydrogels of reduced stiffness, especially for high volume fraction of CS-nb-*endo* ϕ_{endo}, consistent with the lower reactivity of CA-*endo* leading to fewer crosslink points (Figure 7-9).

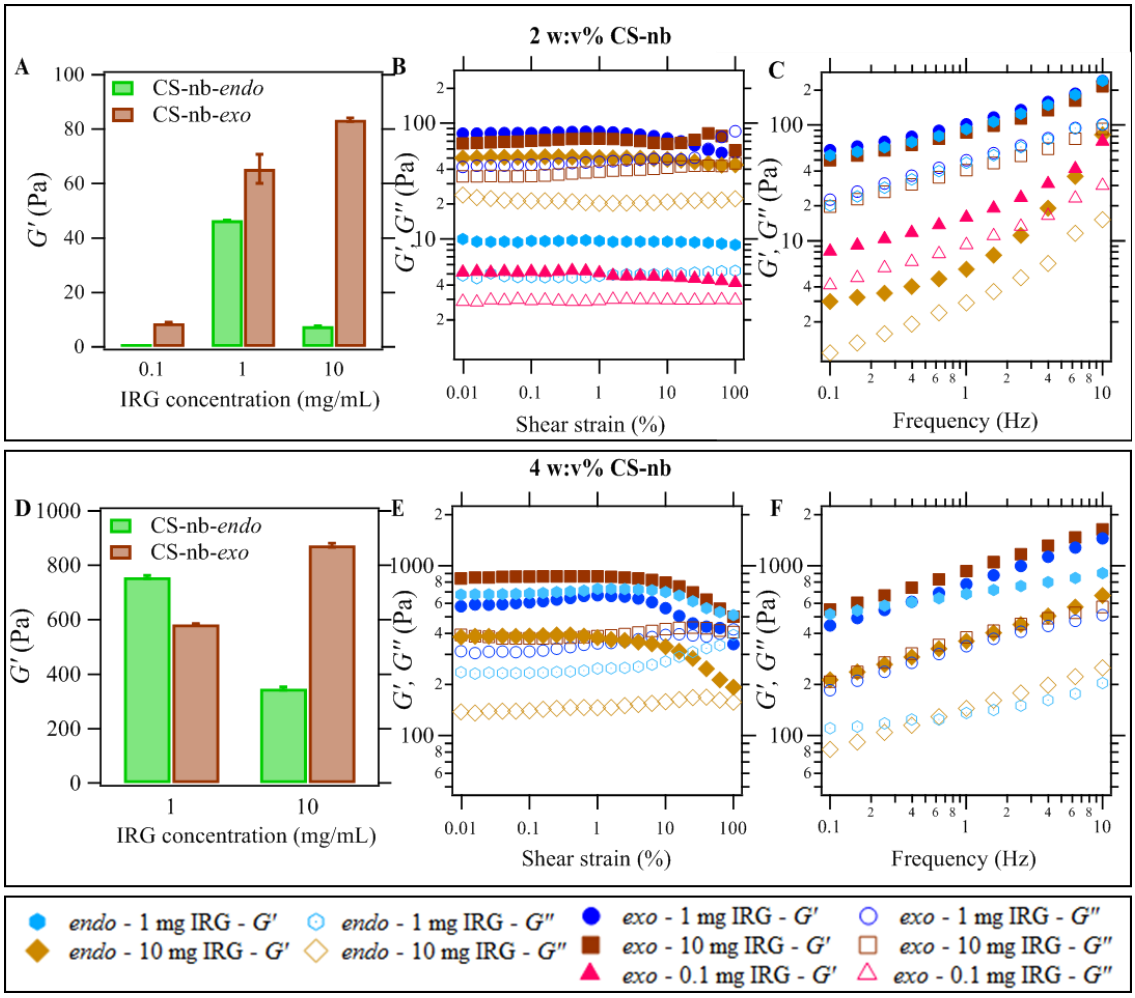

*Figure 7-8. Rheology measurements of CS-nb-*endo *and* -exo *hydrogels: averaged G' obtained by amplitude sweep of the* -endo *and the* -exo *hydrogels with varying IRG concentrations at CS concentration of 2 (A) or 4% (D). Amplitude sweep (B, E) and frequency sweep (C, F) of CS hydrogels respectively at 2 or 4 w:v% with varying IRG concentrations.*

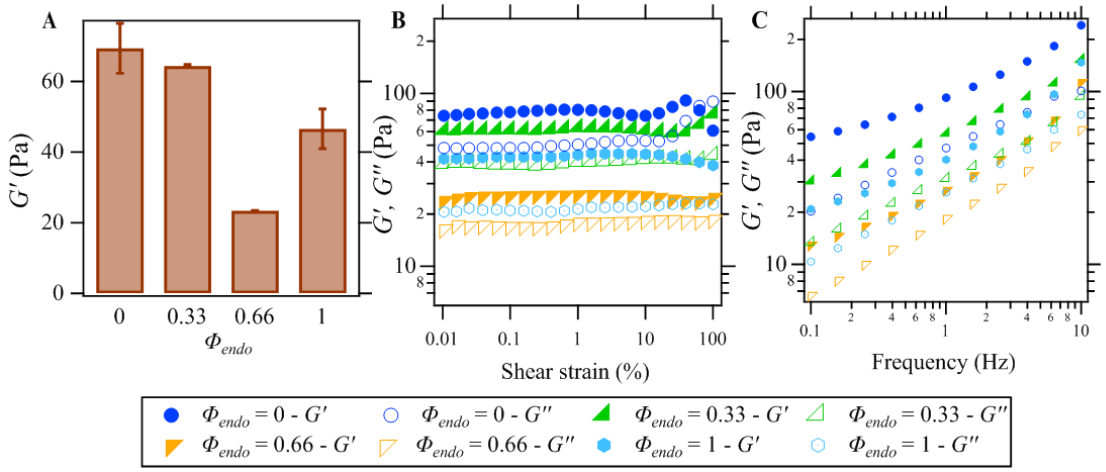

Figure 7-9. Mixed -endo/-exo *hydrogel rheological properties when varying the ratio of CS-nb-endo ϕ_{endo} from 0 to 1: A) average G', B) amplitude sweep and C) frequency sweep.*

7.3.4.3 Microstructure: SEM

The internal structure and the porosity of the hydrogels were further investigated with SEM (Figure 7-10). All hydrogels present a typical polydisperse honeycomb-like structure with pore dimensions ranging between ~ 30 and ~ 150 µm on average. Interestingly, both CS-nb-*endo* and -*exo* presented internal nanopores with diameters estimated by SEM of respectively ~ 60 and ~ 40 nm. This feature, not observed on the covalent hydrogel, supports the formation of hydrophobic cavities after combination of IRG with nb. These nanopores should allow for higher encapsulation efficiency compare to simple entrapment and could be beneficial in drug delivery applications.

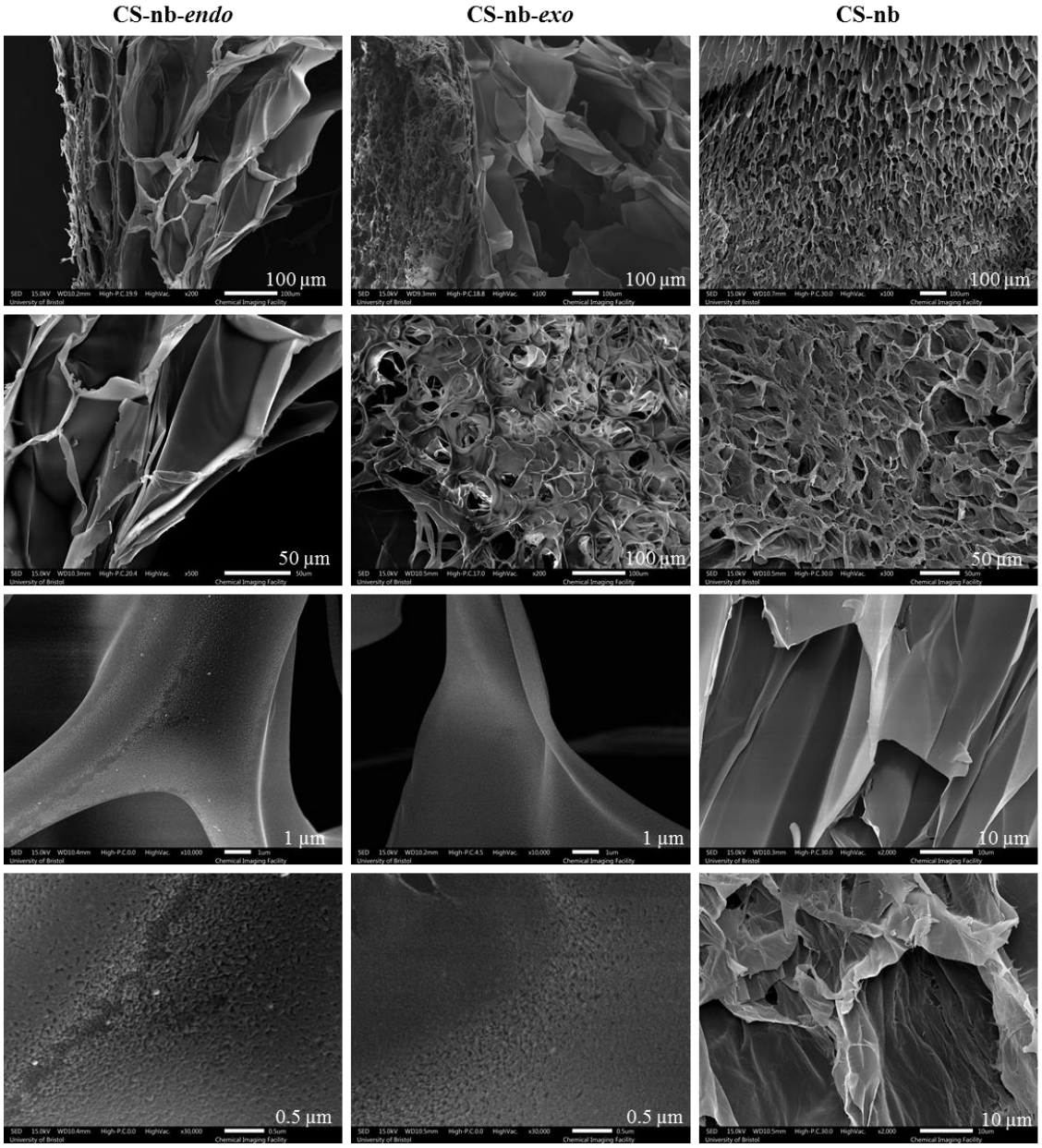

Figure 7-10. SEM images of non-covalent and covalent (HS-PEG$_2$-SH crosslinked) hydrogels.

Table 7-3. Dimensional characteristics of the hydrogel networks obtained from rheology and SEM.

	Rheology			SEM	
	G' **(Pa)**	ρ_s **(mol/m³)**	ξ_a **(nm)**	$d_{nanopores}$ **(nm)**	$d_{micropores}$ **(µm)**
Covalent	1268 ± 337	0.510	18.4	-	32 ± 12
-*endo*	47 ± 6	0.021	53.5	66 ± 10	56 ± 25
-*exo*	65 ± 5	0.032	46.2	53 ± 17	52 ± 17

7.3.4.4 SANS

The structural differences observed by SEM between the covalent and the non-covalent hydrogels were further confirmed by SANS (Figure 7-11). As for the covalent hydrogels the scattering intensity increased in the low *q* region confirming the formation of large assemblies (see section 4.4.2.4 in Chapter 4). However, while the increase was following a power-law for chemically crosslinked CS-nb hydrogels, CS-nb-*endo* and -*exo* presented a small shoulder characteristic of a second length scale in the material. The scattering intensity was modelled using Eq. 6-1:

$$I(q) = \frac{I_L(0)}{\left(1 + \frac{D+1}{3}\xi^2 q^2\right)^{D/2}} + I_s(0)e^{-\frac{R_g^2 q^2}{3}} + background \qquad (6\text{-}1)$$

where the scattering from the polymer chains is represented by a modified Lorentzian function accounting for the mass fractal *D* due to hydrogen bonding present in the network, while the exponential describes the aggregate size. While this model gave a poor description of the covalent networks, it fitted very well the SANS profile of the physical hydrogels, confirming the presence of objects of a second dimension ~ 55 nm for CS-nb-*exo* and ~ 100 nm for CS-nb-*endo* which could correspond to the nanopore dimensions in their swollen state. The mass fractal was *D* was ~ 2.6 at the origin but quickly increased to ~ 3 over a larger *q* range, consistent with the presence of small, swollen objects. The mesh size of the resulting networks were ~ 27 nm which is comparable to their covalent counterpart as opposed to ξ ~ 50 nm suggested by rheology. These differences likely arise from the heterogeneous structure of CS-nb hydrogels.

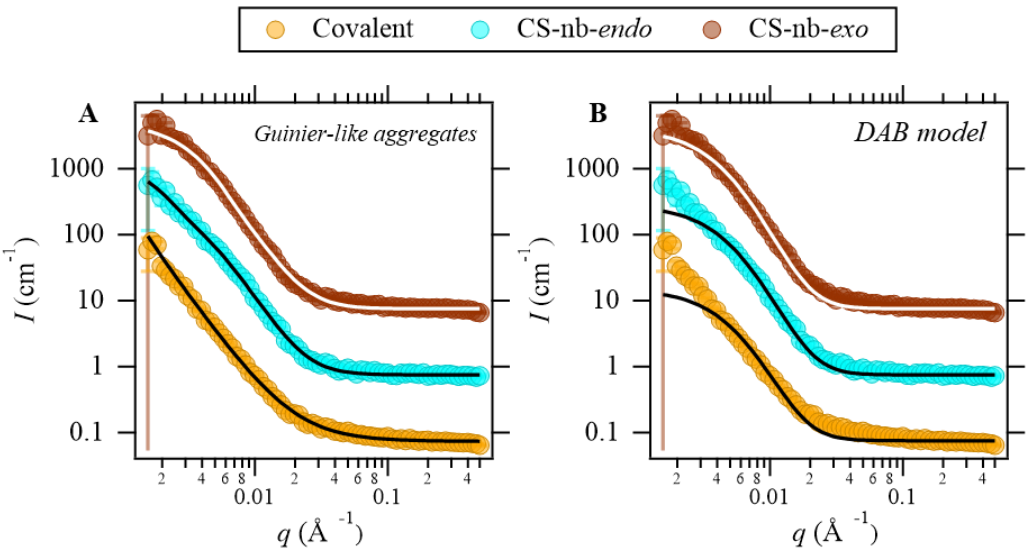

*Figure 7-11. SANS data of CS-nb-*endo *and* exo *hydrogels compared to a covalent network. Fitted data are shown as a plain line. Data have been offset (10x) on the y-axis for clarity*

As the presence of the nanopores suggested sharp boundaries between swollen polymer chains and hydrophobic cavities the correlation length L_c of the hydrogels were obtained with the DAB model (Eq. 2-30):

$$I(q) = A\frac{L_c^3}{\left(1+q^2L_c^2\right)^2} + background \qquad (2\text{-}30)$$

L_c has been assimilated to the hydrogel mesh size ξ in some cases such as physical polysaccharide hydrogels.[238] This very simple model contains a single parameter. Although the fits were not as good as with the introduction of an exponential term the values of L_c and ξ compare well with each other, comforting the presence of two very different elements in the system – and further supporting these nanopores.

Table 7-4. Comparative dimensional characteristics of the hydrogel networks obtained from rheology, SEM and SANS.

	Rheology	**SEM**	**SANS**				
	ξ_a (nm)	**d_p (nm)**	**R_g (nm)**	**D**	**ξ (nm)**	**χ^2**	**DAB - L_c (nm)**
Covalent	18.4	-	-	2.43	18.4 ± 3.2	12.5	-
-endo	53.5	66 ± 10	120 ± 22	3.18	26.2 ± 2.3	1.95	20.4 ± 0.3
-exo	46.2	53 ± 17	52 ± 1.4	3.05	27.1 ± 0.8	6.10	23.4 ± 0.3

7.3.5 Hydrogel cytotoxicity

Hydrogel cytotoxicity was assessed against HDF cell lines as described in section 4.3.12 in Chapter 4. Both gels presented significant toxicity as assessed by metabolic activity measurements, with cell viability ~ 30 % and ~ 10 % after 1 and 3 days, respectively (Figure 7-12A). Microscopy imaging suggests poor spreading and attachment of the cells on the hydrogels, as shown by their spherical morphology once seeded on the hydrogel (Figure 7-12B-E), as observed for the covalent hydrogels (see section 4.4.5 in Chapter 4). This is consistent with previous studies reporting HDF culture on hydrogels of significantly higher mechanical properties ($G' > 0.5$ kPa) or bioactive scaffolds presenting RGD peptides, gelatin or collagen sequences, as discussed previously for the covalent hydrogels (section 4.4.5 in Chapter 4). On the other hand, this range of elastic modulus match well brain tissues, where elastic moduli ranging between 100 and 500 Pa have proven beneficial to the differentiation of NSC into primary neuron cells,[301] while the composition of the ECM of these soft tissues is very different from that of skin.[270]

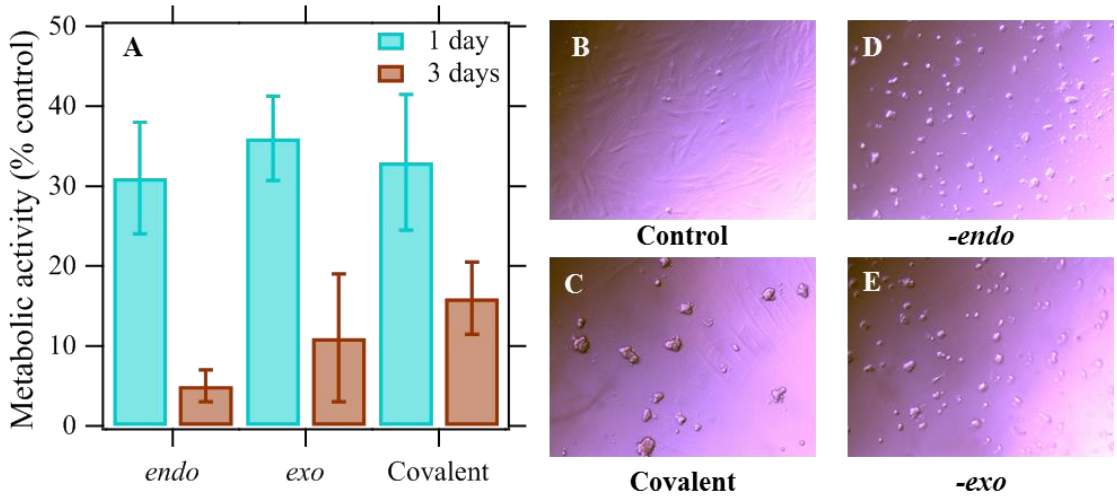

Figure 7-12. Hydrogel toxicity to HDF cells: metabolic activity (A) and cell morphology of cells seeded on plate (B), on covalent (C), -endo *(D) or* -exo *(E) hydrogels.*

Mauri *et al.* studied the effect of RGD functionalization of synthetic hydrogels for neural cell culture. Neither the mechanical properties nor the cell growth and survival were drastically different after RGD conjugation, with only a slight improvement in cell survival.[302] Several CS-based hydrogels have been reported for neural tissue engineering, owing to its ability to induce neuronal differentiation - in addition to its porosity and biocompatibility.[303] Several studies have focused on physical hydrogels, including polysaccharide blends with alginate or agarose as well as thermo-sensitive systems based on CS/glycerophosphate.[165, 270, 303] Valmikinathan *et al.* reported a photo-induced hydrogel from a methacrylated CS which

supported neural stem cell culture without any peptide functionalisation while favouring cell differentiation into astrocytes and tubulin positive neurons.[304] The similar rheological properties (G' ~ 100 Pa) and the highly porous structure (pore sizes ~ 5 – 20 µm) are comparable to the described *endo*- and *exo*- CS hydrogels. These similarities suggest these new non-covalent hydrogels could be good candidates for neural tissue growth, while the extremely fast gelation kinetics would allow for *in-situ* gelation. In addition, the covalent recombination of the photoinititor reduces possible toxicity, while the mild and fast gelation mechanism should allow for the encapsulation of growth factors into the gels, whose release kinetics is expected to be highly impacted by the presence of the internal nanopores.

7.4 Conclusions

A new series of non-covalent hydrogels was obtained by covalent recombination of IRG radicals with the alkene group of norbornene followed by hydrophobicity-driven supramolecular assembly. To the best of our knowledge, it had not been reported before. These materials, which were not intended for SB treatment, presented a nano-porous structure with internal pore diameters of ~ 50 – 100 nm and whose rheological properties could be tuned between ~ 20 and ~ 800 Pa depending on the polymer concentration but also on the stereochemistry of the carbic anhydride used. An increase in the *endo* composition of CS-nb led to weaker hydrogels of bigger nanopore diameters compared to their *exo*- counterpart. These nano-pores could be very attractive for biomedical applications as it should allow for more efficient encapsulation and the release kinetics should be further investigated. In addition, their very fast gelation kinetics make them usable for *in-situ* applications. Although these hydrogels could not support HDF cell growth, their tuneable softness and porous architecture should be suitable for neuron cell growth, hypothesis which will be investigated in the future.

8 Conclusions and future work

8.1 General outcomes

Spina Bifida (SB) is the most common birth defect with 0.2 % occurrence worldwide. It is due to foetus' spine failing to close during the first month of pregnancy, exposing the nerves to the amniotic fluid and resulting in their consequent non-reversible damage, leading to life long. cognitive and psychometric disturbances. To date no treatment exists, and the only hope lies in invasive *in utero* surgery. However, a pioneering "double hit hypothesis" conjectures that covering the opening in the spinal cord at the early stage of pregnancy would prevent or alleviate such damage.

The aim of this project was to develop a simple, biocompatible material which could be injected into the uterus to cover the defect and either seal and protect it from the amniotic fluid or to act as a scaffold to favour a tissue engineering approach by taking advantage of the unique *in utero* environment and the small size of the defect. The material of choice for this application is a hydrogel, which is an excellent mimics of tissue environment and favours cell growth. The properties required for these two approaches are drastically different, and so two types of hydrogels were developed: a "classic" polymer crosslinking providing a favourable environment for cell growth, and a crosslinked microgels-based approach, expected to result in stronger, less swellable materials and prevent nerves damage from the amniotic fluid.

Chitosan (CS), a naturally occurring cationic polysaccharide, was selected as hydrogel precursor for its similarity with glycosaminoglycans of cell membrane favouring cell growth and wound healing, as justified in Chapter 3. A major limit of CS processability – its poor water-solubility – was efficiently addressed by the concomitant introduction of a carboxylate group along with a photo-activable norbornene (nb) moiety. The resulting derivative, CS-nb, was very stable in solution but spontaneously reacted with thiols in the presence of UV light and of an adequately chosen photo-initiator. This is a major improvement over classic photoreactive methacrylated CS derivatives which are prone to uncontrolled acrylate polymerisation. In addition, the procedure involved a single step and required cheap starting materials, while the functionalisation of the final polymer was readily controlled by playing on the reaction conditions. If nb-functionalised (bio)materials are very common, this is the first report of a nb CS-functionalised derivative.

The high reactivity of CS-nb towards thiols allowed for the rapid and efficient synthesis of a variety of hydrogels whose physical properties were investigated by a combination of

SEM, rheology, swelling ratio measurements and SANS in Chapter 4. All methods were consistent with the formation of highly swellable, pH- and ionic strength-responsive hydrogels presenting wide pores and tuneable mechanical properties, which could be matched with a variety of tissues. In addition, the resulting hydrogels were skin-adhesive, could be sterilised and generated *in situ* in biologically relevant fluids. As these hydrogels were intended as scaffolds to support cell growth and tissue regeneration, their cytotoxicity was assessed against two cell lines – placenta cells and dermo fibroblasts, a frequent model for wound healing studies. Although CS is structurally similar to the ECM it did not allow for efficient cell adhesion and consequent growth. This, however, was readily solved by incorporating modest amounts of collagen, another FDA-approved protein used in wound management. These new materials presented very different mechanical properties and internal structure. All these results design CS-nb as a promising precursor for applications for *in utero* management of SB-complicated pregnancies.

The second approach based on microgels as hydrogel precursors required first to establish a robust synthesis method. A reverse nano-emulsion template, selected for its simplicity and its versatility, was optimised in terms of surfactant and oil composition and extensively studied by DLS and SANS to confirm its robustness towards microgel synthesis conditions, as presented in Chapter 5. The final microgel dimension could be varied by tuning the polymer concentration in solution, the crosslinking density or the nature of the crosslinker used and presented a pH- and salt-responsive behaviour, as shown by DLS and SANS, as seen in Chapter 6. In addition, the resulting microgel building blocks were non-toxic to dermo fibroblasts over a period of 5 days. Finally, under-reticulated microgels could be further functionalised using remaining nb moieties, validating the ability to use them as crosslinkable precursors. These results design CS-nb as a versatile precursor for both hydrogels and microgels synthesis for biomedical applications, although more biologically-relevant tests should be performed on the microgels and the resulting DX systems.

Finally, the functionalisation of CS with pure *endo* or *exo* carbic anhydride, initially intended to study the impact of CS crosslinking chirality on the hydrogel properties, resulted in the unexpected formation of hydrogels even in the absence of crosslinkers. This unprecedented gelation was attributed to hydrophobic interactions resulting from the photoinitiator recombination with nb, as presented in Chapter 7. The resulting materials were much weaker than their covalent analogues, but they also presented internal nano-pores evidenced by SEM and SANS which could be beneficial for controlled release or depollution

applications if they are accessible to small molecules. Although these materials were too weak to support cell growth – and could therefore not be used in the management of SB – literature precedent on materials of similar properties suggest they could be good substrate for neural cells. In addition, this side-reaction could be of interest to the scientific community as Irgacure 2959 and the thiol-ene reaction are widely used in material chemistry and in the biomedical research area.

8.2 Future directions

8.2.1 Polymer design

As discussed in Chapter 3, CS-nb presents improved solubility in water, resulting in a mildly acidic solution; CS-nb could not be dissolved in PBS nor in cell media. When the hydrogel is generated *in situ* this acidity will be immediately neutralised by surrounding physiological buffers and should not lead to severe toxicity. This mildly acidic conditions, however, limits topical applications or hydrogel loading with fragile biomolecules such as proteins or growth factors and cells, both of which are very promising in the management of various wounds.

To overcome solubility issues, CS-nb was further reacted with succinic anhydride to introduce new carboxylate functions. The resulting material was also skin adhesive, sterilisable and gelled *in situ*; in addition, it could be dissolved over a wide range of pHs including PBS and cell media. The resulting hydrogels remain to be fully characterised to see how this functionalisation expends on its biological applications.

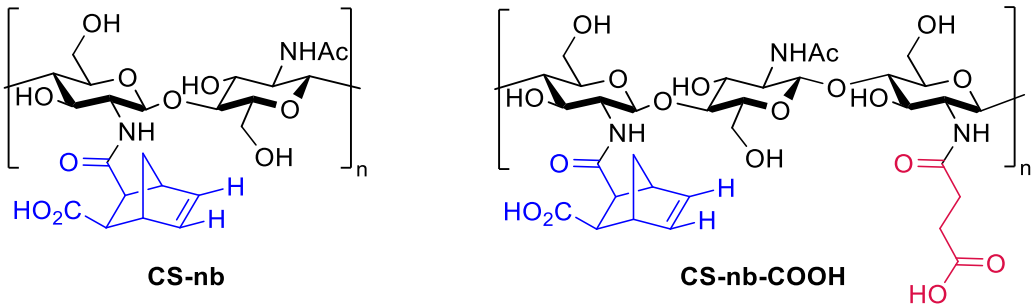

Figure 8-1. Chemical structure of CS-nb and the new water-soluble CS-nb-COOH.

8.2.2 Hydrogel structure and applications

The hydrogels described in Chapter 4 presented a heterogeneous structure and tuneable mechanical properties, as well as excellent biocompatibility towards RGD-mediated cell adhesion motives upon addition of collagen. Although several works highlight the need for hydrogel heterogeneity to favour cell growth, control over the final structure remains very desirable. A way to achieve more uniform structure could be to use multi-arm thiolated

crosslinkers, which are considered as model hydrogel precursors. Chirality also plays a crucial role in mechanical properties[299] and replacing *endo*-carbic anhydride for the less common *exo* derivative could be an elegant way to favour polymer self-organisation, as suggested with the unexpected formation of CS-nb non-covalent hydrogels. It is unrealistic – and undesired - to achieve hydrogel uniformity starting from a polydisperse and randomly functionalised precursor such as CS-nb but a more defined structure can be expected.

The introduction of UV-light *in vivo* may result in local toxicity due to the propagation of free radicals. The very fast gelation kinetics is expected to limit this toxicity; a safer alternative would be to use visible light initiators such as Eosin Y[71] or riboflavin;[72] camphorquinone, currently used in the curing of dental resins[305] is a poor initiator in the thiol-ene reaction.[306]

Although a key step for hydrogel biocompatibility, the introduction of collagen required acidic conditions for solubility, complicating biomedical applications. A less invasive way to reach a similar goal would be to functionalise CS-nb with RGD peptides bearing thiol or tetrazine moieties. Another strategy could result in the introduction of bioactive thiolated crosslinkers such as hyaluronic acid, collagen – thiolated and appropriately functionalised for water-solubility - or gelatin – a denaturated form of collagen. In addition, thiolated peptide-cleavable crosslinkers could be incorporated to allow for cells to modulate their matrix according to their needs.

Owing to the high reactivity of the thiol-ene chemistry, controlled amount of norbornene could be left unreacted to further functionalise the hydrogel surface in a later stage. Tetrazines could also be used for this step, and their excellent biorthogonality and high kinetics should even allow to perform this step *in situ*. Adequate hydrogel surface functionalisation with peptides, proteins or antibodies would allow to favour biological mechanisms such as healing, cell recruitment or adhesion.

8.2.3 Microgel applications

CS-nb microgels, as presented in Chapter 6, were non-toxic and could be readily functionalised using pendant norbornene moieties. This opens two areas of possible applications: surface functionalisation for selective properties such as cell targeting or coating, and the use of microgels as macromers for hydrogel formation.

In the first case microgels would be intended as advanced nano-materials by taking advantage of both the functionalisable surface - allowing for specific cell targeting for instance as presented in section 8.2.2 - and of the swollen core, in which small molecules such as drugs

or therapeutic peptides could be encapsulated prior to their release. The pH-responsivity of the microgels, whose swelling increases under acidic conditions, could be an efficient way to deliver drugs to tumours or to infected areas, where the environment is slightly acidic. Very preliminary results were obtained with Doxorubicin, a common anti-cancer drug presenting significant side-effects,[307] confirming its successful encapsulation; its release, however, remains to be demonstrated. The need for a photoinitiator and UV light in the crosslinking step may damage the incorporated molecule, which must be verified prior to encapsulation.

Microgels can be used as hydrogel building blocks either as crosslinkers by reaction with polymers or by crosslinking with complementary functionalised microgels. Both approaches have been shown to result in more homogeneous networks and therefore present improved mechanical properties. Very preliminary results showed that CS-nb microgels bearing remaining norbornene groups reacted with thiolated crosslinkers to give hydrogels for a minimum concentration of 2 w:v%. The resulting materials have not yet been analysed. In addition, complementary functionalised thiolated CS microgels have not yet been synthesized; a difficulty will be to limit disulphide bond formation at the high concentration needed for microgel crosslinking, which will require the use of reducing agents such as TCEP or of acidic conditions, both of which may impact on the final toxicity of the material. An alternative could be to synthesise the microgels through thiol-ene and then to introduce a protected thiol or a masked tetrazine using unreacted norbornene through thiol-ene photoclick. Protected thiols include thiocarbamates and aromatic nitro derivatives, most of which have a light-responsive deprotection mechanism.[308] Dihydrotetrazines have also been used to this end as they are not reactive towards alkenes but can be selectively activated by photo-catalysed oxidation, which has been reported for the synthesis of cell-encapsulated hydrogels with red light.[87] This would require more synthetic efforts, especially as tetrazine synthesis is challenging.

8.2.4 Non-covalent hydrogels

The main interest of these non-covalent hydrogels results from their unique internal structure and these interesting nanopores, which could be taken advantage of either as adsorbents or for slow release applications if the pore dimension allows. These materials are extremely soft which is desirable for neural cell growth, a hypothesis which will be tested in the future. Finally, preliminary results showed that dilute solutions of CS-nb-*endo* and -e*xo* resulted in the formation of nanoparticles under gelation conditions driven by the formation of hydrophobic regions. These materials of diameters ~ 400 nm without optimisation of the reaction conditions.

This hydrophobic effect could be of interest for the encapsulation and release of hydrophobic drugs, a complementary type to those that could be encapsulated onto CS-nb microgels.

8.2.5 Spina Bifida treatment

In the context of SB several requirements must be met which differ for the two intended approaches – tissue engineering and wound healing or sealant. As introduced in Chapter 1 tissue-engineering approaches require the design of a scaffold in which cells can grow to regenerate the skin around the defect, which calls for biodegradable hydrogels possibly loaded with stem cells or growth factors. On the other hand, a sealant will not repair the defect and must therefore not be degraded whilst providing efficient adhesion, creating an efficient barrier to the amniotic fluid and being elastically deformed as the foetus will grow over pregnancy. In addition, both materials must be sterilisable, non-toxic and adhere to skin (Table 8-1).

Table 8-1. Summary of the key properties required, reached and remaining to be studied for in utero *management of SB with the two approaches taken.*

Property	Tissue Engineering Approach	Sealant approach
Immediate skin adhesion	Yes	Unknown
Low adhesion post-injection	Yes (no more radicals)	Unknown
Injectability and in situ formation	Yes	Unknown
Sterilisation	Yes	Unknown
Non-toxicity	Yes (requires collagen)	Yes (microgels)
Nerve repair	Unknown	Unknown
Defect repair	Unknown	Unknown
Biodegradable	Unknown	Unknown
Elasticity	Yes (rheology) – n/a	Unknown
AF-impermeable	No - n/a	Unknown

The hydrogels presented in Chapter 4 meet some of these criteria as sterilisable, skin-adhesives – although the adhesions should be quantified – and non-toxic elastic materials. Although hydrogel swelling contributes to its skin mimetic it can also affect its adhesion or compress tissues as it expands. [309] CS-nb swelling was limited in the presence of salts and should therefore be a reasonably good adhesive. The next steps should include to test the wound healing ability and the lysozyme-mediated biodegradability of the network. CS degradability

is generally slow as it is a non-human polysaccharide, but the incorporation of collagen or cell-sacrificial crosslinkers should allow to alter this. Finally, *in utero* environment is very rich in stem cells and how CS-nb hydrogels can accommodate them and direct their differentiation to a specific cell type remains to be elucidated. Mechanical properties (rheology and stiffness)[310, 311] and fractal dimensions[271] are three known factors to impact on cell differentiation which can be modulated for these hydrogels. If these tests are satisfying, the materials could be further tested in Leuven (Belgium) on SB animal models in the next years.

The sealant strategy relies on microgels as crosslinkers to reduce the network mesh size, its swelling and thus create a barrier from the amniotic fluid. This work focused on the synthesis and characterisation of these building blocks and achieved two milestones along this path: the proof of concept of their functionalisation – and hence the feasibility of the crosslinking – and the demonstration of the non—toxicity of the microgels. Although encouraging, these facts are in no way enough. Skin adhesion is expected due to the formation of free radicals which will react with the skin; similarly crosslinked microgel degradation kinetics is expected to be slow, as demonstrated for crosslinked hyaluronic acid microgels.[132] All other steps remain to be studied, starting with the characterisation of the resulting hydrogels and their bio-compatibility.

9 References

1. Mitchell, L. E.; Adzick, N. S.; Melchionne, J.; Pasquariello, P. S.; Sutton, L. N.; Whitehead, A. S., Spina bifida. *The Lancet 364* (9448), 1885-1895.

2. Song, R. B.; Glass, E. N.; Kent, M., Spina Bifida, Meningomyelocele, and Meningocele. *Vet Clin North Am Small Anim Pract* **2016,** *46* (2), 327-45.

3. Atta, C. A. M.; Fiest, K. M.; Frolkis, A. D.; Jette, N.; Pringsheim, T.; St Germaine-Smith, C.; Rajapakse, T.; Kaplan, G. G.; Metcalfe, A., Global Birth Prevalence of Spina Bifida by Folic Acid Fortification Status: A Systematic Review and Meta-Analysis. *American Journal of Public Health* **2015,** *106* (1), e24-e34.

4. What is spina bifida? Spina bifida treatment at Midwest Fetal Care Center. https://www.childrensmn.org/services/care-specialties-departments/fetal-medicine/conditions-and-services/spina-bifida/.

5. Coleman, B. G.; Langer, J. E.; Horii, S. C., The Diagnostic Features of Spina Bifida: The Role of Ultrasound. *Fetal Diagnosis and Therapy* **2015,** *37* (3), 179-196.

6. Apkon, S. D.; Grady, R.; Hart, S.; Lee, A.; McNalley, T.; Niswander, L.; Petersen, J.; Remley, S.; Rotenstein, D.; Shurtleff, H.; Warner, M.; Walker Jr, W. O., Advances in the Care of Children with Spina Bifida. *Advances in Pediatrics* **2014,** *61* (1), 33-74.

7. Hutchins, G. M.; Meuli, M.; Meuli-Simmen, C.; Jordan, M. A.; Heffez, D. S.; Blakemore, K. J., Acquired Spinal Cord Injury in Human Fetuses with Myelomeningocele. *Pediatric Pathology & Laboratory Medicine* **1996,** *16* (5), 701-712.

8. Dorothea Stiefel; Andrew J. Copp; Martin Meuli, Fetal spina bifida in a mouse model: loss of neural function in utero. *Journal of Neurosurgery: Pediatrics* **2007,** *106* (3), 213-221.

9. Encinas, J. L.; Garcia-Cabezas, M. A.; Barkovich, J.; Fontecha, C. G.; Peiro, J. L.; Soto, G. M.; Borrell, V.; Reillo, I.; Lopez-Santamaria, M.; Tovar, J. A.; Farmer, D. L., Maldevelopment of the cerebral cortex in the surgically induced model of myelomeningocele: implications for fetal neurosurgery. *J Pediatr Surg* **2011,** *46* (4), 713-22.

10. Meuli, M.; Meuli-Simmen, C.; Yingling, C. D.; Hutchins, G. M.; Timmel, G. B.; Harrison, M. R.; Adzick, N. S., In utero repair of experimental myelomeningocele saves neurological function at birth. *Journal of Pediatric Surgery* **1996,** *31* (3), 397-402.

11. Kohl, T.; Hering, R.; Heep, A.; Schaller, C.; Meyer, B.; Greive, C.; Bizjak, G.; Buller, T.; van de Vondel, P.; Gogarten, W.; Bartmann, P.; Knöpfle, G.; Gembruch, U.,

Percutaneous Fetoscopic Patch Coverage of Spina Bifida Aperta in the Human – Early Clinical Experience and Potential. *Fetal Diagnosis and Therapy* **2006,** *21* (2), 185-193.

12. Adzick , N. S.; Thom , E. A.; Spong , C. Y.; Brock , J. W. I.; Burrows , P. K.; Johnson , M. P.; Howell , L. J.; Farrell , J. A.; Dabrowiak , M. E.; Sutton , L. N.; Gupta , N.; Tulipan , N. B.; D'Alton , M. E.; Farmer , D. L., A Randomized Trial of Prenatal versus Postnatal Repair of Myelomeningocele. *New England Journal of Medicine* **2011,** *364* (11), 993-1004.

13. Watanabe, M.; Kim, A. G.; Flake, A. W., Tissue Engineering Strategies for Fetal Myelomeningocele Repair in Animal Models. *Fetal Diagnosis and Therapy* **2015,** *37* (3), 197-205.

14. Perrini, M.; Barrett, D.; Ochsenbein-Koelble, N.; Zimmermann, R.; Messersmith, P.; Ehrbar, M., A comparative investigation of mussel-mimetic sealants for fetal membrane repair. *Journal of the Mechanical Behavior of Biomedical Materials* **2016,** *58*, 57-64.

15. Bilic, G.; Brubaker, C.; Messersmith, P. B.; Mallik, A. S.; Quinn, T. M.; Haller, C.; Done, E.; Gucciardo, L.; Zeisberger, S. M.; Zimmermann, R.; Deprest, J.; Zisch, A. H., Injectable candidate sealants for fetal membrane repair: bonding and toxicity in vitro. *American Journal of Obstetrics and Gynecology* **2010,** *202* (1), 85.e1-85.e9.

16. Peiro, J. L.; Fontecha, C. G.; Ruano, R.; Esteves, M.; Fonseca, C.; Marotta, M.; Haeri, S.; Belfort, M. A., Single-Access Fetal Endoscopy (SAFE) for myelomeningocele in sheep model I: amniotic carbon dioxide gas approach. *Surgical Endoscopy* **2013,** *27* (10), 3835-3840.

17. Fontecha, C. G.; Peiro, J. L.; Sevilla, J. J.; Aguirre, M.; Soldado, F.; Fresno, L.; Fonseca, C.; Chacaltana, A.; Martinez, V., Fetoscopic coverage of experimental myelomeningocele in sheep using a patch with surgical sealant. *European Journal of Obstetrics & Gynecology and Reproductive Biology* **2011,** *156* (2), 171-176.

18. Balkenende, D. W. R.; Winkler, S. M.; Messersmith, P. B., Marine-inspired polymers in medical adhesion. *European Polymer Journal* **2019,** *116*, 134-143.

19. Haller, C. M.; Buerzle, W.; Kivelio, A.; Perrini, M.; Brubaker, C. E.; Gubeli, R. J.; Mallik, A. S.; Weber, W.; Messersmith, P. B.; Mazza, E.; Ochsenbein-Koelble, N.; Zimmermann, R.; Ehrbar, M., Mussel-mimetic tissue adhesive for fetal membrane repair: An ex vivo evaluation. *Acta Biomaterialia* **2012,** *8* (12), 4365-4370.

20. Kivelio, A.; Dekoninck, P.; Perrini, M.; Brubaker, C. E.; Messersmith, P. B.; Mazza, E.; Deprest, J.; Zimmermann, R.; Ehrbar, M.; Ochsenbein-Koelble, N., Mussel mimetic tissue

adhesive for fetal membrane repair: initial in vivo investigation in rabbits. *European Journal of Obstetrics & Gynecology and Reproductive Biology* **2013,** *171* (2), 240-245.

21. Fauza, D. O.; Jennings, R. W.; Teng, Y. D.; Snyder, E. Y., Neural stem cell delivery to the spinal cord in an ovine model of fetal surgery for spina bifida. *Surgery* **2008,** *144* (3), 367-373.

22. Vig, K.; Chaudhari, A.; Tripathi, S.; Dixit, S.; Sahu, R.; Pillai, S.; Dennis, V.; Singh, S., Advances in Skin Regeneration Using Tissue Engineering. *International Journal of Molecular Sciences* **2017,** *18* (4), 789.

23. Bedian, L.; Villalba-Rodríguez, A. M.; Hernández-Vargas, G.; Parra-Saldivar, R.; Iqbal, H. M. N., Bio-based materials with novel characteristics for tissue engineering applications – A review. *International Journal of Biological Macromolecules* **2017,** *98*, 837-846.

24. Chuah, Y. J.; Peck, Y.; Lau, J. E. J.; Hee, H. T.; Wang, D.-A., Hydrogel based cartilaginous tissue regeneration: recent insights and technologies. *Biomaterials Science* **2017,** *5* (4), 613-631.

25. Rai, V.; Dilisio, M. F.; Dietz, N. E.; Agrawal, D. K., Recent Strategies in Cartilage Repair: A Systemic Review of the Scaffold Development and Tissue Engineering. *Journal of Biomedical Materials Research Part A* **2017**, n/a-n/a.

26. Zhou, X.; Zhang, N.; Mankoci, S.; Sahai, N., Silicates in orthopedics and bone tissue engineering materials. *Journal of Biomedical Materials Research Part A* **2017**, n/a-n/a.

27. Mogoşanu, G. D.; Grumezescu, A. M., Natural and synthetic polymers for wounds and burns dressing. *International Journal of Pharmaceutics* **2014,** *463* (2), 127-136.

28. Habibovic, P.; Barralet, J. E., Bioinorganics and biomaterials: Bone repair. *Acta Biomaterialia* **2011,** *7* (8), 3013-3026.

29. Baino, F.; Novajra, G.; Vitale-Brovarone, C., Bioceramics and Scaffolds: A Winning Combination for Tissue Engineering. *Frontiers in Bioengineering and Biotechnology* **2015,** *3* (202).

30. Guan, X.; Avci-Adali, M.; Alarçin, E.; Cheng, H.; Kashaf, S. S.; Li, Y.; Chawla, A.; Jang, H. L.; Khademhosseini, A., Development of hydrogels for regenerative engineering. *Biotechnology Journal* **2017**, 1600394-n/a.

31. Chaudhari, A.; Vig, K.; Baganizi, D.; Sahu, R.; Dixit, S.; Dennis, V.; Singh, S.; Pillai, S., Future Prospects for Scaffolding Methods and Biomaterials in Skin Tissue Engineering: A Review. *International Journal of Molecular Sciences* **2016,** *17* (12), 1974.

32. Wong, V. W.; Gurtner, G. C., Tissue engineering for the management of chronic wounds: current concepts and future perspectives. *Experimental Dermatology* **2012,** *21* (10), 729-734.

33. Chua, A. W. C.; Khoo, Y. C.; Tan, B. K.; Tan, K. C.; Foo, C. L.; Chong, S. J., Skin tissue engineering advances in severe burns: review and therapeutic applications. *Burns & Trauma* **2016,** *4* (1), 3.

34. Gu, X.; Ding, F.; Williams, D. F., Neural tissue engineering options for peripheral nerve regeneration. *Biomaterials* **2014,** *35* (24), 6143-6156.

35. Subramanian, A.; Krishnan, U. M.; Sethuraman, S., Development of biomaterial scaffold for nerve tissue engineering: Biomaterial mediated neural regeneration. *Journal of Biomedical Science* **2009,** *16* (1), 108.

36. Bullard, K. M.; Longaker, M. T.; Lorenz, H. P., Fetal Wound Healing: Current Biology. *World Journal of Surgery* **2003,** *27* (1), 54-61.

37. Larson, B. J.; Longaker, M. T.; Lorenz, H. P., Scarless Fetal Wound Healing: A Basic Science Review. *Plastic and reconstructive surgery* **2010,** *126* (4), 1172-1180.

38. Herrera, S. R. F.; Leme, R. J. d. A.; Valente, P. R.; Caldini, É. G.; Saldiva, P. H. N.; Pedreira, D. A. L., Comparison between two surgical techniques for prenatal correction of meningomyelocele in sheep. *Einstein (São Paulo)* **2012,** *10*, 455-461.

39. Saadai, P.; Nout, Y. S.; Encinas, J.; Wang, A.; Downing, T. L.; Beattie, M. S.; Bresnahan, J. C.; Li, S.; Farmer, D. L., Prenatal repair of myelomeningocele with aligned nanofibrous scaffolds—a pilot study in sheep. *Journal of Pediatric Surgery* **2011,** *46* (12), 2279-2283.

40. Saadai, P.; Wang, A.; Nout, Y. S.; Downing, T. L.; Lofberg, K.; Beattie, M. S.; Bresnahan, J. C.; Li, S.; Farmer, D. L., Human induced pluripotent stem cell-derived neural crest stem cells integrate into the injured spinal cord in the fetal lamb model of myelomeningocele. *Journal of Pediatric Surgery* **2013,** *48* (1), 158-163.

41. Amniotic Mesenchymal Stem Cells Enhance Normal Fetal Wound Healing. **2011,** *20* (6), 969-976.

42. Dionigi, B.; Ahmed, A.; Brazzo, J.; Connors, J. P.; Zurakowski, D.; Fauza, D. O., Partial or complete coverage of experimental spina bifida by simple intra-amniotic injection of concentrated amniotic mesenchymal stem cells. *Journal of Pediatric Surgery* **2015,** *50* (1), 69-73.

43. Shieh, H. F.; Tracy, S. A.; Hong, C. R.; Chalphin, A. V.; Ahmed, A.; Rohrer, L.; Zurakowski, D.; Fauza, D. O., Transamniotic stem cell therapy (TRASCET) in a rabbit model of spina bifida. *Journal of Pediatric Surgery* **2019,** *54* (2), 293-296.

44. Long, C.; Lankford, L.; Wang, A., Stem cell-based *in utero* therapies for spina bifida: implications for neural regeneration. **2019,** *14* (2), 260-261.

45. administration, F. FDA Regulation of Human Cells, Tissues, and Cellular and Tissue-Based Products (HCT/P's) Product List. https://www.fda.gov/vaccines-blood-biologics/tissue-tissue-products/fda-regulation-human-cells-tissues-and-cellular-and-tissue-based-products-hctps-product-list (accessed 30/08/2019).

46. McCormack, J. Facts for Spina Bifida Life Expectancy and Unexpected Death. https://www.medichere.com/life-expectancy/spina-bifida-life-expectancy.html.

47. Zhu, J.; Marchant, R. E., Design properties of hydrogel tissue-engineering scaffolds. *Expert Review of Medical Devices* **2011,** *8* (5), 607-626.

48. Guo, J. L.; Kim, Y. S.; Mikos, A. G., Biomacromolecules for Tissue Engineering: Emerging Biomimetic Strategies. *Biomacromolecules* **2019**.

49. Jaipan, P.; Nguyen, A.; Narayan, R. J., Gelatin-based hydrogels for biomedical applications. *MRS Communications* **2017,** *7* (3), 416-426.

50. Hersel, U.; Dahmen, C.; Kessler, H., RGD modified polymers: biomaterials for stimulated cell adhesion and beyond. *Biomaterials* **2003,** *24* (24), 4385-4415.

51. Wichterle, O.; Lim, D., Hydrophilic Gels for Biological Use. *Nature* **1960,** *185* (4706), 117-118.

52. Zhu, J., Bioactive Modification of Poly(ethylene glycol) Hydrogels for Tissue Engineering. *Biomaterials* **2010,** *31* (17), 4639-4656.

53. Guan, X.; Avci-Adali, M.; Alarçin, E.; Cheng, H.; Kashaf, S. S.; Li, Y.; Chawla, A.; Jang, H. L.; Khademhosseini, A., Development of hydrogels for regenerative engineering. **2017,** *12* (5), 1600394.

54. Chocholata, P.; Kulda, V.; Babuska, V., Fabrication of Scaffolds for Bone-Tissue Regeneration. **2019,** *12* (4), 568.

55. Buwalda, S. J.; Boere, K. W. M.; Dijkstra, P. J.; Feijen, J.; Vermonden, T.; Hennink, W. E., Hydrogels in a historical perspective: From simple networks to smart materials. *Journal of Controlled Release* **2014,** *190*, 254-273.

56. Ghobril, C.; Grinstaff, M. W., The chemistry and engineering of polymeric hydrogel adhesives for wound closure: a tutorial. *Chemical Society Reviews* **2015,** *44* (7), 1820-1835.

57. Siegwart, D. J.; Oh, J. K.; Matyjaszewski, K., ATRP in the design of functional materials for biomedical applications. *Progress in Polymer Science* **2012,** *37* (1), 18-37.

58. Ercole, F.; Thissen, H.; Tsang, K.; Evans, R. A.; Forsythe, J. S., Photodegradable Hydrogels Made via RAFT. *Macromolecules* **2012,** *45* (20), 8387-8400.

59. Sakai, T.; Matsunaga, T.; Yamamoto, Y.; Ito, C.; Yoshida, R.; Suzuki, S.; Sasaki, N.; Shibayama, M.; Chung, U.-i., Design and Fabrication of a High-Strength Hydrogel with Ideally Homogeneous Network Structure from Tetrahedron-like Macromonomers. *Macromolecules* **2008,** *41* (14), 5379-5384.

60. Shibayama, M., Exploration of Ideal Polymer Networks. **2017,** *372* (1), 7-13.

61. Saffer, E. M.; Lackey, M. A.; Griffin, D. M.; Kishore, S.; Tew, G. N.; Bhatia, S. R., SANS study of highly resilient poly(ethylene glycol) hydrogels. *Soft Matter* **2014,** *10* (12), 1905-1916.

62. Coviello, T.; Grassi, M.; Rambone, G.; Santucci, E.; Carafa, M.; Murtas, E.; Riccieri, F. M.; Alhaique, F., Novel hydrogel system from scleroglucan: synthesis and characterization. *Journal of Controlled Release* **1999,** *60* (2), 367-378.

63. Dhanasingh, A.; Salber, J.; Moeller, M.; Groll, J., Tailored hyaluronic acid hydrogels through hydrophilic prepolymer cross-linkers. *Soft Matter* **2010,** *6* (3), 618-629.

64. Martínez-Mejía, G.; Vázquez-Torres, N. A.; Castell-Rodríguez, A.; del Río, J. M.; Corea, M.; Jiménez-Juárez, R., Synthesis of new chitosan-glutaraldehyde scaffolds for tissue engineering using Schiff reactions. *Colloids and Surfaces A: Physicochemical and Engineering Aspects* **2019,** *579*, 123658.

65. Khanmohammadi, M.; Dastjerdi, M. B.; Ai, A.; Ahmadi, A.; Godarzi, A.; Rahimi, A.; Ai, J., Horseradish peroxidase-catalyzed hydrogelation for biomedical applications. *Biomaterials Science* **2018,** *6* (6), 1286-1298.

66. Jiang, Y.; Chen, J.; Deng, C.; Suuronen, E. J.; Zhong, Z., Click hydrogels, microgels and nanogels: Emerging platforms for drug delivery and tissue engineering. *Biomaterials* **2014,** *35* (18), 4969-4985.

67. Kolb, H. C.; Finn, M. G.; Sharpless, K. B., Click Chemistry: Diverse Chemical Function from a Few Good Reactions. *Angewandte Chemie International Edition* **2001,** *40* (11), 2004-2021.

68. Binder, W. H.; Sachsenhofer, R., 'Click' Chemistry in Polymer and Materials Science. **2007,** *28* (1), 15-54.

69. Meng, X.; Edgar, K. J., "Click" reactions in polysaccharide modification. *Progress in Polymer Science* **2016,** *53*, 52-85.

70. Lin, C. C.; Ki, C. S.; Shih, H., Thiol-norbornene photo-click hydrogels for tissue engineering applications. *J Appl Polym Sci* **2015,** *132* (8).

71. Shih, H.; Lin, C.-C., Visible-Light-Mediated Thiol-Ene Hydrogelation Using Eosin-Y as the Only Photoinitiator. *Macromolecular Rapid Communications* **2013,** *34* (3), 269-273.

72. Lee, H. J.; Fernandes-Cunha, G. M.; Myung, D., In situ-forming hyaluronic acid hydrogel through visible light-induced thiol-ene reaction. *Reactive and Functional Polymers* **2018,** *131*, 29-35.

73. Wang, Z.; Jin, X.; Dai, R.; Holzman, J. F.; Kim, K., An ultrafast hydrogel photocrosslinking method for direct laser bioprinting. *RSC Advances* **2016,** *6* (25), 21099-21104.

74. Nair, D. P.; Podgórski, M.; Chatani, S.; Gong, T.; Xi, W.; Fenoli, C. R.; Bowman, C. N., The Thiol-Michael Addition Click Reaction: A Powerful and Widely Used Tool in Materials Chemistry. *Chemistry of Materials* **2014,** *26* (1), 724-744.

75. Kharkar, P. M.; Rehmann, M. S.; Skeens, K. M.; Maverakis, E.; Kloxin, A. M., Thiol–ene Click Hydrogels for Therapeutic Delivery. *ACS Biomaterials Science & Engineering* **2016,** *2* (2), 165-179.

76. Wu, D.-C.; Loh, X. J.; Wu, Y.-L.; Lay, C. L.; Liu, Y., 'Living' Controlled in Situ Gelling Systems: Thiol−Disulfide Exchange Method toward Tailor-Made Biodegradable Hydrogels. *Journal of the American Chemical Society* **2010,** *132* (43), 15140-15143.

77. Ravasco, J. M. J. M.; Faustino, H.; Trindade, A.; Gois, P. M. P., Bioconjugation with Maleimides: A Useful Tool for Chemical Biology. **2019,** *25* (1), 43-59.

78. Ossipov, D. A.; Hilborn, J., Poly(vinyl alcohol)-Based Hydrogels Formed by "Click Chemistry". *Macromolecules* **2006,** *39* (5), 1709-1718.

79. Hu, X.; Li, D.; Zhou, F.; Gao, C., Biological hydrogel synthesized from hyaluronic acid, gelatin and chondroitin sulfate by click chemistry. *Acta Biomaterialia* **2011,** *7* (4), 1618-1626.

80. Crescenzi, V.; Cornelio, L.; Di Meo, C.; Nardecchia, S.; Lamanna, R., Novel Hydrogels via Click Chemistry: Synthesis and Potential Biomedical Applications. *Biomacromolecules* **2007,** *8* (6), 1844-1850.

81. DeForest, C. A.; Polizzotti, B. D.; Anseth, K. S., Sequential click reactions for synthesizing and patterning three-dimensional cell microenvironments. *Nature Materials* **2009,** *8*, 659.

82. DeForest, C. A.; Anseth, K. S., Cytocompatible click-based hydrogels with dynamically tunable properties through orthogonal photoconjugation and photocleavage reactions. *Nature Chemistry* **2011,** *3*, 925.

83. García-Astrain, C.; Algar, I.; Gandini, A.; Eceiza, A.; Corcuera, M. Á.; Gabilondo, N., Hydrogel synthesis by aqueous Diels-Alder reaction between furan modified methacrylate and polyetheramine-based bismaleimides. **2015,** *53* (5), 699-708.

84. Yu, F.; Cao, X.; Li, Y.; Zeng, L.; Zhu, J.; Wang, G.; Chen, X., Diels–Alder crosslinked HA/PEG hydrogels with high elasticity and fatigue resistance for cell encapsulation and articular cartilage tissue repair. *Polymer Chemistry* **2014,** *5* (17), 5116-5123.

85. Wei, H.-L.; Yang, Z.; Zheng, L.-M.; Shen, Y.-M., Thermosensitive hydrogels synthesized by fast Diels–Alder reaction in water. *Polymer* **2009,** *50* (13), 2836-2840.

86. Desai, R. M.; Koshy, S. T.; Hilderbrand, S. A.; Mooney, D. J.; Joshi, N. S., Versatile click alginate hydrogels crosslinked via tetrazine-norbornene chemistry. *Biomaterials* **2015,** *50*, 30-7.

87. Truong, V. X.; Tsang, K. M.; Ercole, F.; Forsythe, J. S., Red Light Activation of Tetrazine–Norbornene Conjugation for Bioorthogonal Polymer Cross-Linking across Tissue. *Chemistry of Materials* **2017**.

88. Carthew, J.; Frith, J. E.; Forsythe, J. S.; Truong, V. X., Polyethylene glycol–gelatin hydrogels with tuneable stiffness prepared by horseradish peroxidase-activated tetrazine–norbornene ligation. *Journal of Materials Chemistry B* **2018,** *6* (9), 1394-1401.

89. Alge, D. L.; Azagarsamy, M. A.; Donohue, D. F.; Anseth, K. S., Synthetically Tractable Click Hydrogels for Three-Dimensional Cell Culture Formed Using Tetrazine–Norbornene Chemistry. *Biomacromolecules* **2013,** *14* (4), 949-953.

90. Pupkaite, J.; Rosenquist, J.; Hilborn, J.; Samanta, A., Injectable Shape-Holding Collagen Hydrogel for Cell Encapsulation and Delivery Cross-linked Using Thiol-Michael Addition Click Reaction. *Biomacromolecules* **2019**.

91. McOscar, T. V. C.; Gramlich, W. M. J. C., Hydrogels from norbornene-functionalized carboxymethyl cellulose using a UV-initiated thiol-ene click reaction. **2018,** *25* (11), 6531-6545.

92. Perera, M. M.; Ayres, N., Gelatin based dynamic hydrogels via thiol-norbornene reactions. *Polymer Chemistry* **2017,** *8* (44), 6741-6749.

93. Shih, H.; Lin, C.-C., Cross-Linking and Degradation of Step-Growth Hydrogels Formed by Thiol–Ene Photoclick Chemistry. *Biomacromolecules* **2012,** *13* (7), 2003-2012.

94. Fairbanks, B. D.; Love, D. M.; Bowman, C. N., Efficient Polymer-Polymer Conjugation via Thiol-ene Click Reaction. *Macromolecular Chemistry and Physics* **2017,** *218* (18), 1700073-n/a.

95. Hoyle, C. E.; Lee, T. Y.; Roper, T., Thiol–enes: Chemistry of the past with promise for the future. **2004,** *42* (21), 5301-5338.

96. Munoz, Z.; Shih, H.; Lin, C.-C., Gelatin hydrogels formed by orthogonal thiol-norbornene photochemistry for cell encapsulation. *Biomaterials Science* **2014,** *2* (8), 1063-1072.

97. Ooi, H. W.; Mota, C.; ten Cate, A. T.; Calore, A.; Moroni, L.; Baker, M. B., Thiol–Ene Alginate Hydrogels as Versatile Bioinks for Bioprinting. *Biomacromolecules* **2018,** *19* (8), 3390-3400.

98. Gramlich, W. M.; Kim, I. L.; Burdick, J. A., Synthesis and orthogonal photopatterning of hyaluronic acid hydrogels with thiol-norbornene chemistry. *Biomaterials* **2013,** *34* (38), 9803-11.

99. Sawicki, L. A.; Kloxin, A. M., Design of thiol–ene photoclick hydrogels using facile techniques for cell culture applications. *Biomaterials Science* **2014,** *2* (11), 1612-1626.

100. Deligkaris, K.; Tadele, T. S.; Olthuis, W.; van den Berg, A., Hydrogel-based devices for biomedical applications. *Sensors and Actuators B: Chemical* **2010,** *147* (2), 765-774.

101. Ebara, M.; Kotsuchibashi, Y.; Uto, K.; Aoyagi, T.; Kim, Y.-J.; Narain, R.; Idota, N.; Hoffman, J. M., Smart Hydrogels. In *Smart Biomaterials*, Springer Japan: Tokyo, 2014; pp 9-65.

102. Strandman, S.; Zhu, X. X., Self-Healing Supramolecular Hydrogels Based on Reversible Physical Interactions. *Gels* **2016,** *2* (2), 16.

103. Chatterjee, S.; Hui, P. C.-l.; Kan, C.-w., Thermoresponsive Hydrogels and Their Biomedical Applications: Special Insight into Their Applications in Textile Based Transdermal Therapy. **2018,** *10* (5), 480.

104. Mørch, Ý. A.; Donati, I.; Strand, B. L., Effect of Ca2+, Ba2+, and Sr2+ on Alginate Microbeads. *Biomacromolecules* **2006,** *7* (5), 1471-1480.

105. Narayanan, R. P.; Melman, G.; Letourneau, N. J.; Mendelson, N. L.; Melman, A., Photodegradable Iron(III) Cross-Linked Alginate Gels. *Biomacromolecules* **2012,** *13* (8), 2465-2471.

106. Kaushik, N.; Kaushik, N.; Pardeshi, S.; Sharma, J.; Lee, S.; Choi, E., Biomedical and Clinical Importance of Mussel-Inspired Polymers and Materials. *Marine Drugs* **2015,** *13* (11), 6792.

107. Saunders, B. R.; Laajam, N.; Daly, E.; Teow, S.; Hu, X.; Stepto, R., Microgels: From responsive polymer colloids to biomaterials. *Advances in Colloid and Interface Science* **2009,** *147-148*, 251-262.

108. Plamper, F. A.; Richtering, W., Functional Microgels and Microgel Systems. *Accounts of Chemical Research* **2017,** *50* (2), 131-140.

109. McClements, D. J., Designing biopolymer microgels to encapsulate, protect and deliver bioactive components: Physicochemical aspects. *Advances in Colloid and Interface Science* **2017,** *240*, 31-59.

110. Richtering, W.; Saunders, B. R., Gel architectures and their complexity. *Soft Matter* **2014,** *10* (21), 3695-3702.

111. Gutiérrez, J. M.; González, C.; Maestro, A.; Solè, I.; Pey, C. M.; Nolla, J., Nano-emulsions: New applications and optimization of their preparation. *Current Opinion in Colloid & Interface Science* **2008,** *13* (4), 245-251.

112. Solans, C.; Izquierdo, P.; Nolla, J.; Azemar, N.; Garcia-Celma, M. J., Nano-emulsions. *Current Opinion in Colloid & Interface Science* **2005,** *10* (3–4), 102-110.

113. Riegger, B. R.; Bäurer, B.; Mirzayeva, A.; Tovar, G. E. M.; Bach, M., A systematic approach of chitosan nanoparticle preparation via emulsion crosslinking as potential adsorbent in wastewater treatment. *Carbohydrate Polymers* **2018,** *180* (Supplement C), 46-54.

114. Karthik, P.; Ezhilarasi, P. N.; Anandharamakrishnan, C., Challenges associated in stability of food grade nanoemulsions. *Critical Reviews in Food Science and Nutrition* **2017,** *57* (7), 1435-1450.

115. Griffin, W. C., Classification of surface-active agents by HLB. *Journal of the Society of Cosmetic Chemists* **1949,** *1*, 311-326.

116. ICI Americas, i., *The HLB system : a time-saving guide to emulsifier selection*. ICI Americas, Inc.: 1984.

117. Landfester, K., Polyreactions in Miniemulsions. **2001,** *22* (12), 896-936.

118. Izquierdo, P.; Feng, J.; Esquena, J.; Tadros, T. F.; Dederen, J. C.; Garcia, M. J.; Azemar, N.; Solans, C., The influence of surfactant mixing ratio on nano-emulsion formation by the pit method. *Journal of Colloid and Interface Science* **2005,** *285* (1), 388-394.

119. Gupta, A.; Eral, H. B.; Hatton, T. A.; Doyle, P. S., Nanoemulsions: formation, properties and applications. *Soft Matter* **2016,** *12* (11), 2826-2841.

120. Fu, G.-D.; Jiang, H.; Yao, F.; Xu, L.-Q.; Ling, J.; Kang, E.-T., Preparation of Fluorescent Organometallic Porphyrin Complex Nanogels of Controlled Molecular Structure via Reverse-Emulsion Click Chemistry. **2012,** *33* (18), 1523-1527.

121. Gupta, A.; Badruddoza, A. Z. M.; Doyle, P. S., A General Route for Nanoemulsion Synthesis Using Low-Energy Methods at Constant Temperature. *Langmuir* **2017,** *33* (28), 7118-7123.

122. Heller, D. A.; Levi, Y.; Pelet, J. M.; Doloff, J. C.; Wallas, J.; Pratt, G. W.; Jiang, S.; Sahay, G.; Schroeder, A.; Schroeder, J. E.; Chyan, Y.; Zurenko, C.; Querbes, W.; Manzano, M.; Kohane, D. S.; Langer, R.; Anderson, D. G., Modular 'Click-in-Emulsion' Bone-Targeted Nanogels. *Advanced Materials* **2013,** *25* (10), 1449-1454.

123. Bencherif, S. A.; Washburn, N. R.; Matyjaszewski, K., Synthesis by AGET ATRP of Degradable Nanogel Precursors for In Situ Formation of Nanostructured Hyaluronic Acid Hydrogel. *Biomacromolecules* **2009,** *10* (9), 2499-2507.

124. Fu, J., Strong and tough hydrogels crosslinked by multi-functional polymer colloids. **2018,** *56* (19), 1336-1350.

125. Hu, J.; Hiwatashi, K.; Kurokawa, T.; Liang, S. M.; Wu, Z. L.; Gong, J. P., Microgel-Reinforced Hydrogel Films with High Mechanical Strength and Their Visible Mesoscale Fracture Structure. *Macromolecules* **2011,** *44* (19), 7775-7781.

126. Li, P.; Xu, K.; Tan, Y.; Lu, C.; Li, Y.; Wang, P., A novel fabrication method of temperature-responsive poly(acrylamide) composite hydrogel with high mechanical strength. *Polymer* **2013,** *54* (21), 5830-5838.

127. Zhang, J.-T.; Keller, T. F.; Bhat, R.; Garipcan, B.; Jandt, K. D., A novel two-level microstructured poly(N-isopropylacrylamide) hydrogel for controlled release. *Acta Biomaterialia* **2010,** *6* (10), 3890-3898.

128. Sivakumaran, D.; Maitland, D.; Oszustowicz, T.; Hoare, T., Tuning drug release from smart microgel–hydrogel composites via cross-linking. *Journal of Colloid and Interface Science* **2013,** *392*, 422-430.

129. Newsom, J. P.; Payne, K. A.; Krebs, M. D., Microgels: Modular, tunable constructs for tissue regeneration. *Acta Biomaterialia* **2019,** *88*, 32-41.

130. Karg, M.; Pich, A.; Hellweg, T.; Hoare, T.; Lyon, L. A.; Crassous, J. J.; Suzuki, D.; Gumerov, R. A.; Schneider, S.; Potemkin, I. I.; Richtering, W., Nanogels and Microgels: From Model Colloids to Applications, Recent Developments, and Future Trends. *Langmuir* **2019,** *35* (19), 6231-6255.

131. Douglas, A. M.; Fragkopoulos, A. A.; Gaines, M. K.; Lyon, L. A.; Fernandez-Nieves, A.; Barker, T. H., Dynamic assembly of ultrasoft colloidal networks enables cell invasion within restrictive fibrillar polymers. **2017,** *114* (5), 885-890.

132. Jia, X.; Yeo, Y.; Clifton, R. J.; Jiao, T.; Kohane, D. S.; Kobler, J. B.; Zeitels, S. M.; Langer, R., Hyaluronic Acid-Based Microgels and Microgel Networks for Vocal Fold Regeneration. *Biomacromolecules* **2006,** *7* (12), 3336-3344.

133. Jha, A. K.; Malik, M. S.; Farach-Carson, M. C.; Duncan, R. L.; Jia, X., Hierarchically structured, hyaluronic acid-based hydrogel matrices via the covalent integration of microgels into macroscopic networks. *Soft Matter* **2010,** *6* (20), 5045-5055.

134. Rose, J. C.; Gehlen, D. B.; Haraszti, T.; Köhler, J.; Licht, C. J.; De Laporte, L., Biofunctionalized aligned microgels provide 3D cell guidance to mimic complex tissue matrices. *Biomaterials* **2018,** *163*, 128-141.

135. Z., Hu.; X., Lu.; J., Gao.; C., Wang., Polymer Gel Nanoparticle Networks. *Advanced Materials* **2000,** *12* (16), 1173-1176.

136. Cho, E. C.; Kim, J.-W.; Fernández-Nieves, A.; Weitz, D. A., Highly Responsive Hydrogel Scaffolds Formed by Three-Dimensional Organization of Microgel Nanoparticles. *Nano Letters* **2008,** *8* (1), 168-172.

137. Griffin, D. R.; Weaver, W. M.; Scumpia, P. O.; Di Carlo, D.; Segura, T., Accelerated wound healing by injectable microporous gel scaffolds assembled from annealed building blocks. *Nature Materials* **2015,** *14* (7), 737-744.

138. Zhou, W.; Stukel, J. M.; Cebull, H. L.; Willits, R. K., Tuning the Mechanical Properties of Poly(Ethylene Glycol) Microgel-Based Scaffolds to Increase 3D Schwann Cell Proliferation. **2016,** *16* (4), 535-544.

139. Xin, S.; Wyman, O. M.; Alge, D. L., Assembly of PEG Microgels into Porous Cell-Instructive 3D Scaffolds via Thiol-Ene Click Chemistry. **2018,** *7* (11), 1800160.

140. Liu, R.; Milani, A. H.; Freemont, T. J.; Saunders, B. R., Doubly crosslinked pH-responsive microgels prepared by particle inter-penetration: swelling and mechanical properties. *Soft Matter* **2011,** *7* (10), 4696-4704.

141. Liu, R.; Milani, A. H.; Saunders, J. M.; Freemont, T. J.; Saunders, B. R., Tuning the swelling and mechanical properties of pH-responsive doubly crosslinked microgels using particle composition. *Soft Matter* **2011,** *7* (19), 9297-9306.

142. Thaiboonrod, S.; Milani, A. H.; Saunders, B. R., Doubly crosslinked poly(vinyl amine) microgels: hydrogels of covalently inter-linked cationic microgel particles. *Journal of Materials Chemistry B* **2014,** *2* (1), 110-119.

143. Cui, Z.; Wang, W.; Obeng, M.; Chen, M.; Wu, S.; Kinloch, I.; Saunders, B. R., Using intra-microgel crosslinking to control the mechanical properties of doubly crosslinked microgels. *Soft Matter* **2016,** *12* (33), 6985-6994.

144. Milani, A. H.; Bramhill, J.; Freemont, A. J.; Saunders, B. R., Swelling and mechanical properties of hydrogels composed of binary blends of inter-linked pH-responsive microgel particles. *Soft Matter* **2015,** *11* (13), 2586-2595.

145. Lu, D.; Zhu, M.; Wang, W.; Wu, S.; Saunders, B. R.; Adlam, D. J.; Hoyland, J. A.; Hofzumahaus, C.; Schneider, S.; Landfester, K., Do the properties of gels constructed by interlinking triply-responsive microgels follow from those of the building blocks? *Soft Matter* **2019,** *15* (4), 527-536.

146. Milani, A. H.; Freemont, A. J.; Hoyland, J. A.; Adlam, D. J.; Saunders, B. R., Injectable Doubly Cross-Linked Microgels for Improving the Mechanical Properties of Degenerated Intervertebral Discs. *Biomacromolecules* **2012,** *13* (9), 2793-2801.

147. Zhu, M.; Lu, D.; Wu, S.; Lian, Q.; Wang, W.; Lyon, L. A.; Wang, W.; Bártolo, P.; Saunders, B. R., Using green emitting pH-responsive nanogels to report environmental changes within hydrogels: a nanoprobe for versatile sensing. *Nanoscale* **2019,** *11* (24), 11484-11495.

148. Radhakrishnan, J.; Subramanian, A.; Krishnan, U. M.; Sethuraman, S., Injectable and 3D Bioprinted Polysaccharide Hydrogels: From Cartilage to Osteochondral Tissue Engineering. *Biomacromolecules* **2017,** *18* (1), 1-26.

149. Khan, F.; Ahmad, S. R., Polysaccharides and Their Derivatives for Versatile Tissue Engineering Application. *Macromolecular Bioscience* **2013,** *13* (4), 395-421.

150. Dragan, E. S.; Dinu, M. V., Polysaccharides constructed hydrogels as vehicles for proteins and peptides. A review. *Carbohydrate Polymers* **2019,** *225*, 115210.

151. Pawar, S. N.; Edgar, K. J., Alginate derivatization: a review of chemistry, properties and applications. *Biomaterials* **2012,** *33* (11), 3279-305.

152. Lee, K. Y.; Mooney, D. J., Alginate: properties and biomedical applications. *Prog Polym Sci* **2012,** *37* (1), 106-126.

153. Reakasame, S.; Boccaccini, A. R., Oxidized Alginate-Based Hydrogels for Tissue Engineering Applications: A Review. *Biomacromolecules* **2018,** *19* (1), 3-21.

154. Balakrishnan, B.; Jayakrishnan, A., Self-cross-linking biopolymers as injectable in situ forming biodegradable scaffolds. *Biomaterials* **2005,** *26* (18), 3941-3951.

155. Chen, F.; Tian, M.; Zhang, D.; Wang, J.; Wang, Q.; Yu, X.; Zhang, X.; Wan, C., Preparation and characterization of oxidized alginate covalently cross-linked galactosylated chitosan scaffold for liver tissue engineering. *Materials Science and Engineering: C* **2012,** *32* (2), 310-320.

156. Kasaai, M. R., Determination of the degree of N-acetylation for chitin and chitosan by various NMR spectroscopy techniques: A review. *Carbohydrate Polymers* **2010,** *79* (4), 801-810.

157. Croisier, F.; Jérôme, C., Chitosan-based biomaterials for tissue engineering. *European Polymer Journal* **2013,** *49* (4), 780-792.

158. Bernkop-Schnürch, A.; Dünnhaupt, S., Chitosan-based drug delivery systems. *European Journal of Pharmaceutics and Biopharmaceutics* **2012,** *81* (3), 463-469.

159. Bhattarai, N.; Gunn, J.; Zhang, M., Chitosan-based hydrogels for controlled, localized drug delivery. *Adv Drug Deliv Rev* **2010,** *62* (1), 83-99.

160. Sahariah, P.; Másson, M., Antimicrobial Chitosan and Chitosan Derivatives: A Review of the Structure–Activity Relationship. *Biomacromolecules* **2017,** *18* (11), 3846-3868.

161. de Moraes Crizel, T.; de Oliveira Rios, A.; D. Alves, V.; Bandarra, N.; Moldão-Martins, M.; Hickmann Flôres, S., Active food packaging prepared with chitosan and olive pomace. *Food Hydrocolloids* **2018,** *74*, 139-150.

162. Lee, S.-M.; Liu, K.-H.; Liu, Y.-Y.; Chang, Y.-P.; Lin, C.-C.; Chen, Y.-S., Chitosonic(®) Acid as a Novel Cosmetic Ingredient: Evaluation of its Antimicrobial, Antioxidant and Hydration Activities. *Materials* **2013,** *6* (4), 1391-1402.

163. Saporito, F.; Sandri, G.; Rossi, S.; Bonferoni, M. C.; Riva, F.; Malavasi, L.; Caramella, C.; Ferrari, F., Freeze dried chitosan acetate dressings with glycosaminoglycans and traxenamic acid. *Carbohydrate Polymers* **2018,** *184*, 408-417.

164. Tiwari, S.; Patil, R.; Bahadur, P., Polysaccharide Based Scaffolds for Soft Tissue Engineering Applications. **2019,** *11* (1), 1.

165. Boecker, A.; Daeschler, S. C.; Kneser, U.; Harhaus, L., Relevance and Recent Developments of Chitosan in Peripheral Nerve Surgery. **2019,** *13* (104).

166. Zeng, K.; Groth, T.; Zhang, K., Recent Advances in Artificially Sulfated Polysaccharides for Applications in Cell Growth and Differentiation, Drug Delivery, and Tissue Engineering. **2019,** *20* (6), 737-746.

167. Zhang, L.; Li, K.; Xiao, W.; Zheng, L.; Xiao, Y.; Fan, H.; Zhang, X., Preparation of collagen–chondroitin sulfate–hyaluronic acid hybrid hydrogel scaffolds and cell compatibility in vitro. *Carbohydrate Polymers* **2011,** *84* (1), 118-125.

168. Fan, M.; Ma, Y.; Tan, H.; Jia, Y.; Zou, S.; Guo, S.; Zhao, M.; Huang, H.; Ling, Z.; Chen, Y.; Hu, X., Covalent and injectable chitosan-chondroitin sulfate hydrogels embedded with chitosan microspheres for drug delivery and tissue engineering. *Materials Science and Engineering: C* **2017,** *71*, 67-74.

169. Alinejad, Y.; Adoungotchodo, A.; Hui, E.; Zehtabi, F.; Lerouge, S., An injectable chitosan/chondroitin sulfate hydrogel with tunable mechanical properties for cell therapy/tissue engineering. *International Journal of Biological Macromolecules* **2018,** *113*, 132-141.

170. Collins, M. N.; Birkinshaw, C., Hyaluronic acid based scaffolds for tissue engineering--a review. *Carbohydr Polym* **2013,** *92* (2), 1262-79.

171. Lam, J.; Truong, N. F.; Segura, T., Design of cell-matrix interactions in hyaluronic acid hydrogel scaffolds. *Acta Biomater* **2014,** *10* (4), 1571-80.

172. Loebel, C.; Szczesny, S. E.; Cosgrove, B. D.; Alini, M.; Zenobi-Wong, M.; Mauck, R. L.; Eglin, D., Cross-Linking Chemistry of Tyramine-Modified Hyaluronan Hydrogels Alters Mesenchymal Stem Cell Early Attachment and Behavior. *Biomacromolecules* **2017,** *18* (3), 855-864.

173. Stefanello, T. F.; Couturaud, B.; Szarpak-Jankowska, A.; Fournier, D.; Louage, B.; Garcia, F. P.; Nakamura, C. V.; De Geest, B. G.; Woisel, P.; van der Sanden, B.; Auzely-Velty, R., Coumarin-containing thermoresponsive hyaluronic acid-based nanogels as delivery systems for anticancer chemotherapy. *Nanoscale* **2017,** *9* (33), 12150-12162.

174. Dicker, K. T.; Gurski, L. A.; Pradhan-Bhatt, S.; Witt, R. L.; Farach-Carson, M. C.; Jia, X., Hyaluronan: A simple polysaccharide with diverse biological functions. *Acta Biomaterialia* **2014,** *10* (4), 1558-1570.

175. Basu, A.; Kunduru, K. R.; Abtew, E.; Domb, A. J., Polysaccharide-Based Conjugates for Biomedical Applications. *Bioconjugate Chemistry* **2015,** *26* (8), 1396-1412.

176. Cumpstey, I., Chemical Modification of Polysaccharides. *ISRN Organic Chemistry* **2013,** *2013*, 27.

177. Koschella, A.; Fenn, D.; Illy, N.; Heinze, T., Regioselectively Functionalized Cellulose Derivatives: A Mini Review. *Macromolecular Symposia* **2006,** *244* (1), 59-73.

178. Fox, S. C.; Li, B.; Xu, D.; Edgar, K. J., Regioselective Esterification and Etherification of Cellulose: A Review. *Biomacromolecules* **2011,** *12* (6), 1956-1972.

179. Pierre, G.; Punta, C.; Delattre, C.; Melone, L.; Dubessay, P.; Fiorati, A.; Pastori, N.; Galante, Y. M.; Michaud, P., TEMPO-mediated oxidation of polysaccharides: An ongoing story. *Carbohydrate Polymers* **2017,** *165*, 71-85.

180. Bragd, P. L.; van Bekkum, H.; Besemer, A. C., TEMPO-Mediated Oxidation of Polysaccharides: Survey of Methods and Applications. *Topics in Catalysis* **2004,** *27* (1), 49-66.

181. Šedová, P.; Buffa, R.; Kettou, S.; Huerta-Angeles, G.; Hermannová, M.; Leierová, V.; Šmejkalová, D.; Moravcová, M.; Velebný, V., Preparation of hyaluronan polyaldehyde—a precursor of biopolymer conjugates. *Carbohydrate Research* **2013,** *371*, 8-15.

182. Jaušovec, D.; Vogrinčič, R.; Kokol, V., Introduction of aldehyde vs. carboxylic groups to cellulose nanofibers using laccase/TEMPO mediated oxidation. *Carbohydrate Polymers* **2015,** *116*, 74-85.

183. Kristiansen, K. A.; Potthast, A.; Christensen, B. E., Periodate oxidation of polysaccharides for modification of chemical and physical properties. *Carbohydrate Research* **2010,** *345* (10), 1264-1271.

184. Parikka, K.; Leppänen, A.-S.; Pitkänen, L.; Reunanen, M.; Willför, S.; Tenkanen, M., Oxidation of Polysaccharides by Galactose Oxidase. *Journal of Agricultural and Food Chemistry* **2010,** *58* (1), 262-271.

185. Yoo, S.-H.; Lee, J.-S.; Park, S. Y.; Kim, Y.-S.; Chang, P.-S.; Lee, H. G., Effects of selective oxidation of chitosan on physical and biological properties. *International Journal of Biological Macromolecules* **2005,** *35* (1–2), 27-31.

186. Huerta-Angeles, G.; Nemcova, M.; Prikopova, E.; Smejkalova, D.; Pravda, M.; Kucera, L.; Velebny, V., Reductive alkylation of hyaluronic acid for the synthesis of biocompatible hydrogels by click chemistry. *Carbohydr Polym* **2012,** *90* (4), 1704-11.

187. Chen, H.; Xing, X.; Tan, H.; Jia, Y.; Zhou, T.; Chen, Y.; Ling, Z.; Hu, X., Covalently antibacterial alginate-chitosan hydrogel dressing integrated gelatin microspheres containing tetracycline hydrochloride for wound healing. *Materials Science and Engineering: C* **2017,** *70, Part 1*, 287-295.

188. Lee, K. Y.; Bouhadir, K. H.; Mooney, D. J., Controlled degradation of hydrogels using multi-functional cross-linking molecules. *Biomaterials* **2004,** *25* (13), 2461-2466.

189. Grover, G. N.; Braden, R. L.; Christman, K. L., Oxime Cross-Linked Injectable Hydrogels for Catheter Delivery. *Advanced Materials* **2013,** *25* (21), 2937-2942.

190. Bordenave, N.; Grelier, S.; Coma, V., Advances on Selective C-6 Oxidation of Chitosan by TEMPO. *Biomacromolecules* **2008,** *9* (9), 2377-2382.

191. Nathalie, C.; Xavier, G.; Pierre, W.; Jean Le, B.; Sylvia, C.-J., Design Polysaccharides of Marine Origin: Chemical Modifications to Reach Advanced Versatile Compounds. *Current Organic Chemistry* **2014,** *18* (7), 867-895.

192. Cheng, H. N.; Gu, Q.-M., Enzyme-Catalyzed Modifications of Polysaccharides and Poly(ethylene glycol). *Polymers* **2012**.

193. Huerta-Angeles, G.; Šmejkalová, D.; Chládková, D.; Ehlová, T.; Buffa, R.; Velebný, V., Synthesis of highly substituted amide hyaluronan derivatives with tailored degree of substitution and their crosslinking via click chemistry. *Carbohydrate Polymers* **2011,** *84* (4), 1293-1300.

194. Pawar, S. N.; Edgar, K. J., Chemical Modification of Alginates in Organic Solvent Systems. *Biomacromolecules* **2011,** *12* (11), 4095-4103.

195. Sahoo, S.; Chung, C.; Khetan, S.; Burdick, J. A., Hydrolytically Degradable Hyaluronic Acid Hydrogels with Controlled Temporal Structures. *Biomacromolecules* **2008,** *9* (4), 1088-1092.

196. Gavalyan, V. B., Synthesis and characterization of new chitosan-based Schiff base compounds. *Carbohydrate Polymers* **2016,** *145*, 37-47.

197. Yavvari, P. S.; Srivastava, A., Robust, self-healing hydrogels synthesised from catechol rich polymers. *Journal of Materials Chemistry B* **2015,** *3* (5), 899-910.

198. Verlee, A.; Mincke, S.; Stevens, C. V., Recent developments in antibacterial and antifungal chitosan and its derivatives. *Carbohydrate Polymers* **2017,** *164*, 268-283.

199. Sashiwa, H.; Yamamori, N.; Ichinose, Y.; Sunamoto, J.; Aiba, S.-i., Chemical Modification of Chitosan, 17. *Macromolecular Bioscience* **2003,** *3* (5), 231-233.

200. Mourya, V. K.; Inamdar, N. N., Trimethyl chitosan and its applications in drug delivery. *Journal of Materials Science: Materials in Medicine* **2008,** *20* (5), 1057.

201. Usman, A.; Zia, K. M.; Zuber, M.; Tabasum, S.; Rehman, S.; Zia, F., Chitin and chitosan based polyurethanes: A review of recent advances and prospective biomedical applications. *Int J Biol Macromol* **2016,** *86*, 630-45.

202. Ryu, J. H.; Lee, Y.; Kong, W. H.; Kim, T. G.; Park, T. G.; Lee, H., Catechol-Functionalized Chitosan/Pluronic Hydrogels for Tissue Adhesives and Hemostatic Materials. *Biomacromolecules* **2011,** *12* (7), 2653-2659.

203. Prabaharan, M.; Mano, J. F., Stimuli-Responsive Hydrogels Based on Polysaccharides Incorporated with Thermo-Responsive Polymers as Novel Biomaterials. *Macromolecular Bioscience* **2006,** *6* (12), 991-1008.

204. Tizzotti, M.; Charlot, A.; Fleury, E.; Stenzel, M.; Bernard, J., Modification of Polysaccharides Through Controlled/Living Radical Polymerization Grafting—Towards the Generation of High Performance Hybrids. **2010,** *31* (20), 1751-1772.

205. Pei, M.; Mao, J.; Xu, W.; Zhou, Y.; Xiao, P., Photocrosslinkable chitosan hydrogels and their biomedical applications. *0* (0).

206. Rask, F.; Dallabrida, S. M.; Ismail, N. S.; Amoozgar, Z.; Yeo, Y.; Rupnick, M. A.; Radisic, M., Photocrosslinkable chitosan modified with angiopoietin-1 peptide, QHREDGS, promotes survival of neonatal rat heart cells. **2010,** *95A* (1), 105-117.

207. Elchinger, P.-H.; Faugeras, P.-A.; Boëns, B.; Brouillette, F.; Montplaisir, D.; Zerrouki, R.; Lucas, R., Polysaccharides: The "Click" Chemistry Impact. *Polymers* **2011,** *3* (4), 1607.

208. Kirschning, A.; Dibbert, N.; Dräger, G., Chemical Functionalization of Polysaccharides—Towards Biocompatible Hydrogels for Biomedical Applications. **2018,** *24* (6), 1231-1240.

209. Famili, A.; Rajagopal, K., Bio-Orthogonal Cross-Linking Chemistry Enables In Situ Protein Encapsulation and Provides Sustained Release from Hyaluronic Acid Based Hydrogels. *Molecular Pharmaceutics* **2017,** *14* (6), 1961-1968.

210. Jirawutthiwongchai, J.; Krause, A.; Draeger, G.; Chirachanchai, S., Chitosan-Oxanorbornadiene: A Convenient Chitosan Derivative for Click Chemistry without Metal Catalyst Problem. *ACS Macro Letters* **2013,** *2* (3), 177-180.

211. Zhou, Y.; Zhao, S.; Zhang, C.; Liang, K.; Li, J.; Yang, H.; Gu, S.; Bai, Z.; Ye, D.; Xu, W., Photopolymerized maleilated chitosan/thiol-terminated poly (vinyl alcohol) hydrogels as potential tissue engineering scaffolds. *Carbohydrate Polymers* **2018,** *184*, 383-389.

212. Liu, H.; Wang, C.; Li, C.; Qin, Y.; Wang, Z.; Yang, F.; Li, Z.; Wang, J., A functional chitosan-based hydrogel as a wound dressing and drug delivery system in the treatment of wound healing. *RSC Advances* **2018,** *8* (14), 7533-7549.

213. administration, F. Dermal Fillers Approved by the Center for Devices and Radiological Health. https://www.fda.gov/medical-devices/cosmetic-devices/dermal-fillers-approved-center-devices-and-radiological-health (accessed 06/09/2019).

214. Larson, B. J., Longaker, M. T., Lorenz, H. P, Scarless fetal wound healing: a basic science review. *Plastic and Reconstructive Surgery* **2010,** *126* (4), 1172-1180.

215. Bhattacharjee, S., DLS and zeta potential – What they are and what they are not? *Journal of Controlled Release* **2016,** *235*, 337-351.

216. Heenan, R. K.; Rogers, S. E.; Turner, D.; Terry, A. E.; Treadgold, J.; King, S. M., Small Angle Neutron Scattering Using Sans2d. *Neutron News* **2011,** *22* (2), 19-21.

217. Heenan, R.; King, S.; Turner, D. S.; Treadgold, J. R., SANS2D at the ISIS Second Target Station. **2006**.

218. Wignall, G. D.; Bates, F. S., Absolute calibration of small-angle neutron scattering data. **1987,** *20* (1), 28-40.

219. Chaboussant, G.; Désert, S.; Lavie, P.; Brûlet, A., PA20 : A new SANS and GISANS project for soft matter, materials and magnetism. *Journal of Physics: Conference Series* **2012,** *340*, 012002.

220. Hammouda, B., *Probing Nanoscale Structures – The SANS Toolbox*. Available online: 2009.

221. Castellanos, M. M.; McAuley, A.; Curtis, J. E., Investigating Structure and Dynamics of Proteins in Amorphous Phases Using Neutron Scattering. *Computational and Structural Biotechnology Journal* **2017,** *15*, 117-130.

222. Malo de Molina, P.; Zhang, M.; Bayles, A. V.; Helgeson, M. E., Oil-in-Water-in-Oil Multinanoemulsions for Templating Complex Nanoparticles. *Nano Letters* **2016,** *16* (12), 7325-7332.

223. Wertheim, M. S., Exact Solution of the Percus-Yevick Integral Equation for Hard Spheres. *Physical Review Letters* **1963,** *10* (8), 321-323.

224. Shibayama, M.; Tanaka, T.; Han, C. C., Small angle neutron scattering study on poly(N‐isopropyl acrylamide) gels near their volume‐phase transition temperature. **1992,** *97* (9), 6829-6841.

225. Hammouda, B., A new Guinier–Porod model. *Journal of Applied Crystallography* **2010,** *43*, 716-719.

226. Foster, T.; Sottmann, T.; Schweins, R.; Strey, R., Small-angle neutron scattering from giant water-in-oil microemulsion droplets. I. Ternary system. **2008,** *128* (5), 054502.

227. Gradzielski, M.; Langevin, D.; Magid, L.; Strey, R., Small-Angle Neutron Scattering from Diffuse Interfaces. 2. Polydisperse Shells in Water-n-Alkane-C10E4 Microemulsions. *The Journal of Physical Chemistry* **1995,** *99* (35), 13232-13238.

228. Bagger-Jörgensen, H.; Olsson, U.; Mortensen, K., Microstructure in a Ternary Microemulsion Studied by Small Angle Neutron Scattering. *Langmuir* **1997,** *13* (6), 1413-1421.

229. Lisy, V.; Brutovsky, B., Interpretation of static and dynamic neutron and light scattering from microemulsion droplets: Effects of shape fluctuations. *Physical Review E* **2000,** *61* (4), 4045-4053.

230. Foster, T.; Sottmann, T.; Schweins, R.; Strey, R., Small-angle-neutron-scattering from giant water-in-oil microemulsion droplets. II. Polymer-decorated droplets in a quaternary system. **2008,** *128* (6), 064902.

231. Horkay, F.; Hecht, A. M.; Mallam, S.; Geissler, E.; Rennie, A. R., Macroscopic and microscopic thermodynamic observations in swollen poly(vinyl acetate) networks. *Macromolecules* **1991,** *24* (10), 2896-2902.

232. Mallam, S.; Horkay, F.; Hecht, A. M.; Rennie, A. R.; Geissler, E., Microscopic and macroscopic thermodynamic observations in swollen poly(dimethylsiloxane) networks. *Macromolecules* **1991,** *24* (2), 543-548.

233. Gomes, C.; Dias, R. C. S.; Costa, M. R. P. F. N., Static Light Scattering Monitoring and Kinetic Modeling of Polyacrylamide Hydrogel Synthesis. **2019,** *7* (4), 237.

234. Chalal, M.; Ehrburger-Dolle, F.; Morfin, I.; Bley, F.; Aguilar de Armas, M.-R.; López Donaire, M.-L.; San Roman, J.; Bölgen, N.; Pişkin, E.; Ziane, O.; Casalegno, R., SAXS Investigation of the Effect of Temperature on the Multiscale Structure of a Macroporous Poly(N-isopropylacrylamide) Gel. *Macromolecules* **2010,** *43* (4), 2009-2017.

235. Hammouda, B.; Ho, D. L.; Kline, S., Insight into Clustering in Poly(ethylene oxide) Solutions. *Macromolecules* **2004,** *37* (18), 6932-6937.

236. Mears, S. J.; Deng, Y.; Cosgrove, T.; Pelton, R., Structure of Sodium Dodecyl Sulfate Bound to a Poly(NIPAM) Microgel Particle. *Langmuir* **1997,** *13* (7), 1901-1906.

237. Hyland, L. L.; Taraban, M. B.; Hammouda, B.; Bruce Yu, Y., Mutually reinforced multicomponent polysaccharide networks. **2011,** *95* (12), 840-851.

238. Hyland, L. L.; Taraban, M. B.; Feng, Y.; Hammouda, B.; Yu, Y. B., Viscoelastic properties and nanoscale structures of composite oligopeptide-polysaccharide hydrogels. *Biopolymers* **2012,** *97* (3), 177-88.

239. Debye, P.; Bueche, A. M., Scattering by an Inhomogeneous Solid. **1949,** *20* (6), 518-525.

240. Soni, V. K.; Stein, R. S., Light scattering studies of poly(dimethylsiloxane) solutions and swollen networks. *Macromolecules* **1990,** *23* (25), 5257-5265.

241. Crompton, K. E.; Forsythe, J. S.; Horne, M. K.; Finkelstein, D. I.; Knott, R. B., Molecular level and microstructural characterisation of thermally sensitive chitosan hydrogels. *Soft Matter* **2009,** *5* (23), 4704-4711.

242. Ryu, J.; Kim, S.; Oh, I.; Kato, S.; Kosuge, T.; Sokolova, A. V.; Lee, J.; Otsuka, H.; Sohn, D., Internal Structure of Hyaluronic Acid Hydrogels Controlled by Iron(III) Ion–Catechol Complexation. *Macromolecules* **2019**.

243. Saunders, B. R., On the Structure of Poly(N-isopropylacrylamide) Microgel Particles. *Langmuir* **2004,** *20* (10), 3925-3932.

244. Stieger, M.; Richtering, W.; Pedersen, J. S.; Lindner, P., Small-angle neutron scattering study of structural changes in temperature sensitive microgel colloids. **2004,** *120* (13), 6197-6206.

245. Stieger, M.; Pedersen, J. S.; Lindner, P.; Richtering, W., Are Thermoresponsive Microgels Model Systems for Concentrated Colloidal Suspensions? A Rheology and Small-Angle Neutron Scattering Study. *Langmuir* **2004,** *20* (17), 7283-7292.

246. Aguirre, G.; Deniau, E.; Brûlet, A.; Chougrani, K.; Alard, V.; Billon, L., Versatile oligo(ethylene glycol)-based biocompatible microgels for loading/release of active bio(macro)molecules. *Colloids and Surfaces B: Biointerfaces* **2019,** *175*, 445-453.

247. Berndt, I.; Pedersen, J. S.; Lindner, P.; Richtering, W., Influence of Shell Thickness and Cross-Link Density on the Structure of Temperature-Sensitive Poly-N-Isopropylacrylamide−Poly-N-Isopropylmethacrylamide Core−Shell Microgels Investigated by Small-Angle Neutron Scattering. *Langmuir* **2006,** *22* (1), 459-468.

248. Schneider, F.; Balaceanu, A.; Feoktystov, A.; Pipich, V.; Wu, Y.; Allgaier, J.; Pyckhout-Hintzen, W.; Pich, A.; Schneider, G. J., Monitoring the Internal Structure of Poly(N-vinylcaprolactam) Microgels with Variable Cross-Link Concentration. *Langmuir* **2014,** *30* (50), 15317-15326.

249. Dawn, A.; Kumari, H., Low Molecular Weight Supramolecular Gels Under Shear: Rheology as the Tool for Elucidating Structure–Function Correlation. **2018,** *24* (4), 762-776.

250. Hirai, A.; Odani, H.; Nakajima, A., Determination of degree of deacetylation of chitosan by 1H NMR spectroscopy. *Polymer Bulletin* **1991,** *26* (1), 87-94.

251. Li, C.; Han, Q.; Guan, Y.; Zhang, Y., Michael reaction of chitosan with acrylamides in an aqueous alkali–urea solution. *Polymer Bulletin* **2015,** *72* (8), 2075-2087.

252. Kast, C. E.; Bernkop-Schnürch, A., Thiolated polymers — thiomers: development and in vitro evaluation of chitosan–thioglycolic acid conjugates. *Biomaterials* **2001,** *22* (17), 2345-2352.

253. Bernkop-Schnürch, A.; Hornof, M.; Zoidl, T., Thiolated polymers—thiomers: synthesis and in vitro evaluation of chitosan–2-iminothiolane conjugates. *International Journal of Pharmaceutics* **2003,** *260* (2), 229-237.

254. Yu, L. M. Y.; Kazazian, K.; Shoichet, M. S., Peptide surface modification of methacrylamide chitosan for neural tissue engineering applications. **2007,** *82A* (1), 243-255.

255. Hachet, E.; Sereni, N.; Pignot-Paintrand, I.; Ravaine, V.; Szarpak-Jankowska, A.; Auzely-Velty, R., Thiol-ene clickable hyaluronans: from macro-to nanogels. *J Colloid Interface Sci* **2014,** *419*, 52-5.

256. Presolski, S. I.; Hong, V. P.; Finn, M. G., Copper-Catalyzed Azide-Alkyne Click Chemistry for Bioconjugation. *Curr Protoc Chem Biol* **2011,** *3* (4), 153-162.

257. Kim, S.; Cui, Z.-K.; Koo, B.; Zheng, J.; Aghaloo, T.; Lee, M., Chitosan–Lysozyme Conjugates for Enzyme-Triggered Hydrogel Degradation in Tissue Engineering Applications. *ACS Applied Materials & Interfaces* **2018,** *10* (48), 41138-41145.

258. Su, J., Thiol-Mediated Chemoselective Strategies for In Situ Formation of Hydrogels. **2018,** *4* (3), 72.

259. Bravo-Osuna, I.; Teutonico, D.; Arpicco, S.; Vauthier, C.; Ponchel, G., Characterization of chitosan thiolation and application to thiol quantification onto nanoparticle surface. *International Journal of Pharmaceutics* **2007,** *340* (1), 173-181.

260. Ellman, G. L.; Courtney, K. D.; Andres, V.; Featherstone, R. M., A new and rapid colorimetric determination of acetylcholinesterase activity. *Biochemical Pharmacology* **1961,** *7* (2), 88-95.

261. Moser, M.; Schneider, R.; Behnke, T.; Schneider, T.; Falkenhagen, J.; Resch-Genger, U., Ellman's and Aldrithiol Assay as Versatile and Complementary Tools for the Quantification of Thiol Groups and Ligands on Nanomaterials. *Analytical Chemistry* **2016,** *88* (17), 8624-8631.

262. Sornkamnerd, S.; Okajima, M. K.; Kaneko, T., Tough and Porous Hydrogels Prepared by Simple Lyophilization of LC Gels. *ACS Omega* **2017,** *2* (8), 5304-5314.

263. Wisniewska, M. A.; Seland, J. G.; Wang, W., Determining the scaling of gel mesh size with changing crosslinker concentration using dynamic swelling, rheometry, and PGSE NMR spectroscopy. **2018,** *135* (45), 46695.

264. Fraser, A. K.; Ki, C. S.; Lin, C.-C., PEG-Based Microgels Formed by Visible-Light-Mediated Thiol-Ene Photo-Click Reactions. *Macromolecular Chemistry and Physics* **2014,** *215* (6), 507-515.

265. Williams, C. G.; Malik, A. N.; Kim, T. K.; Manson, P. N.; Elisseeff, J. H., Variable cytocompatibility of six cell lines with photoinitiators used for polymerizing hydrogels and cell encapsulation. *Biomaterials* **2005,** *26* (11), 1211-1218.

266. Lee, S.; Park, Y. H.; Ki, C. S., Fabrication of PEG-carboxymethylcellulose hydrogel by thiol-norbornene photo-click chemistry. *Int J Biol Macromol* **2016,** *83*, 1-8.

267. Mergy, J.; Fournier, A.; Hachet, E.; Auzély-Velty, R., Modification of polysaccharides via thiol-ene chemistry: A versatile route to functional biomaterials. *Journal of Polymer Science Part A: Polymer Chemistry* **2012,** *50* (19), 4019-4028.

268. Chang, C.; He, M.; Zhou, J.; Zhang, L., Swelling Behaviors of pH- and Salt-Responsive Cellulose-Based Hydrogels. *Macromolecules* **2011,** *44* (6), 1642-1648.

269. Ye, D.; Chang, C.; Zhang, L., High-Strength and Tough Cellulose Hydrogels Chemically Dual Cross-Linked by Using Low- and High-Molecular-Weight Cross-Linkers. *Biomacromolecules* **2019,** *20* (5), 1989-1995.

270. Li, X.; Katsanevakis, E.; Liu, X.; Zhang, N.; Wen, X., Engineering neural stem cell fates with hydrogel design for central nervous system regeneration. *Progress in Polymer Science* **2012,** *37* (8), 1105-1129.

271. Hung, K.-C.; Jeng, U. S.; Hsu, S.-h., Fractal Structure of Hydrogels Modulates Stem Cell Behavior. *ACS Macro Letters* **2015,** *4* (9), 1056-1061.

272. Gupta, A.; Kowalczuk, M.; Heaselgrave, W.; Britland, S. T.; Martin, C.; Radecka, I., The production and application of hydrogels for wound management: A review. *European Polymer Journal* **2019,** *111*, 134-151.

273. Moore, A. L.; Marshall, C. D.; Barnes, L. A.; Murphy, M. P.; Ransom, R. C.; Longaker, M. T., Scarless wound healing: Transitioning from fetal research to regenerative healing. **2018,** *7* (2), e309.

274. Achterberg, V. F.; Buscemi, L.; Diekmann, H.; Smith-Clerc, J.; Schwengler, H.; Meister, J.-J.; Wenck, H.; Gallinat, S.; Hinz, B., The Nano-Scale Mechanical Properties of the Extracellular Matrix Regulate Dermal Fibroblast Function. *Journal of Investigative Dermatology* **2014,** *134* (7), 1862-1872.

275. Wong, M. K.; Shawky, S. A.; Aryasomayajula, A.; Green, M. A.; Ewart, T.; Selvaganapathy, P. R.; Raha, S., Extracellular matrix surface regulates self-assembly of three-dimensional placental trophoblast spheroids. *PLOS ONE* **2018,** *13* (6), e0199632.

276. Çolak, A.; Li, B.; Blass, J.; Koynov, K.; del Campo, A.; Bennewitz, R., The mechanics of single cross-links which mediate cell attachment at a hydrogel surface. *Nanoscale* **2019,** *11* (24), 11596-11604.

277. Jiang, Y.; Deng, Y.; Tu, Y.; Ay, B.; Sun, X.; Li, Y.; Wang, X.; Chen, X.; Zhang, L., Chitosan-based asymmetric topological membranes with cell-like features for healthcare applications. *Journal of Materials Chemistry B* **2019,** *7* (16), 2634-2642.

278. Park, K. M.; Joung, Y. K.; Park, K. D.; Lee, S. Y.; Lee, M. C. J. M. R., RGD-Conjugated chitosan-pluronic hydrogels as a cell supported scaffold for articular cartilage regeneration. **2008,** *16* (6), 517-523.

279. Deng, Y.; Ren, J.; Chen, G.; Li, G.; Wu, X.; Wang, G.; Gu, G.; Li, J., Injectable in situ cross-linking chitosan-hyaluronic acid based hydrogels for abdominal tissue regeneration. *Scientific Reports* **2017,** *7* (1), 2699.

280. Reyna-Urrutia, V. A.; Mata-Haro, V.; Cauich-Rodriguez, J. V.; Herrera-Kao, W. A.; Cervantes-Uc, J. M., Effect of two crosslinking methods on the physicochemical and biological properties of the collagen-chitosan scaffolds. *European Polymer Journal* **2019,** *117*, 424-433.

281. da Silva, M. A.; Bode, F.; Drake, A. F.; Goldoni, S.; Stevens, M. M.; Dreiss, C. A., Enzymatically Cross-Linked Gelatin/Chitosan Hydrogels: Tuning Gel Properties and Cellular Response. **2014,** *14* (6), 817-830.

282. Yang, H.; Shen, L.; Bu, H.; Li, G., Stable and biocompatible hydrogel composites based on collagen and dialdehyde carboxymethyl cellulose in a biphasic solvent system. *Carbohydrate Polymers* **2019,** *222*, 114974.

283. Hook, B. D. A.; Dohle, W.; Hirst, P. R.; Pickworth, M.; Berry, M. B.; Booker-Milburn, K. I., A Practical Flow Reactor for Continuous Organic Photochemistry. *The Journal of Organic Chemistry* **2005,** *70* (19), 7558-7564.

284. Davies, R.; Graham, D.; Vincent, B., *Water-cyclohexane-"Span 80"-"Tween 80" systems: Solution properties and water/oil emulsion formation*. 1987; Vol. 116, p 88-99.

285. Michel, S. E. S.; Dutertre, F.; Denbow, M. L.; Galan, M. C.; Briscoe, W. H., Facile Synthesis of Chitosan-Based Hydrogels and Microgels through Thiol–Ene Photoclick Cross-Linking. *ACS Applied Bio Materials* **2019,** *2* (8), 3257-3268.

286. Paul, A.; Fallis, I.; Cooper, C.; Wess, T.; Thomas, K.; Heenan, R.; King, S.; Griffiths, P., A contrast variation small-angle scattering study of the microstructure of 2,5-dimethyl-7-hydroxy-2,5-diazaheptadecane–toluene–butanol oil-in-water metallomicroemulsions. *Soft Matter* **2010,** *6* (11), 2552-2556.

287. P. Lindner, T. Z., Scattering by Microemulsions. In *Neutrons, X-rays and Light: Scattering Methods Applied to Soft Condensed Matter*, North-Holland, Ed. Elsevier: 2002; pp 317-350.

288. Devaraj, N. K.; Hilderbrand, S.; Upadhyay, R.; Mazitschek, R.; Weissleder, R., Bioorthogonal Turn-On Probes for Imaging Small Molecules inside Living Cells. **2010,** *49* (16), 2869-2872.

289. Evans, H. L.; Nguyen, Q.-D.; Carroll, L. S.; Kaliszczak, M.; Twyman, F. J.; Spivey, A. C.; Aboagye, E. O., A bioorthogonal 68Ga-labelling strategy for rapid in vivo imaging. *Chemical Communications* **2014,** *50* (67), 9557-9560.

290. Goycoolea, F. M.; Lollo, G.; Remuñán-López, C.; Quaglia, F.; Alonso, M. J., Chitosan-Alginate Blended Nanoparticles as Carriers for the Transmucosal Delivery of Macromolecules. *Biomacromolecules* **2009,** *10* (7), 1736-1743.

291. Kocak, G.; Tuncer, C.; Bütün, V., pH-Responsive polymers. *Polymer Chemistry* **2017,** *8* (1), 144-176.

292. Everaers, R.; Grosberg, A. Y.; Rubinstein, M.; Rosa, A., Flory theory of randomly branched polymers. *Soft Matter* **2017,** *13* (6), 1223-1234.

293. Mohammed, M. A.; Syeda, J. T. M.; Wasan, K. M.; Wasan, E. K., An Overview of Chitosan Nanoparticles and Its Application in Non-Parenteral Drug Delivery. **2017,** *9* (4), 53.

294. Wang, Q. Z.; Chen, X. G.; Liu, N.; Wang, S. X.; Liu, C. S.; Meng, X. H.; Liu, C. G., Protonation constants of chitosan with different molecular weight and degree of deacetylation. *Carbohydrate Polymers* **2006,** *65* (2), 194-201.

295. Fan, M.; Hu, Q., Chitosan-LiOH-urea aqueous solution--a novel water-based system for chitosan processing. *Carbohydr Res* **2009,** *344* (7), 944-7.

296. Li, C.; Han, Q.; Guan, Y.; Zhang, Y., Thermal gelation of chitosan in an aqueous alkali-urea solution. *Soft Matter* **2014,** *10* (41), 8245-8253.

297. Knall, A.-C.; Slugovc, C., Inverse electron demand Diels-Alder (iEDDA)-initiated conjugation: a (high) potential click chemistry scheme. *Chemical Society Reviews* **2013,** *42* (12), 5131-5142.

298. Oliveira, B. L.; Guo, Z.; Bernardes, G. J. L., Inverse electron demand Diels–Alder reactions in chemical biology. *Chemical Society Reviews* **2017,** *46* (16), 4895-4950.

299. Worch, J. C.; Prydderch, H.; Jimaja, S.; Bexis, P.; Becker, M. L.; Dove, A. P., Stereochemical enhancement of polymer properties. *Nature Reviews Chemistry* **2019**.

300. Xu, Y.-M.; Li, K.; Wang, Y.; Deng, W.; Yao, Z.-J., *Mononuclear Nickel(II) Complexes with Schiff Base Ligands: Synthesis, Characterization, and Catalytic Activity in Norbornene Polymerization*. 2017; Vol. 9, p 105.

301. Saha, K.; Keung, A. J.; Irwin, E. F.; Li, Y.; Little, L.; Schaffer, D. V.; Healy, K. E., Substrate Modulus Directs Neural Stem Cell Behavior. *Biophysical Journal* **2008,** *95* (9), 4426-4438.

302. Mauri, E.; Sacchetti, A.; Vicario, N.; Peruzzotti-Jametti, L.; Rossi, F.; Pluchino, S., Evaluation of RGD functionalization in hybrid hydrogels as 3D neural stem cell culture systems. *Biomaterials Science* **2018,** *6* (3), 501-510.

303. Kornev, V. A.; Grebenik, E. A.; Solovieva, A. B.; Dmitriev, R. I.; Timashev, P. S., Hydrogel-assisted neuroregeneration approaches towards brain injury therapy: A state-of-the-art review. *Computational and Structural Biotechnology Journal* **2018,** *16*, 488-502.

304. Valmikinathan, C. M.; Mukhatyar, V. J.; Jain, A.; Karumbaiah, L.; Dasari, M.; Bellamkonda, R. V., Photocrosslinkable chitosan based hydrogels for neural tissue engineering. *Soft Matter* **2012,** *8* (6), 1964-1976.

305. Jakubiak, J.; Allonas, X.; Fouassier, J. P.; Sionkowska, A.; Andrzejewska, E.; Linden, L. Å.; Rabek, J. F., Camphorquinone–amines photoinitating systems for the initiation of free radical polymerization. *Polymer* **2003,** *44* (18), 5219-5226.

306. Cramer, N. B.; Bowman, C. N., CHAPTER 1 Thiol‐ene and Thiol‐yne Chemistry in Ideal Network Synthesis. In *Thiol-X Chemistries in Polymer and Materials Science*, The Royal Society of Chemistry: 2013; pp 1-27.

307. Shafei, A.; El-Bakly, W.; Sobhy, A.; Wagdy, O.; Reda, A.; Aboelenin, O.; Marzouk, A.; El Habak, K.; Mostafa, R.; Ali, M. A.; Ellithy, M., A review on the efficacy and toxicity of different doxorubicin nanoparticles for targeted therapy in metastatic breast cancer. *Biomedicine & Pharmacotherapy* **2017,** *95*, 1209-1218.

308. Klán, P.; Šolomek, T.; Bochet, C. G.; Blanc, A.; Givens, R.; Rubina, M.; Popik, V.; Kostikov, A.; Wirz, J., Photoremovable Protecting Groups in Chemistry and Biology: Reaction Mechanisms and Efficacy. *Chemical Reviews* **2013,** *113* (1), 119-191.

309. Shazly, T. M.; Baker, A. B.; Naber, J. R.; Bon, A.; Van Vliet, K. J.; Edelman, E. R., Augmentation of postswelling surgical sealant potential of adhesive hydrogels. **2010,** *95A* (4), 1159-1169.

310. Pek, Y. S.; Wan, A. C. A.; Ying, J. Y., The effect of matrix stiffness on mesenchymal stem cell differentiation in a 3D thixotropic gel. *Biomaterials* **2010,** *31*.

311. Discher, D. E.; Janmey, P. A.; Wang, Y.-L., Tissue Cells Feel and Respond to the Stiffness of Their Substrate. *Science* **2005,** *310*.